CONTINUOUS RAM EXTRUSION OF POLYMERS

by

BASILIO YI

January 1975

Thesis presented for the degree of

Doctor of Philosophy

of the

University of London

Department of Mechanical Engineering
Imperial College of Science and Technology
London SW7 2BX

ABSTRACT

The present work describes an experimental and theoretical investigation into a novel method of extruding polymers in which the melting and mixing (plasticating) functions can be controlled largely independently of output rate, thus providing the process with extra versatility.

A machine based on a prototype model consisting essentially of a pair of rams used for pumping polymer through an annular plasticating cell formed by a rotating mandrel inside a barrel was constructed, and various aspects of its performance were studied experimentally.

The operations involved in the process, namely the feeding of the solid polymer, the melting of the feedstock and the flow and mixing of the resulting melt were analysed theoretically. The outcome of this was a computer model for predicting the performance of the machine. Satisfactory correlation of theoretical results with experimental ones was obtained and the model was used for studying the effects of varying operating conditions, material properties and extruder channel geometry on the process. Likely output rates from scaled-up versions of the present extruder were also determined using the theoretical model.

In general, the results obtained have confirmed the versatility and flexibility of the method and its commercial success is envisaged in certain types of applications.

ACKNOWLEDGEMENTS

I would like to thank my supervisor, Dr R.T. Fenner, for his advice and encouragement during the course of this project.

I also wish to thank the staff of the Polymer Processing Laboratory for their valuable assistance in carrying out the experimental work, in particular Mr S.G.W.G. Watts and Mr H. Weinberg who executed much of the detailed design work on the rig.

Thanks are also due to Miss E.A. Quin for the accomplished typing of the manuscript.

Finance for the project was provided by the Science Research Council.

Lastly, I wish to express my gratitude to my parents who made everything possible.

B. Yi
January 1975

CONTENTS

Tables, plates or figures related to a particular chapter appear at the end of that chapter.

NOTATION

Most of the symbols used are defined as they arise. Some of the more frequent and important ones are listed here for convenience.

b	:	temperature coefficient of viscosity at constant shear rate
c_m	:	melt specific heat at constant pressure
c_s	:	specific heat of solid polymer
dW^*	:	*melting rate
D_c	:	internal diameter of feed cylinder
E_p	:	rate of storage of pressure energy
E_T	:	rate of storage of thermal energy
H	:	**local thickness
H_o	:	*initial melt film thickness
k	:	ratio of lateral to axial pressure
km	:	thermal conductivity of polymer melt
ks	:	thermal conductivity of solid polymer
L_s	:	length of compacted solid material in feed cylinder
$\dot{m}$	:	**mass flow rate
$\dot{M}$	:	mass output rate of extruder
n	:	power-law index
p	:	pressure in the material
$p_{bb,\ etc.}$	:	axial pressure at section bb, etc.
p_o	:	pressure exerted by feed ram
$p_{r,\theta}$	:	normal stresses in cylindrical coordinate system
p_T	:	pressure transmitted through material
p_z	:	pressure in the flow direction
$p_{\nu,\phi}$	:	normal stresses in spherical coordinate system

P_z : pressure gradient

Q : volumetric output rate of extruder

R : radius of feed cylinder

R_i : shaft radius

R_o, R'_o : outside radius of annulus

T : temperature

T_b : barrel temperature

T_B : block temperature

T_m : melting point of polymer

T_o : datum temperature for viscosity determinations

T_r : boundary temperature

T_{room} : room temperature

T_{shaft} : shaft temperature

T' : initial temperature profile

$\overline{T}$: bulk mean temperature

U_r : relative velocity

v : melt velocity due to motion of plug

v_x : velocity component in melt flow

v_z : velocity component in melt flow

V : velocity of shaft

V_p : velocity of plug

V_{sz} : velocity of solid bed in z-direction

$\dot{W}$: shaft power

$\dot{W}_T$: total power consumption

z_L : melting zone length

β : angle between feed cylinders and barrel axis

$\dot{\gamma}_o$: datum shear rate for evaluation of viscosities

δ : polymer/metal angle of friction

δ_i : internal angle of friction

Δp_L : pressure drop in melting zone

ΔR, $\Delta R'$: annular gap

η : +variable in stress distribution

λ : latent heat of fusion

μ : '*apparent viscosity of polymer melt

μ_f : polymer/metal coefficient of friction

μ_i : internal coefficient of friction

μ_o : datum viscosity

ξ : +variable in stress distribution

π_p : '*dimensionless pressure gradient

π_Q : '*dimensionless volumetric flow rate

ρ_B : bulk density of granular polymer

ρ_m : density of melt

ρ_s : density of solid polymer

σ : +parameter with units of stress

$\sigma_{n,t}$: normal stresses in nt coordinate system

$\sigma_{x,y,z}$: normal stresses in rectangular coordinate system

$\sigma_{1,2,3}$: principal stresses

τ : '*shear stress in melt film

τ_{nt} : shear stress in nt coordinate system

$\tau_{xy,\ etc.}$: shear stresses in rectangular coordinate system

ω_{sub} : inclination of line of discontinuity denoted by sub

$\emptyset$: +angle between x-axis and direction of σ_1

Φ : integration constant

' * also subscripted by 1 referring to melt film adjacent to barrel

and by 2 referring to melt film adjacent to shaft

** same as above but also subscripted by s referring to the solid polymer

+ also subscripted by a number to denote value of variable in a region

by a letter to denote value of variable at a point

and by two letters to denote value of variable along a line

Because of the large number of variables involved, some symbols may have more than one meaning. Confusion should not arise from this however, since they are defined and used locally only.

CHAPTER 1

INTRODUCTION

1.1 The Role of Extrusion in the Polymer Processing Industry

The polymer processing industry uses a variety of machines in the operations which transform a raw material into the finished product. For example, the basic polymer is first produced from relatively simple chemicals in a reactor by the process called polymerisation. From the chemical reactor, the material is fed into a homogeniser where it is thoroughly mixed, the purpose of which is to create a product with properties as uniform as possible. The most commonly used homogenisers are large screw extruders, the design of which is a highly specialised subject [1].

The material leaving the homogeniser is usually solidified in a convenient form, e.g. powder, granules, beads, etc., and stored for future use. The virgin polymer is often not of immediate practical use and many additives such as colour pigments, fillers, lubricants, etc., are compounded with the basic polymer to give what is generally known as a "plastic", at an intermediate stage before final product shaping occurs. At this stage therefore, the polymer has to be remelted and thoroughly mixed once more. For this operation, again screw devices are the most popular ones and they are found in, besides plasticating extruders for continuous extrusion, many plasticating units for injection and blow moulding machines.

Screw plasticating units and plasticating extruders are very similar both in their physical appearance and in operation. They only differ in that pressure generation in plasticating units is not a prime requirement whilst in the extruder, the ability to maintain a uniform

pressure is essential for continuous product extrusion. They both share the common requirements of producing the right amount of molten material with a deformation and thermal history as uniform as possible. In the extruder this process must be continuous and for moulding purposes it may be intermittent.

It is in the extrusion and injection moulding section of the industry that competition is keenest and therefore it is not surprising to find the very wide variety of machines available in the market. Although the number of injection moulding machines in operation by far exceeds that of plasticating extruders, extrusion is equally important in terms of the tonnage of material that is processed annually. Included in this are the extrudates for other processes like vacuum forming, film blowing and coating applications.

There are other processes like casting and calendering which have not been mentioned so far. These are only a very small activity compared with extrusion. Thus, considering that many plasticating units function like extruders, there is no doubt that extrusion is a very important operation in the polymer processing industry either in the production of raw materials as in the homogenisation of newly polymerised materials, or as an intermediate operation like that found in plasticating units for moulding machines, or as a product finishing process such as in the continuous extrusion of profiles.

1.2 The Single Screw Extruder and its Principles of Operation

It should now be clear that during its processing history, a polymer is likely to pass at least once through an extruder. It is also a fact that this extruder is likely to be one of the single screw type, though twin and multiple screw extruders are becoming more widely used. In

view of this high popularity of single screw extruders, it may be possible to conclude that they must be extremely satisfactory in operation. This, however, is not necessarily so and there are signs that they may not cope with future demands.

In searching for higher productivity, processors have demanded advanced equipment from the machinery manufacturers in order to achieve higher output rates, better mixing and more uniform extrusion pressures. As an example, screw extruders are being built larger and larger both in diameter and length to diameter ratio. Associated with these developments, technical problems like heat transfer to and from the polymer and the inability to remove fast enough the entrapped air and volatiles in the material as it melts are created. The latter problem was solved by the use of twin stage screws, but this only makes the extruder less versatile and therefore limits its applications.

Although the design of screw extruders has been considerably improved recently by adopting a more scientific approach [2,3,4,5], and some of the less well understood processes occurring inside the screw extruder such as melting [5,6] and conveying of solids [5,7,8] have been more closely examined, there are still many problems which remain unsolved. Some of these are inherent in the screw extrusion process and are therefore unavoidable no matter how improved the design technique may be. For example, an increase in the degree of mixing is inevitably associated with an increase in the melt temperature. Clever design can reduce this effect but cannot eliminate it [1].

A brief consideration of the metering section of a single screw extruder will help to appreciate some of the problems met in the design and operation of this type of processing machinery. The mechanism by which the polymer melt is conveyed along the screw channel results

mainly from the viscous dragging action that the barrel exerts on the material by virtue of the rotation of the screw inside the barrel. Since the melt is subjected to shear forces, a pressure gradient must prevail for equilibrium of forces to exist. In general, a positive pressure gradient is set up along the flow direction. This mechanism is in effect responsible for the pressure generation ability of the single screw extruder. The effect of a positive pressure gradient is to cause a back flow of the melt, the net flow rate being given by the combined drag and pressure flows.

From this simple description it is easy to see that the output rate of a single screw extruder is dependent mainly on the downstream velocity component of the barrel relative to the screw. In general, the output rate is approximately proportional to the screw's rotational speed. The pressure that can be generated by a screw processing a given material is dependent on the magnitude of the viscous shear forces and these in turn depend on the velocity gradients. Thus, for a given material and screw, the pressure generated again depends mainly on the speed of the screw.

The polymer melt temperature in the screw channel is dependent on the amount of heat generated by viscous dissipation and the heat exchange that takes place between the metal boundaries and the melt. Contribution from this latter source is usually small because of the low thermal conductivity of polymers whilst viscous dissipation may be considerable in the usually shallow channels in the metering section. The heat dissipated depends to a large extent on the shear rates, for a given material, and therefore it can be said that the mean temperature of the melt will also depend to a large extent on the speed of the screw.

Mixing in a screw extruder occurs by a process of shearing. The

transverse component of the velocity of the barrel relative to the shaft creates a recirculating flow in the plane normal to the downstream flow direction and this contributes a large proportion to the overall amount of mixing imparted to the material. Increase in screw speed leads to higher shear rates but since the material remains for a shorter period in the extruder the bulk mean mixing remains approximately constant.

It may therefore be deduced from above that one of the major disadvantages of the single screw extruder is that many important parameters such as output rate, extrusion pressure and mean melt temperature are closely interrelated and cannot be controlled independently of each other since they all depend to a certain degree on one single variable - the screw speed. Mixing in general depends on the screw design.

In fact, the single screw extruder is a rather inflexible machine in that it lacks controls. Apart from barrel and occasionally screw temperature controls, both of which are not very effective in large machines, and the back pressure usually regulated by a die restrictor valve, the only easily controllable variable remaining is the screw speed.

This drawback should become clear by considering a practical example: a processor operating a particular screw extruder may wish to increase its output rate to remain competitive. This is achieved by increasing the screw speed. He may then find that the melt temperature becomes excessive to the point that thermal degradation occurs and hence obtain an unacceptable product. Screw and barrel cooling may improve the situation, but because of the poor thermal conductivity of the material this is not very effective. Conversely, he may find that on processing a new material, thermal and shear degradation occurs and

therefore the screw speed must be reduced, resulting in loss of production capacity and hence lower profit margins.

1.3 The Need for Improved and Novel Design of Processing Machinery

The example given above is typical of the problems that may occur in practice. Advanced screw design can in part solve some of these problems, but then the extruder may become too specialised and it is possible to find that its usefulness is limited to a specific family of polymers if not a particular grade of the polymer only. The versatility of the machine is therefore reduced.

The example also illustrates clearly how important it is to be able to control plasticating functions independently from the output rate. For this reason alone it is worth investigating new processes. Apart from the necessity of meeting present day requirements, it is also essential to consider possible future demands.

There is an increasing need to exploit more fully the properties of plastics, and to use them more efficiently. In this context, processing machinery must be able to produce the plastic component efficiently and without deteriorating its final properties, i.e. better control over processing must be provided.

Shortage of raw materials means that suitable waste polymer must be recycled and machinery capable of reprocessing these will be required.

New generations of polymers will tend to have superior properties which may pose processing problems to existing machinery. New equipment must be developed so that they are capable of processing these materials economically and in large quantities.

In conclusion, there is a clear need for progress and advancement in the field of plastics processing machinery. The scope for novel and

improved design of extruders is enormous. Not only refinements of existing extruder designs is necessary, but also new processing principles should be investigated towards the evolution of a more universal processing machine. This can therefore be regarded as one of the major aims of the present work.

The following section reviews some of the more interesting developments on processing machinery.

1.4 Some Recent Developments in Processing Machinery

In recent years, some interesting devices for melting solid polymers and pumping the melts have been reported [9,10]. The principles of operation of some of these machines were entirely different from that of single screw extruders, whilst others still retained a conventional screw or a modified screw to provide additional functions. Examples of the latter type include the melting plate screw extruder [11] and the Maillefer screw extruder [12].

In the melting plate extruder, the melting process has been completely removed from the screw. Instead, a rotating hot plate under the screw is used to melt the material by conduction. The rotation of the plate being slow enough to allow the material to be completely melted before it is scraped from the plate and picked up by the screw flights. The screw extruder then merely performs the mixing and pumping functions in a way very similar to that of melt fed homogenisers.

The Maillefer extruder uses a double channelled screw, one channel diverging and the other one converging. The purpose of this was to separate the newly melted polymer from the compacted solid polymer and hence to improve the overall melting capacity of the extruder. Thus, the melt is collected over the screw flights in the diverging channel

whilst the solid polymer moves in the converging channel. The remainder of the screw channel is similar to that in the metering section of a conventional screw extruder and most of the mixing and pumping action is generated in this section.

The other type of devices can be classed as screwless extruders. Amongst these are the elastic melt extruder [13] and the hydrodynamic extruder [14]. Both extruders derive their pumping capacity from the shearing of the material between a rotating plate and a stationary plate. The principles of pressure generation are, however, different in that the elastic melt extruder exploits the elastic properties of polymer melts whilst the hydrodynamic extruder exploits the viscous properties of polymer melts. In both extruders, melting occurs by heat conduction from the hot plates to the polymer and by viscous dissipation. Also, the degree of mixing and extrusion pressure are highly interdependent and controlled by the speed of the rotating plate and the gap between the plates. The elastic melt extruder also suffered the disadvantage in that pumping capacity was poor. To boost the pumping capacity of this extruder, a device combining the elastic melt extruder with a conventional metering screw in tandem was built and patented [15]. More recently the elastic melt extruder was improved by using a scroll to boost feeding and pumping [16].

An interesting plasticating unit was developed by Borg-Warner [17] for use in injection moulding machines, replacing the common screw plasticating units. It consists essentially of an annular shear cell formed by a cone rotating inside a cylinder. The solid feedstock is initially delivered by a screw and is then forced by a ram into the converging annular gap where the material is melted and mixed by the shearing action between the cone and the cylinder. The polymer melt is

then forced by the ram into a reservoir through a valve. The reservoir can hold a predetermined amount of material which is injected subsequently into the mould by a piston, with the inlet valve to the reservoir closed. Many advantages have been claimed by the makers of the unit [18]. It is a very efficient melting and mixing device, but it is not suitable for continuous output applications such as extrusion of continuous sections.

Another method of melting polymeric materials is by adiabatic compression. The IKV in Aachen has developed an ultra-high pressure plasticating unit [19] which exploits this principle. In this device a very high pressure ram is used to force solid material through very narrow slits. As the material flows through the nips, the enthalpy increase caused by the compression is sufficient to melt the polymer. A special advantage of this method is that the heating effect is produced almost instantaneously and in the material itself. By adequate design, such as avoiding long flow paths and selecting moderate nip sizes, it is possible to reach exceptionally short residence times. This is of particular importance for readily decomposable materials and materials incorporating blowing agents for obvious reasons. For many practical purposes, however, the material emerging from these plasticating units would have to be fed into conventional metering screw extruders for additional mixing and to provide a continuous flow of material where necessary. Machines with multiple high pressure plasticating units, to even out output pulsations, supplying a common mixer have also been suggested.

The plasticating unit of the Teledynamic injection moulding machine [20] also uses high pressure compression for melting. In this machine material is melted by intermittent hammering of the solid feedstock in a

compression chamber. The material is forced into an injection cylinder as it melts, and then into the mould. Very little mixing is imparted to the material in this device.

At the Imperial College an extruder using rollers [21] has been developed. This is very similar to the common twin-roller mills used for rubber processing. But unlike a rubber mill, it is capable of developing adequate pressure to force the material through a die. Melting of the polymer occurs by heat conducted from the rollers and also by viscous dissipation in the thin melt films that separate the solid feedstock from the surface of the rollers. It has been used successfully for reprocessing scrap material, but pressure generation was poor for certain applications.

Westover [22] described a continuous flow ram type extruder which exploits the positive pumping action of rams. Two opposing rams are used to feed the material into the central section of a common cylinder. As the material moves along the cylinder, it is melted by heat conducted from the hot metal walls of the cylinders. A shuttle valve in the middle of the cylinder in effect creates two independent feed cylinders. The molten material from each cylinder is discharged through this common shuttle valve into two independent reservoirs. It is then extruded from these reservoirs by a second pair of rams through the same shuttle valve and finally through the die. The shuttle valve has no external connections and is actuated automatically by the feed rams pressure transmitted through the polymer melts. The use of two pairs of rams (4 in all) and the ingenious shuttle valve maintains a continuous flow of material through the die. An ultra-high molecular weight linear polyethylene which presented serious processing problems in screw machines because of its resistance to internal shear and its lack of

resistance to slip at the metal-polymer interface was successfully processed with this extruder, thus demonstrating the advantages of a positive displacement pumping system. Melting by heat conduction, however, would have been a limitation to commercial applications for this extruder.

1.5 Objective of the Present Project

From the limited number of processing machinery presented above, it appears that many of these developments were carried out with the objective of improving a particular aspect of a more complex process. In particular, two distinct functions have been considered, namely plasticating and pumping. A machine in which both of these functions could be performed efficiently and independently of each other was thought to be worth investigating.

The present work is concerned with a screwless plasticating extruder. As a plasticating extruder, the main functions that it is required to perform adequately are to melt the solid polymer feedstock, to mix it and finally to pump the melt through a die, preferably giving a continuous output.

The principal aim of the project was to design and develop an extruder in which the plasticating functions, i.e. melting and mixing, could be controlled to a large extent independently of the output rate, thus overcoming one of the major disadvantages of single screw extruders.

Though it was easy to criticise the single screw extruder for its lack of versatility due to its lack of independent control for each function, so far there is no alternative machine as simple as a screw extruder which can match its performance. It is certainly not intended for the present extruder to be a replacement for screw extruders, rather

to be used where its extra versatility and flexibility over screw extruders prove it worthwhile, such as for plastication and homogenisation of difficult to process materials like high viscosity materials of the future or even present day scrap polymeric materials.

Though in conception it should be a plasticating extruder, the principles of operation should also be applicable to homogenisers in which the material is fed in as hot melt. It is hoped that some of the advances made towards the evolution of a more universal processing machine may be of use to the polymer processing industry.

1.6 Outline of the Thesis

The major part of this thesis describes theoretical studies of the processes occurring in the extruder which led to the formulation of a mathematical model for the extrusion process. The main purposes for a theoretical model were threefold:

1. To assess the effects on the process caused by varying operating conditions.
2. To predict the performance of machines when processing materials characterised by different properties.

and 3. To provide a valuable design aid which can be used to study the effects of varying the geometry and physical size of the extruder.

The processes occurring in the extruder consisted mainly of feeding of solid polymer, melting and extrusion of the melt through the die. These were amenable to analysis individually and the overall model was derived by combining the separate models for each process.

In chapter 2, the extruder and its operation are described. Also presented in this chapter are results obtained from a series of experimental tests carried out with the extruder. The main purpose for the experimental programme was to evaluate the performance of the existing extruder operating under various conditions with a number of different materials and to provide some means of assessing the validity of the theoretical models.

Chapters 3 and 4 describe in detail the models for the feeding and melting zones respectively. For each zone, theoretical models with varying degrees of assumptions are derived and results for each model are presented and commented upon.

In chapter 5 the complete model for the plasticating extruder is considered. Its validity is checked by comparing theoretical with experimental results. The results of computer simulations based on this model are also presented in this chapter, including results for scaling-up based on the melting performance of the extruder.

Finally, in chapter 6 some brief considerations on the economics of the process are presented, general conclusions are drawn and suggestions for further work are made.

CHAPTER 2

THE CONTINUOUS RAM EXTRUSION METHOD

2.1 Introduction

The plasticating extrusion process comprises the following four important operations:

1. Melting of the solid polymer feedstock.
2. Mixing of the polymer melt.
3. Pressurisation of the homogeneous melt.
4. Extrusion through a die.

Since the process is continuous, all four operations must occur simultaneously. Analysis of these operations individually led to the conception of the basic operating principles for the continuous ram extruder. Considering melting first, one of the simplest ways of melting the solid polymer is to supply heat by conduction. This method is, however, not very effective in view of the low thermal conductivity of polymers which would require long periods of time. Additional heat for melting can be generated by shear in polymer melt films adjacent to the solid material which is to be melted. Mixing is accomplished by shearing the melt and it is therefore evident that melting by heat derived from viscous dissipation and mixing by shear can be achieved simultaneously. This was the principle used in the highly efficient Borg-Warner plasticating unit and was also the principle adopted for the present extruder.

Next, a pumping system which could be controlled independently of the melting and mixing function was required. The ram with its positive

displacement action was ideally suited for this purpose as the pressure that a ram can exert on any material is virtually unaffected by the nature of the medium being pumped. Ram extrusion is by no means a new process. In fact, the use of rams for extrusion and injection moulding purposes has only been discarded in favour of screw devices because of the prohibitive lengths of time necessary to completely melt the material in a ram device. The other disadvantages are that the process is necessarily discontinuous and very little mixing can be imparted to the melt. On the other hand, the main advantage of the ram for extrusion purposes is its positive pumping action, and the facility to set extrusion pressures independently of other variables. When used in the present extruder, the only disadvantage that a ram had was that the output was discontinuous. By using more than one ram, however, a continuous output could be maintained and a very efficient pumping system would be obtained as exemplified by the Westover ram extruder. Combining this pumping system with the shear cell, a device in which plasticating function could be separately controlled from the pumping function was evolved.

The final shape adopted for the experimental extruder consisted of a pair of rams feeding material into an annular plasticating cell formed by an externally heated barrel and a rotating mandrel inside the barrel. Two rams only were used for simplicity of construction. A prototype extruder was built to test the principles adopted. Details of this machine and some earlier experimental results and performance data obtained with this machine have been reported elsewhere [23]. A new and improved version was built following the original one.

In this chapter, therefore, some of the descriptions have already been given previously [23]. Most of it, however, contains supplementary

and new information.

2.2 Development of the Machine

Originally, a very simple machine consisting of a pair of high pressure rams feeding solid polymer into a plasticating cell was constructed. The major components were attached to a large metal block in which three passages were machined, two feed passages and the other being the initial section of the plasticating cell - Figure 2.1. As an indication of the size, the internal barrel diameter was 44.5 mm. The very large block was necessary to guard against the risk of fatigue failure and to contain working pressures of up to 69 MN/m^2. Some flexibility and versatility was built into the machine at this preliminary stage such as the segmented barrel which could permit the variation of the length of the annular region coupled with the facility for changing plasticating shafts of different diameters without major disassembly in order to vary the size of the annular gap. The drive for the shaft was provided by an electric motor via a reduction gearbox with stepless changes and finally via a chain. The rams were driven by pressurised oil in an hydraulic system consisting of a motor, pumps, solenoid valves and hydraulic cylinders.

Basically, the principle of operation was as follows: solid material was fed via hoppers mounted over apertures machined in the feed cylinders. It was pushed forward by the rams into the annular region where it was melted by heat conducted from the externally heated barrel and by heat generated by viscous dissipation due to shearing of the melt films formed. The same shearing action of the shaft mixed the polymer melt which was finally expelled through the die. The rams were cycled alternately in order to maintain a continuous flow of melt through the

die. This was done either manually or automatically by microswitch operated solenoid valves in the hydraulic circuit. The microswitches were operated by arms attached to the rams. The cycling was arranged in such a way that there was always some pressure exerted on the material. This was achieved by retracting a ram to take a new charge of material before the other reached the end of its active stroke. This sometimes caused the material to flow from one feed cylinder to the other instead of into the barrel. To counteract this, two metal keys were inserted on top and bottom of the bore in the block (the initial section of the annular cell) with a small clearance with the shaft, thus in effect creating two separate feed chambers as shown in Figure 2.1.

The controllable variables were, apart from the barrel temperature, the shaft speed, and the maximum pressure exerted by the oil in the rams by means of pressure relief valves. The former mainly controlling the plasticating rate and the latter the output rate.

This machine gave a good output rate for its size compared with screw extruders, and proved that the method adopted allowed the plasticating rate to be controlled largely independently of output rate. From its operation, various observations were made for the construction of an improved version. Among these observations were:

1. The large metal block heated up during a run and this caused the output rate to change.
2. Polymer melt leaked through the seal at the journal bearing formed by the rear section of the main block and the shaft.
3. Plasticating shaft power was a limiting factor for higher output rates.
4. Extrudate uniformity was moderate at high output rates.

5. Effective pumping action was reduced when one of the rams retracted.

An improved version of the extruder was then designed and built with a view to include the required modifications and other improvements in general. Figure 2.2 shows a diagram of the improved extruder.

2.3 The Improved Ram Extruder

2.3.1 The main block

With the extruder described above, it was found that the main block temperature would increase during a run due to heat conducted from the barrel and to friction at the journal bearing between the shaft and the block. The consequence of this temperature rise was to affect significantly the output rate. Particularly at high pressures and speeds, the output rate increased considerably with the block temperature, for example, by as much as 1.6 kg/h per ^{o}C change in block temperature for a basically 16-20 kg/h machine processing low density polyethylene (LDPE). This effect was attributed to the fact that as the temperature of the block increased, the resistance to feeding decreased to the point that a lubricating melt film was formed and hence higher output rates were obtained [23].

For simplicity, the main block had no means of temperature control, thus grossly overlooking the above effect. Clearly, adequate means of temperature control are required for steady state operation. Alternatively, the block could be allowed to heat up to its equilibrium temperature, but this precluded the possibility of operating at an optimum preselected temperature. It was therefore suggested that a modified block should be used with a temperature control system which

would permit both heating and cooling. A fluid medium flowing through passages in the block was a suitable method, although this presented some structural problems as pressures in the block were to be of the order of 45 MN/m^2. The original block was designed to withstand higher pressures, but because of the other improvements described below it was possible to operate at lower pressures yet to maintain high output rates with the new design. This was beneficial because the fabricated block of the improved extruder was structurally weaker than the solid block used in the prototype machine.

The final block is a fabricated unit consisting of a thick main tube to which two smaller feed tubes are welded symmetrically with their axes at 30° angles to the barrel axis - Figure 2.2. This construction permitted the use of jackets welded around the tubes through which temperature controlling fluid media could flow. The angle between the feed passages and the barrel axis was 45° in the original extruder in order to reduce the overall physical size of the block and to leave enough room for the feed cylinders to clear the bearing housing. In the new extruder it was possible to reduce the angle to 30°. This brought additional advantages in that the flow passages became more streamlined and hence offerred less resistance to the rams and also the lateral forces exerted by the incoming material on the shaft was smaller and hence reducing any sideways bending of the shaft and giving a longer life to the shaft.

The main tube provides support for the plasticating shaft in the form of a journal bearing and also forms the initial length of the barrel extension. Brass collars are fitted to the shaft in this region to act as bearing surfaces. From experience with the prototype extruder, at high extrusion temperatures it was possible for melt films to form in

this region and under pressure this could leak towards the bearing housing. The rear of the block has large machined slots so that any leakage that may occur flows to the atmosphere rather than forcing into the bearing housing. Also a port leading straight from the journal bearing surface to the atmosphere is available through which further melt leakage can be bled off. This port can be plugged if necessary. To further reduce the leakage of melt through the shaft seal, this region is water cooled by circulating water at room temperature through a jacket welded around the main tube at the rear of the block. The external surface of the main tube encased by the water cooling jacket is grooved in order to aid heat dissipation. This has an additional benefit in that it prevents heat from being conducted into the bearing housing which is also water cooled. This not only increases the life of the bearings but also that of the actual journal bearing and shaft seal which tend to wear out fairly quickly.

Thick steel flanges are welded onto the ends of the tubes and these are used for attaching the shaft bearing housing and the barrel to the main tube and the feed cylinders to the other two tubes. The casing of the main block is then completed by two side plates joining the feed cylinders flanges to the barrel flange thus adding considerable strength and rigidity to the construction in order to withstand the high pressures. The top and bottom of the block are covered by steel plates bolted onto the flanges, further strengthening the block.

Steel keys are also used in this extruder to create two separate feed chambers. The keys are brass tipped to reduce wear of the shaft due to any possible contact. The feed tubes are vented for removal of air and volatiles.

2.3.2 Main block temperature control system

Heating oil is used as the block temperature control medium and flows inside the jackets welded around the rear of the feed tubes and the front section of the block. Two separate but interconnected oil circuits are used, one for the front section and another for the feed tubes. The two jackets at the rear of the feed tubes are connected in series. The block is thus divided effectively into two zones for temperature control purposes. This permits setting different temperatures along the feed passages in the block.

In each oil circuit an electric motor drives an oil pump sending oil through an electrical resistance heater, an oil cooler and then through the jackets. The temperature of the oil is controlled by thermostatic switches which cut out the electrical heaters when the oil temperatures reach a preset value. The actual temperature of the block, measured by thermocouples embedded in the feed tubes is regulated by another set of controllers which not only cut out the oil heaters but also open the cooling water valves to the oil coolers when the block temperature exceeds the preset value for each zone. Both sets of controllers can be overridden manually if required. The two independent oil circuits are interconnected via a common expansion tank and the oil is continuously recirculated through each circuit.

2.3.3 The barrel, bearing housing and feed cylinders

In anticipation of the need for removing heat from the barrel particularly when viscous heat generation becomes excessive, e.g. when extruding high viscosity materials, a water cooling system has been incorporated in the barrel. Water flows inside three jackets spaced along the barrel. Under the jackets, the barrel has helical grooves

machined on its outer surface and these act as flow passages for the water. Electrical resistance heaters are mounted over the jackets and they maintain the barrel at preset temperatures via thyristor proportional controllers. The barrel is divided into two zones for temperature control purposes. The cooling water supplies to each jacket are independent of each other and the amount of cooling depends on the water flow rates.

Unlike the sectioned barrel of the prototype extruder, the present one is of fixed length. It is attached to the main block via a reducer plate which forms a tapered converging annulus with the shaft. The converging channel imposes some degree of compression to the material and this assists the melting process. The reducer plate is also heated externally by an electrical resistance heater and contains extensions of the keys used to create the independent feed chambers.

At the front end of the barrel a breaker plate is used before the final lace die which is also heated externally by an electrical resistance heater. The breaker plate is a disc with a number of small perforations. The die is bolted externally to facilitate die changes.

At the other end of the extruder, the shaft bearing housing is bolted onto the rear flange of the main block. The shaft loads are transmitted to the bearings via a sleeve to which the shaft is keyed externally. This arrangement permits the removal of the shaft without affecting the bearing assembly. The front of the bearing housing is sealed, against melt leakage by a tapered brass collar around the shaft at the entry into the bearing housing.

The feed cylinders are bolted onto the two remaining flanges of the main block and are also cooled by water flowing inside the jackets. The purpose of this is to reduce the friction between the feed cylinder walls

and the feedstock and also to prevent premature melting of the feedstock which could block the feed passages. Without cooling, the feed cylinders could be heated up considerably by heat conducted from the block. The length of the feed cylinders is the same as the stroke of the rams. Square hopper apertures are machined in the feed cylinders and on top of these, hoppers are fitted.

The hydraulic cylinders are attached to the feed cylinders by tie bars. The whole assembly is bolted on top of a steel cabinet which houses the block temperature control systems and also the control valves for all the water cooling.

The new extruder is about the same size as the original one, with an internal barrel diameter of 44.5 mm. Details of the major dimensions are given in Table 2.1. Plate 2.1 shows a general view of the extruder.

2.3.4 Plasticating shaft and its drive

The plasticating shaft drive is similar to that of the prototype extruder, but because of lack of plasticating power detected previously, the motor is a more powerful one. It has been upgraded from 7.5 kW to 11 kW. The range of shaft speeds is about the same (60-380 rpm), and it is set remotely by a handwheel via a flexible cable connected directly to the speed variator. The final drive to the shaft is through a pair of flexible couplings. This arrangement allows some degree of freedom in the alignment of the rig. The shaft is cylindrical along most of its length except at the initial section which tapers from the diameter of the main tube in the block to its nominal diameter of 38.1 mm. Apart from the physical requirement of reducing the diameter of the rear of the shaft to its nominal diameter, the taper also serves to reduce the amount of bending of the shaft due to lateral forces exerted by the rams

and transmitted through the feedstock. It also decreases the volume of the dead spots in this region of the extruder where material could accumulate and stay in the machine eventually degrading.

Unlike the shafts used in the prototype extruder, the front end of the shaft does not terminate abruptly. Instead a pointed brass tip is screwed onto its front end. The tip is made of brass so that wear of the steel barrel does not occur if excessive pressures at the rams bend the shaft enough for contact to occur with the barrel. Due to a mistake, the shaft was made considerably shorter than the barrel so that a melt reservoir has been unintentionally created at the front of the barrel before the breaker plate. This had a beneficial action in damping fluctuations in the output rate which were observed with the previous machine.

Only a single shaft was manufactured to use in this machine, but it was designed so that shaft changes are facilitated.

2.3.5 Hydraulic system

As in the prototype extruder, the reciprocating feed rams in the improved extruder are driven by oil in an hydraulic system. From theoretical considerations on the system employed in the prototype machine, it was calculated that at best only 14% of the rated power of the electric motor used for the oil pumps was available as useful power for the feeding process. This low use of the total power available is inherent in the ram feed process in that at least half of each ram cycle is unproductive and that not all of each feed stroke is used effectively. A possible way to improve the power transfer from the pump motor to the feeding process was to use smaller rams which allowed for higher cycling rates and to upgrade the pressure rating of the system so that higher oil

pressures could be tolerated.

Thus, in the improved extruder, the hydraulic cylinders used are 82.6 mm bore x 152.3 mm stroke compared with 152.3 mm bore x 101.6 stroke in the original version of the machine, and the maximum allowed oil pressure is 11 MN/m^2 compared with 7.6 MN/m^2. Though the oil pressures can be higher in the new machine, the actual pressure exerted by the ram on the feedstock is lower than in the prototype extruder because of the lower ratios of hydraulic piston diameter to feed ram diameter. Initially higher pressure rating pumps were used, but these failed in operation due to manufacturing faults. The original oil pumps with a maximum pressure rating of 11.0 MN/m^2 were used thereafter. Because of this, the maximum power available from the hydraulic system for feeding purposes in the improved extruder is about the same as that in the old one, i.e. 2 kW per ram. In practice the ram power is well below this. Thus little improvement has been introduced into the hydraulic system in terms of power transfer efficiency. The complete hydraulic system is shown diagrammatically in Figure 2.3. The two oil pumps are driven by a 30 kW motor mounted on top of the oil tank. Oil is pumped directly to the piston through solenoid valve 4 which determines which side of the piston is to be pressurised. On the forward stroke, the oil in the low pressure side passes through valves 5, 6, 7 and 8 before it is returned to the tank. On the return stroke the oil flows directly to the tank. The maximum oil pressures are preset at the relief valves 2 and any exhausted oil is returned to the oil tank. An oil cooler is used to provide a small amount of cooling to the oil whose temperature increases slightly after prolonged periods of operation. This is not shown in the oil circuit diagram of Figure 2.3.

2.3.6 Control of the feeding system

Two modes of cycling the rams are possible with the system in use. One in which each ram is actuated independently of the other by means of manual switches and the other in which the cycling of the rams is controlled automatically by means of microswitches actuated by arms attached to the rams. In this latter mode of operation, the cycling of one ram is dependent on the cycling of the other. This will become clearer when the automatic mode of operation is described in detail below.

The speed of the ram during its forward stroke is controlled by valves 6 and 8 in Figure 2.3. When the solenoid valve 5 is not in operation, only valve 8 has flow rate control functions. In general, valve 5 is actuated when the ram has travelled already some distance during a feed stroke. The forward stroke can therefore be considered as consisting of two stages, the first in which the speed is controlled by valve 8 and the second by valves 6 and 8. Provided that valve 6 is not fully closed, the second stage is usually faster than the first stage. The purpose of this is to compensate for the loss of feeding of material to the barrel when one of the rams retracts by increasing the feed rate of the other ram. In the return stroke, both flow rate control valves 6 and 8 become inoperative since the oil is bypassed in valve 8 and is checked by valve 7.

The solenoid valves are all operated by relays triggered by the microswitches. Figure 2.4 shows typical positions for the microswitches used in the automatic mode of control. In all, four switches are actuated by each ram along its stroke. Switches LHF and RHF cause the left hand ram and the right hand ram respectively to move forward. Switches LHZON and RHZON are actuated simultaneously as LHF and RHF.

The function of these two switches is to reset switches LHZ and RHZ respectively ready into operation. Switch LHZ provides two functions simultaneously, it causes the right hand ram to retract and brings into operation the second stage flow rate control valve for the left hand ram. Switch RHZ has the opposite functions to LHZ. Switches RHZOFF and LHZOFF cancel the switching action of switches RHZ and LHZ respectively.

In order to visualise the motion of the rams, Figure 2.4 shows a typical arrangement of the positions of the rams. Having actuated switch LHF, the left hand ram moves forward. Since LHZON was also actuated, LHZ is ready for operation. As the ram continues to move forward, RHZOFF is actuated and this neutralises any switching action of RHZ. In the meantime, the right hand ram continues to stay as its forward position under pressure. When LHZ is next actuated, the right hand ram retracts whilst the left hand ram moves at a higher speed because LHZ also brings into operation the second stage flow rate control valve for the left hand ram. In its return stroke, the right hand ram actuates RHZ but this has no effect since its switching action had already been cancelled by RHZOFF. When RHF is actuated, the right hand ram changes direction of movement and begins its forward stroke, at the same time RHZ is ready again for action since RHZON was actuated. As the right hand ram moves forward, LHZOFF is actuated which cancels the switching action of LHZ and when RHZ is actuated by the ram when it reaches that position in its forward stroke, the left hand ram retracts and the second stage flow rate control valve for the right hand ram is brought into action. When the left hand ram has reached its fully retracted position, the cycle is repeated.

It is thus clear that the left hand ram cannot return until RHZ is actuated by the right hand ram in its forward stroke and vice-versa. In

this way the cycling of one ram is dependent on that of the other. For optimum output uniformity, the position of switches LHZ and RHZ is critical. Switches LHF/LHZON and RHF/RHZON are set at the maximum rearward position for each ram. Plate 2.4 shows the microswitches displaced at typical positions.

In the manual mode of operation, all switches become inoperative except for LHZ and RHZ. These, however, do not perform the dual function described above but only switch on the second stage flow rate control valves. Two independent switches for each ram are used to control the motion of the rams, one to cause the ram to move forward and the other to retract it. In this mode of operation, therefore, the cycling of each ram is completely independent of the other.

Two mode selector switches are provided, one for each mode of operation.

2.4 Instrumentation

The principal performance parameters of the process to be measured were the output rate, the melt temperatures, the pressure in the melt and the power consumption which depended on the operating conditions, i.e. the plasticating shaft speed, the pressure exerted by the rams, and the temperatures set along the barrel and the main block.

A convenient method for measuring output rate was to weigh a sample of the extrudate collected over an adequate period of time.

Melt temperatures were measured by thermocouples placed at four tappings along the barrel section as shown in Figure 2.2. Direct readings of the temperatures were recorded on a calibrated six-channel chart recorder.

Pressures in the material were measured at four tappings along the

barrel, opposite the melt thermocouple tappings. Either grease filled Bourdon type gauges or pressure transducers connected to an ultra-violet recorder via bridge amplifiers could be used to register the pressures - Plate 2.2.

The torque transmitted by the shaft was measured by a torque transducer installed on the final shaft drive, between the flexible couplings. When the set up was calibrated, the torque could be read off a voltmeter directly. The shaft speed was measured by a magnetic pulse pick up integral with the torque transducer - Plate 2.3. Its value was also indicated on a calibrated meter.

The oil pressure for the rams was indicated by Bourdon type gauges, but these were mainly used for setting the maximum oil pressures for each ram. In general, they were shut off afterwards to prevent fatigue damage. A recording of the actual oil pressure driving the rams could be obtained on the U.V. recorder using pressure transducers with bridge amplifiers.

Displacement transducers made up of simple variable electrical resistances with a constant voltage supply were used to record the positions of the rams on the U.V. recorder. The rheostats were linked directly to the rams as shown in Plate 2.4. From the recordings of the position of the rams, the cycling rate could be determined and also the speed of the ram, if required, could be calculated by measuring the slope of the tracing.

Two control thermocouples connected in parallel for each barrel temperature control zone were used. They were embedded in the wall of the barrel at 3.2 mm from the internal surface of the barrel. The temperatures measured by the thermocouples and the preset temperatures were registered on thyristor proportional controllers.

Thermocouples were also embedded in the feed cylinders in the main block for temperature measuring and control purposes. Plate 2.5 shows details of the block and the position of the thermocouples.

Apart from this main instrumentation, other gauges were provided to indicate the temperature of the cooling water for the feed cylinder and the shaft seal, and the pressures in the heating oil circuits.

Plate 2.6 shows the main control cabinet housing the electrical systems and some instrumentation.

Plate 2.7 shows the hydraulics control cabinet. The flow rate control valves and the pressure relief valves can be seen together with the pressure gauges used for setting the maximum oil pressure.

Details of the instrumentation are given in Table 2.1.

2.5 The Experimental Programme

2.5.1 Objective of the experiments

A series of tests were carried out initially with the extruder to measure its general performance. This consisted mainly of measurements of output rates, mechanical power consumption and melt temperatures as functions of the two major independent variables, namely the rotational speed of the shaft and the pressure exerted by the rams.

A number of materials were processed to test the versatility of the extruder and to study its behaviour. The materials used were LDPE granules, high density polyethylene (HDPE) granules, polystyrene (PS) beads and polypropylene (PP) granules.

In addition to these general measurements, detailed data was also collected for some of the test runs with the aim of providing a basis for comparison with theoretically predicted results in order to assess the validity of the theoretical models developed to describe the ram extrusion

process.

2.5.2 Experimental procedure

This section briefly describes the procedure adopted for the experimental tests.

The heating systems were switched on at the beginning of each series of tests carried out during each day. When the chosen temperatures were reached, the shaft drive motor was switched on and the rams brought into action. With the ram cycling in the manual mode, each ram was brought to the end of either its forward or backward stroke and keeping the solenoid valves open, the maximum oil pressure for each ram was set at the pressure relief valves. With the selected material for the test in the hoppers, the ram cycling was switched to the automatic mode and the material that was inside the barrel at the start was flushed out. Note: this machine is not self clearing and there is always material left inside the extruder at the end of each run.

The position of the microswitches LHZ and RHZ (Figure 2.4) and the opening of the flow rate control valves 6 and 8 (Figure 2.3) were adjusted by a trial and error method until a flow of the polymer melt at the exit of the die as even as possible was obtained. To assist this operation, the pressure registered by the pressure gauges placed along the barrel was monitored. The most uniform flow occurred when the pressure fluctuations were smallest. Though this adjustment was carried out at specific shaft speed and ram pressure, it was found that it was adequate to maintain uniform output under different shaft speeds and oil pressures.

Having established the optimum positions for the microswitches and the optimum openings of the flow rate control valves and with the barrel and block temperatures at preset values, the remaining independent

variables affecting the performance of the extruder, when processing a given material, were the maximum oil pressure at the rams and the shaft speed. With the maximum oil pressure already preset at the pressure relief valves, the output rate and other dependent variables like melt temperature and torque transmitted through the shaft were measured for a range of shaft speeds. This was repeated for different maximum oil pressure settings.

Occasionally the oil pressures selected were in excess of the design limits and therefore were maintained only for a short period, long enough to gather the required performance data but short enough to avoid mechanical deterioration of the extruder. This was done for testing extreme operating conditions on the extruder's performance.

For some tests, the extrudate was laced in a water cooling bath by passing it over a set of pulleys and using a roller take off, and was subsequently granulated for reuse. It was possible to assess the uniformity of the output by examining the variation in the cross section of the lace prior to granulation. This granulated material was normally used for starting purposes, i.e. flushing the old material in the extruder out and setting the positions of the microswitches and openings of the oil flow rate control valves.

2.5.3 Measurement and accuracy of experimental data

Before carrying any detailed analysis of the data collected experimentally, the accuracy of these must be considered.

In the measurements of output rates, the weighing accuracy was better than 0.1% and any significant error came only from the timing of the interruption of the melt flow at the exit of the die or at the granulator (when this was used) when collecting the sample. Even

allowing for a couple of seconds in timing error, the overall accuracy was within 1%. Water absorption in the cooling bath was sufficiently insignificant with the materials used to have affected the weight of the extrudate collected. At least two samples were collected for each test and a mean output rate evaluated.

The shaft power consumption was obtained from measurements of the shaft speed and the torque transmitted through the shaft. Because of the position at which the torque transducer was mounted the power consumption calculated did not include motor, reduction gearbox and chain drive losses, but included losses in the shaft bearings. Unfortunately, these bearing losses could not be measured because the extruder could not run 'dry'. The semi-permanent mounting of the torque transducer rendered its calibration before each days test inconvenient and therefore once it was calibrated off the rig, its calibration was not checked again until after a period of months. It was found that it remained constant during these periods. Calibration of the torque transducer was carried out statically by applying a known load at a given leverage. According to the manufacturers instructions, this gave an accuracy of about 3-5%.

The calibration of the shaft speed meter was checked occasionally with a hand held tachometer which was inherently very accurate. The differences were not more than 2 rpm which represented an average error of about 1% in the range of speeds used in the experiments.

During a run no fluctuations in the shaft speed were detectable from the meter and it remained constant, independent of the load. Fluctuations in the torque were large enough to show on the meter and these were due to the intermittent flow of material in the separate feed chambers at the initial region of the barrel. These fluctuations were more significant than any inherent inaccuracy of the torque measuring system quoted by its

manufacturers. For the purposes of measuring overall performance the nominal values for the shaft speed and torque were adequate.

The barrel temperatures were read off the indicators of the thyristor proportional controllers which held the barrel temperature to $\pm$ 1°C of the set temperature. The quoted accuracy of the set temperature was $\pm$ 0.25% and that for the indicated temperature was $\pm$ 1%.

The block temperatures and the melt temperatures were read off the multi-channel chart recorder with an accuracy of $\pm$ 1%. The melt temperatures were measured by thermocouples inserted through the barrel wall. Because of this arrangement, the barrel temperatures could influence considerably the values measured by the thermocouples. A discussion on melt temperature measurement in plastics processing machinery is outside the scope of this thesis but it suffices here to say that errors as high as 30% can exist in such arrangements which are most undesirable.

When the extrudate was not laced, its temperature was measured by a hand held thermocouple probe connected to a direct reading meter. Though the accuracy of the instrument was 1%, it was difficult to keep the probe in the melt stream and the meter reading tended to drift, therefore not too much reliance was placed upon this.

For the general results, the pressures measured along the barrel were read off directly from the Bourdon type gauges. The accuracy of the instruments used was poor. But the fluctuations in the melt pressure were sufficiently large for the inaccuracies of the gauges to be insignificant. The maximum and minimum pressures registered during a ram cycle were recorded. For a considerable part of each cycle, the pressure remained fairly steady, changing at a very slow rate. This value was also recorded. Clearly these results were inadequate for

more detailed analysis and they served only to give an order of magnitude of pressures in the barrel.

The ram oil pressures could be read off more easily from the Bourdon type gauges but again the fluctuations due to the pumping system were more significant than any inaccuracies of the instruments.

For the more detailed results, calibrated pressure transducers were used and a continuous monitoring of the pressures was obtained on an U.V. recorder. The accuracy of the combined pressure monitoring system was estimated to be better than 2%. However, because of the fluctuations in pressures the estimated accuracy of 2% becomes meaningless when nominal values only were used.

The displacement transducers had an accuracy of about 4%. But when used for determining cycling rates, the accuracy was better than 1%.

2.5.4 Results and discussions

In this section quantitative results are summarised in graphical form and discussed. Apart from these, observations made during the tests are presented and commented upon.

I Quantitative results

Figures 2.5 to 2.8 show the output rate plotted against the maximum oil pressure at the rams when processing LDPE, HDPE, PP and PS respectively. The range of shaft speeds used was from 60 to 240 rpm. The maximum oil pressure rather than the actual ram pressure was selected as the independent variable affecting most the output rates. This was justified in that during all test runs, the oil pressure in the hydraulic cylinders was at its maximum preset value for most of the active strokes of each feed ram. The actual ram pressure could be obtained by

multiplying the value of the oil pressure by the appropriate scaling factor given by the square of the ratio of the piston diameter to the ram diameter, in the present extruder being approximately 3.45.

The fact that maximum oil pressure was reached in all the cases underlines that the output rates were limited only by the pressures available at the rams and that plasticating capacity was adequate to meet these output rates. In all the graphs shown, the output rate for a given shaft speed increases with increasing oil pressure. If the oil pressure had been increased indefinitely, clearly the output rate would have not increased accordingly because under these conditions it would have been limited by the plasticating capacity of the extruder, and also once the oil pressure was sufficient to drive the rams at their maximum cycling rate, no further increase in feeding can occur. In all the experiments the maximum oil pressures preset at the pressure relief valves were the same for both rams.

In some of the results shown in Figures 2.5 to 2.8 the oil pressure exceeds the rated value of 11 MN/m^2. Test runs were carried out at these extreme conditions to test if the plasticating capacity could meet the requirements for larger output rates. It appears that the present extruder has adequate plasticating capacity to match its pumping capacity.

Figures 2.9 to 2.11 show the melt temperature measured by the thermocouple at position A in Figure 2.2 plotted against output rate for the two extreme shaft speeds, i.e. 60 and 240 rpm. No valid results were obtained for PP because the temperature at this location was outside the nominal range of the temperature recording instrument used. In general, the melt temperatures decrease with increasing output rate. This is explained in that at low flow rates, the residence time of the material in the extruder is longer and hence more energy is received by

each particle of material flowing along the extruder channel and hence its temperature becomes higher. These results also confirm that the output melt temperatures can be controlled by varying the shaft speed. However, a change in shaft speed to control the melt temperature and mixing also affects the output rate if the ram was operating at a fixed pressure as shown by the graphs of Figures 2.5 to 2.8. Ideally an output rate dependent on ram pressure only was desirable, but as shown, for a given pressure the output rate increases with increasing shaft speed and vice versa. This phenomenon is inherent in the process and can be attributed in a crude and simple manner to the non-Newtonian behaviour of polymer melts. Thus, if the overall pressure gradient along the extruder channel is maintained constant, and because an increase in shaft speed reduces the apparent viscosity of the melt due to higher shear rates and temperatures and hence the overall resistance to flow decreases, the same pressure gradient would clearly drive more material through the channel giving higher output rates. Also at higher shaft speeds the solid material melts sooner and the flow channel is filled with more polymer melt than solid material which in general requires higher pressures to be pumped.

At first it may appear therefore that the major aim for the development of such an extruder, i.e. the independent control of plasticating functions from the pumping function has not been achieved. In practice, however, the procedure would have been to select first the shaft speed to give the required plasticating performance and then to select the ram pressures which gave the appropriate output rate for the chosen shaft speed. In this way plasticating rate is controlled quite independently of output rate. This clearly represents a considerable advantage for this ram extruder over the single screw extruder in which

such a degree of control is very difficult to achieve without a change in the screw design.

The specific mechanical power consumption expressed as the work done per unit mass of material processed has been plotted against output rate in Figures 2.12 to 2.15. The specific shaft power consumption decreases with increasing output rates as expected. Thus, in terms of mechanical power consumption only, it is more economical to operate at higher output rates than at lower output rates, and at lower shaft speeds than higher ones, as long as plasticating performance and the amount of mixing imparted to the material are adequate. These results also confirm the results shown in the graphs of Figures 2.9 to 2.11 in that at low output rates the energy supplied to unit mass of material is higher and hence the higher melt temperatures measured.

Considering the results for LDPE only, at typical commercial output rates for the present size of machine, the specific shaft power consumed is only 0.15 kWh/kg. This, however, cannot be compared directly with the screw power in single screw extruders since some of the power is used for conveying purposes in the screw extruder. To the shaft power must be added the power of the rams and the total should be comparable with that of a screw extruder with similar performance. For a typical output rate of 40 kg/h of LDPE, the total power from the rams was estimated at 0.75 kW based on the force exerted by the rams, the effective length of each stroke and the ram cycling rate. This implies that the total specific mechanical power consumption was estimated at about 0.17 kWh/kg and this compares favourably in terms of energy economy with the 0.19 kWh/kg considered as the necessary power consumption for a screw extruder producing good quality LDPE melt.

II Observations

Initially, the main observations made during the operation of the extruder were directly concerned with the effects of the improvements and the modifications introduced in the new extruder.

(i) Main block temperature

One of the main improvements in the new design was the provision of a temperature control system for the main block. This proved to be satisfactory in operation and temperatures achieved in the block of the improved extruder were considerably higher than those in the prototype extruder, e.g. 150 to 175°C after a warming up period of 2 to 3 hours compared with 90 to 110°C for the same period of time in the old extruder depending on the barrel temperature.

At these relatively high temperatures feeding of the material occurred without problems when processing the materials mentioned above. Since these block temperatures were in excess of their softening points a melt film would have formed between the solid feedstock and the walls of the feed tube and it would have acted as a lubricating layer. In general, high block temperatures are helpful in that the pressure losses in the feeding zone are smaller because of the possible existence of lubricating polymer melt films and hence the full pressure provided by the hydraulic system may be used to yield higher output rates. However, this does not mean that it is a necessary condition for successful operation of the ram extruder that the block temperature should be higher than the softening point of the material though such a condition is favoured for more efficient use of the pumping capacity of the extruder.

The maximum block temperatures achieved initially were of the order of 130 to 140°C. It was found that most of the heat conveyed by the heating oil was lost in the piping system to the main block. With the piping insulated by asbestos tape and the block cavities filled with glass wool, the maximum temperatures achieved were around 150 to 175°C. At these maximum values, the block temperature remained fairly steady. The amount of heat supplied by the oil heaters balanced the natural losses in the system and it was found that the action of the controllers both for the block temperature and the heating oil's temperature was not required. The full current was supplied continuously to the electrical oil heaters and the coolers were never operated. At temperatures lower than these, it was found that the controllers worked efficiently by simply cutting off the current supply to the heaters and restoring this when the temperature decreased enough. In this way, the main block temperature was maintained within 2% of the preset value. In the automatic temperature control mode, when the temperatures were well over the preset value, the oil coolers were brought into operation. These reduced the temperature of the heating oil considerably and a lengthy period of time was required for the block temperature to be restored to its preset value again.

(ii) Shaft seal leakage

The leakage of molten polymer past the shaft seal was slightly reduced by the water cooling in this region. Despite this, leakage still remains a problem to overcome. It was more pronounced when processing LDPE than with other materials. Very little leakage

occurred with PP. Clearly the less viscous the melt the greater is the leakage. Two possible methods should be suitable to reduce leakage. First, more efficient seals could be tried and evolved, and second, inserts to modify the flow passages could be used to streamline the flow of the material into the barrel from the feed cylinders and thus preventing the feedstock from moving towards the rear of the annular channel and eventually leaking out past the shaft seal.

(iii) Control of feed rams

The other major modification to the extruder was the improvement of the hydraulic system to drive the rams. Because of the failure of the new oil pumps, the lower pressure pumps from the prototype extruder were used instead. The resistance to flow offerred by the material to the feed rams was such that the maximum preset oil pressure was reached in all the experimental runs. Even if the uprated pumps had been used, the full pressure of the oil would have not been adequate to overcome easily the resistance of the material as some tests at high pressure have shown. Under these conditions, the speed of the rams was controlled by the resistance to flow of the material and most of the oil was exhausted through the pressure relief valves during the active stroke of each ram. Also, at these conditions, the oil flow rate control valves used to adjust the speed of the rams became ineffective and they were left fully open. The optimum output uniformity was thus achieved by the adjustment of the position of microswitches LHZ and RHZ only (see Figure 2.4).

(iv) Output uniformity

Visual inspection of the melt leaving the die revealed that substantial changes in the melt stream could occur during each ram cycle. When the extrudate was laced, fairly uniform lace was produced but this could not be relied upon as an accurate indication of the uniformity of the output since the uniformity of the cross section of the lace was more dependent on the hauling-off speed of the pulling rollers than on the uniformity of the extrusion pressures. However, measurements of lace diameters were made at equally spaced intervals along some lace samples and variations as high as 50% from the mean diameter were obtained, reducing to 7% when the hauling speed and the ram cycling were adequately adjusted. These statistical results cannot be considered as very significant because in addition to the effects of the hauling speed on the lace uniformity, the measurement of 'diameters' was not very satisfactory. For the drawing of a cooling melt against flat pulleys and the consequent deformation of the initially circular cross section of the lace when leaving the die implied that 'diameters' measured were not those of a true circular cross section but a mean value of a somewhat oval cross section.

A better indication of output uniformity was obtained from the pressure variations at the die. Figure 2.16 shows a typical recording of the melt pressure at position 2 in Figure 2.2. This is by no means the most uniform pressure recording obtained, rather it was chosen as one which shows typically the pressure changes. The vertical lines are at 1 second intervals and the total time shown is that for two cycles, one for each ram. In the case shown, one

of the rams was cycling faster than the other due to differences in the position of microswitches and also in the feeding resistance of the material in each feed chamber. The sudden drops in pressure occurred when each ram retracted to take a new charge of material.

In chapter 5 it is shown that the volumetric flow rate of the melt, through the circular die and the breaker plate consisting of a number of cylindrical passages, is proportional to $[\text{pressure gradient}]^{1/n}$ where $0 < n \leqslant 1$. When applied here, the pressure measured by the transducer at position 2 in Figure 2.2 can be considered as proportional to the pressure gradient along the flow channel from the point of measurement to the exit of the die since at this point the pressure is atmospheric. Thus, it can be seen that the change in the flow rate during a cycle can be considerable since a small change in the pressure gradient may produce a large change in the flow rate, the effect being more marked the more non-Newtonian the material is, i.e. the smaller the value of n, typically $n = 0.5$ for polymer melts. Visually, a sudden reduction in flow rate could be detected at the exit of the die when these pressure drops occurred.

Figure 2.16 shows that for about 80% of the cycle time the pressure changes are slow and small. Under these conditions the change in the output rate could not be detected visually and the lace produced during this part of the cycle proved to be fairly uniform.

(v) Solids feeding

Some solids feeding problems occurred when processing certain materials. With LDPE granules no feeding problems were

encountered but when PS granules were used, these tended to jam in the feed passages inside the main block.

Several reasons for jamming to occur were possible. The temperature of the feed passage walls might have been unfavourable for a particular material. For instance, too high a temperature in the block could lead to premature melting of the feedstock which could turn into a solidly compacted aggregate difficult to break so that flow through the junction of the feed cylinder with the barrel could not occur; and too low a temperature would result in considerable pressure losses through friction of the solid material against the walls of the feed passages. In the following chapter 3 some methods of estimating values for the frictional losses are considered. It will be seen that Coulomb friction between solid polymer particles and metal walls can lead to considerable pressure losses.

The relationship between the physical size of each solid particle of material and the flow channel dimensions is also significant since bridging of the solid particles may occur. The larger the size of the polymer granules the more susceptible it is for bridging to occur. For example, when processing two similar PS, one in the form of reactor beads and the other in the form of comparatively larger granules, with the extruder set at the same operating conditions, jamming of the feed passages occurred persistently with the larger granules whilst no feed problems were met with the smaller beads.

Another factor affecting the feeding of solids is the internal coefficient of friction of the granular material, i.e. the friction offerred by a particle of the material to its surrounding particles.

Clearly the higher the internal coefficient of friction of a granular material the higher is its resistance to flow (or deformation) and thus higher ram pressures are required to maintain an adequate flow rate.

For some materials, e.g. LDPE granules, these factors affecting the feeding process were not critical since high pressures and adequate block temperatures could overcome any jamming of the feed passages. But the low heating capacity of the main block and the pressures permitted both in the hydraulic circuit and the main block were sometimes limitations with other materials, e.g. PS granules.

Though high block temperatures may assist the feeding process by producing a layer of melt and hence change the nature of the friction from a Coulomb to a viscous type, it was observed that, if the temperatures were high enough for the feedstock to be completely melted in each of the feed chambers created by the keys, feeding efficiency could be reduced considerably. When each feed chamber was filled by melt rather than solid polymer, as one ram pushed the material forward the pressure was readily transmitted to the other feed chamber through the polymer melt. Thus, when the other ram retracted, the pressure exerted by the ram still moving forward was enough to force considerable amounts of material into the feed cylinder of the retracting ram, reducing the amount of material fed into the barrel. Had the feed chambers contained solid rather than molten polymer, this would have not occurred since pressures are not so readily transmitted through the solid polymer and also the keys would have prevented the flow of solid polymer from one feed chamber to the other one.

When processing very finely granulated material, e.g. PS reactor beads, on the return stroke of each ram, some of the material in the hopper falling on the surface of the ram was dragged backwards and out of the feed cylinder. This could be considered as a large amount of leakage, but since this material could be easily collected and replaced into the hoppers, the overall loss of material was insignificant.

(vi) Plasticating power

The maximum plasticating shaft power drawn from the 11 kW drive motor was measured at 9.3 kW. The maximum plasticating shaft power available in the prototype extruder was only 2.8 kW. Comparing the output capacity for the two machines when processing LDPE, the improved extruder gave a maximum output rate about twice that obtained with the prototype extruder. This large increase in the output rate cannot be attributed only to the increase in the plasticating power but also to the other improvements mentioned in this chapter, in particular to higher block temperatures. In general, the use of a more powerful motor to drive the shaft improved the overall performance of the extruder.

(vii) Output rates

Simple calculations as to the maximum obtainable output rates, based on the pumping capacity of the hydraulic system, revealed where changes were necessary if these high output rates are to be achieved.

A feeding rate of 60 gm/stroke of LDPE granules was determined experimentally. This was the amount of material falling

into each feed cylinder through the hopper apertures with the rams fully retracted. It was found that the level of material in the hoppers did not affect this. At the maximum cycling rate of the rams, about 35 cycles/min, measured without any material being fed in, the combined output rate given by the two rams would have been 250 kg/h of LDPE. In practice a maximum of 40 kg/h only has been obtained, with the rams cycling at a rate considerably lower than the maximum possible. If the full pumping capacity of the extruder is to be realised, higher working pressures must be allowed both in the main block and in the hydraulic system. However, it is just as well that the rams do not travel at their maximum speed since output uniformity would have been extremely poor. Also, plasticating rate would have certainly been a limiting factor.

(viii) Other aspects

In addition to the materials used above, a PVC compound was tried with the ram extruder. This proved to be unsuccessful but the main reason for this was that the operating conditions were not favourably set for this material. With the ram extruder, it is necessary to flush out the material left in the extruder after the previous run when a new material is extruded. This may pose some problems, particularly if the maximum processing temperature of the new material is below the softening point of the material left in the extruder from the previous run. This was the case experienced with PVC. The processing temperatures were excessive for this material and thermal degradation occurred with the result that the complete flow passages were blocked by degraded PVC. With the other material used, thermal degradation occurred only with PP

when processed at very high shaft speeds, but no blocking of the flow passages occurred.

In the feed chambers formed by the initial lengths of the plasticating shaft and barrel and the metal keys, some dead spots where the material may be trapped exist. These, however, were not very critical since the material here tended to leak past the shaft seal rather than move towards the die.

At very high extrusion pressures, the force exerted by the rams on the feedstock and transmitted to the shaft laterally were large enough to deflect it considerably to the point that the brass tip of the shaft rubbed against the barrel wall. Occasionally, some brass particles were found with the extrudate. Clearly, a more rigid shaft was preferred if this was to be avoided.

In general, all the other improvements and modifications to the prototype extruder were found to be effective. In particular, the cooling system for different parts like the bearing housing and the initial section of the feed cylinders under the hoppers were found to be most useful in keeping their temperature low at room temperature.

It was found that barrel cooling was not required with the polymeric materials processed though this facility adds further flexibility to the machine particularly when very viscous polymers are handled. In general, the barrel temperatures in the ram extruder were set higher than in screw extruders when processing a given material. This improved the melting rate and also higher output rates have been obtained by increasing the barrel temperature.

With the operating conditions and materials tested, no increase in barrel temperature was detected when the shaft speed was

increased. It was noted that once the extruder was running steadily, very little barrel heating was required. More recently, a pulverised rubber has been successfully processed by this extruder. With this material an enormous amount of heat was generated by the rotation of the shaft and barrel cooling was necessary.

Though facilities were provided for changing the die and the plasticating shaft, all the experiments were carried out using the same set of die and shaft. The dimensions of these are given in Table 2.1.

2.6 Conclusions

A ram extruder for polymers giving a continuous output has been designed and built based on a prototype machine. Many improvements and modifications were incorporated in the new design adding further flexibility and versatility to the process. The overall performance has been greatly improved by these changes. The two main functions of a plasticating extruder, namely plastication and pumping of the polymer melt were separated in the ram extruder so that independent control of each function from the other was possible. This was a major advantage over conventional screw extruders. For plasticating purposes the shearing action in an annular channel provided by a stationary barrel and a rotating mandrel inside the barrel was exploited, whilst the melt pumping action was derived from hydraulically driven rams. To maintain a continuous flow of material through the die more than one ram was required and in the present extruder the minimum of two rams was selected for simplicity. In this way the plasticating rate was mainly controlled by the shear rate on the material in the annular cell by varying the

shaft speed, and the output rate was controlled by varying the pressures exerted by the rams.

In practice, the two functions are not entirely independent of each other because of the physical nature of the materials processed, in particular, the non-Newtonian behaviour of the polymer melts, and it is also clear that the output rate of the machine cannot exceed the rate at which material is plasticated. However, because of the control facilities, they are independent of each other to a large extent. Thus, for example, a reduction in output melt temperature may be accomplished by a reduction in shaft speed which controls the plasticating rate. Though a reduction in output rate may occur as a result of an increase in flow resistance by reducing the shaft speed, in the continuous ram extruder this loss of output rate can be compensated readily by increasing the ram pressures and hence demonstrating the versatility of the process.

Output rates obtained with the present size of extruder were satisfactory and it proved to be more economical in terms of specific power consumption than a comparable single screw extruder. With the continuous ram extruder it is more economical to operate at large output rate but the savings become smaller when output rates become excessive. The output uniformity was, however, inferior to that of a screw extruder due to the intermittent pumping action of the rams, but for non-continuous applications such as injection and blow moulding the ram extruder can be operated successfully as a plasticating unit in which the condition of the polymer melt delivered can to a large extent be controlled independently of the rate at which the polymer is to be supplied.

Some minor technical faults were experienced with the extruder such

as lack of stiffness of the plasticating shaft, leakage of material in certain places and unreliability of some mechanical components. These can, however, be cured relatively easily and cannot therefore be regarded as limitations of the process.

A major problem encountered in this particular extruder was the jamming of the feed passages by solid material when processing under incorrectly set operating conditions. Towards this, the relatively small dimensions of the flow passages in the solids feeding zone of the extruder encouraged bridging to occur particularly when large size granules were fed in. This, however, should not occur in future and larger versions of the ram extruder. Also, better understanding of the frictional behaviour of granulated polymers should ease these difficulties by aiding the selection of right conditions for the feeding zone.

Another problem inherent in the process is that the machine is not self clearing. This may pose some difficulties depending on the material that is to be processed and the material left in the extruder from the previous run. Wood flour has been tried as a flushing medium but it proved to be inadequate because it jammed the feed passages and eventually compacted solidly. At the present LDPE is used at the end of each run to fill the extruder since this material is relatively easy to process and therefore causes little problem in restarting the machine.

In conclusion, apart from some minor problems mainly peculiar to the present extruder which can be solved relatively easily anyway, the continuous ram extrusion method developed in the present work meets the major requirements for a universal processing machine where plasticating rate can be controlled largely independently from the output rate. As such, its eventual commercial success is envisaged because of its

versatility and flexibility.

Even if its output uniformity cannot match demands for product extrusion, the continuous ram extruder should find a place in the market as an homogeniser. Also, its positive pumping action and the ability to accept feedstock under various forms makes it suitable for certain applications, particularly for reprocessing scrap plastics.

Table 2.1

Specifications of the Extruder

and its Instrumentation

(i) Main physical dimensions

Diameter of feed cylinders and rams:	44.5 mm
Length of feed cylinders and rams:	152.0 mm
Nominal length of feed tubes in main block:	267.0 mm
Hopper aperture:	44.5 x 44.5 mm
Internal barrel diameter:	44.5 mm
Nominal length to diameter ratio (L/D) of barrel:	12:1
Length of barrel reducer plate:	60.5 mm
Effective barrel length (12D + Barrel reducer plate + Section in main block):	635.0 mm
Effective length of plasticating shaft:	510.0 mm
Plasticating shaft diameter:	3.8 mm
Clearance between shaft and feed chamber keys:	1.6 mm
Breaker plate:	95 holes of 3.2 mm diameter x 20.3 mm length
Extrusion die:	3.2 mm diameter x 31.8 mm length

(ii) Barrel temperature control system

Barrel heaters:	Electrical resistance 3 x 500 W
Barrel reducer plate heater:	Electrical resistance 1000 W
Die heater:	Electrical resistance 150 W
Temperature controllers:	2 x West Gardian type Q3X Thyristor Proportional Controllers range 0 - 400°C
	Also cooled by water circulating through helical grooves on the outside surface of the barrel under the heaters. Three independently cooled regions are provided and control is by degree of valve opening.

(iii) Main block temperature control system

Oil pump capacity:	52 dm^3/min
Pump motor:	1.5 kW
Oil heaters:	2 x 750 + 1500 W
Main block temperature controllers:	'Eurotherm' model PI range 0 - 400°C
Oil temperature controllers:	'Rototherm' range 0 - 400°C

Note: This is duplicated for the two control zones with the heating oil sharing a common expansion tank. Oil coolers are also included in the system.

(iv) Hydraulic system for feed rams

Pumps motor:	30 kW
Oil pumps:	2 x 83 dm^3/min, maximum pressure 11 MN/m^2
Hydraulic cylinders:	82.6 mm bore x 152.3 mm stroke with 44.5 mm rod

Control valves and complete oil circuit as shown in Figure 2.3.

(v) Plasticating shaft drive

Electric motor:	11 kW
Variable speed drive:	'Kopp' variator range 60 - 380 rpm
Shaft torque transducer:	'Vibro-Meter' type TG100
Torque transducer amplifier:	'Vibro-Meter' 8-MCA-1/A plus 8-MCA-P-1/A
Shaft speed pick up:	'Vibro-Meter' type JP/1412 magnetic pulse pick up integral with torque transducer
Shaft speed indicator:	'Vibro-Meter' type AR1-1/A

(vi) Other instrumentation

Pressure transducers:	'Dynisco' type PT420
Bridge amplifiers:	'Flyde' Model 154-ABS
U.V. recorder:	'S.E. Oscillograph' 2112
Multi-channel recorder:	'Ether' type 7056

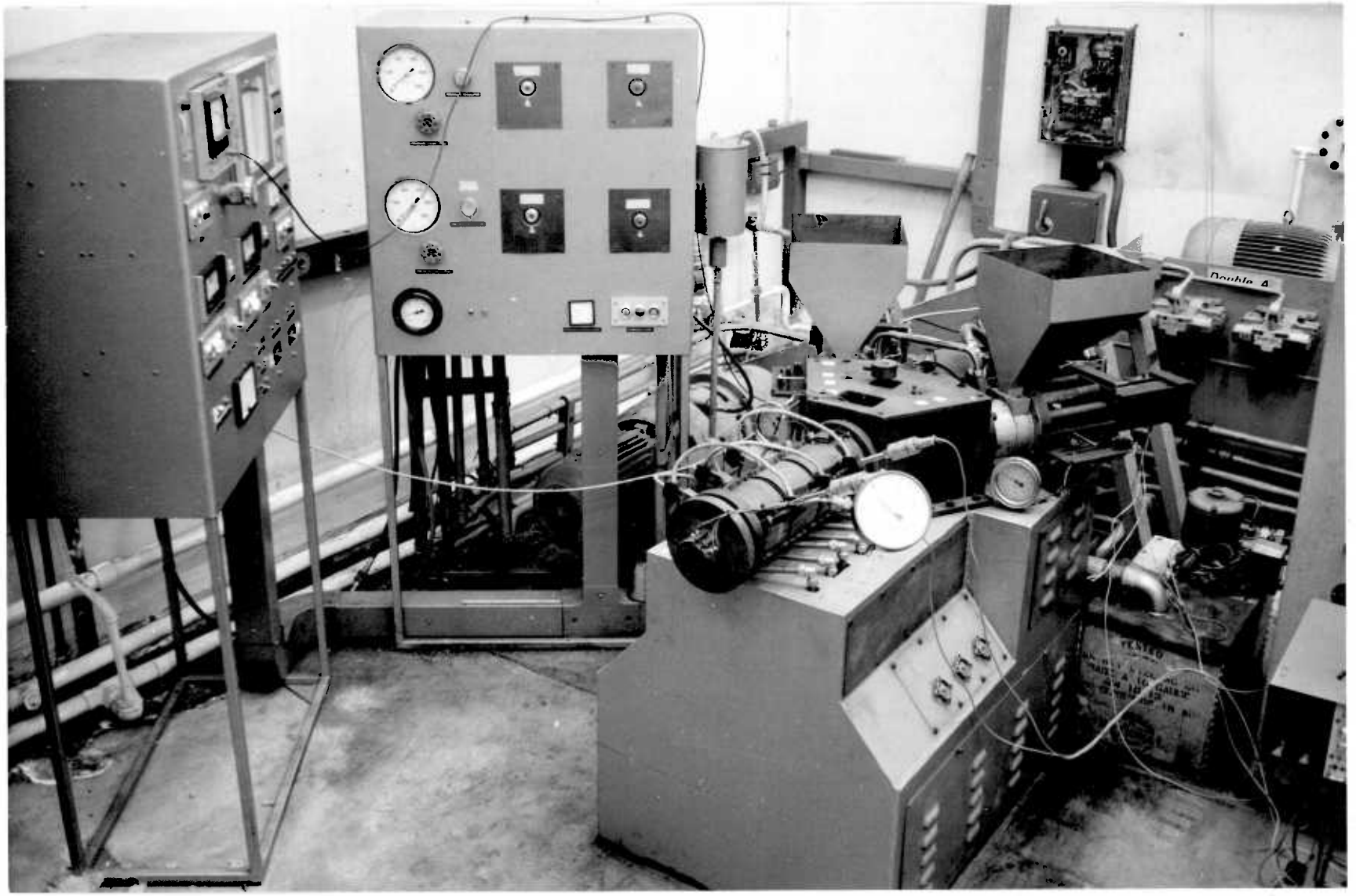

PLATE 2.1 - GENERAL VIEW OF THE CONTINUOUS RAM EXTRUDER

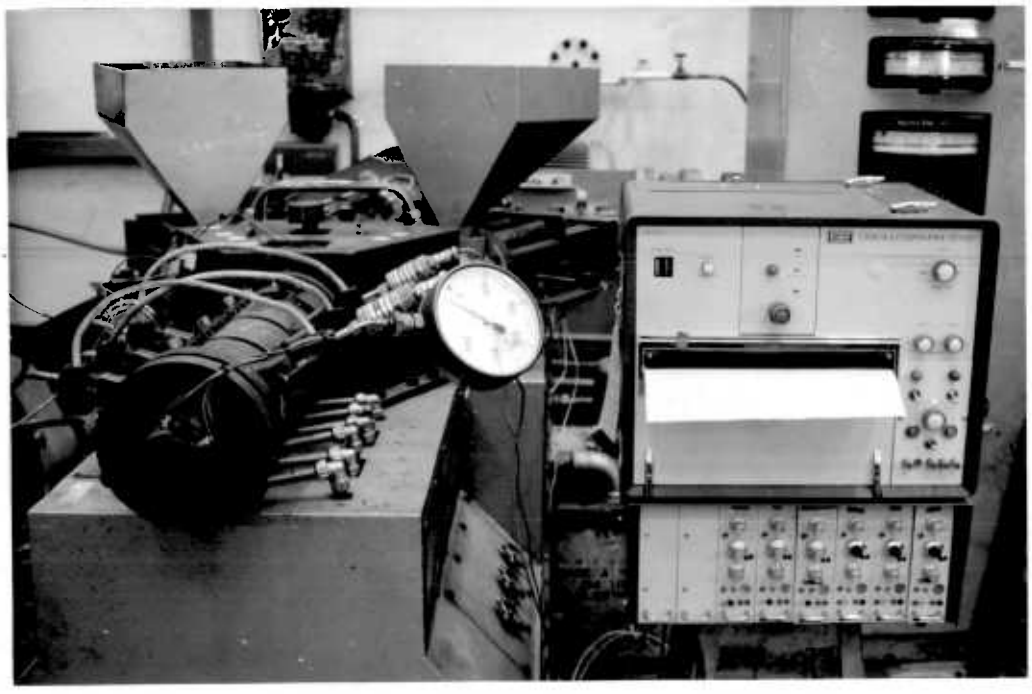

PLATE 2.2 - INSTRUMENTATION FOR PRESSURE RECORDING

1 - PRESSURE TRANSDUCERS

2 - BRIDGE AMPLIFIERS

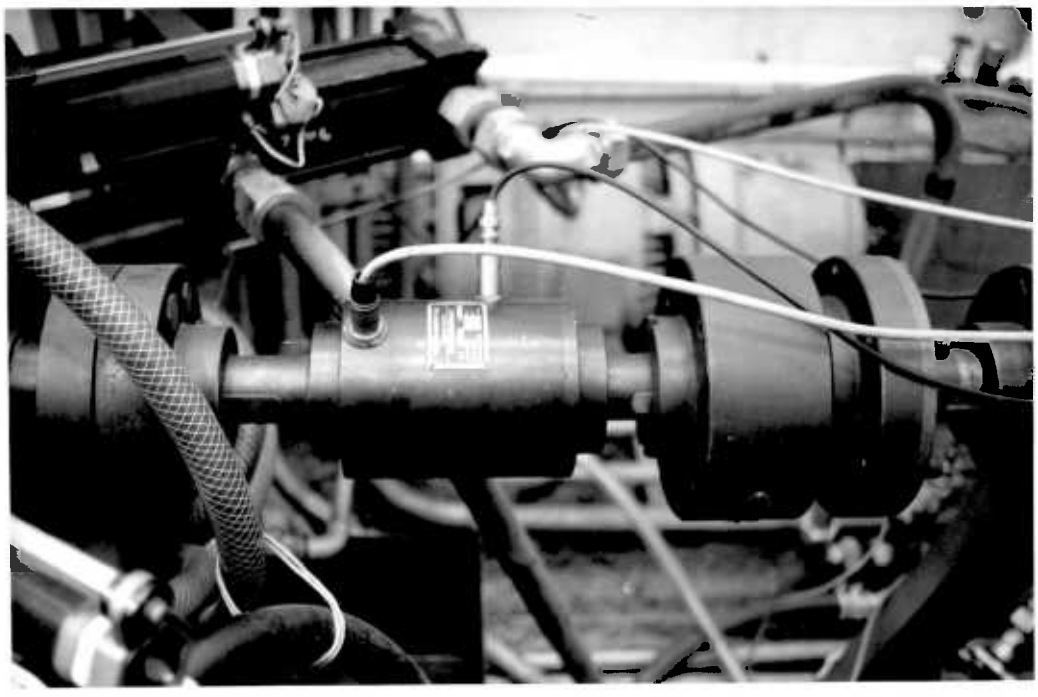

PLATE 2.3 - SHAFT DRIVE WITH TORQUE TRANSDUCER AND MAGNETIC PULSE PICK-UP FOR SHAFT SPEED MEASUREMENT

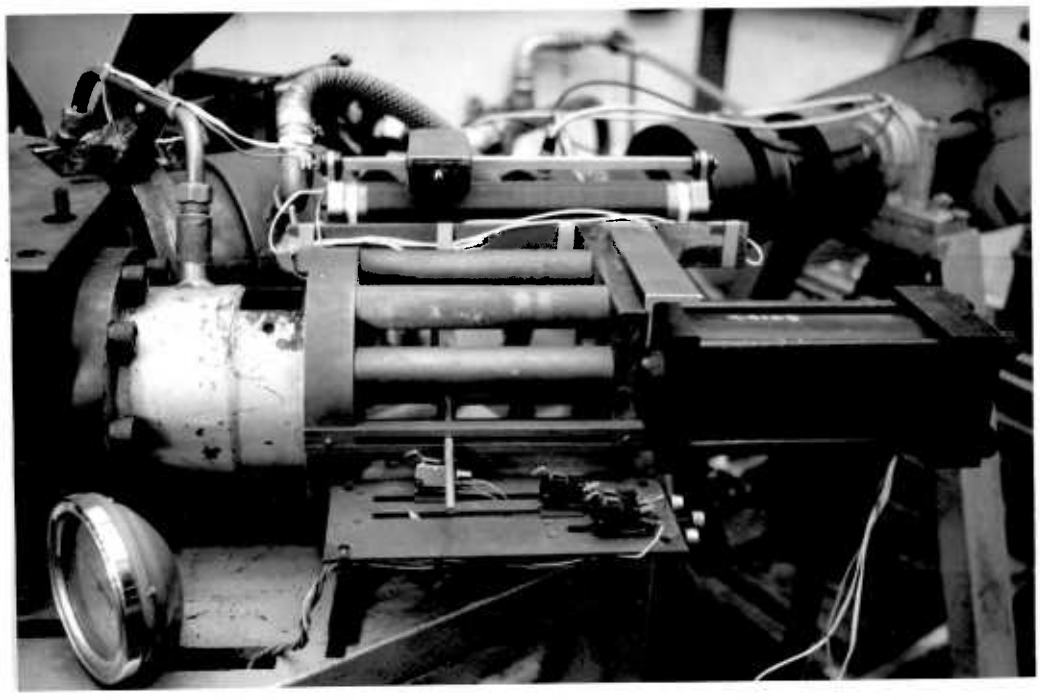

PLATE 2.4 - FEED CYLINDER, HYDRAULIC CYLINDER, MICROSWITCHES TABLE AND DISPLACEMENT TRANSDUCER (RHEOSTAT)

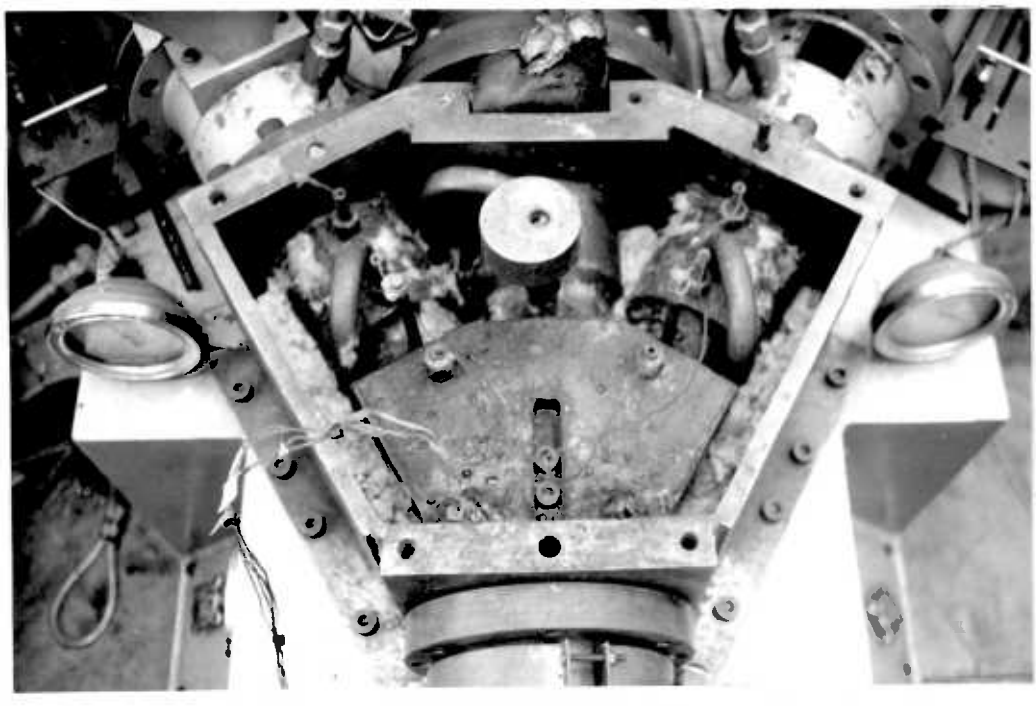

PLATE 2.5 - DETAILS OF THE MAIN BLOCK SHOWING THE OIL AND WATER JACKETS, VENTING PORTS, THERMOCOUPLE PROBES AND SOME GLASS WOOL INSULATION

PLATE 2.6 - MAIN CONTROL CABINET

3 - RPM INDICATOR

4 - MULTI-CHANNEL TEMPERATURE RECORDER

5 - BARREL TEMPERATURE CONTROLLERS

6 - MAIN BLOCK TEMPERATURE CONTROLLERS

7 - SHAFT TORQUE INDICATOR

PLATE 2.7 - CONTROL CABINET FOR THE HYDRAULIC SYSTEM

8 - PRESSURE RELIEF VALVE ADJUSTERS

9 - FLOW RATE CONTROL VALVE ADJUSTERS

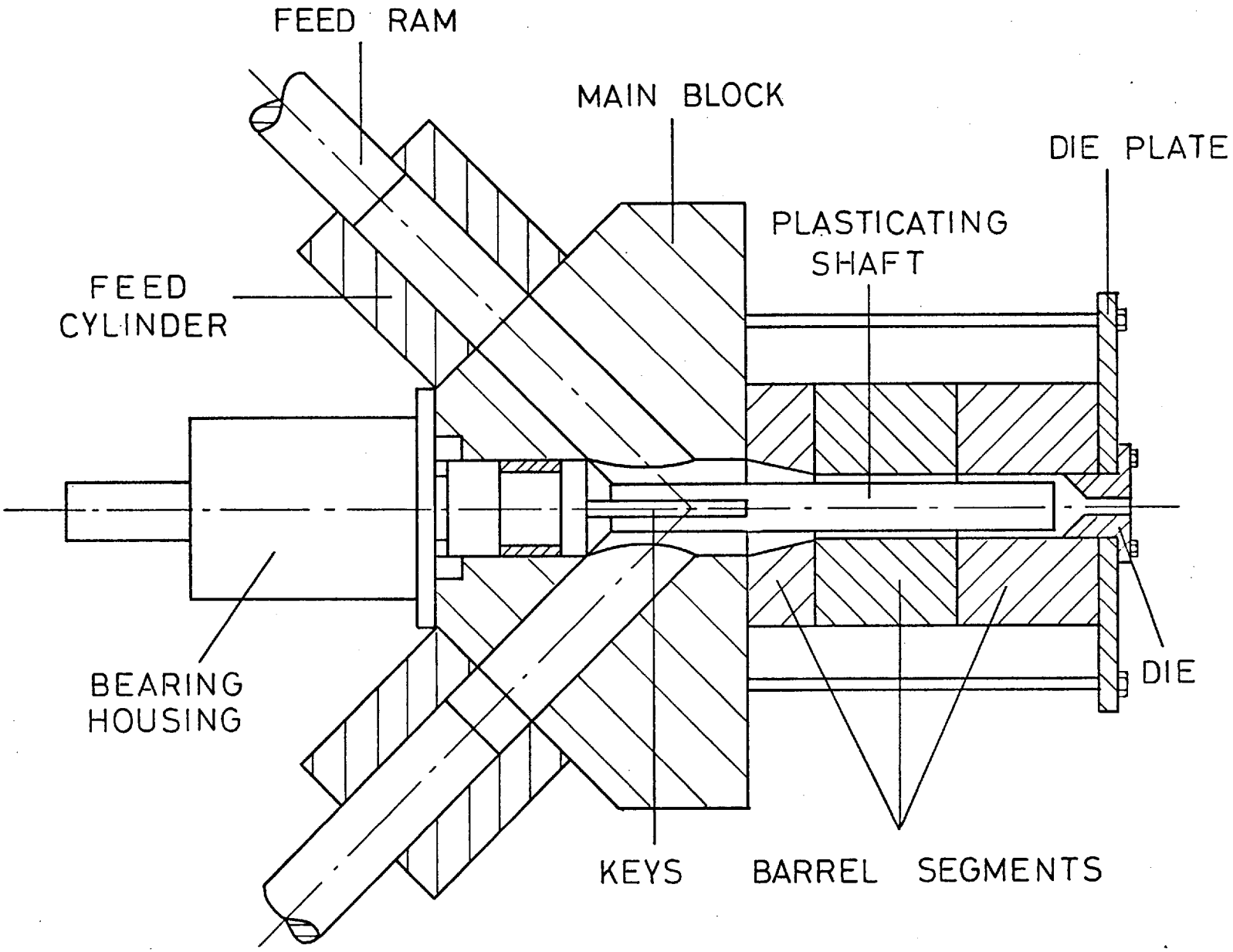

Fig. 2.1 - Cross section of the prototype extruder

1, 2, 3, 4 - PRESSURE TAPPINGS

A, B, C, D - MELT THERMOCOUPLES

E, F, G, H - BARREL TEMPERATURE CONTROL THERMOCOUPLES

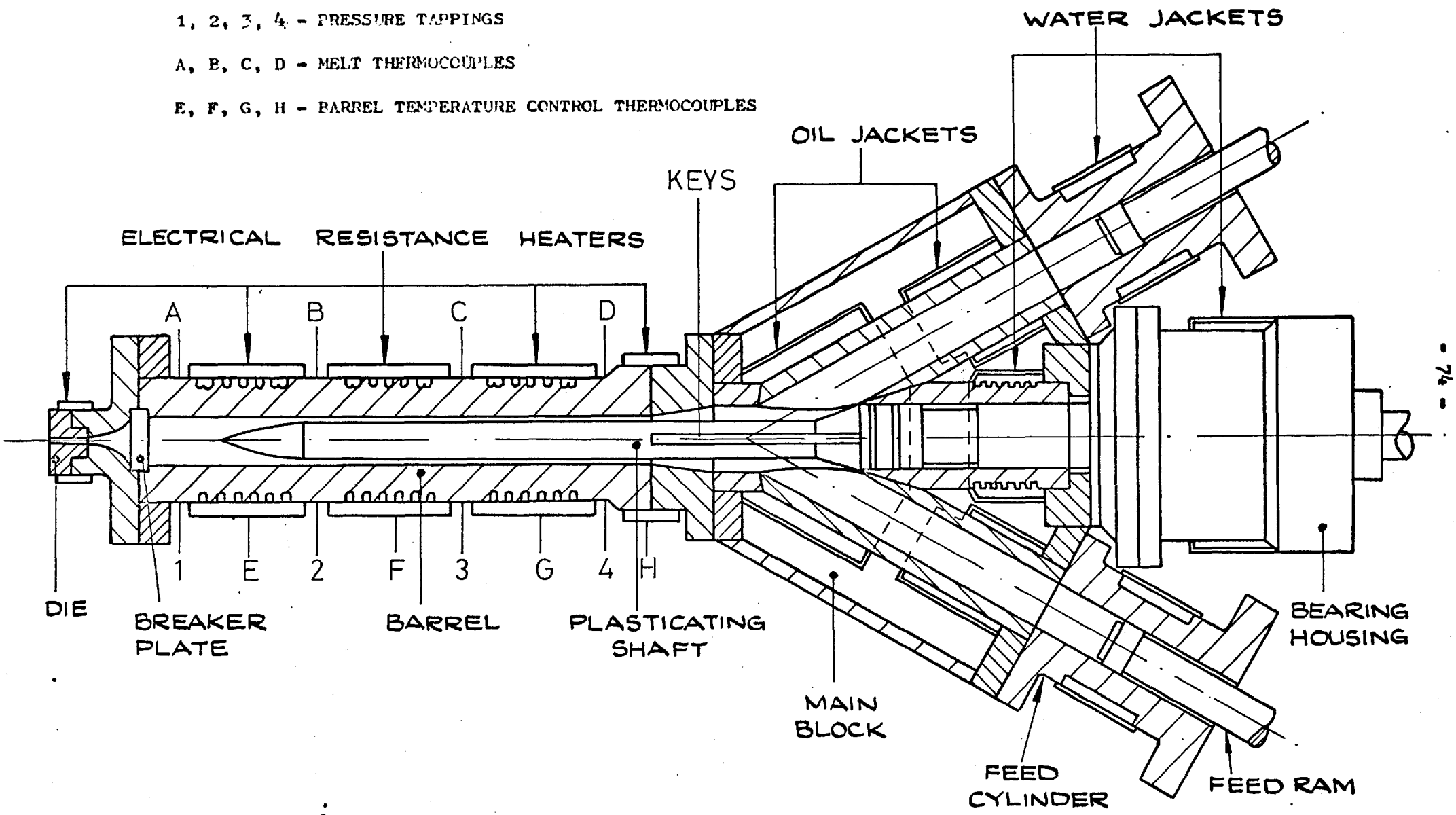

FIG. 2.2 CROSS SECTION OF THE IMPROVED EXTRUDER

4 - DIRECTION CONTROL

5 - SECOND STAGE SOLENOID VALVE

6 - SECOND STAGE FLOW RATE CONTROL

7 - NON-RETURN CHECK VALVE

8 - OVERALL FLOW RATE CONTROL

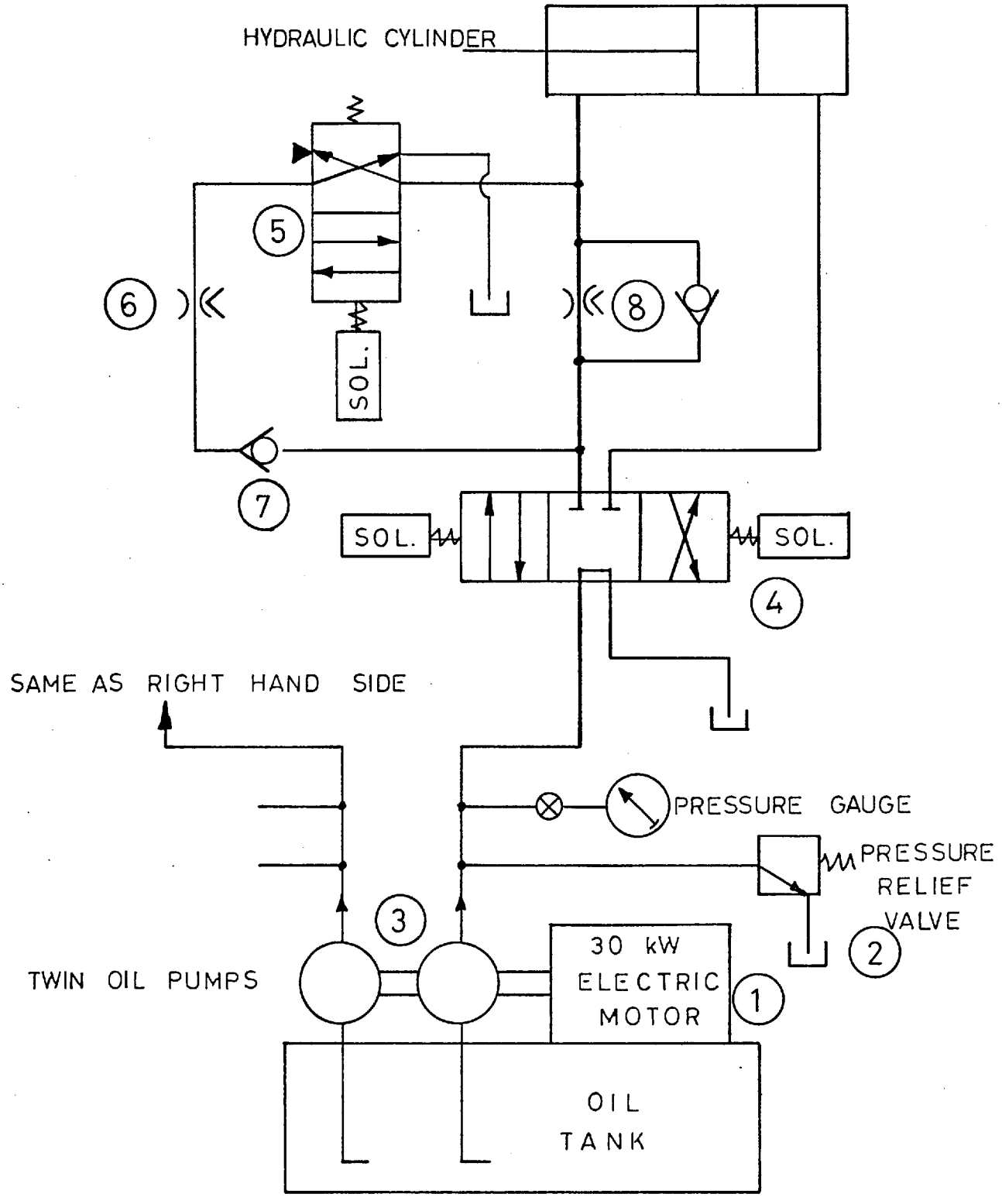

FIG. 2.3 - HYDRAULIC SYSTEM

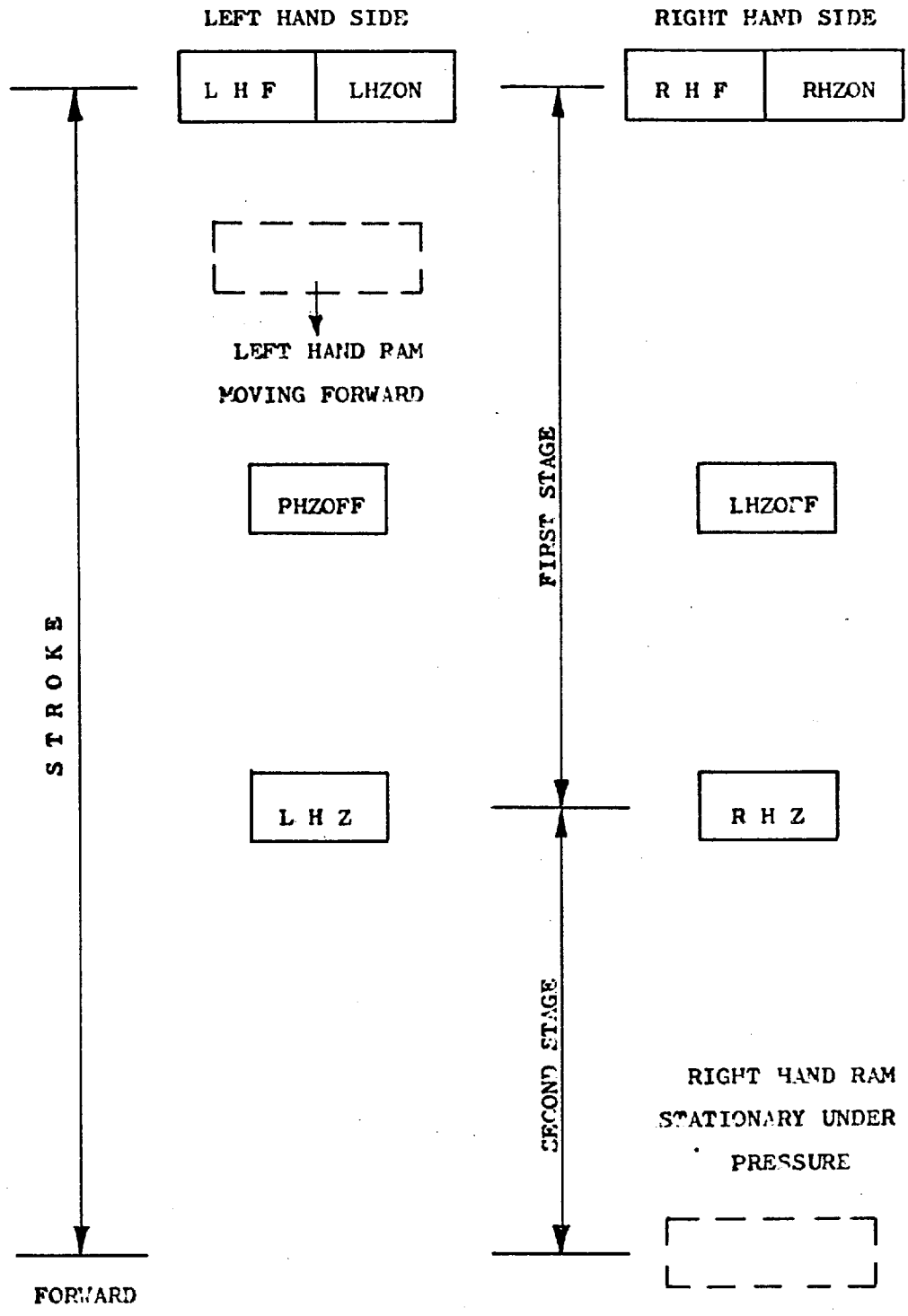

FIG. 2.4 - POSITION OF MICROSWITCHES FOR AUTOMATIC CYCLING OF THE RAMS

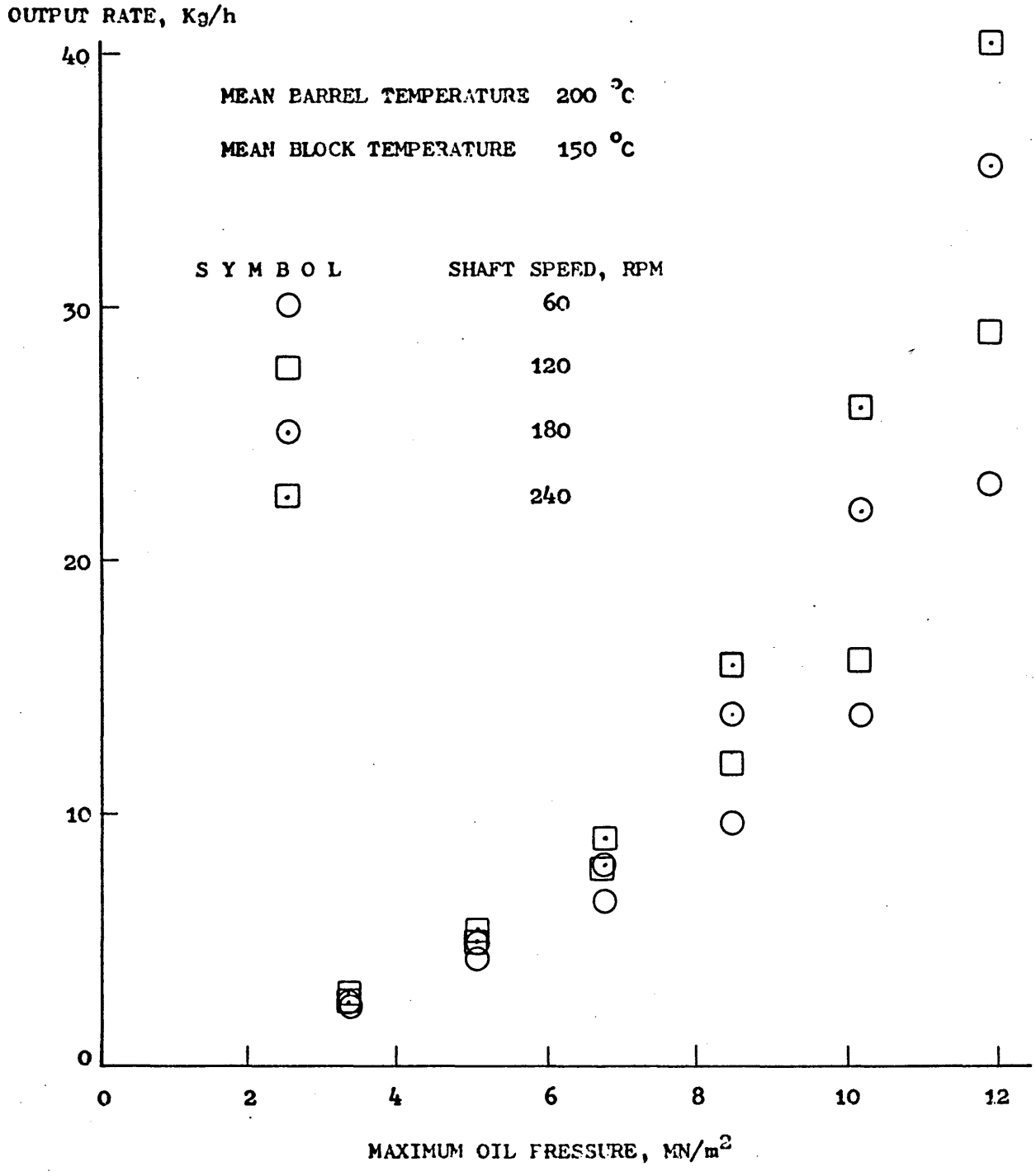

FIG. 2.5 - OUTPUT RATE PLOTTED AGAINST MAXIMUM OIL PRESSURE IN THE RAMS FOR LDPE

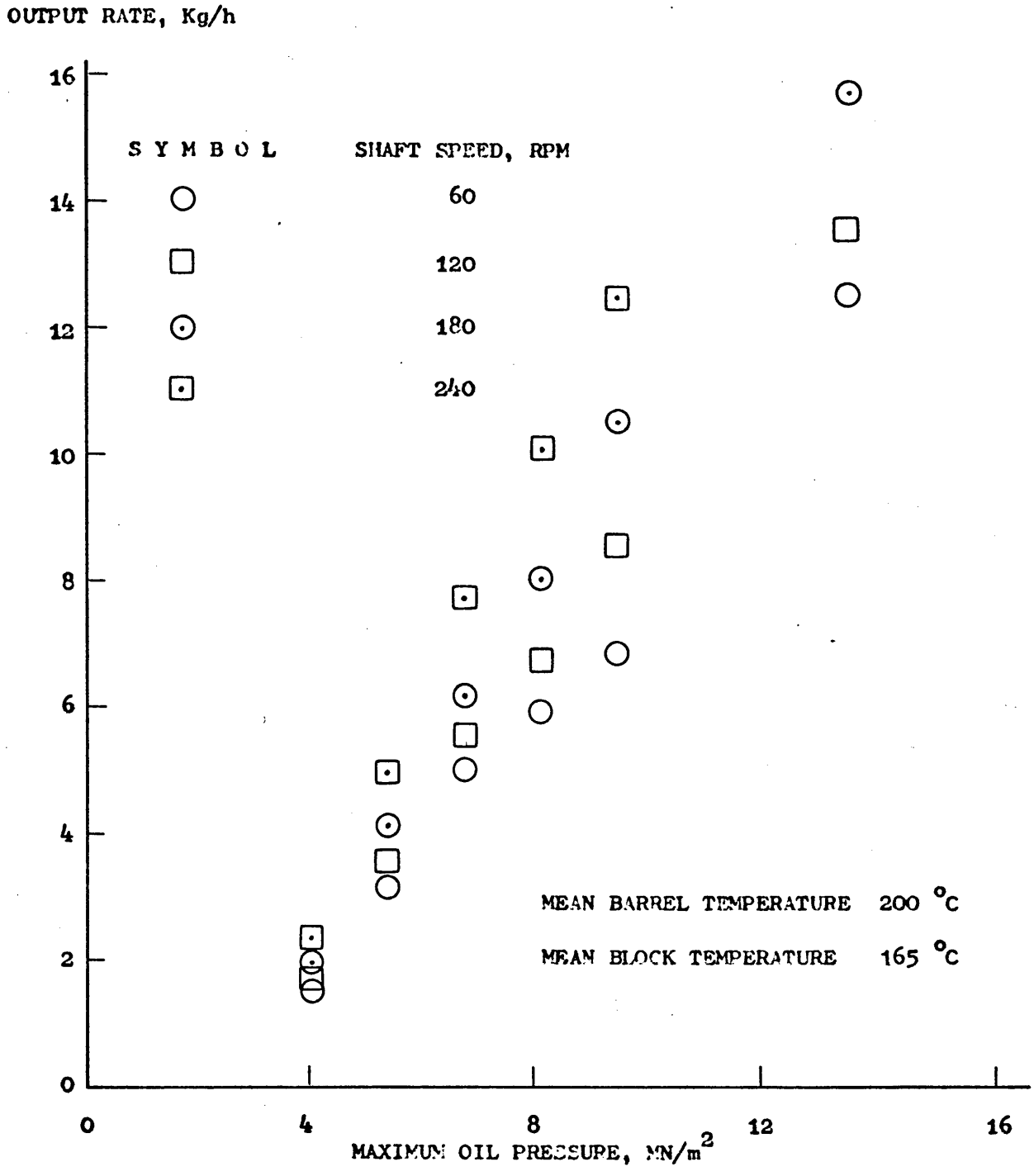

FIG. 2.6 - OUTPUT RATE PLOTTED AGAINST MAXIMUM OIL PRESSURE IN THE RAMS FOR HDPE

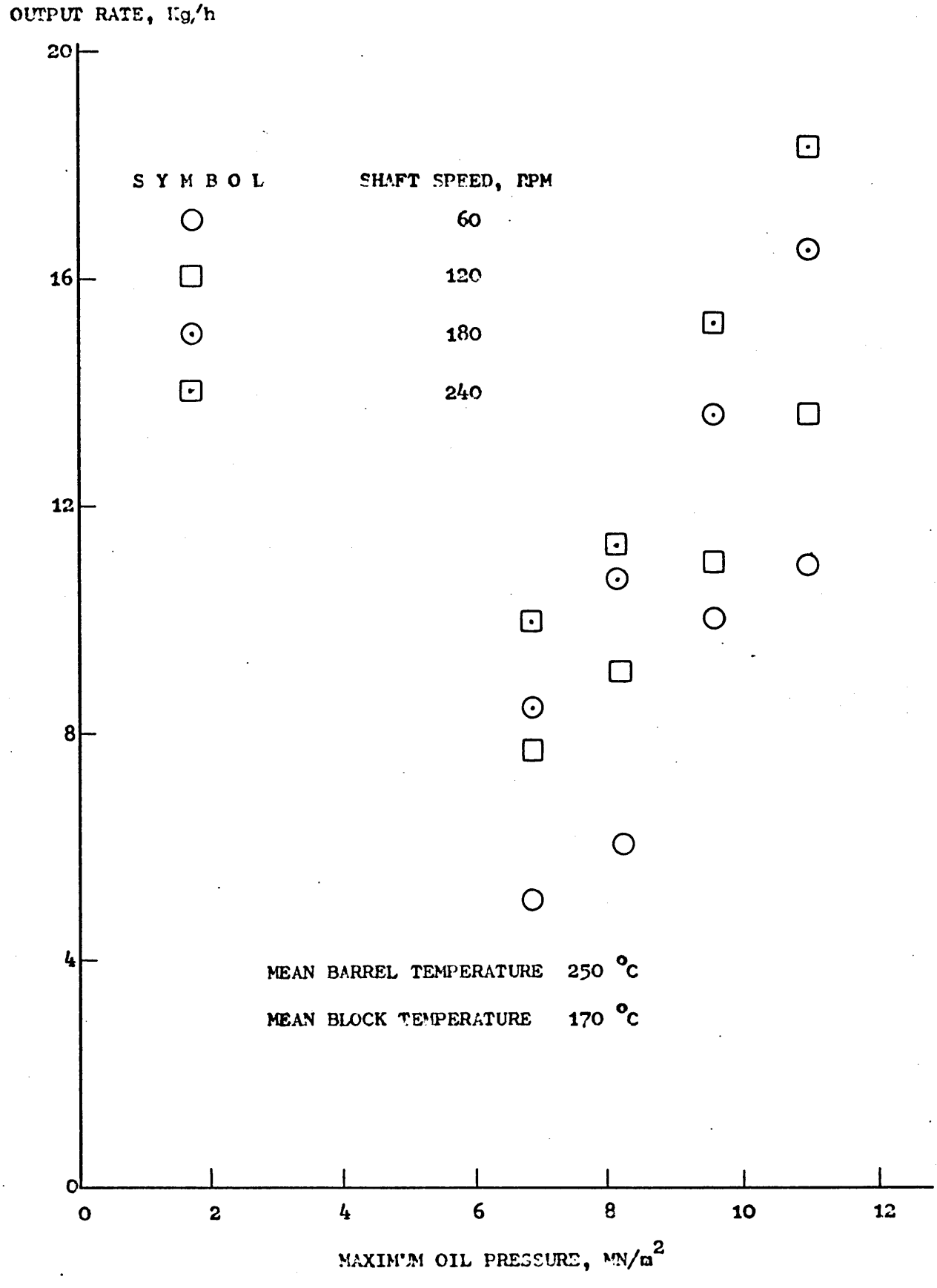

FIG. 2.7 - OUTPUT RATE PLOTTED AGAINST MAXIMUM OIL PRESSURE IN THE RAMS FOR PP

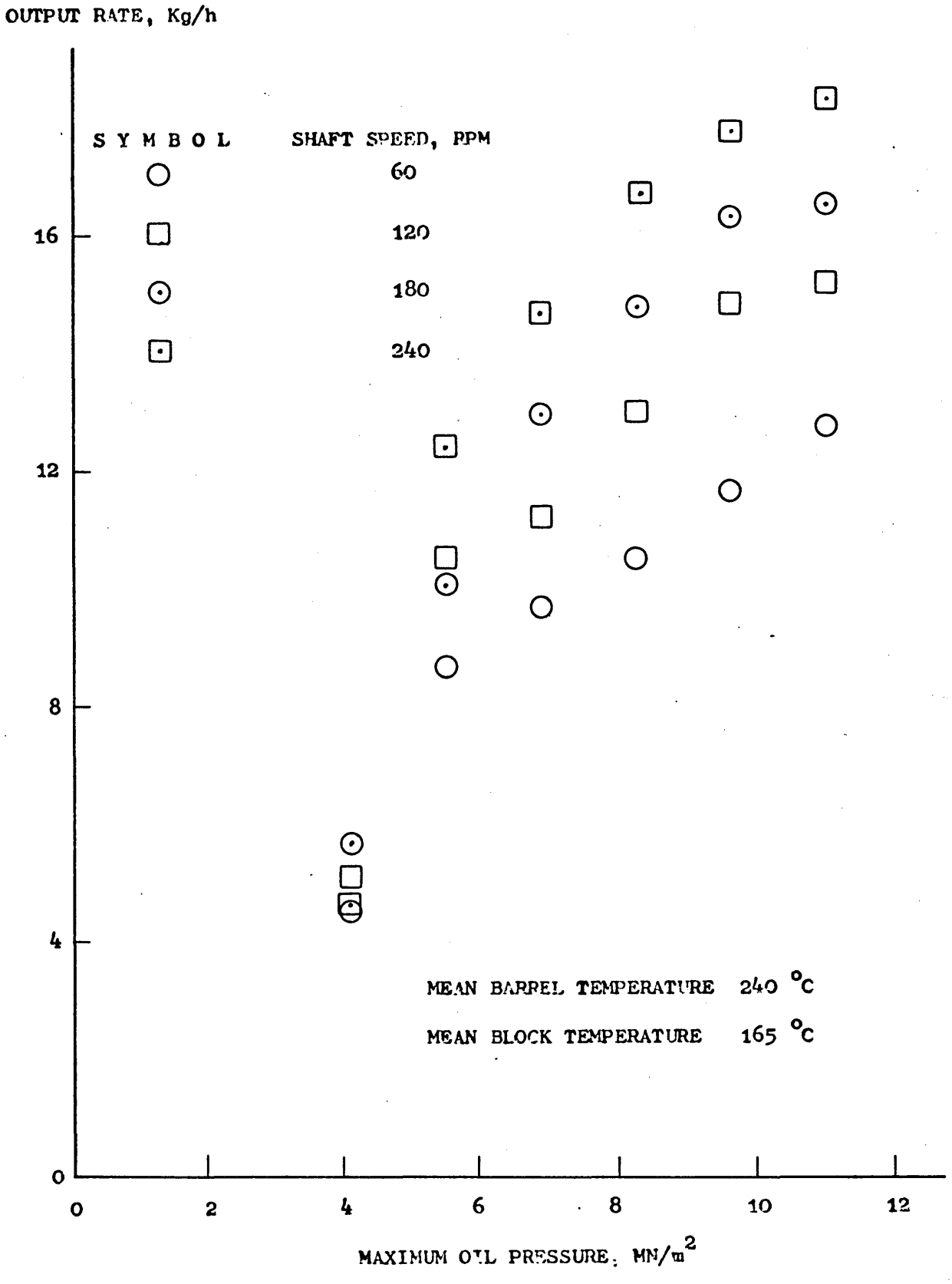

FIG. 2.8 - OUTPUT RATE PLOTTED AGAINST MAXIMUM OIL PRESSURE IN THE RAMS FOR PS

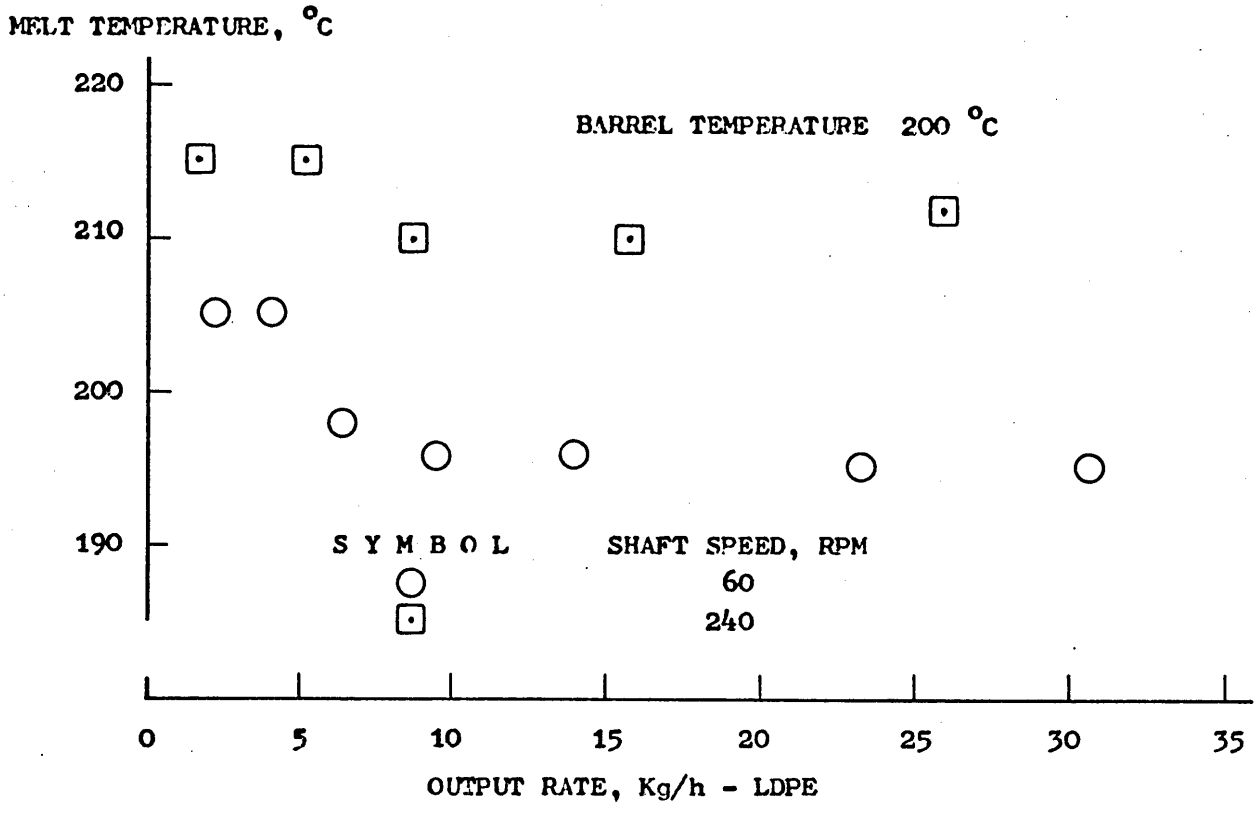

FIG. 2.9 - MELT TEMPERATURE AT THE END OF THE ANNULAR CHANNEL PLOTTED AGAINST OUTPUT RATE

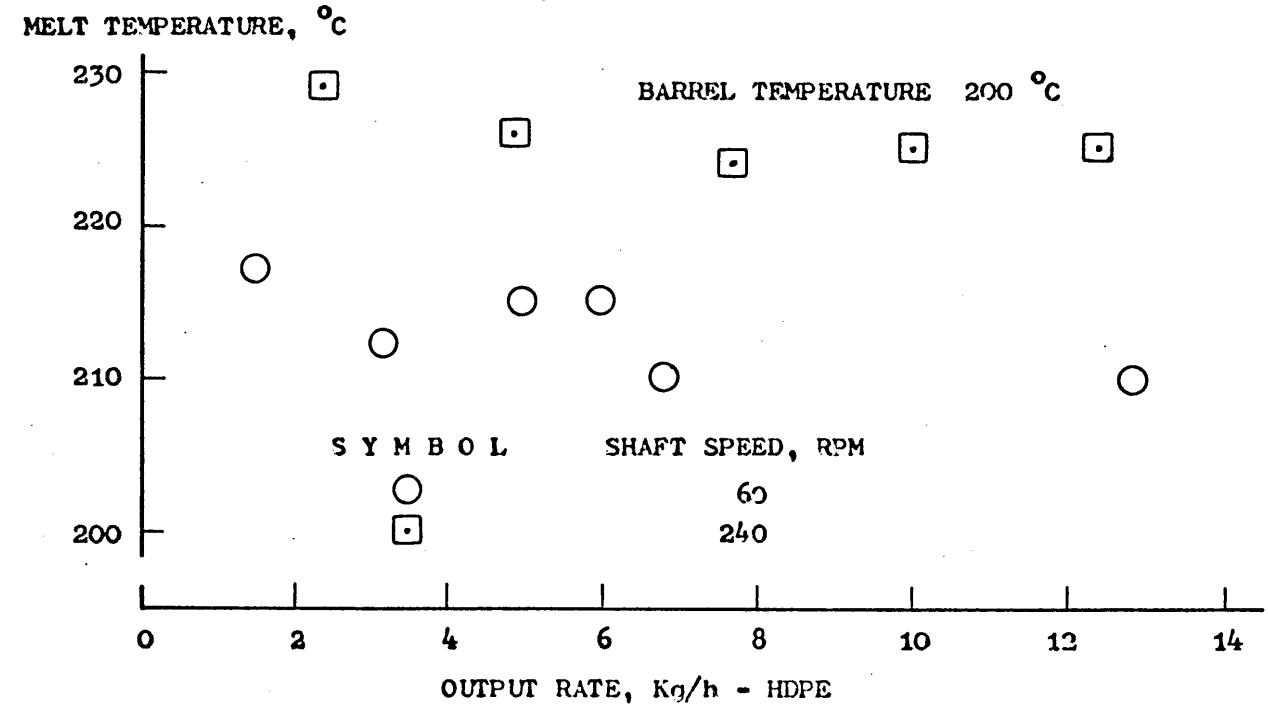

FIG. 2.10 - MELT TEMPERATURE AT THE END OF THE ANNULAR CHANNEL PLOTTED AGAINST OUTPUT RATE

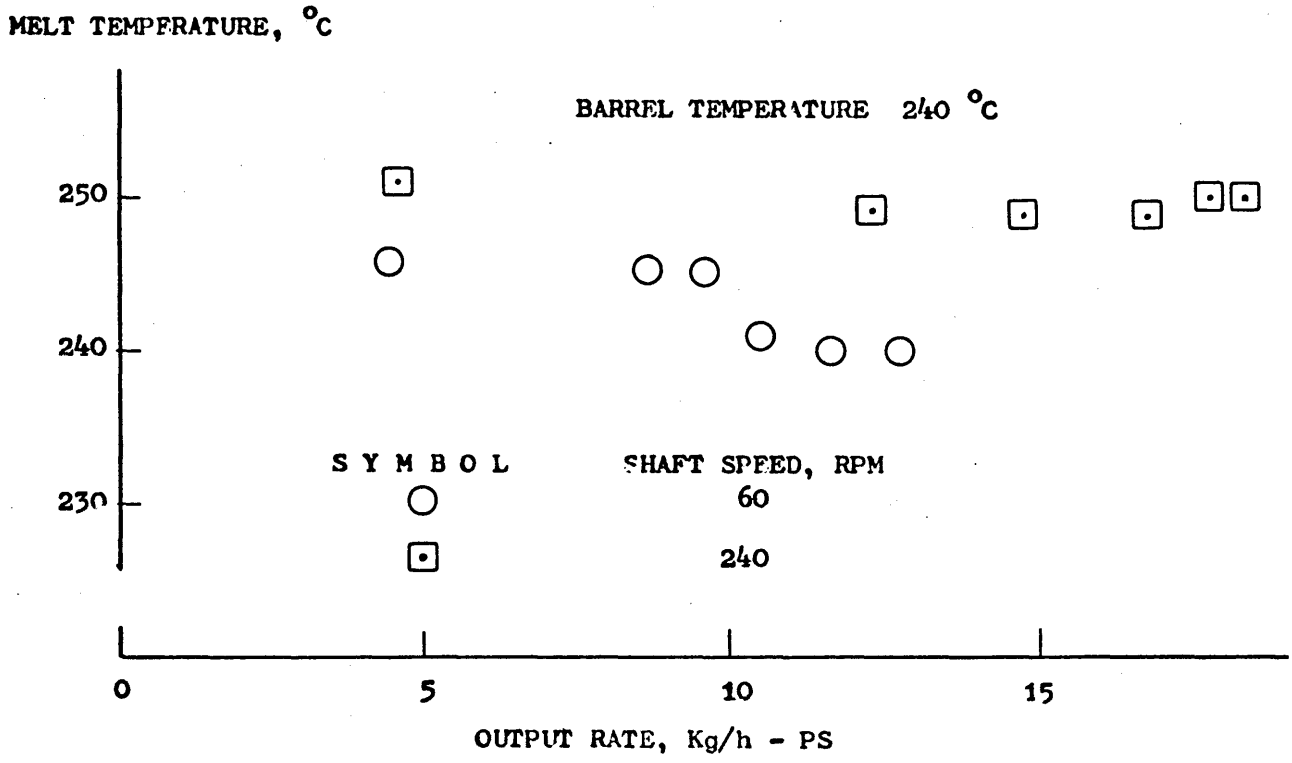

FIG. 2.11 - MELT TEMPERATURE AT THE END OF THE ANNULAR CHANNEL PLOTTED AGAINST OUTPUT RATE

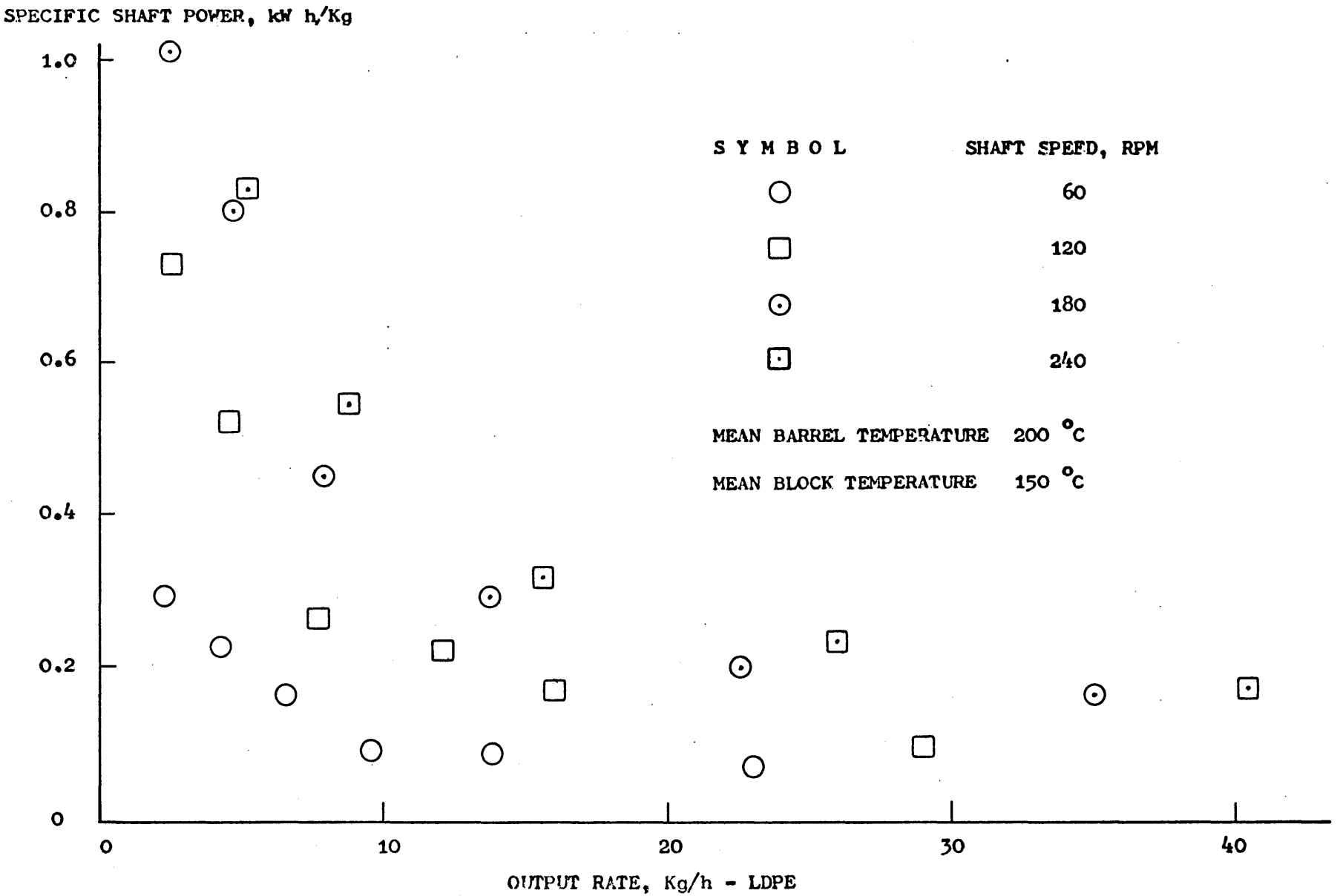

FIG. 2.12 - SPECIFIC SHAFT POWER CONSUMPTION PLOTTED AGAINST OUTPUT RATE

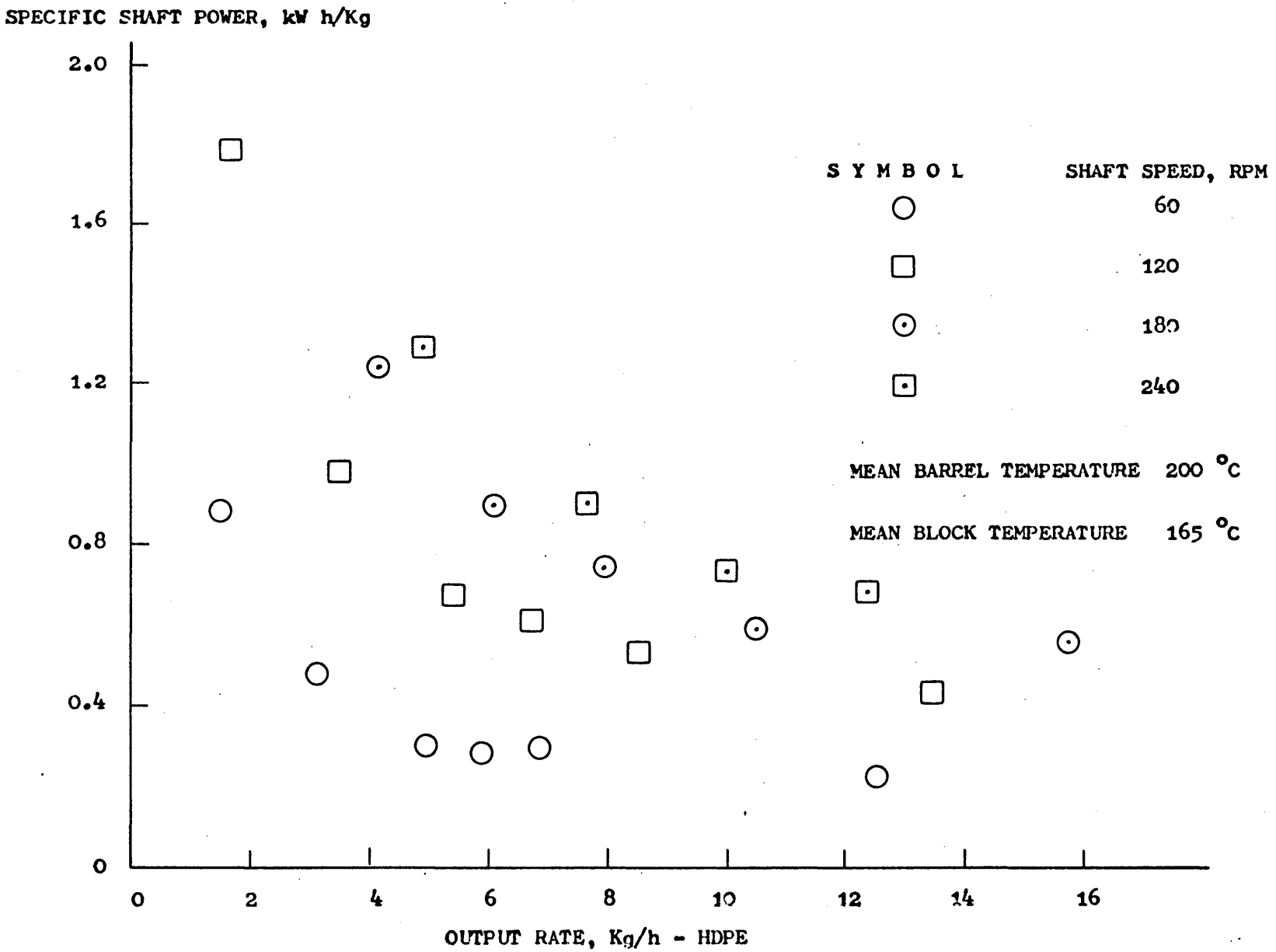

FIG. 2.13 - SPECIFIC SHAFT POWER CONSUMPTION PLOTTED AGAINST OUTPUT RATE

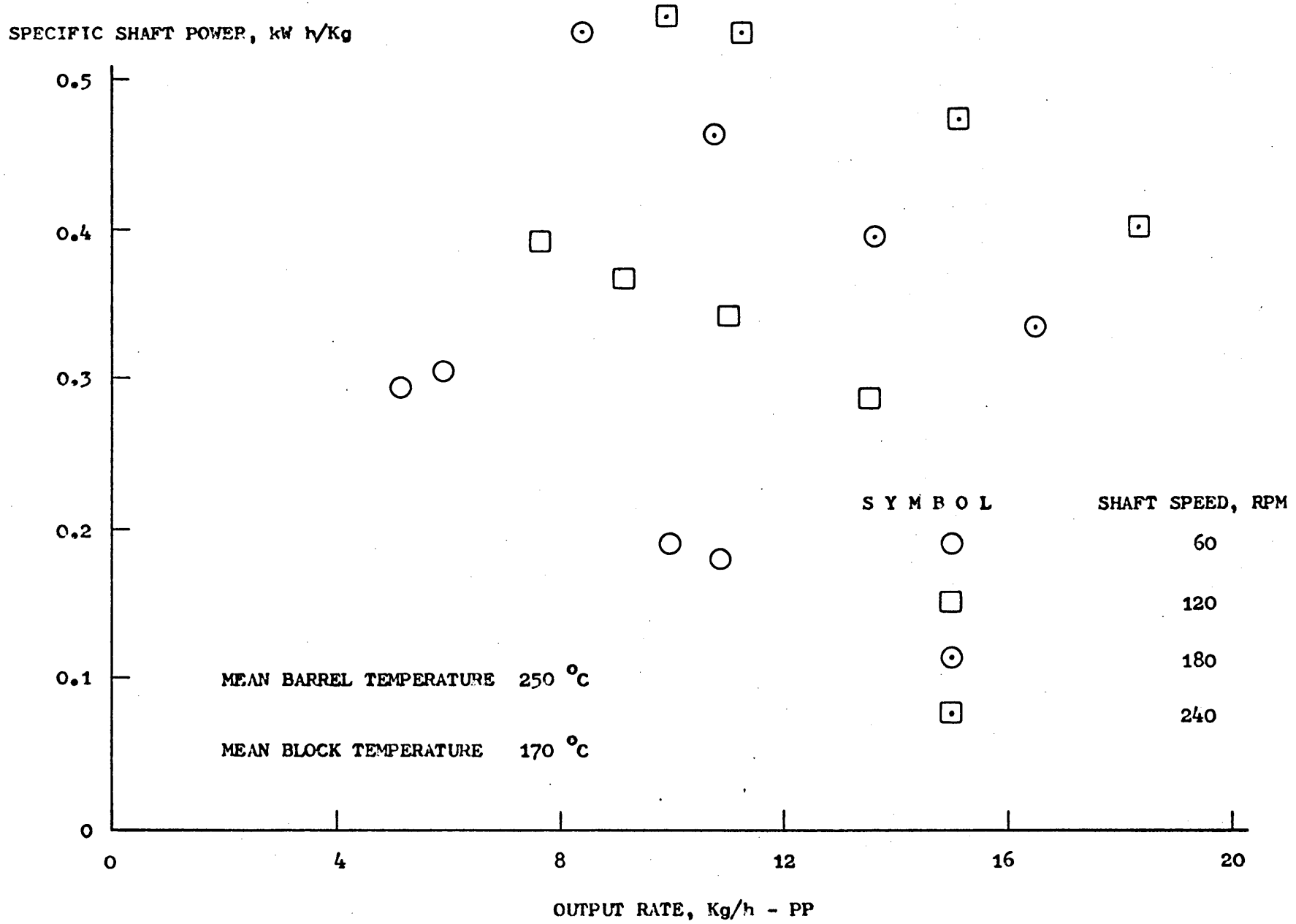

FIG. 2.14 - SPECIFIC SHAFT POWER CONSUMPTION PLOTTED AGAINST OUTPUT RATE

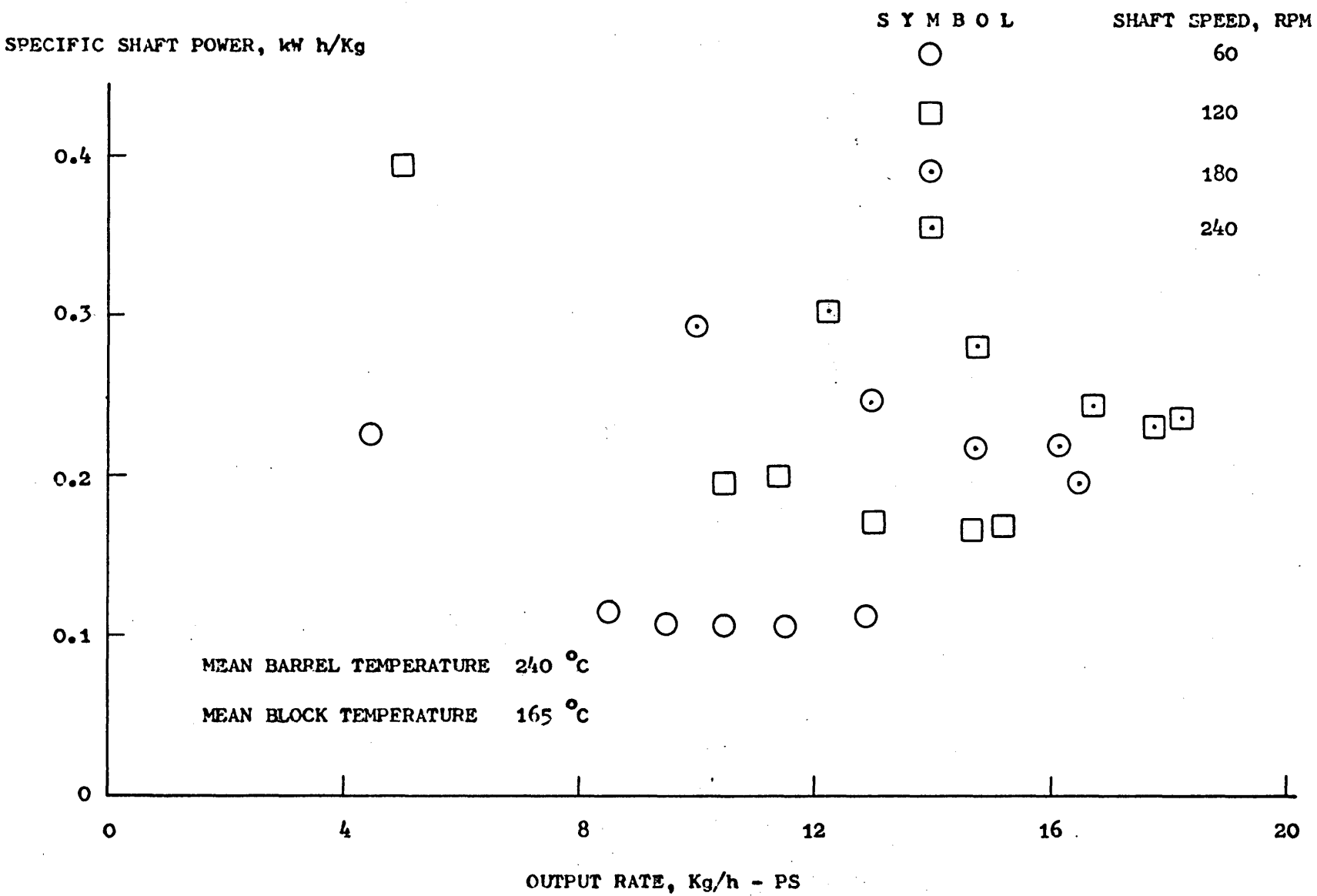

FIG. 2.15 - SPECIFIC SHAFT POWER CONSUMPTION PLOTTED AGAINST OUTPUT RATE

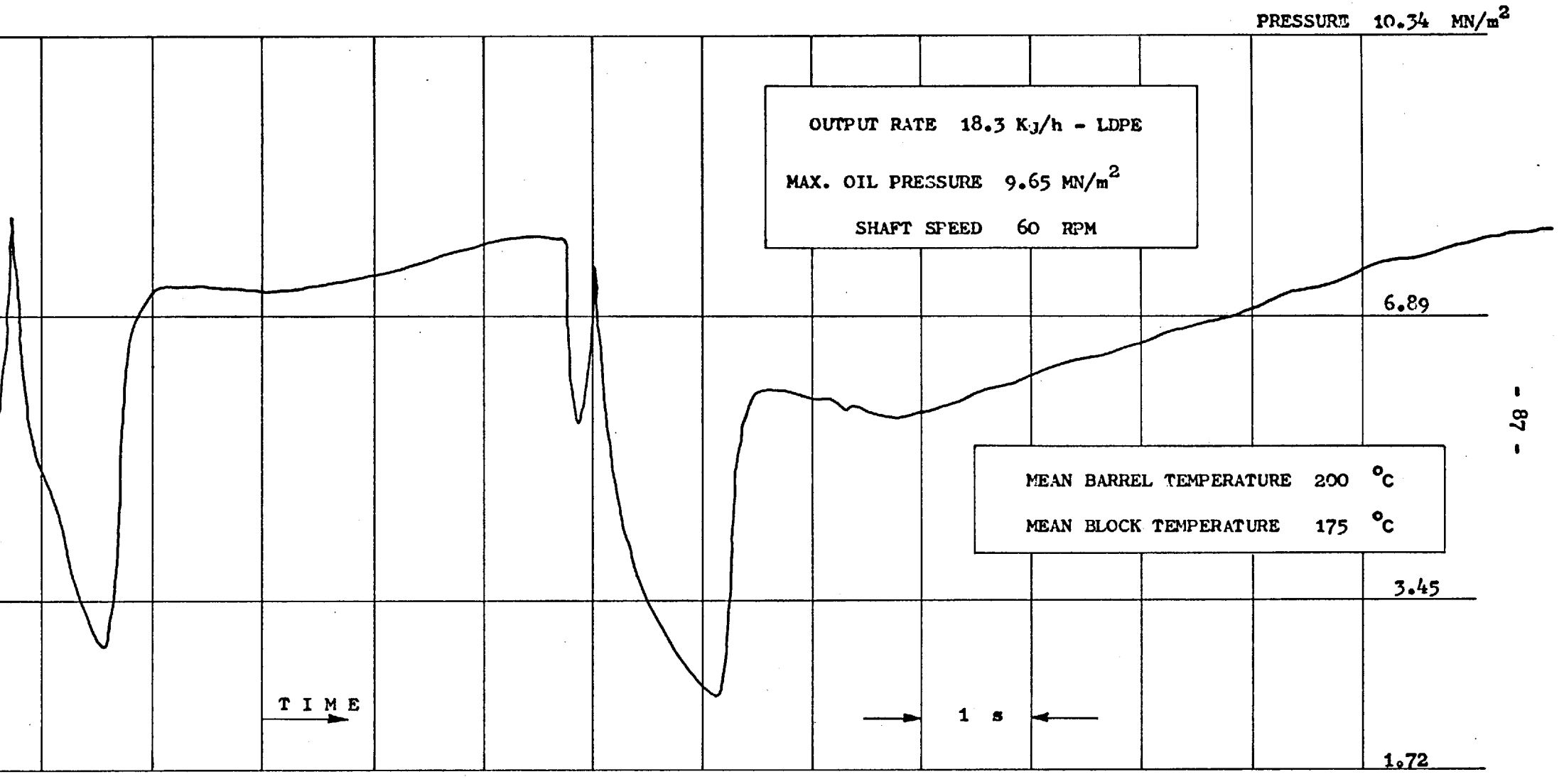

FIG. 2.16 - VARIATION OF THE MELT PRESSURE AT THE END OF THE ANNULAR CHANNEL OVER TWO CYCLES, ONE FOR EACH FEED RAM

CHAPTER 3

THEORETICAL ANALYSIS OF THE FEEDING ZONE

3.1 Introduction

This chapter describes procedures for calculating pressure losses in the solids feeding zone of the continuous ram extruder.

The maximum pressures exerted by the feed rams on the material determine to a large extent the output rate of the machine. For this reason, one of the major aspects of the analysis of the feeding zone is the prediction of pressure losses due to friction between the containing walls and the compacted solid mass of polymer.

The term pressure is used here loosely to denote compressive stresses in the granular material. Unlike the pressures in a fluid medium, the stresses at a point in a granular material are not necessarily the same in all directions. Therefore, in the present chapter, pressure will in general refer to the stress in the direction of flow of the granular material.

The flow of the solid feedstock is resisted by frictional forces which are initially of the Coulomb type, i.e. 'dry' friction. As the material moves further into the extruder channel and comes into contact with hotter walls, a melt film begins to form. This melt accumulates and gives rise to the melting mechanism occurring in the annular region of the flow passage. The problem of pressure calculations becomes of a different nature and this is dealt with in the following chapter which considers the melting process in the extruder.

Originally all pressure calculations for the feeding zone were carried out on the assumption that Coulomb frictional forces only prevail in the feeding zone. Whilst this was a reasonable assumption for the

processes in the prototype extruder, in the new extruder viscous forces may exist since the main block in which the feed cylinders are incorporated may reach temperatures well above the melting point of common polymers such that melt film formation in the feed cylinders is very likely to occur. In view of this, the work was later extended to include an analysis in which 'dry' friction gives way to viscous friction in the feed cylinders.

3.2 Geometry of the Feeding Zone

Geometrically, the solids feeding zone can conveniently be regarded as that extending from the face of the ram pushing the polymer to the beginning of the annular region, i.e. from plane AA to BB in Figure 3.1.

For the calculation of the pressure transmitted from plane AA to BB, the region is divided into two, one extending from plane AA to CC and the other one from section CC to BB. The geometry of the region bounded by planes AA and C'C' is simple to describe in that it is cylindrical. The zone bounded by planes C'C' and BB is the intersection of the feed cylinder with the initial length of the barrel and its geometrical description is complex.

An attempt to use the exact geometry of the feeding zone for the purpose of pressure calculations would prove to be difficult and therefore some assumptions regarding the geometry are necessary so that useful solutions may be obtained. The first simplification made is to assume that the cylindrical feed passage extends from plane AA to CC instead of AA to C'C'. This assumption should not introduce large errors since a large part of the perimeter at section CC is cylindrical and also the length L_c is small compared with L_s. The second assumption concerns the region contained by planes CC and BB. Here, more severe

simplifications must be made. The rotation of the shaft is assumed to have an insignificant effect on the frictional forces opposing the flow of the material and therefore it may be considered as stationary. The region is assumed to be that shown in Figure 3.2 contained by the planes BB and CC and bounded by two flat plates extending infinitely in the direction normal to the plane of Figure 3.2. Although these two latter assumptions lead to a situation which bears only limited resemblance to the real case, it is hoped that the solution so obtained is still valid at least to give an indication of the order of magnitude of the pressure losses in this region. It is worth noting though, that the most important geometrical features of this region are retained, namely the convergence of the flow channel from section CC to BB and the inclination - angle β - at which the feed cylinder meets the axis of the barrel.

3.3 Frictional Properties and Compressibility of Granular Polymer

It is appropriate at this stage to discuss some important physical properties relevant to the pressure propagation in granular polymer. These are the coefficient of friction between polymer and metal, the strength of the compacted mass of solid polymer particles and its compressibility.

(a) Coefficient of friction between polymer and metal

The Coulomb type of friction between the polymer and the metal walls can be characterised by a single quantity, the coefficient of friction. This, however, need not be single valued and indeed for a given polymer/metal interface, the value of the coefficient of friction is affected by the following parameters:

1. Sliding velocity of the polymer against the metal wall.
2. Temperature.
3. Pressure at the contact region.
and 4. State of the surfaces depending on the amount of rubbing which has taken place.

Frictional properties of plastics in contact with metals have been studied extensively [24,25,26,27], most of these under idealised conditions, mainly seeking fundamental explanations of the frictional behaviour.

In his work on the processes in the feeding zone of single screw extruders, Schneider [7] investigated the effect of the above parameters on the coefficient of friction between a number of plastics, mainly nylons, and steel. The conclusions from his work are as follows:

1. The effect of the sliding velocity on the coefficient of friction is small, particularly at low temperatures. Within a reasonable range of speeds, the coefficient of friction can be safely assumed to be independent of sliding speed.
2. In general, the coefficient of friction increases with increasing temperature for smeared surfaces, the opposite occurring with clean surfaces.
3. The coefficient of friction decreases with increasing normal pressure.
4. The coefficient of friction is higher for a smeared metal plate than for a clean one.

The major point to draw from this is that the use of single valued

coefficients of friction is unsatisfactory because of their dependence on these parameters and others including humidity, degree of polymerisation and crystallinity, presence of pigments and other additives. It would have been impractical to include all these factors in a theoretical analysis, however, and therefore single valued coefficients of friction must be used in order to obtain useful predictions. Clearly, to minimise the error in these predictions, the values chosen must be as close as possible to those for the actual situation. This often means that it is necessary to obtain the values experimentally under simulated conditions close to the real situation.

(b) Strength of compacted polymer particles

In Figure 3.2, the mass of compacted polymer particles flows from plane CC to plane BB. This flow of material must involve some form of deformation of the solid mass, and the mechanism is likely to be one of shear, that is, particles sliding over each other. The deformation and strength of compacted polymer particles apparently have not been studied as extensively as the other physical properties. Strength and deformation of soils, however, are well established subjects in civil engineering and there are comprehensive texts and literature on the subject of soil mechanics [e.g. 28,29,30,31]. Much of this work can be applied to similar materials which are made up of individual particles. In the present work, most of the ideas are derived from basic soil mechanics principles.

A soil (or any other granular medium) is said to have failed when shearing occurs across a plane on which the ratio of the shear stress to the direct compressive stress reaches a certain critical value. This is known as the Mohr-Coulomb criterion of failure. When equilibrium of

forces in the granular medium exists under these conditions, just before the onset of flow, the material is said to be in a critical state equilibrium.

The ratio of the shear stress on one plane to the direct compressive stress on the same plane is directly analogous to the coefficient of friction between solid bodies and therefore it can be thought of as an internal coefficient of friction. The resistance to flow offerred by this internal friction is thus the basic concept of strength applied to the polymer mass made up of individual particles considered here.

For the present work, the internal coefficient of friction will be assumed to be single valued for a given material on the same grounds as the metal/polymer coefficient of friction was assumed to be single valued. Also, the polymer mass will be assumed to be a cohesionless granular medium. The justification for this being that the cohesivity is small compared with the stresses than can be set up by the very high pressures exerted by the feed rams on the material, and consequently it will have only an insignificant effect on the pressure propagation. It is not difficult to see from these assumptions that in a graph of shear stresses plotted against normal stresses, the relationship between these stresses at the onset of flow would be a straight line through the origin whose slope was equal to the internal coefficient of friction.

Lovegrove [8] discussed some methods for measuring polymer/metal and internal coefficients of friction and has collected some data which have been used in the present work. For most polymers, in the form of beads, granules and powder, the values of the internal coefficient of friction lie in the range of 0.2 to 0.7 for a wide range of temperatures and stresses.

(c) Compressibility

Because the material is fed in loosely and then compacted, its bulk density changes during the feeding process. A relationship between the volumetric change and the pressure is therefore required.

Lovegrove carried out tests using a piston/cylinder arrangement and obtained such relationships experimentally. The change in the height of a cylindrical column of material with the piston force was measured. Clearly, the relationship between the volume and the pressure was not unique because on removing the load there was very little recovery. But the smooth compressibility curve (Load versus Volume) that existed when the pressure was monotonically increased was amenable to mathematical treatment. The formula that best fitted the experimental results was originally proposed by Kawakita et al [32] and for the piston/cylinder arrangement this is

$$\frac{L_o - L}{L} = \frac{a\, d\, p_o}{1 + d\, p_o} \qquad (3.1)$$

where L_o is the length of the uncompacted cylindrical column of material, L is the length when pressure p_o is applied by the piston and a and d are constants. Lovegrove obtained values for a and d for a range of materials and these have been used in the present work.

3.4 Pressure Losses in Feed Cylinders due to Coulomb Friction

The analysis in this section is relevant to the initial region of the solids feeding zone of the extruder consisting of a piston/cylinder arrangement. Its main purpose is the prediction of pressure losses through the column of material as a result of friction.

Before an expression for pressure losses can be derived, it is

necessary to determine relationships between the pressures in different directions in the granular material.

3.4.1 Relationship between stresses in a granular material under pressure

When granular material is compacted in a piston/cylinder arrangement as shown in Figure 3.3, the radial pressure at a point adjacent to the cylinder wall has a different value from that of the axial pressure at the same point.

Although relationships between these pressures can be determined mathematically by considering idealised geometrical and physical properties for the particles [33], such a treatment is not suitable for the present problem because the shape of the particles is not simple to describe and is not unique, their arrangement is unknown and also their size in relation to the flow channel dimensions would have to be considered.

Instead, applying conventional continuum mechanics principles to granular materials, a simple expression relating the principal stresses p_r, p_θ and p_z can be obtained. The modes of deformation of the granular mass in such an arrangement have been discussed by Lovegrove and the conclusion was that the material in equilibrium must be in a critical state. Under this condition

$$p_r = p_\theta = \left(\frac{1 - \sin \delta_i}{1 + \sin \delta_i}\right) p_z \qquad (3.2)$$

where $\tan \delta_i$ is the internal coefficient of friction of the material. This expression has been derived in many textbooks on loose solids, [e.g. 28,29,30,31].

For typical values of δ_i, $k = (1-\sin \delta_i)/(1+\sin \delta_i)$ has values in the range of 0.3 to 0.5. Stepanoff [34] has called this ratio k the 'coefficient of mobility'. The higher the value of k the more 'mobile' is the granular medium.

Schneider [7] using a specially designed apparatus measured the ratio k in cylindrical and annular columns of compacted nylon particles and obtained values for k approximately equal to 0.4. It was also found that k was constant

(i) for a wide range of pressures applied by the piston;

(ii) for different axial positions; and

(iii) for different sizes of nylon granules in various sizes of cylindrical and annular columns.

On this evidence, for each material considered in the present work, k was assumed to be constant throughout the length of the column, and independent of pressures.

3.4.2 Pressure transmitted through a cylindrical column of granular polymer

In addition to the assumptions already made, the concept of a 'semi-particulate' material will be introduced here. This was originally applied by Spencer et al [35] to a similar problem to account for the granular nature of the material. In the present work, such an approach is useful for considering the relatively large degree of compression of the polymer feedstock imposed by the rams during the initial stages of the feeding process.

In this approach the number of particles that constitute the granular

medium and their mode of compaction are considered but the final expression for the pressure transmitted is independent of these. Figure 3.3(a) shows the material in the cylinder/piston arrangement. When the axial pressure p_o is applied by the piston, the column of material reduces from a length L_o, when the pressure is insignificant, to L. If the number of particles per unit area contacting the wall at any z is n_p and the number of particles per unit area in contact over a cross section is n_o, $n_p = n_o$ originally when the pressure exerted by the piston is negligible. Since the number of particles in contact with the cylindrical wall remains the same when the pressure is applied,

$$\int_o^L n_p \, dz = n_o L_o$$

This may be visualised as a regular grid drawn on the cylindrical surface of the material which is then compressed. The number of grid points on the surface remains the same either compressed or before compression has taken place.

Figure 3.3(b) shows the pressures on a typical element δ_z of the granular material. Assuming p_z and p_r to be the forces on each particle, and that p_z is uniform across any circular cross section, the following equation for the equilibrium of forces is obtained:

$$n_p \pi D_c \mu_f p_r \, dz + p_z \frac{n_o \pi D_c^2}{4} = (p_z + d p_z) \frac{n_o \pi D_c^2}{4}$$

Substituting $p_r = k p_z$ into this equation and integrating from z = 0 to z = L,

$$p_T = p_o \exp \left[- \frac{4 \mu_f k}{D_c n_o} \int_o^L n_p \, dz \right]$$

$$\text{i.e.} \qquad p_T = p_o \exp\left[-\frac{4\,\mu_f\, k\, L_o}{D_c}\right] \tag{3.3}$$

where p_T is the pressure transmitted through the cylindrical column of material whose length was originally L_o. Note that n_o is independent of z and n_p and n_o do not appear in equation (3.3). A similar expression was derived by Spencer et al but they assumed $p_r = p_z$. This was later modified by Toor and Eagleton [36] to include the effect $k \neq 1$ which they derived experimentally.

3.4.3 Axial pressure profile in feed cylinders

In the feed tubes of the extruder itself, the column of granular material is built up by successive amounts of material fed in during each active stroke of the feed ram.

Figure 3.4 shows the column of material in the feed tube made up of successive amounts of material fed in. Since recovery of the length of material is very little when the ram pressure is removed in particular if the ram pressures were high, it is assumed that when the ram retracts to take a new charge, the material that had already been compressed does not change in length. Also, no further compression of the material already in the feed cylinder can take place when the ram moves forward again pushing the new charge of material. For the pressure available to compress the material already in the feed cylinder is smaller than the ram pressure exerting on the material in the previous stroke.

With these assumptions, the expression for the pressure transmitted through the column of material in each feed tube of the extruder, was derived as follows. Given the amount of material fed in per stroke, the length of the cylindrical column of uncompacted granular material is

calculated as L_f - Figure 3.4(b). When the pressure p_o is applied by the ram, this column reduces to L_e - Figure 3.4(c). Using equation (3.3) the pressure transmitted to axial location a is

$$p_a = p_o \exp\left[-\frac{4\,\mu_f\,k\,L_f}{D_c}\right]$$

The pressure transmitted to cross section at b is

$$p_b = p_a \exp\left[-\frac{4\,\mu_f\,k\,L'_{ab}}{D_c}\right]$$

where L'_{ab} is the length of the uncompacted column of material from a to b. Since the amount fed in per stroke is constant, $L'_{ab} = L_f$ and therefore

$$p_b = p_a \exp\left[-\frac{4\,\mu_f\,k\,L_f}{D_c}\right]$$

Similarly, the pressure at the following positions, e.g. c, may be calculated. Note that it is not necessary to consider the whole length of each charge of material, for example equation (3.3) is applicable to $L_\alpha < L_e$. Thus, the pressure at CC is

$$p_{CC} = p_c \exp\left[-\frac{4\,\mu_f\,k\,L'_\alpha}{D_c}\right]$$

where L'_α is the uncompacted length of material L_α.

Given the compressibility characteristics of the granular medium, i.e. the constants a and d in equation (3.1),

$$L_f = \left(1 + \frac{a\,d\,p_o}{1 + d\,p_o}\right) L_e$$

and $$L'_{\alpha} = \left(1 + \frac{a\ d\ p_o}{1 + d\ p_o}\right) L_{\alpha}$$

The pressure transmitted to CC across a column of length L_s is therefore

$$p_{CC} = p_o \exp\left\{-\frac{4\ \mu_f\ k\ L_s}{D_c}\left[1 + \frac{a\ d\ p_o}{1 + d\ p_o}\right]\right\} \qquad (3.4)$$

As the ram moves forward, the distance L_s decreases and therefore the pressure at section CC also varies. Equation (3.3) was derived for statical equilibrium and therefore it may appear that it is invalid for the present problem in which the whole column of material is moving. The rate of change of L_s has not been included to give a time dependent solution but if L_s is known at any given instant, equation (3.4) should give the instantaneous pressure at section CC and hence the solution is still valid provided the static and the dynamic coefficients of friction are the same. Toor and Eagleton [36] have found that the difference between these two coefficients was negligible for polystyrene pellets. Here the assumption that the difference between the two coefficients of friction is negligible is made for all the materials considered.

It is worth noting that though equation (3.4) was derived by considering pressure propagation through successive amounts of materials fed in during each active stroke of the ram, it does not contain any term involving L_f. This is a direct result of the semi-particulate approach adopted in deriving equation (3.3) in which the number of contact points rather than the area on which the pressures exert has been considered. Thus, as long as the number of contact points is constant, the distribution of these - represented by the density of the vertical lines in Figure 3.4 - along the length L_s is irrelevant since the effect

is integrated, i.e.

$$\int_{o}^{L_s} n_p \, dz = n_o L'_s$$

where L'_s is the uncompacted length of material in L_s.

3.4.4 Results and discussions

The results presented below are for LDPE granules. The relevant properties for this material are k = 0.337, a = 0.436 and d = 0.234 m^2/MN.

Based on the amount of LDPE granules fed per stroke, L_f was calculated as 68.5 mm. Assuming that the column of material already in the feed cylinder does not move until the newly fed in material has been compressed by a ram pressure p_o to L_e and that no pressure is transmitted to CC until the ram reaches the position as shown in Figure 3.4(c), the two limiting pressure profiles corresponding to this position and to that when the ram reaches its maximum forward position are shown in Figure 3.5. The length L_e can be considered as the effective travel distance of the ram. In the results shown in Figure 3.5 the pressure p_o is 28.6 MN/m^2 corresponding to an hydraulic oil pressure of 8.28 MN/m^2, and L_e = 51 mm using equation (3.1). The nominal length of the feed tube is 267 mm and diameter D_c = 44.5 mm - Table 2.1. The coefficient of friction has a low value of 0.2. With this set of data, the predicted pressures at section CC are only about 10% of the pressure exerted by the ram, representing considerable frictional losses.

Figure 3.6 shows the pressure at section CC expressed as a fraction of the ram pressure p_o. The shaded area represents the range of pressures at CC when the polymer plug moves forward. This graph emphasises that the choice of an adequate value for the polymer/metal

coefficient of friction is critical if predictions are to be accurate. Thus, any factor affecting significantly the coefficient of friction will have considerable effect on the pressure propagation since the pressure losses are very sensitive to changes in the coefficient of friction. Possible factors are the ones already referred to, e.g. temperature, sliding speed, etc.

Similarly, since the product ($\mu_f k$) appears grouped in equation (3.4) and the value of k is of the same order as that of μ_f, the same can be said about the effect of k on the pressure propagation. The ratio k is directly related to the strength of the granular material. Thus, any factor affecting this will have a major effect on pressure losses, for example, the shape of each individual particle, degree of interlocking between the particles and other parameters like temperature, humidity, etc.

3.4.5 Conclusions

A simple formula has been derived for calculating the pressure transmitted through a cylindrical column of granular material. By adopting a semi-particulate approach for setting up a balance of forces in the derivation of the expression, the compressibility of the material was taken into account. This was particularly relevant to the analysis for the pressures in the feed cylinders since considerable compaction of the material can take place in this region.

The sensitivity of the pressure losses to small changes in the polymer/metal coefficient of friction and the strength of the granular mass shows that if accurate predictions are to be obtained, comprehensive data are required which are still lacking at the present.

Without any formal comparison of the predicted results with

experimental results, it was concluded that excessively high pressure losses were predicted for this region of the solids feeding zone. In order to maintain the output rates obtained experimentally, the pressure losses would have to be considerably smaller than those predicted. In practice a melt film must have formed between the solid plug and the cylinder wall and the Coulomb type friction given way to a viscous type friction. The melt film would have acted as a lubricating layer and pressure losses would have been smaller. The present model, however, should be suitable for predicting the pressure transmitted through the initial length of the material which is contained in a water cooled cylinder and hence unlikely that a melt film could have existed.

3.5 Stress Distribution in Granular Polymer Contained by Inclined Walls

The preceding section described a relatively simple method for determining the pressure at plane CC in the solids feeding zone of the extruder - Figure 3.1. It is now required to extend the analysis into the remaining part of the feeding zone. The solution sought is the pressure at plane BB in Figure 3.1, given the uniform pressure at plane CC obtained using equation (3.4).

In order to solve the present problem, several assumptions and simplifications are needed. Some of these, concerning the geometry and relevant physical properties of polymers, have already been discussed. The relevant geometry is that shown in Figure 3.2. Since the material must deform to flow through the converging channel, at a point where sliding of the particles occurs, the ratio of the shear stress to the normal stress on the same plane must be equal to the internal coefficient of friction. Just before flow occurs, the material is therefore in a critical state equilibrium. In the solution presented below, the

critical state of stresses is assumed to exist everywhere within the granular material in this region and the calculations are relevant to static equilibrium. In the real situation, the material is flowing through the region, i.e. the granules of solid polymer are continuously rearranging. Under these conditions the problem becomes a dynamic and extremely complex one for which no satisfactory method of solution has yet been described. Provided that the stresses in the dynamic state are not very different from those existing under static equilibrium, the solution so obtained should be adequate.

Though the criterion for flow of the material to occur is that for an ideal granular medium, the derivation of the equations for the equilibrium of forces within the material will ignore the granular nature of the material, and will be based on area contact rather than point contact. When point contact was considered in the previous section 3.4.2, it eventually lead to the inclusion of the compressibility equation (3.1) in the final result. Here, the area contact approach adopted is justified in that the material in this region may have attained a considerable degree of compaction in which case area contact is more relevant than point contact.

3.5.1 Equations of equilibrium

The problem considered here is one of plane equilibrium. Plane equilibrium is defined as the equilibrium of an infinitely long prismatic body under the action of forces perpendicular to the generators and distributed uniformly in the direction of the generators. Here, the direction of the generators is in the z-direction, perpendicular to the plane of Figure 3.2.

In plane equilibrium, the stress components $\tau_{yz} = \tau_{zx} = 0$ and the

remaining components σ_x, σ_y, σ_z and τ_{xy} are independent of the coordinate z. Consequently, it is sufficient to consider the stress distribution on the x-y plane only. From Figure 3.2 equilibrium of forces on a two dimensional element $\delta_x \times \delta_y$ gives the following equilibrium equations:

$$\left.\begin{aligned} \frac{\partial \sigma_x}{\partial x} + \frac{\partial \tau_{xy}}{\partial y} &= 0 \\ \frac{\partial \tau_{xy}}{\partial x} + \frac{\partial \sigma_y}{\partial y} &= 0 \end{aligned}\right\} \quad (3.5)$$

The convention for positive stresses is as shown in Figure 3.2.

3.5.2 Equation for critical state equilibrium

Equations (3.5) alone with the appropriate boundary conditions are not enough to solve the problem of the stress distribution in the x-y plane. A further equation relating the stress components when the material is in a critical state equilibrium is required to complete the mathematical statement of the problem.

The stress state at any point in the granular medium lies within the shaded part of the Mohr's circle shown in Figure 3.7. The intercepts of the largest circle with the axis of the normal stresses are σ_1 and σ_2, respectively the major and the minor principal stresses. These and the third principal stress σ_3 are given by, (see e.g. [37]),

$$\left.\begin{aligned} \sigma_1 \\ \sigma_2 \end{aligned} = \frac{1}{2}(\sigma_x + \sigma_y) \pm \sqrt{\left[\frac{1}{4}(\sigma_x - \sigma_y)^2 + \tau_{xy}^2\right]} \right\} \quad (3.6)$$

and $$\sigma_2 \leqslant \sigma_3 = \sigma_z \leqslant \sigma_1$$

For a material under critical equilibrium,

$$|\tau_{n't}| = \sigma_n' \tan \delta_i \qquad (3.7)$$

where $\tau_{n't}$ and σ_n' are respectively the shear and normal stresses on a plane perpendicular to direction n' on which the ratio of the shear stress to the normal stress reaches the maximum critical value tan δ_i.

Equation (3.7) defines a straight line on the Mohr's circle diagram and represents the yield loci for the granular medium. Since the material is in a critical state equilibrium, the Mohr's circle which represents the stress state at any point in the granular medium must therefore be tangent to this straight line as shown in Figure 3.8. From this diagram, the following relationship is obtained:

$$(\sigma_1 - \sigma_2) = (\sigma_1 + \sigma_2) \sin \delta_i \qquad (3.8)$$

Substituting equations (3.6) into equation (3.8) and rearranging,

$$\frac{1}{4}(\sigma_x - \sigma_y)^2 + \tau_{xy}^2 = \frac{\sin^2 \delta_i}{4}(\sigma_x + \sigma_y)^2 \qquad (3.9)$$

Equations (3.5) and (3.9) and the appropriate boundary conditions define the stress distribution - σ_x, σ_y and τ_{xy} - in the x-y plane. Note that the remaining stress σ_z is irrelevant to this problem and does not appear in these equations.

3.5.3 Modified equations

Equations (3.5) and (3.9) are not in a convenient form to be solved. Sokolovskii [38] proposed some modifications whereby equation (3.9) was

eliminated and the problem was reduced from a system of three equations to one of two partial differential equations with two unknown variables η and ξ. The resulting pair of simultaneous equations was

$$\left.\begin{aligned} \frac{\partial \eta}{\partial x} + \tan(\phi - \alpha)\frac{\partial \eta}{\partial y} &= 0 \\ \frac{\partial \xi}{\partial x} + \tan(\phi + \alpha)\frac{\partial \xi}{\partial y} &= 0 \end{aligned}\right\} \quad (3.10)$$

where ϕ is the angle between the x-axis and the direction of the major principal stress σ_1 and α is a term containing the internal coefficient of friction. The relationships between η and ξ with the stresses σ_x, σ_y and τ_{xy} are

$$\left.\begin{aligned} 2\phi &= \xi - \eta \\ \cot \delta_i \, \ell n \frac{\sigma}{\sigma_o} &= \xi + \eta \end{aligned}\right\} \quad (3.11)$$

and

$$\left.\begin{aligned} \sigma_x &= \sigma(1 + \sin \delta_i \cos 2\phi) \\ \sigma_y &= \sigma(1 - \sin \delta_i \cos 2\phi) \\ \tau_{xy} &= \sigma \sin \delta_i \sin 2\phi \end{aligned}\right\} \quad (3.12)$$

Thus, given the distribution of η and ξ in the x-y plane, ϕ and σ can be evaluated using equations (3.11) and hence obtain σ_x, σ_y and τ_{xy} using equations (3.12). In equations (3.11) σ_o is an arbitrary stress, and

$$\sigma = \tfrac{1}{2}(\sigma_1 + \sigma_2) \quad (3.13)$$

The full derivation of these equations is given in Appendix A. It is worth noting that equations (3.12) identically satisfy equation (3.9). In fact, this is how only two partial differential equations are required to solve for the distribution of three stress components in the x-y plane, instead of the initial three equations. Mathematically the problem has been reduced to one of determining the distribution of two variables η and ξ in the x-y plane given the appropriate boundary conditions.

3.5.4 Boundary conditions

The stress distributions along the boundaries OP, PQ and OR must be specified in order to obtain the solution for equations (3.10).

Along boundary OP, the stresses are obtained from the analysis of the previous region, i.e. $\sigma_x = p_{CC}$ and $\tau_{xy} = 0$. Since $\tau_{xy} = 0$, σ_x and σ_y must be the principal stresses. Two cases may arise from this stress system - Figure 3.9:

$$\text{(i)} \quad \sigma_x = \sigma_1 \text{ and } \sigma_y = \sigma_2$$

or

$$\text{(ii)} \quad \sigma_x = \sigma_2 \text{ and } \sigma_y = \sigma_1$$

Case (i) corresponds to the critical equilibrium condition which when destroyed results in the flow of the granular media in the direction in which pressure p_{CC} is applied - the active case; and case (ii) corresponds to the critical equilibrium condition which when destroyed results in the flow of the granular material in the opposite direction - the passive case. In the present problem, only the active case is of interest.

The boundary condition along OP can therefore be stated as $\sigma_x = p_{CC} = \sigma_1$ which gives, with equations (3.12)

$$\sigma_{OP} = \frac{p_{CC}}{1 + \sin \delta_i}$$

with $\qquad \phi_{OP} = 0$

Substituting ϕ_{OP} and σ_{OP} into equations (3.11) and selecting the arbitrary stress σ_o as $\sigma_o = \frac{p_{CC}}{1+\sin \delta_i}$, from equations (3.11)

$$\xi_{OP} = \eta_{OP} = 0 \qquad (3.14)$$

The remaining two boundaries are the plates which exert friction on the material opposing its flow under pressure. The values of ξ and η are not fully known at these boundaries, but the coefficient of friction between the granular material and the metal plate provides a relationship between the normal and the shear stresses, σ_t and τ_{nt} respectively - Figure 3.10. This is in the form of

$$- \tau_{nt} = \sigma_t \mu_f \qquad (3.15)$$

[Note - In Figure 3.10 the shear stress τ_{nt} is shown in the direction in which the frictional force of the plate on the material acts, and under the present sign convention it is negative.]

The remaining boundary conditions are obtained from equation (3.15) from which ϕ_{OR} and ϕ_{PQ} are determined as shown below.

The relationships between stresses in the n-t coordinate system and the x-y coordinate system are

$$\left.\begin{aligned} \sigma_n &= \tfrac{1}{2}(\sigma_x + \sigma_y) + \tfrac{1}{2}(\sigma_x - \sigma_y)\cos 2\epsilon + \tau_{xy}\sin 2\epsilon \\ \sigma_t &= \tfrac{1}{2}(\sigma_x + \sigma_y) - \tfrac{1}{2}(\sigma_x - \sigma_y)\cos 2\epsilon - \tau_{xy}\sin 2\epsilon \end{aligned}\right\} \quad (3.16)$$

and $\tau_{nt} = -\tfrac{1}{2}(\sigma_x - \sigma_y)\sin 2\epsilon + \tau_{xy}\cos 2\epsilon$

where ϵ is the angle of rotation between the two sets of coordinates. Substituting equations (3.12) into these, the following are obtained

$$\left.\begin{aligned} \sigma_n &= \sigma\left[1 + \sin\delta_i \cos 2(\phi - \epsilon)\right] \\ \sigma_t &= \sigma\left[1 - \sin\delta_i \cos 2(\phi - \epsilon)\right] \\ \tau_{nt} &= \sigma \sin\delta_i \sin 2(\phi - \epsilon) \end{aligned}\right\} \quad (3.17)$$

Finally, substituting for σ_t and τ_{nt} in equation (3.15) and solving for ϕ, with $\epsilon = \beta$

$$2\phi_{OR} = 2\beta + \delta - \sin^{-1}\left(\frac{\sin\delta}{\sin\delta_i}\right) \quad (3.18)$$

where $\delta = \tan^{-1}\mu_f$. And similarly along boundary PQ,

$$2\phi_{PQ} = -\delta + \sin^{-1}\left(\frac{\sin\delta}{\sin\delta_i}\right) \quad (3.19)$$

The boundary conditions given by equations (3.14), (3.18) and (3.19) are sufficient for the determination of ξ and η in the x-y plane governed by equations (3.10). The method of solution is described below.

3.5.5 Method of solution

It can easily be shown that the basic system of equations (3.10) is of the hyperbolic type [39] and that the two real separate families of characteristics related to this set of hyperbolic equations are given by

$$\left.\begin{aligned} \frac{dy}{dx} &= \tan(\phi - \alpha) \quad , \quad \eta = \text{constant} \\ \text{and} \quad \frac{dy}{dx} &= \tan(\phi + \alpha) \quad , \quad \xi = \text{constant} \end{aligned}\right\} \qquad (3.20)$$

Although a number of techniques are available for solving hyperbolic differential equations, the commonly known 'method of characteristics' [e.g. 39,40,41] is used here in view of the simplicity in which these are expressed - equations (3.20). Thus, along a curve $y = y(x)$ whose slope is $\tan(\phi-\alpha)$, η takes a constant value and similarly ξ remains constant along a curve with slope $\frac{dy}{dx} = \tan(\phi+\alpha)$. Therefore, the field of characteristics in the solution domain consists of lines intersecting at angle 2α and inclined to the x-axis at angle of $\phi \pm \alpha$. Also, at each intersection of the characteristics the values for ξ and η are determined.

The solution is of the 'marching' type and is initiated on boundary OP and propagated through the region of interest, i.e. region OPQR.

(i) Initiation of solution

Given the internal coefficient of friction $\tan \delta_i$, α is obtained from (see Appendix A)

$$2\alpha = \frac{\pi}{2} - \delta_i \qquad (3.21)$$

Along boundary OP, $\phi = \eta = \xi = 0$ and thus the field of characteristics for the region OPD - Figure 3.11 - consists of parallel lines inclined at angles $\pm \alpha$ to the x-axis and the solution is $\eta_7 = \xi_7 = \phi_7 = 0$ throughout this region. It can be shown mathematically that such a solution is unique [39] and the region is termed a constant state region. All variables referring to this region will be subscripted with the reference number 7.

(ii) Propagation of the solution to the boundaries

Having obtained the solution for region OPD, it is next propagated to the other boundaries. Since ξ is constant along a line $\frac{dy}{dx} = \tan(\phi+\alpha)$, $\xi_{PQ} = \xi_7 = 0 = \xi_4 = \xi_a$ at a typical point a as shown in Figure 3.11. Using equations (3.11), $\eta_a = \xi_a - 2\phi_a = -2\phi_{PQ}$ where ϕ_{PQ} is the boundary condition given by equation (3.19). Thus, the region PEF is also a constant state region and is denoted by the subscript 4, and the solution here is

$$\xi_4 = 0 \quad \text{and} \quad \eta_4 = -2\,\phi_{PQ} = -2\,\phi_4$$

A singularity exists at point P in that two characteristics of the same family exist, one at $\frac{dy}{dx} = \tan(\phi_7 - \alpha)$ and the other at $\frac{dy}{dx} = \tan(\phi_4 - \alpha)$. Thus, ξ and η are not single valued at P. The point can be considered as two, P_7 and P_4 as shown in the insert of Figure 3.11, and joined by a line of constant ξ. Thus,

$$\xi_{P_7} = \xi_{P_4} = 0\,, \quad \eta_{P_7} = 0 \quad \text{and} \quad \eta_{P_4} = \eta_4 = -2\phi_4$$

Courant and Friedrichs [42] have shown that between two constant

state regions there is always a region known as a simple wave. The region PDE is a simple wave and $\xi_8 = 0$. The value of η_8 changes from $\eta_8 = 0$ along line PD to $\eta_8 = -2\phi_4$ along line PE. It can be shown that lines like DE are logarithmic spirals, by using polar coordinates [38]. For the present purpose these were approximated by straight lines inclined to the x-axis at an angle

$$\left(\frac{\phi_7 + \phi_4}{2} + \alpha\right)$$

In this way cartesian coordinates can be maintained which are simpler to handle mathematically. Thus, the solution is exactly known within the region OPFED; the only error introduced being that in the approximation of DE by a straight line. This error can be reduced by using a series of straight lines if necessary, with lines like PX leaving P at angles between $(\phi_7 - \alpha)$ and $(\phi_4 - \alpha)$ to the x-axis as shown in Figure 3.12. Given the angle $(\phi_X - \alpha)$, the inclination of the short straight lines from D to E can be determined.

The solution is similarly propagated to boundary OR as shown in Figure 3.11 and $\eta_7 = \eta_6 = \eta_5 = 0$, $\xi_5 = 2\phi_{OR} = 2\phi_5$.

Therefore, given the boundary conditions along OP, PQ and OR, the solution is fully determined in region OPFEDGI. The solution is then propagated to fill the complete region of interest. For example, at point H, $\xi_H = \xi_5$ and $\eta_H = \eta_4$ and hence $\phi_H = \frac{1}{2}(\xi_5 - \eta_4)$. Its coordinates are calculated by approximating GH and EH by straight lines from

$$\frac{y_H - y_G}{x_H - x_G} = \tan\left(\frac{\phi_H + \phi_G}{2} + \alpha\right)$$

and $$\frac{y_H - y_E}{x_H - x_E} = \tan\left(\frac{\phi_H + \phi_E}{2} - \alpha\right)$$

where the only unknowns are y_H and x_H, the coordinates of the point H, and GH and EH are inclined to the x-axis at the mean angles of

$$\left(\frac{\phi_H + \phi_G}{2} + \alpha\right) \quad \text{and} \quad \left(\frac{\phi_H + \phi_E}{2} - \alpha\right)$$

respectively.

(iii) Lines of discontinuity

Due to the steepness of the wall OR a condition may arise where $\phi_5 + \alpha > \phi_7 + \alpha$, i.e. regions 5 and 7 overlap as shown in Figure 3.13. The existence of a region ODJG, mathematically means that there exists a line of discontinuity OJ along which the derivatives of ξ and η with respect to x and y become infinite, i.e. the derivatives of the stresses σ_x, σ_y and τ_{xy} with respect to the coordinates become infinite. Consequently, the values of the stresses must undergo a finite jump. Physically, the line of discontinuity indicates the impossibility of the existence of critical state equilibrium together with a continuous distribution of stresses. The presence of the line of discontinuity establishes that the critical state will be accompanied by elastic zones which in the limit degenerate into lines of discontinuity.

Considering the stresses for the material adjacent to the line of discontinuity as shown in Figure 3.14 it is clear that σ_n and τ_{nt} must remain continuous on either side of the line of discontinuity, but σ_t can have a finite discontinuity. Therefore,

$(\sigma_n)_5 = (\sigma_n)_7$ and $(\tau_{nt})_5 = (\tau_{nt})_7$. Using equations (3.17) these give

$$\sigma_5 \left[1 - \sin \delta_i \cos 2(\phi_5 - \omega)\right] = \sigma_7 \left[1 - \sin \delta_i \cos 2(\phi_7 - \omega)\right]$$

and $$\sigma_5 \sin 2(\phi_5 - \omega) = \sigma_7 \sin 2(\phi_7 - \omega)$$

where ω is the angle between the line of discontinuity and the x-axis. Solving these for σ_5 and ω

$$\left.\begin{aligned} \sigma_5 &= \frac{\sigma_7}{\cos^2\rho}\left\{\sin \delta_i \sin(\phi_7 - \phi_5) - \left[1 - \sin^2\delta_i \cos^2(\phi_7 - \phi_5)\right]^{\frac{1}{2}}\right\}^2 \\ \text{and} \\ 2\omega &= \phi_7 + \phi_5 + \frac{\pi}{2} - \sin^{-1}\left[\sin \delta_i \cos(\phi_7 - \phi_5)\right] \end{aligned}\right\} \quad (3.22)$$

Thus, given the solution for region 7 and the boundary condition $\phi_5 = \phi_{OR}$, ω and σ_5 can be determined from equations (3.22).

The solution consists of two regions of constant state separated by a line of discontinuity. With the values of σ_5 and ϕ_5, η_5 and ξ_5 are obtained from equations (3.11).

(iv) Propagation of lines of discontinuity

In Figure 3.15 the line of discontinuity OJ extends to point L. Since the solution is already known in region 4 applying the same analysis as that for regions 5 and 7 to regions 4 and 9,

$$\sigma_9 = \frac{\sigma_4}{\cos^2\delta_i}\left\{\sin\delta_i \sin(\phi_4 - \phi_9) - \left[1 - \sin^2\delta_i \cos^2(\phi_4 - \phi_9)\right]^{\frac{1}{2}}\right\}^2$$

and

$$2\omega_{KL} = \phi_4 + \phi_9 + \frac{\pi}{2} - \sin^{-1}\left[\sin\delta_i \cos(\phi_4 - \phi_9)\right] \qquad (3.23)$$

Unlike ϕ_5 in equations (3.22), ϕ_9 is unknown in equations (3.23) and therefore σ_9 and ω_{KL} cannot be evaluated immediately. But $\xi_9 = \xi_5$ and using equation (3.11),

$$\phi_9 = \xi_5 - \frac{\cot\delta_i}{2} \ln\frac{\sigma_9}{\sigma_o} \qquad (3.24)$$

Substituting the first of equations (3.23) into equation (3.24),

$$\phi_9 - \xi_5 + \frac{1}{2\tan\delta_i} \ln\left\{\frac{\sigma_4}{\sigma_o \cos^2\delta_i}\left[\sin\delta_i \sin(\phi_4 - \phi_9) - \sqrt{1 - \sin^2\delta_i \cos^2(\phi_4 - \phi_9)}\right]^2\right\} = 0$$

and hence ϕ_9 using a suitable numerical method (see Appendix B). The quantities σ_9 and ω_{KL} are then evaluated from equations (3.23). The angle of line JK with the x-axis was approximated by

$\omega_{JK} = \frac{1}{2}(\omega_{OJ} + \omega_{KL})$.

At point L, again two characteristics of the family $\frac{dy}{dx} = \tan(\phi - \alpha)$ exist, one at $\frac{dy}{dx} = \tan(\phi_9 - \alpha)$ and the other at $\frac{dy}{dx} = \tan(\phi_4 - \alpha)$. If $(\phi_4 - \alpha) < (\phi_9 - \alpha)$ a line of discontinuity LM exists. Given the solution in region 9, the solution in region 10 is obtained in a similar way as in region 5 described in (iii).

The solution is then propagated as previously for the whole domain.

Figure 3.15 shows the different regions in a typical case with lines of discontinuity. Regions 4, 5, 7, 9, 10 and 14 are of constant state. In regions 8 and 11 ξ's remain constant with η's varying, in 12 both ξ and η vary and in 13 η is constant with ξ varying.

(v) Pressure and overall force balance

The aim of this analysis was to determine the axial pressure at section QR. In the example considered in Figure 3.15 the state of stress is constant and fully known in regions 9, 10 and 14, and in region 13 the stresses vary.

Given σ_x, σ_y and τ_{xy} along QR, the components of the stresses normal to QR, p_{QR}, were obtained using equations (3.16). A mean transmitted pressure p_{BB} was calculated from

$$p_{BB} = \int_{s=0}^{s=\overline{QR}} \frac{p_{QR}\, ds}{\overline{QR}}$$

where s is the distance measured along QR. The pressure distribution along SN was linearised as shown in Figure 3.15(b). It was found that the error introduced by this approximation was small.

In order to check the accuracy of the solution, an overall force balance was carried out. This consisted of evaluating all the stress components along OR, PQ and QR and summing up all the forces acting in the positive x-direction and comparing this sum with the sum of all the forces acting in the negative x-direction. The difference between these two gave an indication of the error in the solution.

(vi) Special case: $\delta_i = \delta$

For the case in which the coefficient of friction between metal and polymer and the internal coefficient of friction have the same value, the pattern of characteristics in the solution domain becomes simpler. There are no lines of discontinuity and regions 5 and 4 in Figure 3.11 collapse onto faces OR and PQ respectively. The procedure for propagating the solutions in the x-y plane is the same as with other cases.

A typical field of characteristics is shown in Figure 3.16. Only region 7 is of constant state with $\eta_7 = \xi_7 = \phi_7 = 0$, and regions 6 and 8 are simple waves. At point I, ξ_I is determined from

$$\xi_I = \xi_G = 2\phi_G + \eta_G = 2\phi_{OR} + \eta_7 = 2\phi_{OR}$$

where ϕ_{OR} is one of the boundary conditions. To evaluate $\eta_I = -2\phi_I$, however, it is necessary to determine ϕ_I by the interpolation method indicated by the dotted lines in Figure 3.16. By measuring the angle θ, ϕ_I is obtained from $\phi_I = \theta + \alpha$. The procedure was repeated for the other points R, H and Q and linearised pressure profiles were fitted between these points for calculating the mean pressure across QR - Figure 3.16(b).

3.5.6 Results and discussions

For the results presented here, the distance $\overline{OP}$ was taken as equal to the diameter of the feed cylinder, the distance $\overline{QR}$ as equal to the annular gap in Figure 3.1 at section BB, and the angle between the plates as $\beta = 30^{\circ}$.

A sample solution, for the case of $\delta_i = 30^{\circ}$ and $\delta = 14^{\circ}$, is shown in

Figure 3.15. The compressive stresses, normal to QR along this face are shown in Figure 3.15(b). Note that a discontinuity in the stress distribution occurs at M. This is as expected since regions 9 and 10 are separated by a line of discontinuity. The error in the force balance for this case was only 0.04%.

Figure 3.16 shows the solution for a typical case in which $\delta_i = \delta$. In the example considered, $\delta_i = \delta = 14^o$. All characteristics except OD and PD are strictly curves, but have been approximated by straight lines. In order to obtain the stress distribution along QR it was necessary to, for example, obtain anlge θ for the results at point I. Thus, a suitable point U had to be determined. An adequate method for determining the position of point U based on geometrical considerations was to obtain $\overline{DU}$ from

$$\frac{\overline{DU}}{\overline{DE}} = \frac{\overline{GI}}{\overline{GT}}$$

where $\overline{DE}$, $\overline{GI}$ and $\overline{GT}$ are all known quantities. The lines GT and ET are the characteristics which originate from points G and E and intersect the line QR at I and H respectively. Similarly the values of η and ξ at the points R, H and Q were evaluated and hence the linearised pressure distribution along QR was obtained.

In spite of the crude approximation of relatively long curved lines by straight lines and the 'coarse' interpolation method, the error in the force balance for this case was only 0.5%.

In general, for all the cases considered, no errors greater than 1% in the force balance were encountered.

In Figure 3.17 the overall results are summarised in terms of relationships between the pressure ratio p_{BB}/p_{CC} and the coefficient of

friction μ_f = tan δ for the polymer/metal interface, with the internal angle of friction δ_i as a parameter. The variation of the pressure ratio p_{BB}/p_{CC} with the coefficient of friction μ_f is nearly linear and it decreases as the coefficient of friction increases. Clearly the higher the friction is the lower is the pressure transmitted. Also, the lower the internal coefficient of friction the more 'mobile' is the granular material and therefore the greater are the stresses set up normal to the boundary walls. This leads to greater frictional losses as shown in Figure 3.17 by the decreasing ratios of p_{BB}/p_{CC} with increasing k. In the results shown, the ratio p_{BB}/p_{CC} can take values higher than unity, i.e. $p_{BB} > p_{CC}$ for certain cases. This is a consequence of considering equilibrium of forces only in the derivation of the equations defining the problem. Since the region is a two dimensional wedge, the mean stress on QR assumes values higher than the stress p_{CC} on OP if the frictional forces exerted by the converging walls are sufficiently small.

3.5.7 Conclusions

In order to predict pressure changes in the angled region of the solids feeding zone of the ram extruder, the stress distribution in the region has been investigated. A number of assumptions with varying degrees of accuracy were required so that useful solutions could be obtained.

The hyperbolic partial differential equations describing the problem were relatively simple to solve by the method of characterisitcs. The only difficulties arose from peculiarities to particular sets of circumstances in the form of discontinuities in the solution. These were, however, easily overcome by performing the calculations on a

computer. The method of solution used works only for $\delta \leqslant \delta_i$, as it is apparent from equations (3.18) and (3.19). It was, however, satisfactory for the present problem since δ is unlikely to have values greater than δ_i. Note that the lines in Figure 3.17 terminate where $\delta = \delta_i$.

The assumed geometry was considerably different from the true one, but the main features of the real geometry have been retained, namely the convergence in the flow channel and the inclination of the feed cylinder to the barrel axis. Although the solutions are not strictly applicable to the real situation because of this simplification, they should at least give an order of magnitude of the pressures transmitted through the granular mass of polymer in this region.

The results obtained have shown that the pressure losses in this region are small compared with losses occurring in the preceding region of the feeding zone, i.e. in the feed cylinder.

3.6 Pressures in a Conical Column of Granular Polymer

In the preceding section an analysis was described for calculating pressures transmitted through a granular material contained between two infinite flat walls.

In this section an alternative simplified geometry is investigated to assess the effects of an enclosed converging channel, again with the aim of predicting pressure losses in the region bounded by planes BB and CC shown in Figure 3.1. The flow channel selected was a simple conical converging channel as shown in Figure 3.18. The cross sectional areas at bb and cc were chosen to give a ratio representative of that at BB and CC of the actual extruder and the separation of planes bb and cc was approximated to the mean distance between planes BB and CC.

3.6.1 Equation for equilibrium of a slab

The stresses in the material were assumed to be one-dimensional, i.e. they varied in the flow direction only. Any stress system other than this would have resulted in complicated equilibrium partial differential equations in cylindrical polar coordinates which would have been difficult to solve.

For the simple one-dimensional problem, equilibrium of forces acting on the slab of length δz shown in Figure 3.18 gives

$$-(p_z + dp_z)(D + dD)^2 \frac{\pi}{4} + p_z \frac{\pi D^2}{4} + p_\nu \pi D \, ds \sin \nu + \mu_f p_\nu \pi D \, ds \cos \nu = 0$$

where D is the local diameter of the circular cross section. Using the geometrical relationships,

$$ds \sin \nu = d(D/2) \quad \text{and} \quad ds \cos \nu = d(D/2)$$

the equation is reduced to, after neglecting higher order terms

$$dp_z = 2 \left[p_\nu (1 + \mu_f \cot \nu) - p_z \right] \frac{dD}{D} \qquad (3.25)$$

3.6.2 Pressure transmitted through the granular polymer

In order to integrate equation (3.25) to obtain the variation of p_z with D, it is necessary to obtain an expression for p_ν first. The exact p_ν can only be obtained by solving the full equations involving all the stresses p_z, p_r, p_θ. To avoid this, a technique often used in studies of plastic deformation of metals is applied here to the granular material. This assumes that an infinitesimal element of the zone undergoing flow or deformation may be considered as a spherical

shell as shown in Figure 3.19. The stresses are therefore spherical (see e.g. [43]) with $p_\theta = p_\phi = p_\nu$ and p_z as the principal stresses. Since the material is just about to flow, i.e. in critical equilibrium,

$$p_\nu = \left(\frac{1 - \sin \delta_i}{1 + \sin \delta_i}\right) p_z = k\, p_z \qquad (3.26)$$

Substituting equation (3.26) for p_ν in equation (3.25) and integrating this with the boundary condition $p_z = p_{cc}$ at $D = D_c$, the pressure transmitted to section bb is

$$p_{bb} = p_{cc} \left(\frac{D_b}{D_c}\right)^2 \left[k\,(1 + \mu_f \cot \nu) - 1\right] \qquad (3.27)$$

3.6.3 Results, discussions and conclusions

The ratio p_{bb}/p_{cc} from equation (3.27) has been plotted against the coefficient of friction μ_f in Figure 3.20. The value for k was taken as 0.333 from $k = \frac{1-\sin \delta_i}{1+\sin \delta_i}$ with $\delta_i = 30^\circ$. The diameter D_b was evaluated from

$$\frac{\pi D_b^{\,2}}{4} = A_{bb} \qquad (3.28)$$

where A_{bb} is the shaded area shown in the diagram of the section BB in Figure 3.1, and D_c was taken as the diameter of the feed cylinder. Also, the angle ν was obtained from

$$\tan \nu = \frac{D_c - D_b}{2L_{BC}} \qquad (3.29)$$

where L_{BC} is a mean distance from section BB to CC as shown in Figure 3.1.

The relationship between the pressure ratio and the coefficient of friction obtained using the analysis of the previous section has also been

plotted on the same graph. Considering the differences between the two idealised geometries, the agreement between the two sets of results can be considered to be reasonably good.

For the purpose of estimating pressure drops, either analysis is suitable. Clearly the latter one is considerably simpler to apply. It will be seen later, however, that the conical geometry is not suitable for pressure predictions when the angle between the feed cylinder and the barrel axis is sufficiently large - Chapter 5. Unlike the analysis described in the previous section, there are no limitations to the values that δ_i and δ can take.

3.7 Viscous Friction in Feed Cylinders

The analysis described below is relevant to the calculation of pressure losses in the feed cylinders of the extruder for which an expression was derived in section 3.4. The present analysis differs from that of section 3.4 in that a very thin melt film is assumed to exist between the solid polymer plug and the containing metal cylinder, thus changing the nature of friction from a Coulomb type to a viscous type.

Viscous friction in this case depends on the shear rates in the melt film or the velocity of the solid plug if no slipping occurs at the boundaries of the melt film. Thus, the frictional losses are dependent on the flow rate of the material whilst in the Coulomb friction analysis the transmitted pressure was independent of the relative velocity between the rubbing surfaces. Clearly the analysis of this section applies only when the material is being pushed by the ram and indeed the interest is on the active stroke only when pressure drops are to be predicted in order to determine ram pressures required to maintain a given output rate.

Figure 3.21 shows a diagram of the arrangement in the feed cylinder. The axial pressure in the material p_z is assumed to vary in the z-direction only and uniform across a circular section. It decreases with increasing z due to the shear stresses τ acting in the direction opposite to that of the motion of the plug.

3.7.1 Equation for pressure drop

Assuming the plug to be moving at a uniform velocity V_p, a balance of forces on a typical element of length δz can be written as

$$-dp_z \, \pi R_s^2 = \tau \, 2\pi R_s \, dz$$

where R_s is the local radius of the solid plug. The overall pressure drop over a length L_s of the cylinder (Δp_{L_s}) is obtained by integrating the above equation,

i.e.
$$\Delta p_{L_s} = \int_0^{L_s} -\frac{2\tau}{R_s} \, dz \qquad (3.30)$$

When melting of the solid plug is significant, both τ and R_s change with z as the melt film grows in thickness. In order to evaluate the integral in equation (3.30) it is therefore necessary to obtain expressions for $\tau(z)$ and $R_s(z)$. The full expressions can only be derived after consideration of the melting process operating here and this in turn requires the velocity and temperature analysis for the solid and melt phases of the material. The analysis presented in the remainder of this section has many features in common with that described in chapter 4 which deals with the melting of the polymer in the annular region of the extruder. Thus, reference is occasionally made to chapter 4, but

the present analysis is quite independent from that described later and therefore convenient to be presented here. The assumptions discussed in section 4.4 apply to the following analysis.

3.7.2 Analysis of the melt film

In the analysis of velocity and temperature profiles in the melt film, the effects of the curvature of the cylindrical boundaries are neglected since the film is comparatively thin. Thus, the annular region in which the film is contained can be considered as a slit and rectangular coordinates used. In addition, both the flow and the thermal conditions of the polymer melt will be assumed to be fully developed. By this assumption, the dimensionless velocity and temperature profiles in the melt film remain unchanged with z. The geometry is shown in Figure 3.22. Neglecting the effects of pressure gradients on the velocity profiles in the very thin and viscous melt film, the velocity distribution across the film is given by

$$\frac{d}{dy}\left(\mu \frac{dv}{dy}\right) = 0 \qquad (3.31)$$

with boundary conditions $v(H) = V_p$ and $v(o) = 0$.

The viscosity term μ is related to velocity gradients and temperatures by

$$\mu = \mu_o \left|\frac{dv/dy}{\gamma_o}\right|^{n-1} \exp\left[-b\,(T - T_o)\right]$$

This expression is discussed later in chapter 4 and describes temperature dependent, power-law type of fluids of which polymer melts are typical examples.

For the purpose of the dependence of the viscosity on temperature, a

linear temperature profile across the melt film may be used in order to integrate equation (3.31). Thus, using $T = (T_m - T_B)y/H + T_B$ in the expression for μ and integrating equation (3.31) with the boundary conditions,

$$v = V_p \left(\frac{e^{A_1 y/H} - 1}{e^{A_1} - 1} \right) \qquad (3.32)$$

where $A_1 = \frac{b}{n} (T_m - T_B)$.

The shear stress τ which is independent of y is given by

$$\tau = \mu_o \left| \frac{V_p}{H} \frac{A_1}{(e^{A_1} - 1)} \right|^n \exp \left[-b (T_B - T_o) \right] \qquad (3.33)$$

It is convenient at this stage to derive an expression for the local mass flow rate of the polymer melt. This is obtained from

$$\dot{m} = \rho_m 2\pi (R_s + \frac{H}{2}) \int_o^H v \, dy$$

i.e.
$$\dot{m} = \rho_m 2\pi (R_s + \frac{H}{2}) V_p H \left(\frac{1}{A_1} - \frac{1}{e^{A_1} - 1} \right) \qquad (3.34)$$

using equation (3.32). The temperature distribution across the melt film is determined by

$$km \frac{d^2T}{dy^2} = \tau \left(\frac{dv}{dy} \right)^2$$

with boundary conditions $T(H) = T_m$ and $T(o) = T_B$. Using equation (3.32) and (3.33), the temperature profile is obtained as

$$\frac{T - T_B}{T_m - T_B} = \frac{y}{H} + \frac{A_2}{(T_B - T_m)} \left(\frac{H}{A_1} \right)^2 \left[1 - e^{A_1 y/H} - \frac{y}{H} (1 - e^{A_1}) \right] \qquad (3.35)$$

where $A_2 = \frac{\tau}{km} \frac{V_p}{H} \frac{A_1}{(e^{A_1} - 1)}$

Note that if viscous dissipation in the melt film is small compared with the heat conducted across the thickness of the film, the second term in the right hand side of equation (3.35) reduces to zero and the resulting temperature profile is a linear one, i.e. the same as that assumed for the temperature dependence of viscosity in order to obtain equation (3.32). The importance of viscous dissipation can be assessed by the ratio of heat generated to heat conducted which can be expressed as $\mu V_p^2/km(T_B - T_m)$. Taking typical values for these variables, the ratio is less than 1, i.e. viscous dissipation may be neglected in general, and the temperature profile may be assumed to be linear.

3.7.3 Temperature distribution in the solid plug

Having obtained previously expressions for the velocity and temperature profiles in the melt film, it is now necessary to obtain the temperature distribution in the solid material so that the melting rates can be determined.

The solid material is fed in at room temperature, T_{room}, and its temperature varies radially and in the z-direction as it moves into the feed cylinder. The relevant differential equation is

$$\frac{ks}{r} \frac{\partial}{\partial r} \left(r \frac{\partial T_s}{\partial r} \right) = \rho_s c_s V_p \frac{\partial T_s}{\partial z}$$

One of the boundary conditions for this equation is $T_s = T_m$ at $r = R_s$. Since R_s varies with z due to melting and is not known yet, it is not possible to apply this boundary condition immediately. Assuming that

the film thickness is small compared with the radius of the solid plug, an alternative boundary condition $T_s = T_m$ at $r = R$ can be used for the purpose of determining the temperature distribution in the solid. The other boundary conditions necessary to specify the problem are

$$\left(\frac{\partial T_s}{\partial r}\right)_{r=0} = 0 \quad \text{and} \quad T_s(0,r) = T_{room}.$$

An analytical solution for a similar problem but including other terms in the differential equation was presented by Arpaci [44]. This solution was readily adaptable to the present problem, and after the necessary modifications, the temperature in the solid plug is given by

$$\frac{T_s - T_m}{T_{room} - T_m} = 2 \sum_{n_c=1}^{\infty} \left[\frac{J_o^B(\lambda_{n_c} r)}{\lambda_{n_c} R \, J_1^B(\lambda_{n_c} R)} \exp\left(-\tfrac{1}{2} \frac{\lambda_{n_c}^2 \, z \, k_s}{V_p \, \rho_s \, c_s} \right) \right] \qquad (3.36)$$

where λ_{n_c} are the zeroes of $J_o^B(\lambda_{n_c} R) = 0$, and J_ν^B are Bessel functions of the first kind of order ν.

3.7.4 Development of the melt film

By considering a mass balance over an infinitesimal length δz shown in Figure 3.23, the rate of growth of the melt film is expressed as

$$dW^* = \frac{d\dot{m}}{dz} \, \delta z \qquad (3.37)$$

where dW^* is the melting rate over the length δz.

The amount of energy available to melt the solid material at the melting interface is the heat conducted from the polymer melt into the

interface less that conducted away from the interface into the solid plug. Apart from melting alone, some of the energy is consumed in heating up the solid material from a mean temperature to the melting point and in heating up the newly melted material to a mean melt temperature as it joins the main stream of the melt. This energy balance can be written as

$$\Delta E \, dW^* = \left[km \left(\frac{dT}{dy}\right)_{y=H} - ks \left(\frac{\partial T_s}{\partial r}\right)_{r=R_s} \right] 2\pi R_s \, \delta z \quad (3.38)$$

where ΔE is the mean change in enthalpy, i.e.

$$\Delta E = c_s (T_m - \overline{T}_s) + \lambda + c_m (\overline{T} - T_m) \quad (3.39)$$

assuming a linear relationship between enthalpy and temperature so that single valued c_s and c_m may be used.

Substituting equation (3.34) into equation (3.38) and rearranging,

$$\Delta E \, \rho_m \, V_p \left(\frac{1}{A_1} - \frac{1}{A_1 \, e^{A_1} - 1} \right) \frac{dH}{dz} = km \left(\frac{dT}{dy}\right)_{y=H} - ks \left(\frac{\partial T_s}{\partial r}\right)_{r=R_s} \quad (3.40)$$

This equation was numerically integrated using Euler's Method described in Appendix B and hence the variation of H with z obtained. From this, the shear stress τ given by equation (3.33) and $R_s = R - H$ were evaluated and hence the integral of equation (3.30) obtained numerically.

In equation (3.40), the temperature gradients were obtained by differentiating equations (3.35) and (3.36) with respect to y and r respectively, and the mean temperatures in the expression for ΔE obtained from

$$\overline{T} = \frac{\int_0^H v\,T\,dy}{\int_0^H v\,dy}$$

and $$\overline{T}_s = \int_0^R \frac{T_s}{R}\,dr$$

The full expressions for these are given in Table 3.1.

3.7.5 Procedure for calculations

Ideally the initial condition for starting the numerical integration of equation (3.40) is H(z=0) = 0, i.e. z = 0 where the melt film first appears. This condition cannot be used, however, because when H = 0, the melting mechanism does not operate and therefore the equations derived become invalid. Mathematically, such a boundary condition leads to infinite temperature gradients in the melt film of zero thickness. In the present analysis, the solution is initiated by assuming a typical thickness for the very thin films, i.e. $H(z=0) = H_o$ where H_o is of the order of 0.1 mm.

In addition to the initial melt film thickness, the uniform velocity of the solid plug must be specified. This quantity is derived from the knowledge of the output rate, $\dot{M}$, of the machine. Assuming that half of the output is fed in each cylinder and neglecting the mass flow rate in the thin film initially,

$$V_p = \frac{\dot{M}}{2} \cdot \frac{1}{\rho_s' \pi R^2} \cdot f \qquad (3.41)$$

where ρ_s' is the density of the compacted solid granules and f is a correction factor to allow for the time interval taken by the ram for its

return stroke.

Assuming that the granular material compacts under a ram pressure p_o in the cooled section of the feed cylinder where no melt films exist, the compressibility equation (3.1) is used to obtain the density ρ_s' given the bulk density of the granules, ρ_B. The relevant expression is

$$\rho_s' = \rho_B \left(1 + \frac{a\, dp_o}{1 + dp_o}\right)$$

The factor f is given by 1/f = fraction of the cycle time for the forward stroke and f > 1 always.

The remaining calculations consisted of a straightforward numerical integration of the differential equation (3.40) whose coefficients were evaluated locally. Finally, the integral in equation (3.30) was evaluated to obtain the pressure drop.

The sums $\sum_{n_c=1}^{\infty}$ in the terms $\left(\frac{\partial T_s}{\partial r}\right)_{r=R}$ and $\overline{T}_s$, and also in the Bessel functions, was carried out until the n_cth additional term was less than 0.001% of the total sum of the preceding terms. The entire procedure was programmed and all the calculations were performed on a digital computer.

It is worth noting in this analysis that though mass continuity exists for the melt film in the form of equation (3.37), the overall mass flow rate diminishes along the z-direction. This is a consequence of neglecting the effects of the pressure gradient on the velocity profiles of the melt film and of the assumption that the solid plug velocity remains constant. However, under typical conditions, the mass flow rate computed at $z = L_s$ differed by less than 10% from that computed at $z = 0$. This difference can be considered small enough for the purpose of calculating pressure drops in the solid polymer.

3.7.6 Results and discussions

The following results are relevant to the extrusion of a particular grade of LDPE, the properties of which are given in Table 4.1.

It has been seen previously that as the ram moves forward, the length of the column of material diminishes and consequently the pressure propagated through the column of material to a fixed position like plane CC in Figure 3.1 changes. In the results presented below, the length of the column of material considered is the smallest one, i.e. when the ram is just about to reach its maximum forward position. This has no particular significance apart from the fact that the pressure drops predicted are the smallest ones, and was taken just for a matter of convenience to illustrate the present predictions.

Figure 3.24 shows the variation of the pressure drop with output rate and the cylinder wall temperature. As the wall temperature increases, melting occurs at a higher rate, the film thickness grows faster and consequently the viscous frictional forces diminish, leading to a lower pressure drop. On the other hand, as output rate increases, the frictional forces increase due to higher shear rates in the melt films, and the pressure gradients required to maintain the higher output rates must increase.

The large difference between the two curves underlines the significance of the cylinder wall temperature on melting thus further reinforcing the assumption that heat conduction is predominant in the melt film.

Compared with the results predicted by the analysis of section 3.4, the pressure drops when friction is of the Coulomb type are considerably higher than the ones predicted here. The present results were computed on the assumption that the melt films begin to form immediately the

feedstock enters the heated section of the feed cylinder, the position of which coincides with the maximum forward position of the ram face in the existing machine. In practice this condition may not arise, and it is very likely that a delay occurs before the melt film first appears. Apart from the fact that the initial section of each feed cylinder is water cooled, other reasons for the existence of a delay zone are poor thermal contact between the hot walls and the solid polymer, and the entrapment of newly formed melts in the inter-granular spaces so that the melting mechanism does not operate until enough melt is accumulated.

Assuming that Coulomb friction prevails in the delay zone, the two analyses may be combined to predict first the pressure losses due to 'dry' friction and then due to viscous friction once the melt film begins to develop.

Figure 3.25 shows the variation of the pressure drop with the length of the delay zone, for a typical set of operating conditions with the existing extruder. It is clear from this graph that if the pressure drop predictions are to be accurate, it is necessary to locate accurately the position at which the melt film starts to develop. As the delay zone extends further into the feed cylinder, the effect of the lubricating film on the overall pressure drop decreases and most of the pressure drop occurs in the delay zone due to Coulomb friction.

Though cylinder wall temperatures affect considerably the pressure drops due to viscous friction as shown in Figure 3.24, these are too small to have any significant effect on the overall pressure drop. Thus, the effect of cylinder wall temperature on the curve of Figure 3.25 is negligible as long as the coefficients of friction remain independent of temperature.

Simple calculations have revealed that the additional melting by

heat conduction during the return stroke of each ram did not change the film thickness by more than 5% under typical conditions. This change was small enough to have negligible effect on the pressure losses and hence was not considered in the analysis described above.

3.7.7 Conclusions

The pressure losses in a feed cylinder when a melt film forms between the solid polymer and the walls of the cylinder have been analysed. The analysis was based on the assumption that a melt film of finite thickness exists and that it grows as more solid material is melted and added to it mainly by heat conduction.

The melt film acts as a lubricant between the compacted solid plug and the containing cylinder in which the plug moves, and the result of this is the reduction of the pressure drop by a considerable amount, depending on operating conditions. The sooner the melt film starts forming, the smaller the pressure losses.

If the melt film does not form immediately the solid material comes into contact with hot walls at temperatures above the melting point of the polymer, and this is likely to be the case, then the precise location at which the melt film starts to form must be known in order to obtain accurate predictions. In general such locations must be estimated.

3.8 Conclusions

In this chapter, the pressure losses occurring in the solids feeding zone of the ram extruder have been examined. For analytical purposes, the feeding zone was divided into two parts, one consisting of a plain cylindrical feed passage and the other one somewhat more complex being

the intersection of the feed cylinders with the barrel.

The effect of the presence of melt films in the feed cylinders on the pressure losses has been investigated by extending the analysis to include a viscous type of friction in the feed cylinders. This, however, has not been extended to include the angled section of the feeding zone. It was thought that in this region, the converging flow channel would exert enough pressure on any melt that would have been present to force it into the dead spots of the feed chambers (with the present extruder this melt leaked past the shaft seal and out of the extruder) and/or into the voids within the granular mass of the material so that solid polymer came into contact with the channel walls. In reality, a mixed type of friction, viscous and Coulomb would have been present. Because of the general lack of information on this type of friction, an analysis to include this has not been attempted. Only Coulomb friction has been considered for this zone and two idealised geometries have been analysed.

In general, most of the pressure losses in the feeding zone occurred in the feed cylinders due to Coulomb friction. These losses could be reduced by operating the extruder at high main block temperatures so that lubricating polymer melt layers could be formed. However, this should not be done excessively since premature melting of the feedstock could pose feeding problems.

Table 3.1

(i) Temperature Gradients at the Melting Interface:

$$\left(\frac{dT}{dy}\right)_{y=H} = \frac{T_m - T_B}{H} + \frac{A_2}{A_1^2} H \left[A_1 e^{A_1} + (1 - e^{A_1})\right]$$

$$\left(\frac{\partial T_s}{\partial r}\right)_{r=R_s} \simeq \left(\frac{\partial T_s}{\partial r}\right)_{r=R} = \frac{2}{R} (T_{room} - T_m) \sum_{n_c=1}^{\infty} - \exp\left(-\frac{\lambda_{n_c}^2}{2} \frac{k_s}{V_p \rho_s c_s} z\right)$$

(ii) Bulk Mean Temperatures:

$$\overline{T} = T_B + (T_m - T_B) \frac{A_1/2 - e^{A_1}(1 - 1/A_1) - 1/A_1}{A_1 - e^{A_1} + 1}$$

$$+ A_2 \left(\frac{H}{A_1}\right)^2 \left[\frac{1}{2}(e^{2A_1} - 3 + 2e^{A_1}) - \frac{(1 - e^{A_1})^2}{A_1} + \frac{A_1(1 - e^{A_1})}{2} - A_1\right] \Big/ (A_1 - e^{A_1} + 1)$$

Note: If viscous dissipation in the melt film is neglected, the last term in the right hand side of the equation becomes zero.

$$\overline{T}_s = \overline{T}_s(z) = T_m + 2\,(T_{room} - T_m) \sum_{n_c=1}^{\infty} \left[\frac{\exp\left(- \frac{\lambda_{n_c}^{\,2}}{2} \frac{k_s}{V_p \rho_s c_s} z \right) \int_o^R \frac{J_o{}^B(\lambda_{n_c} r)}{R}\, dr}{\lambda_{n_c} R_s \, J_1{}^B(\lambda_{n_c} R_s)} \right]$$

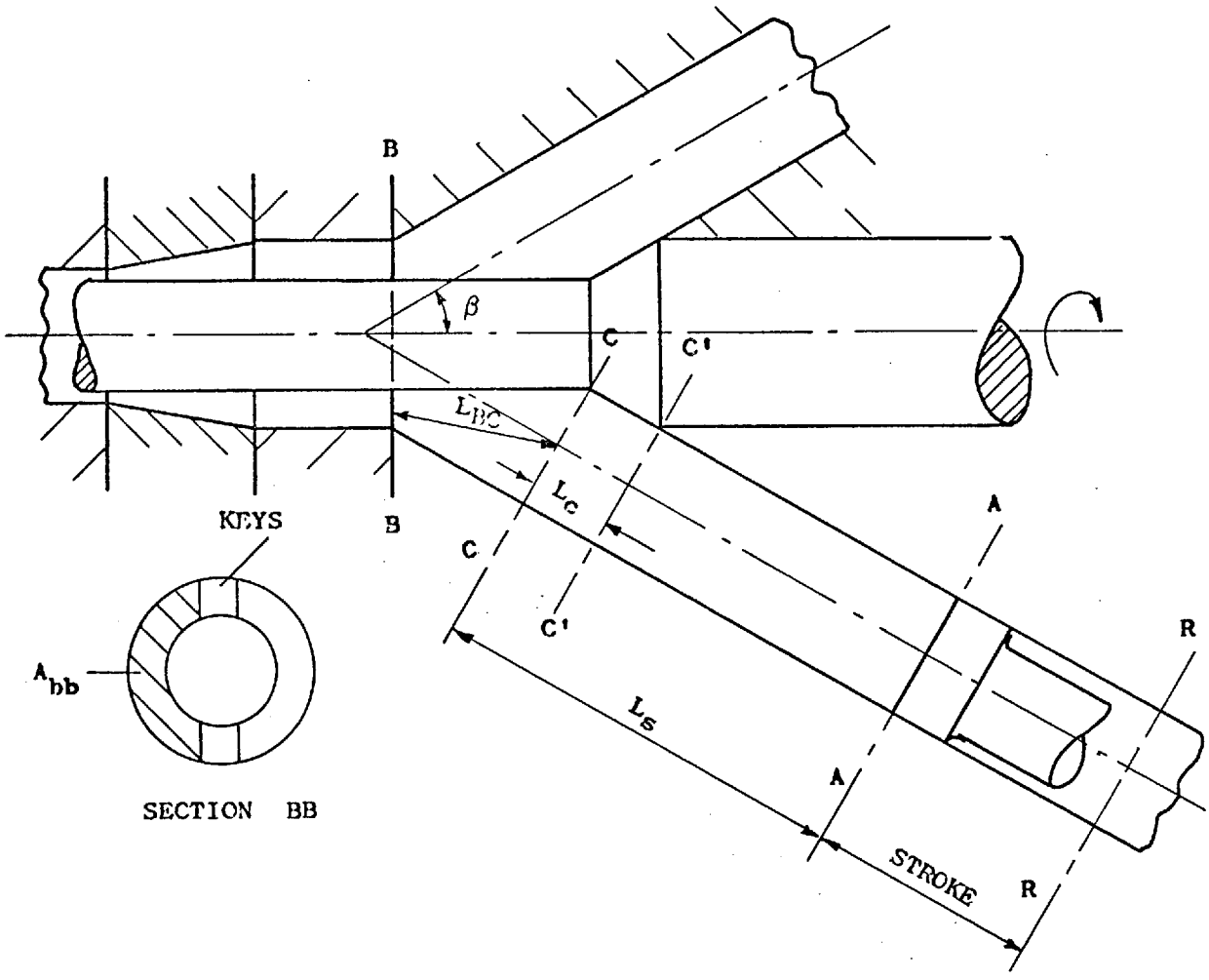

FIG. 3.1 - SOLIDS FEEDING ZONE

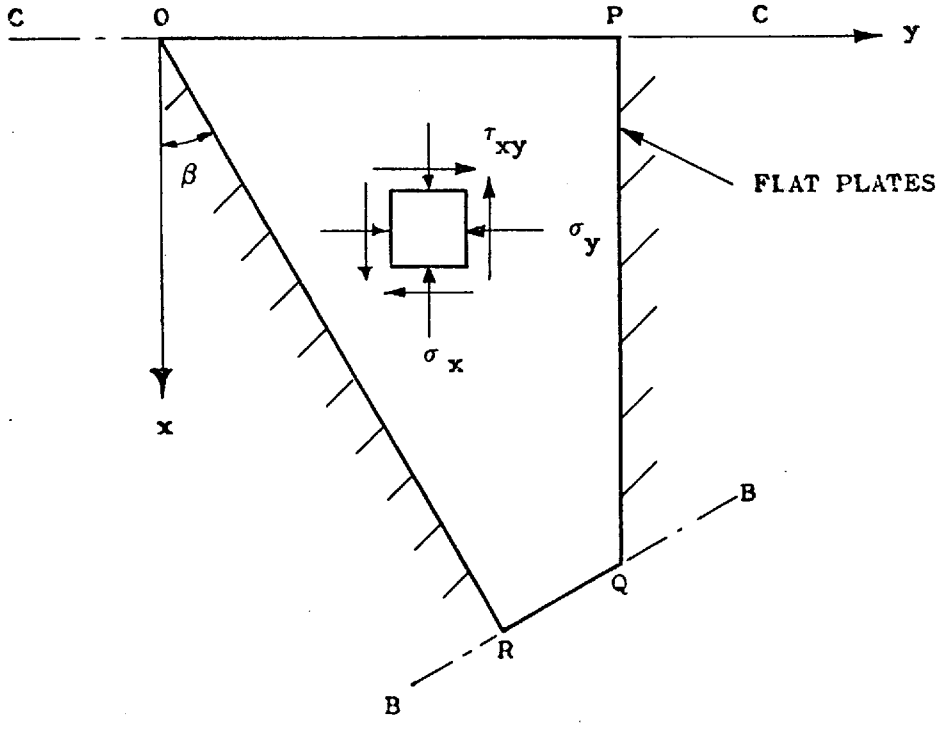

FIG. 3.2 - IDEALISED PART OF THE SOLIDS FEEDING ZONE

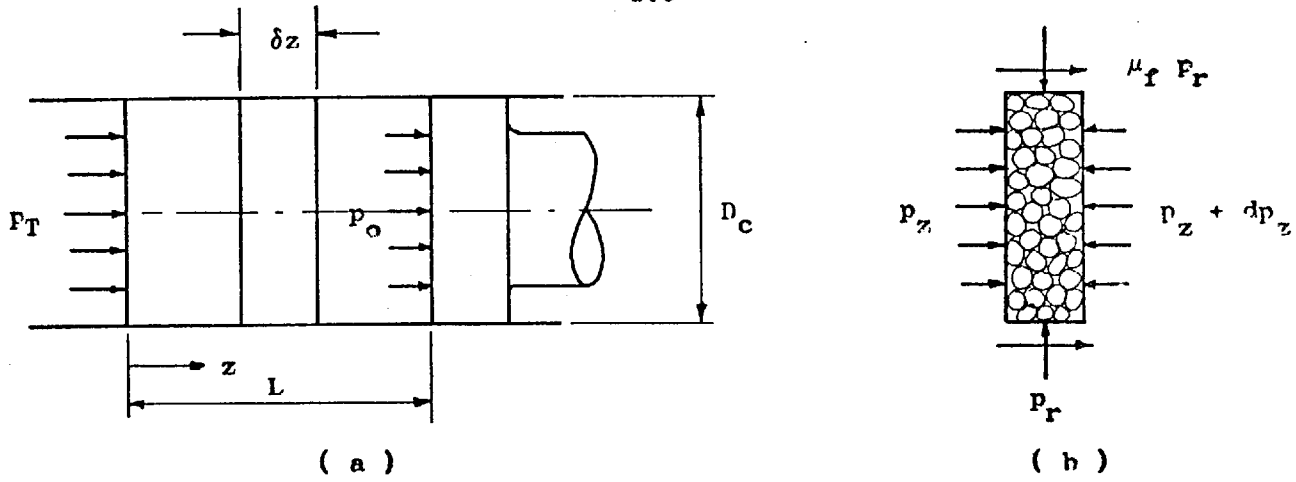

FIG. 3.3 - GRANULAR MATERIAL IN A CYLINDER/PISTON ARRANGEMENT

(a) GEOMETRY AND AXIAL BOUNDARY PRESSURES

(b) PRESSURES ON A TYPICAL ELEMENT OF LENGTH δz

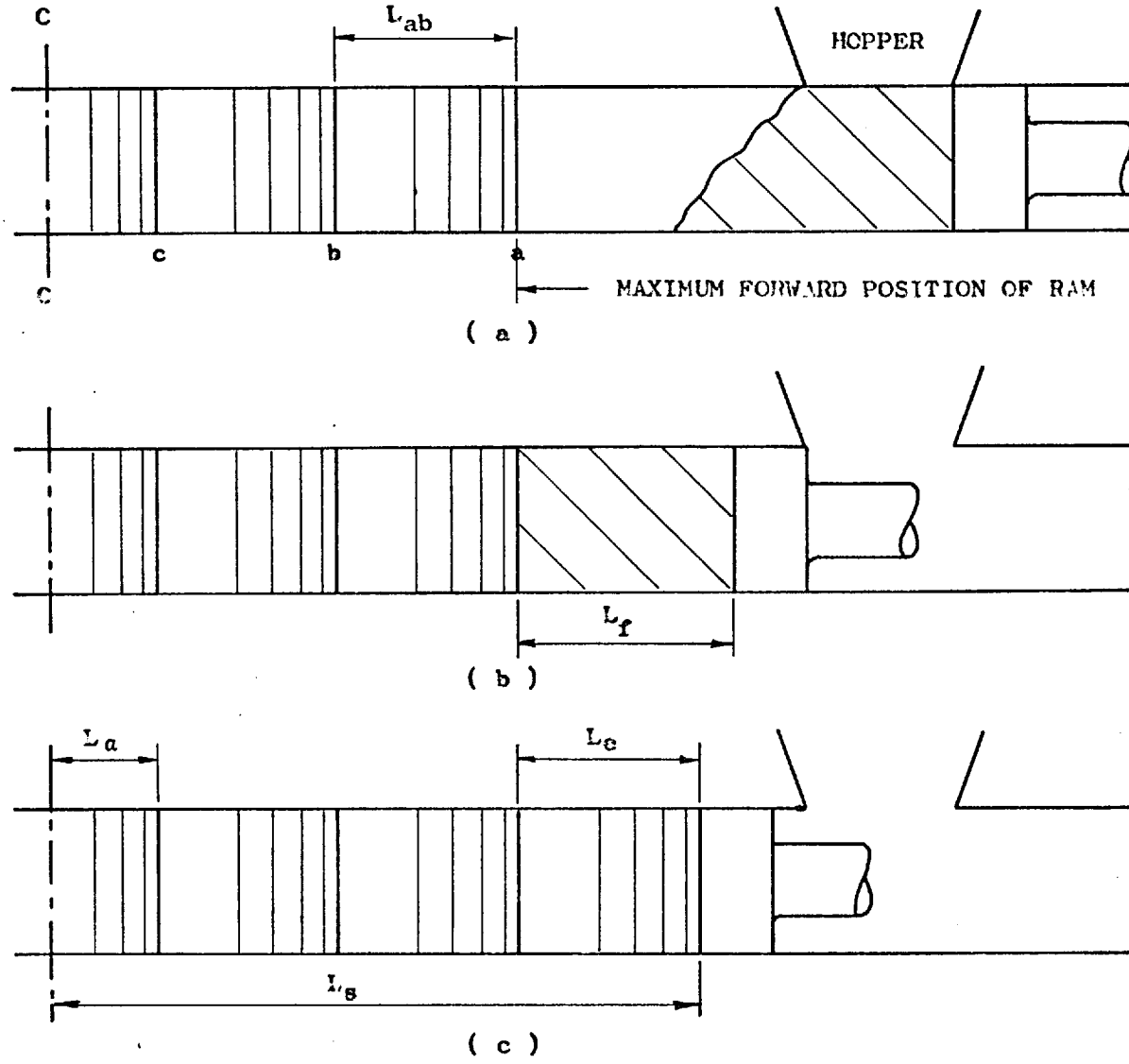

FIG. 3.4 - COMPACTION OF GRANULAR MATERIAL IN FEED CYLINDER

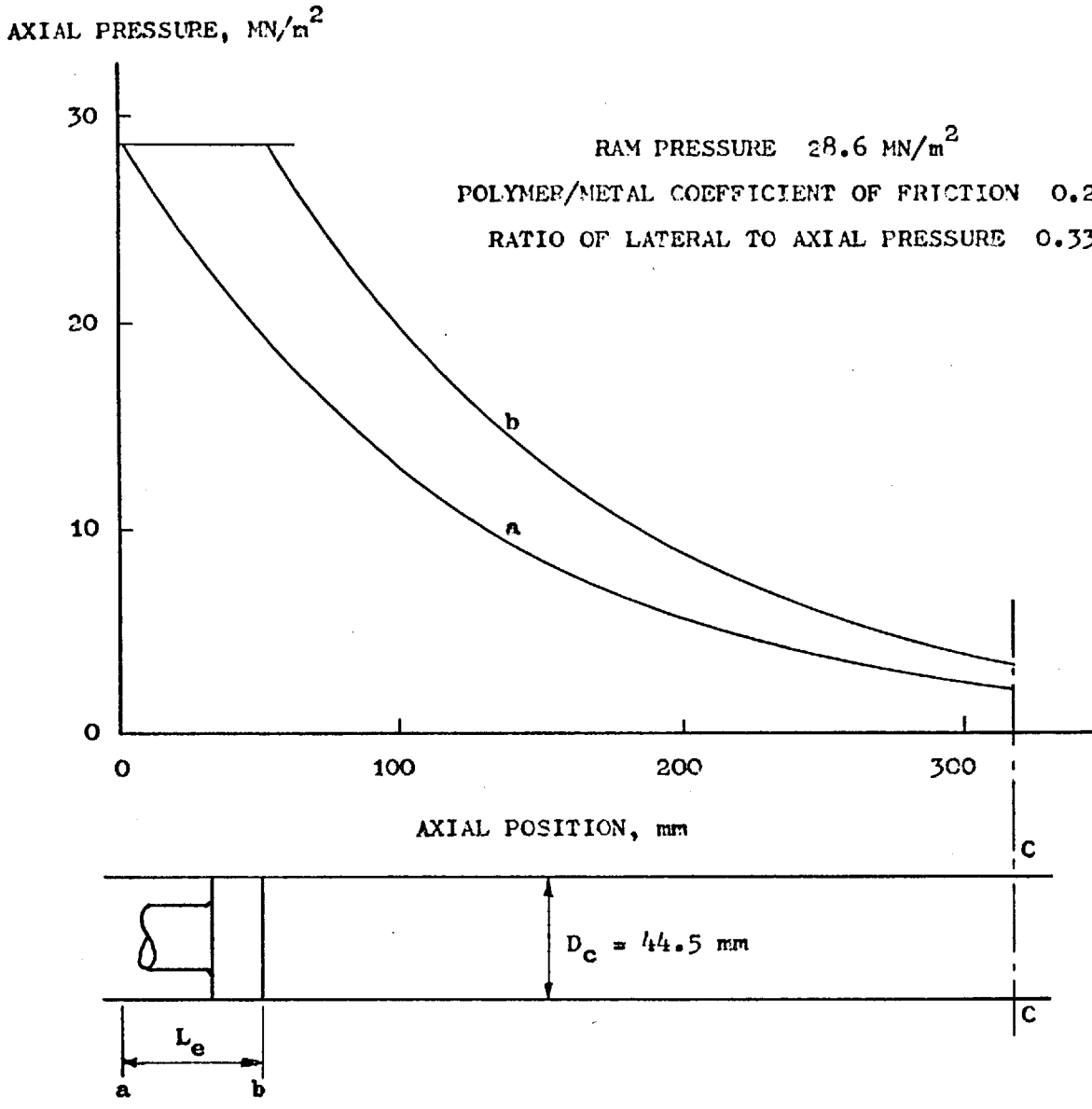

FIG. 3.5 - AXIAL PRESSURE PROFILE ALONG FEED CYLINDER

a - CORRESPONDING TO RAM AT POSITION a

b - " " " " " b

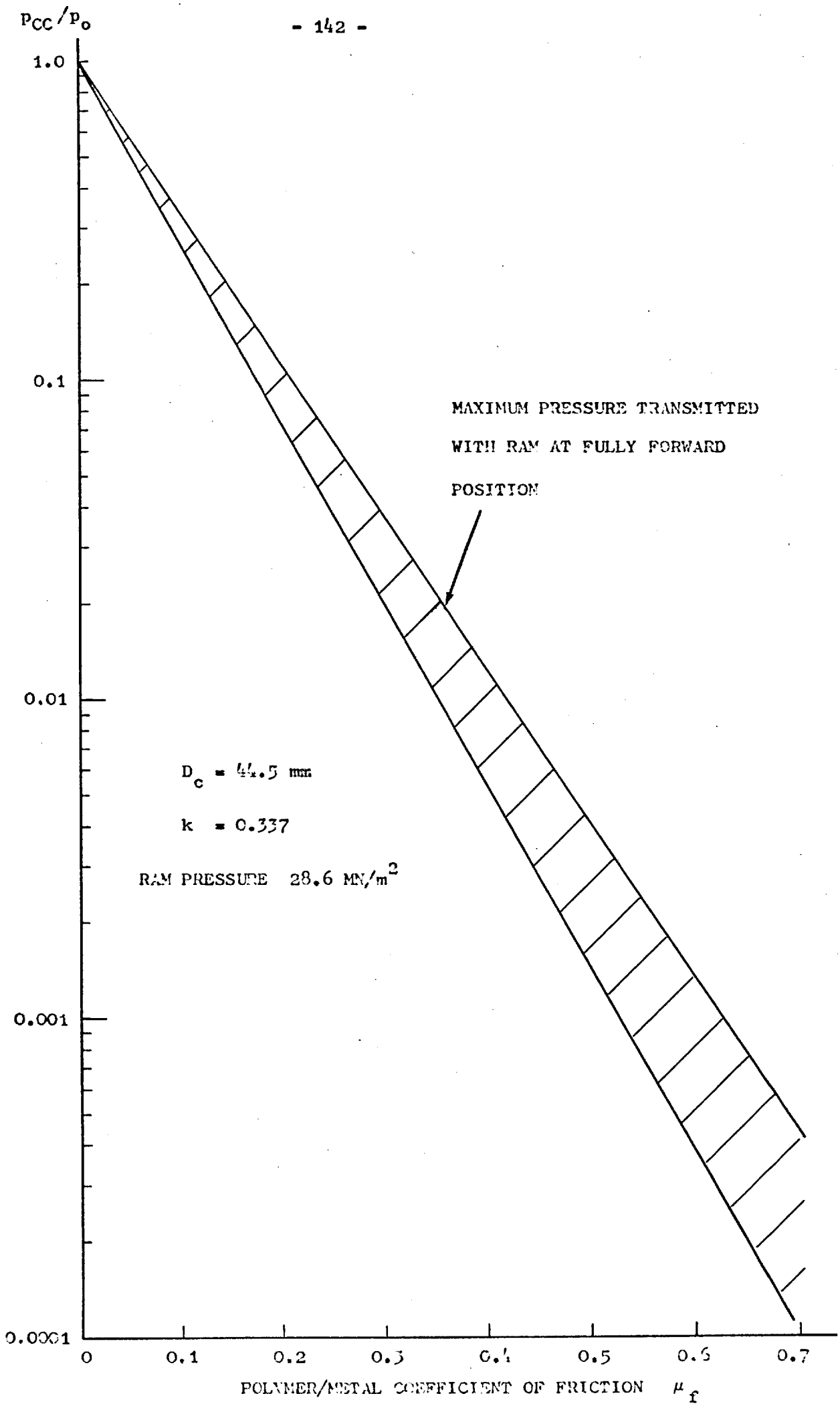

FIG. 3.6 - EFFECT OF μ_f ON PRESSURE TRANSMITTED TO SECTION CC

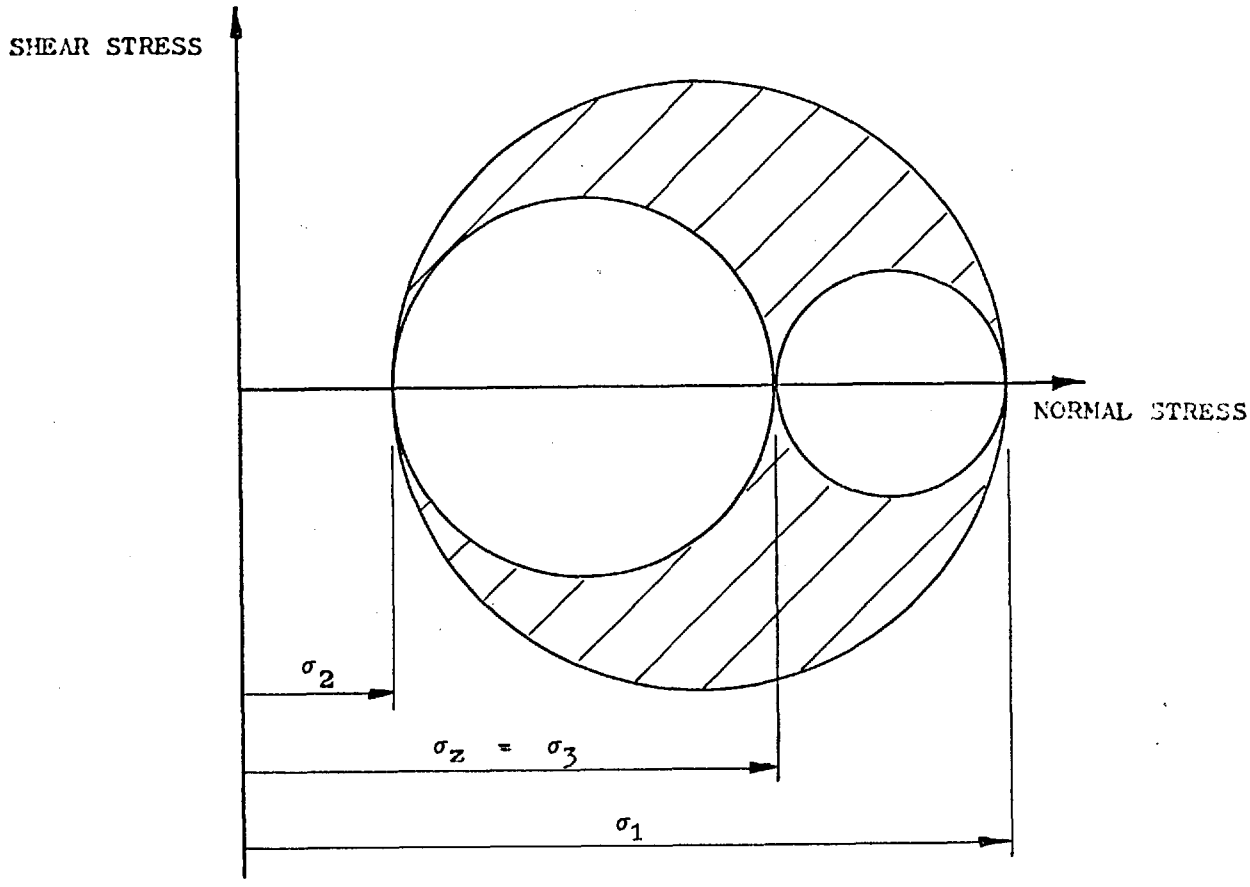

FIG. 3.7 - MOHR'S CIRCLE

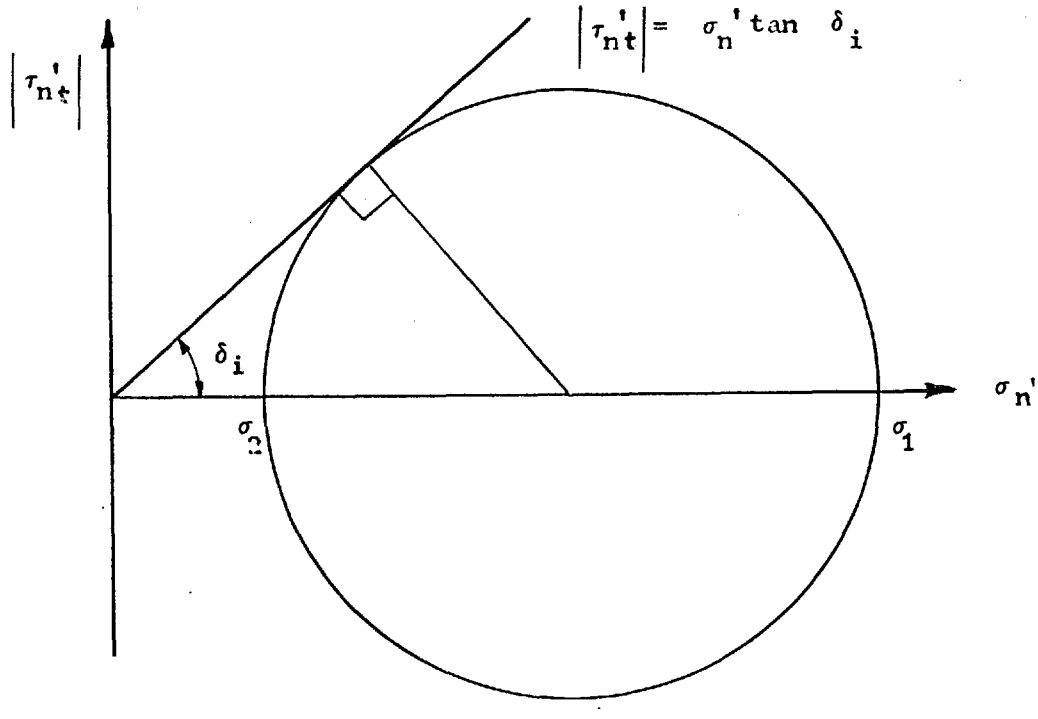

FIG. 3.8 - STRESS STATE IN CRITICAL EQUILIBRIUM

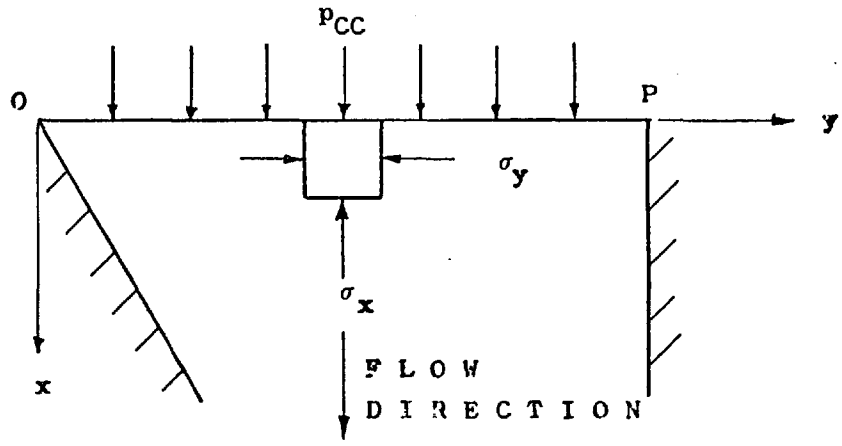

FIG. 3.9 - INITIAL BOUNDARY CONDITION

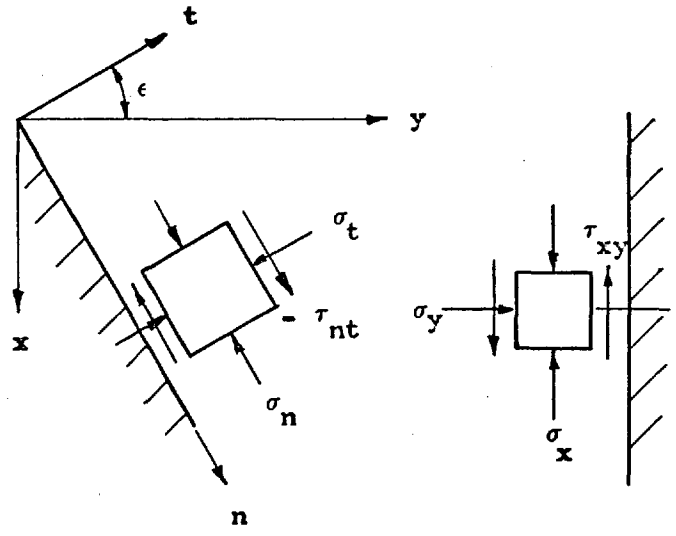

FIG. 3.10 - STRESSES AT BOUNDARIES

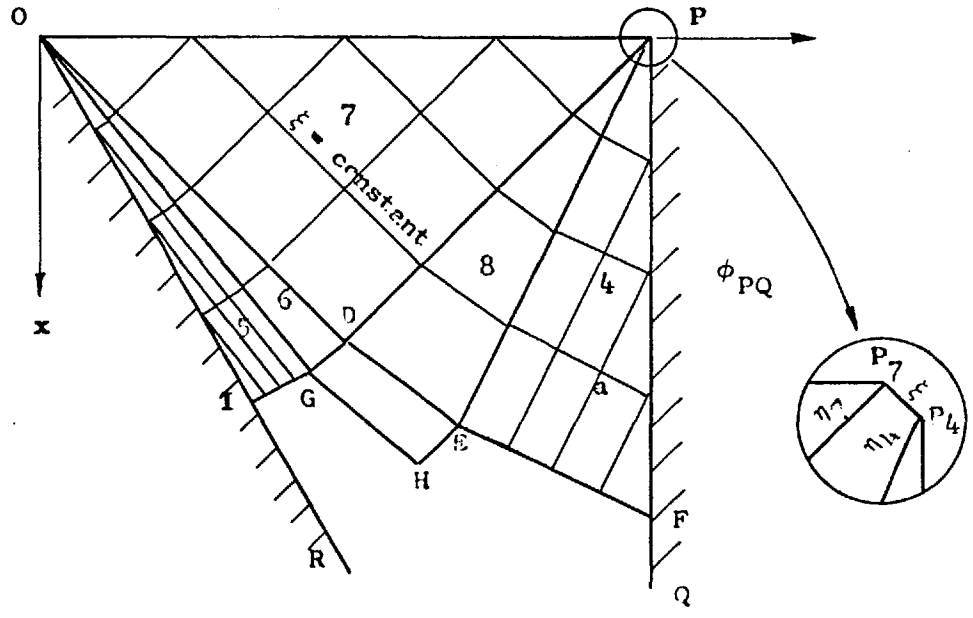

FIG. 3.11 - PROPAGATION OF CHARACTERISTICS

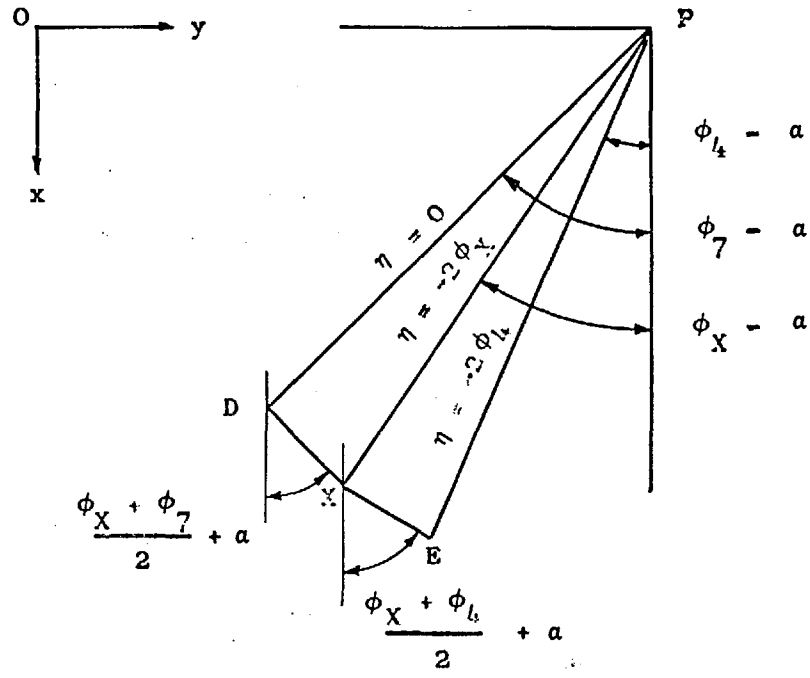

FIG. 3.12 - APPROXIMATION OF CURVE DE BY SHORT STRAIGHT LINES

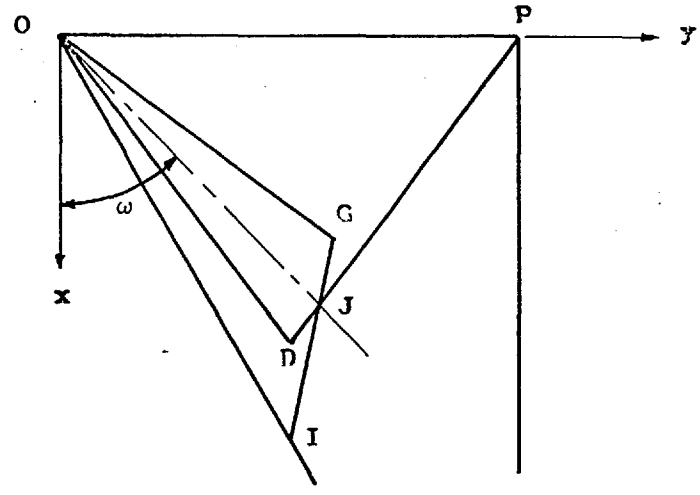

FIG. 3.13 - LINE OF DISCONTINUITY

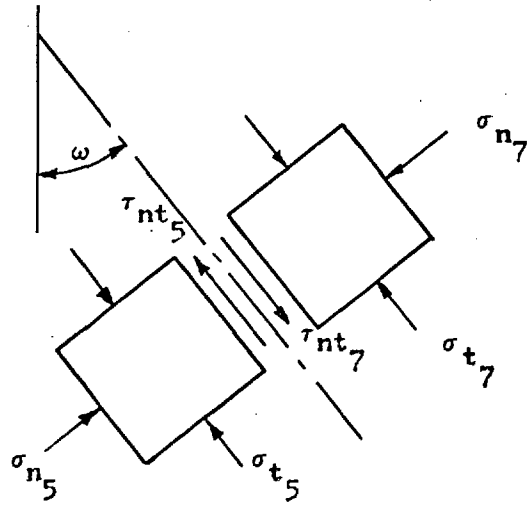

FIG. 3.14 - STRESSES ON ELEMENTS ADJACENT TO A LINE OF DISCONTINUITY

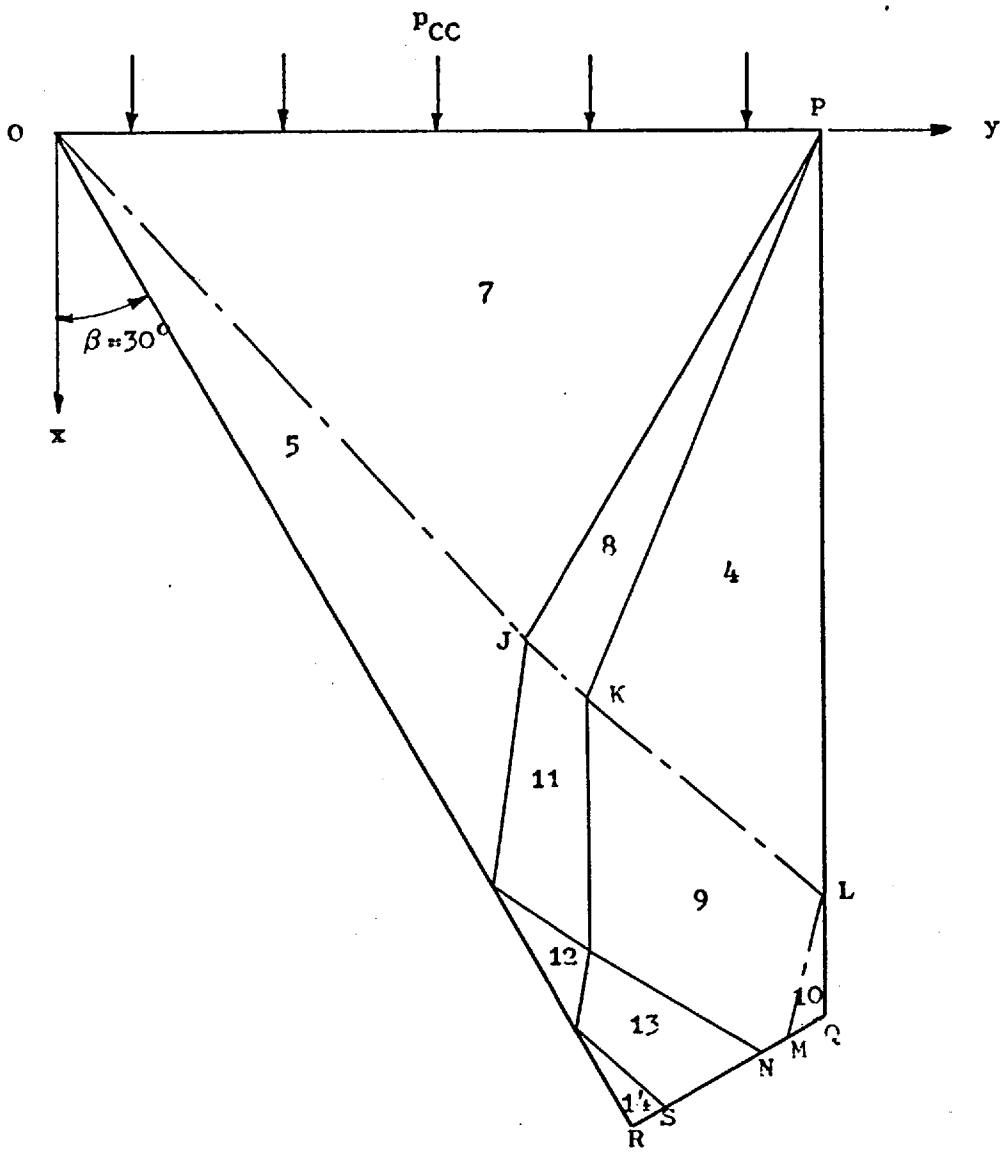

(a)

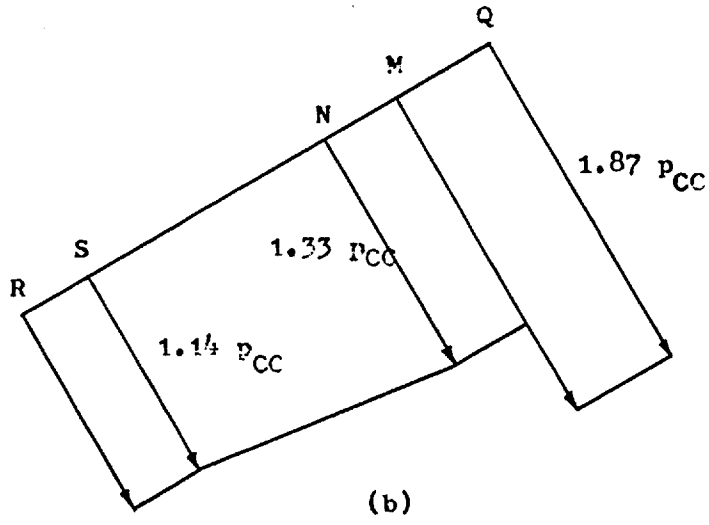

(b)

FIG. 3.15 - SOLUTION FOR $\delta_i = 30^{\circ}$ and $\delta = 14^{\circ}$

(a) - CHARACTERISTICS AND LINES OF DISCONTINUITY

(b) - NORMAL STRESS DISTRIBUTION ALONG Q R

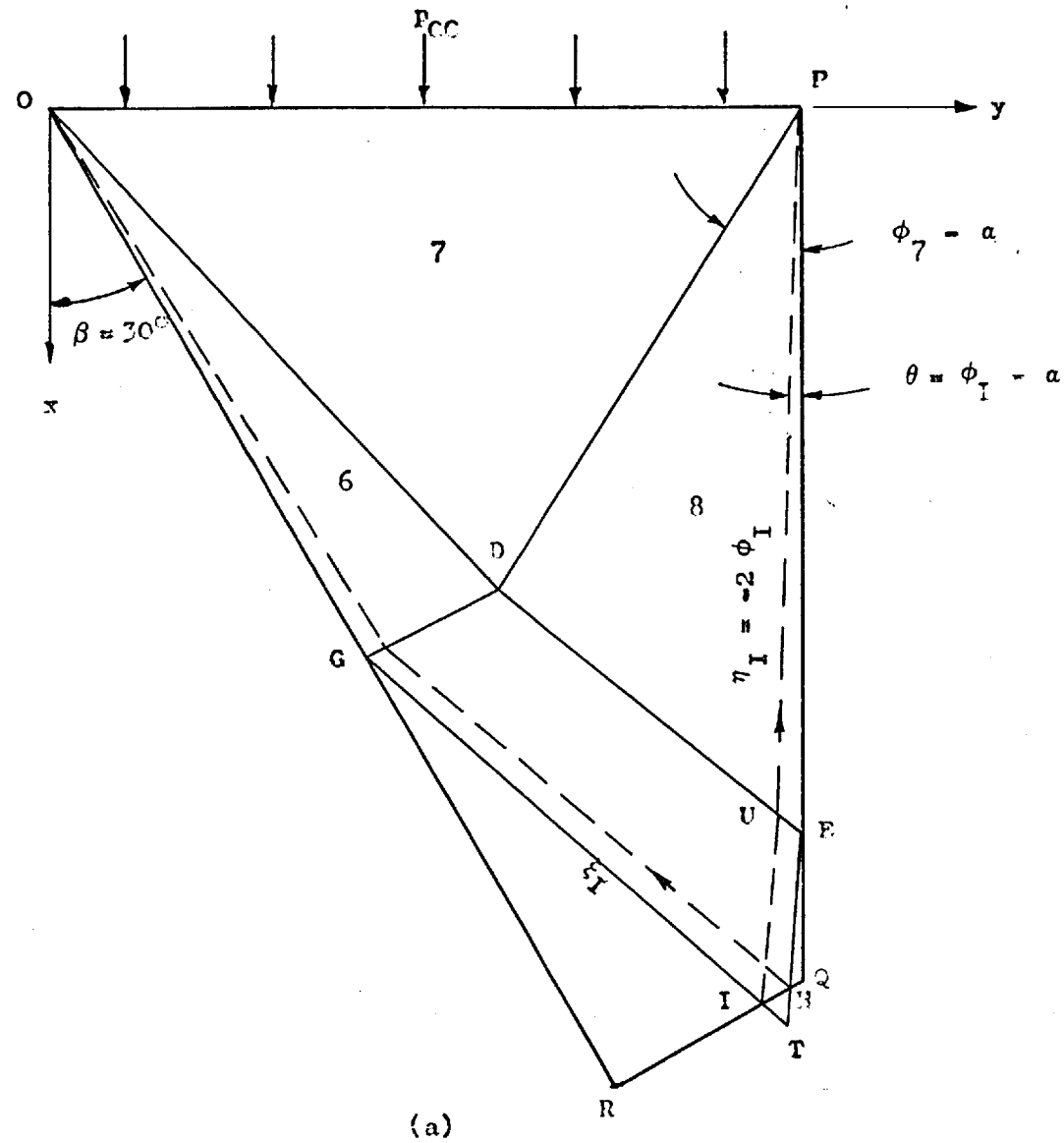

FIG. 3.16 - SOLUTION FOR A SPECIAL CASE $\delta_i = \delta = 14^0$

(a) - CHARACTERISTICS AND INTERPOLATION LINES

(b) - LINEARISED STRESS DISTRIBUTION ON QR

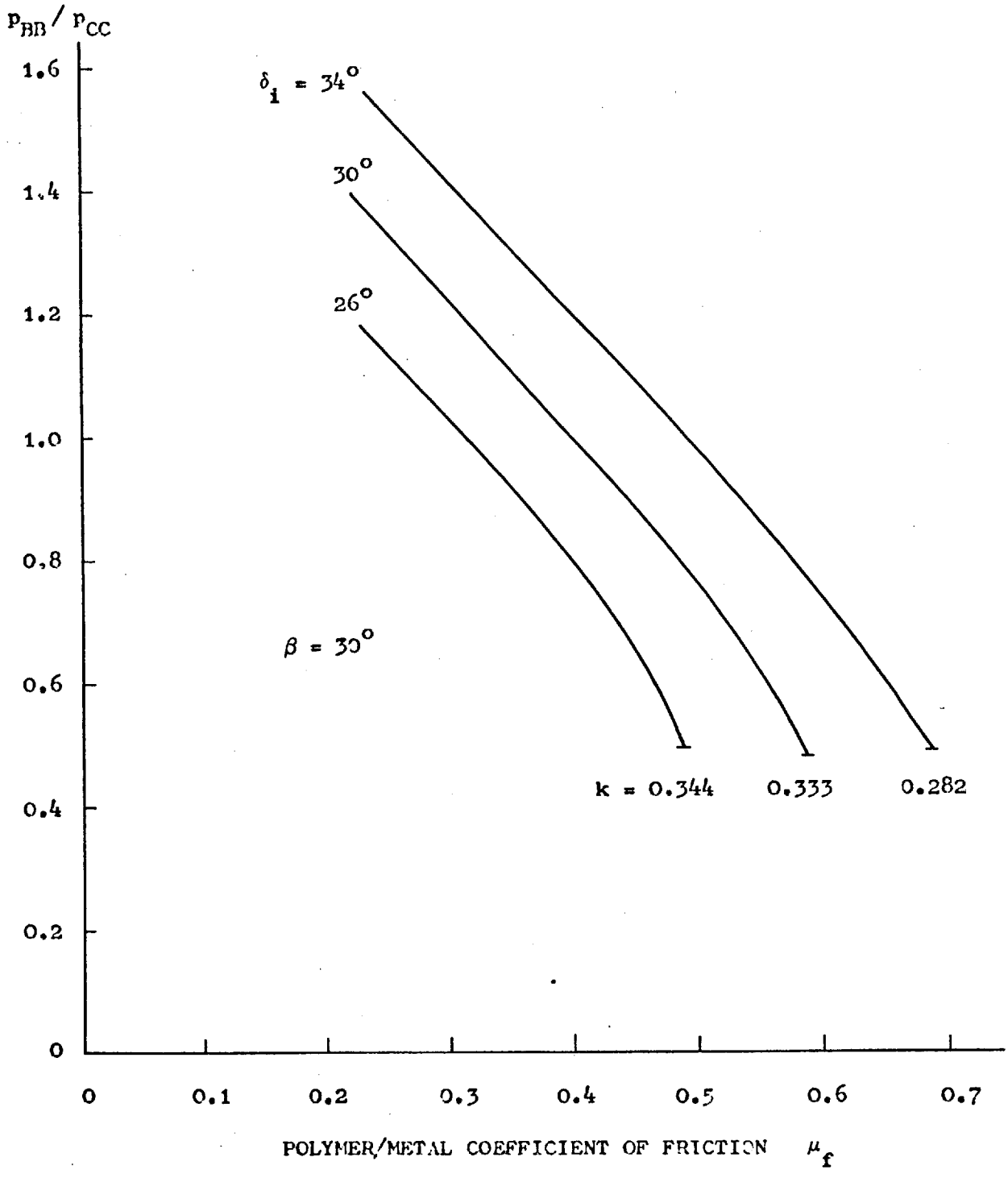

FIG. 3.17 - EFFECT OF μ_f ON THE PRESSURE RATIO p_{BB} / p_{CC}

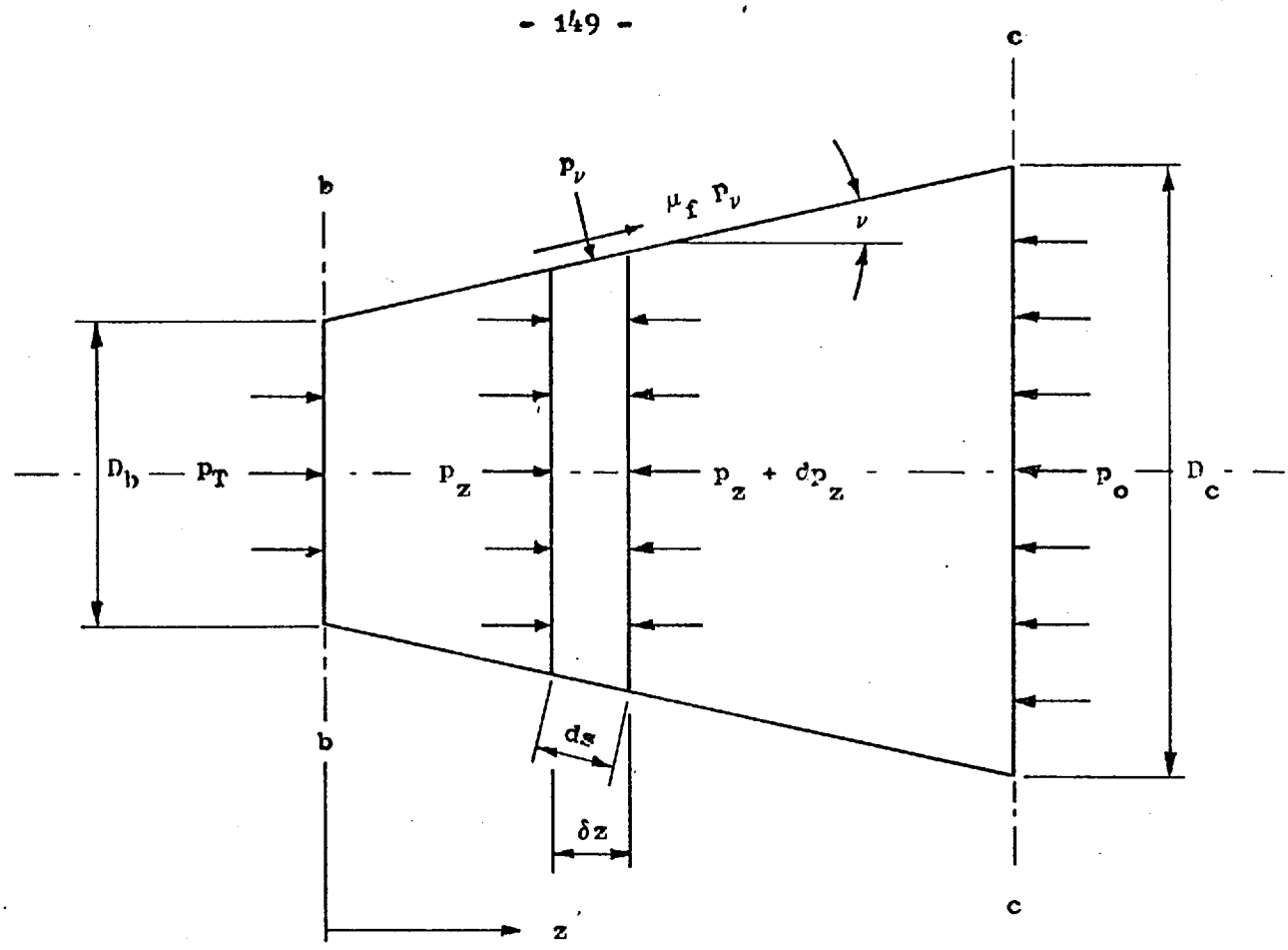

FIG. 3.18 - GEOMETRY AND STRESSES FOR THE CONICAL CHANNEL

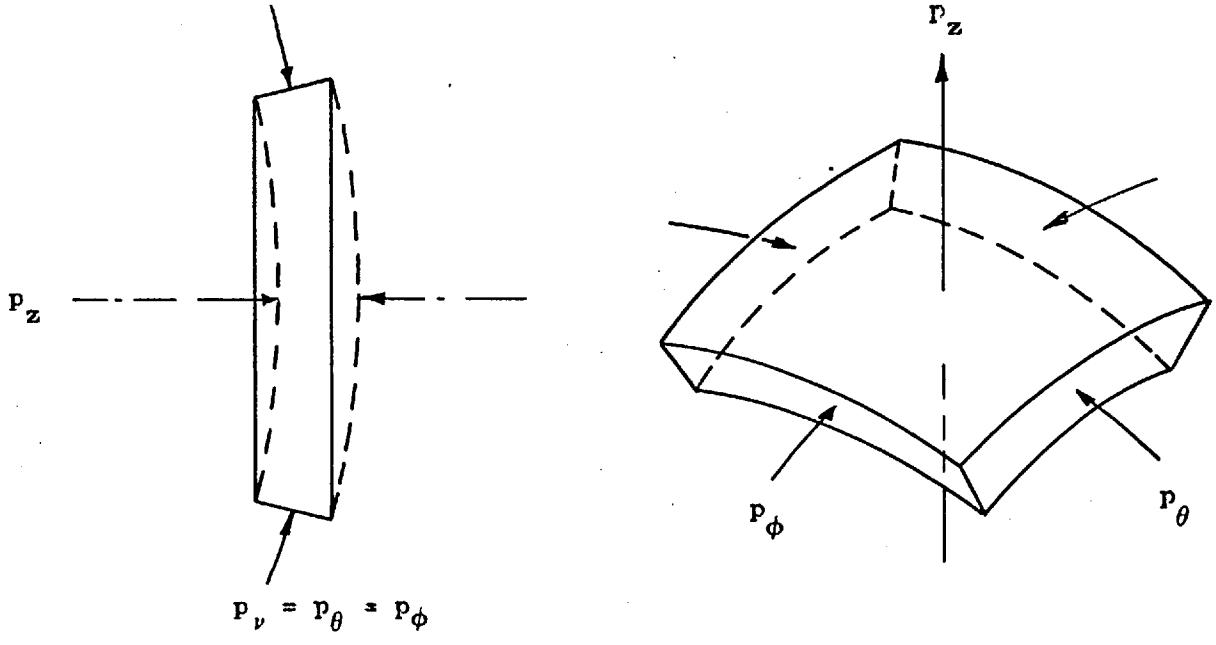

FIG. 3.19 - SPHERICAL SLAB AND STRESSES

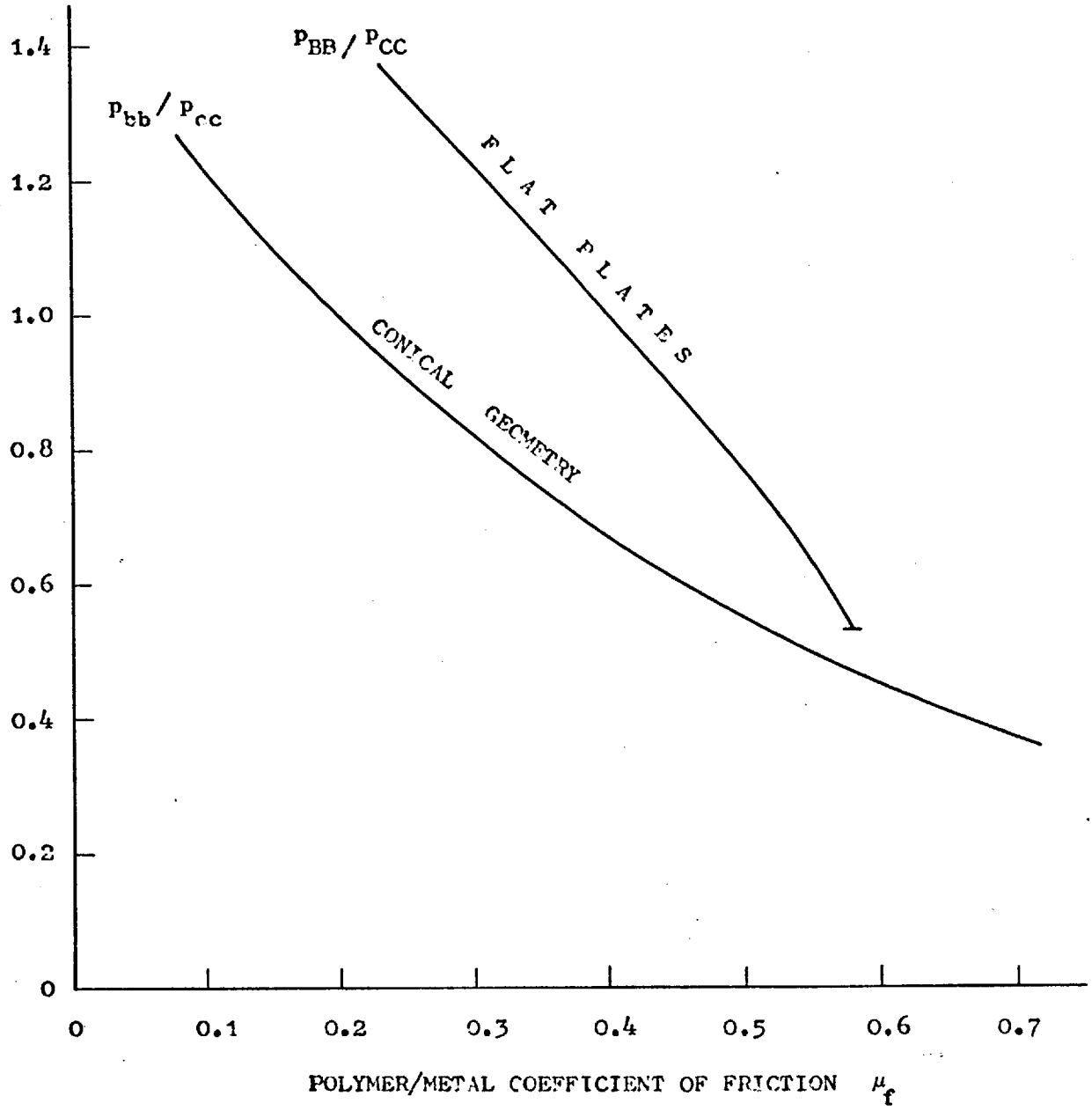

FIG. 3.20 - VARIATION OF THE PRESSURE RATIOS p_{bb}/p_{cc} and p_{BB}/p_{CC} with μ_f

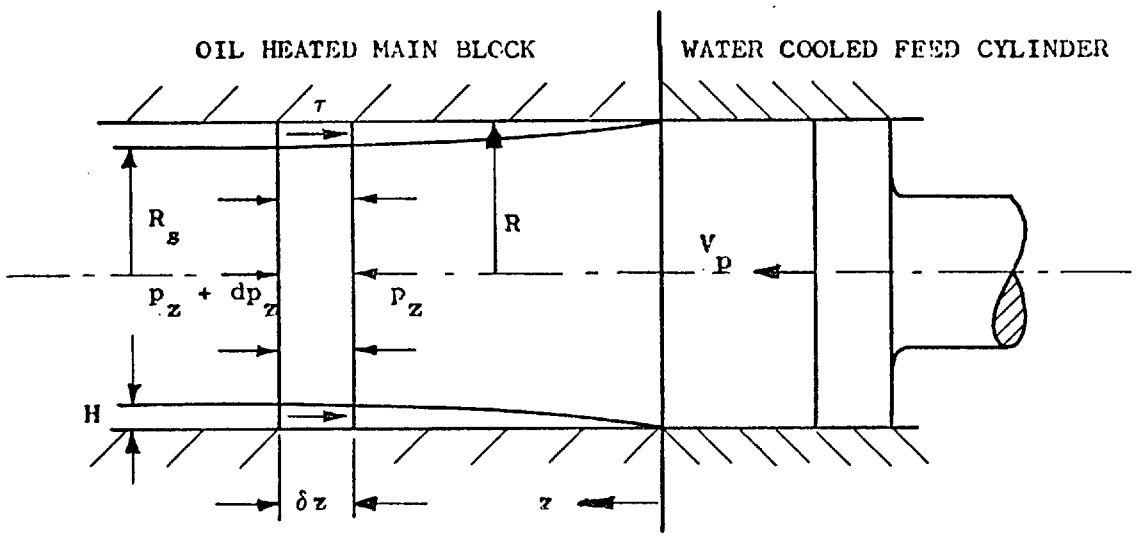

FIG. 3.21 - VISCOUS FRICTION DUE TO POLYMER MELT FILM

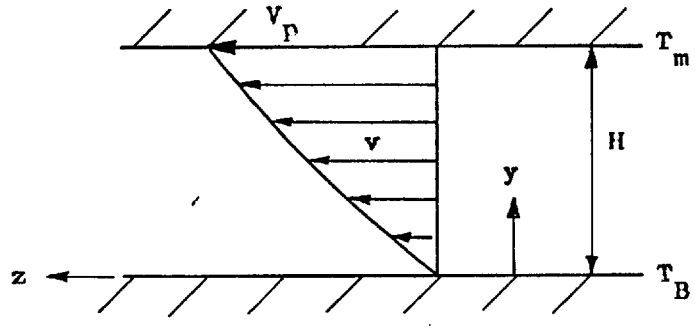

FIG. 3.22 - VELOCITY PROFILE AND BOUNDARY CONDITIONS

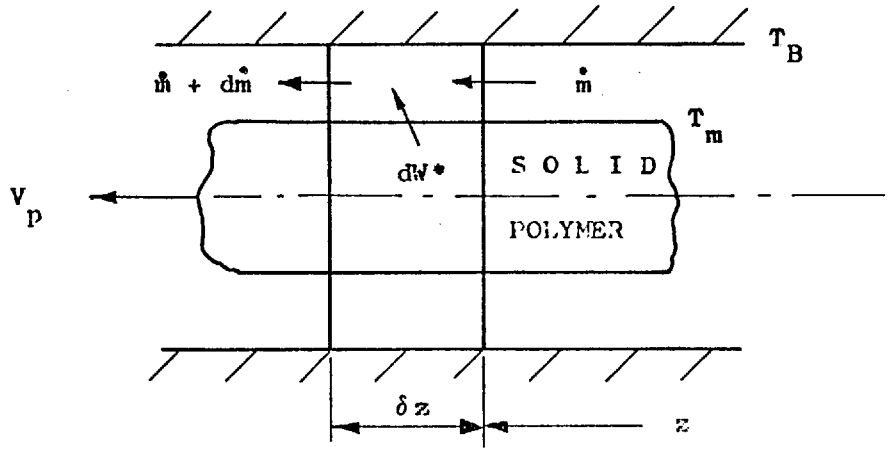

FIG. 3.23 - MELTING OF THE SOLID PLUG

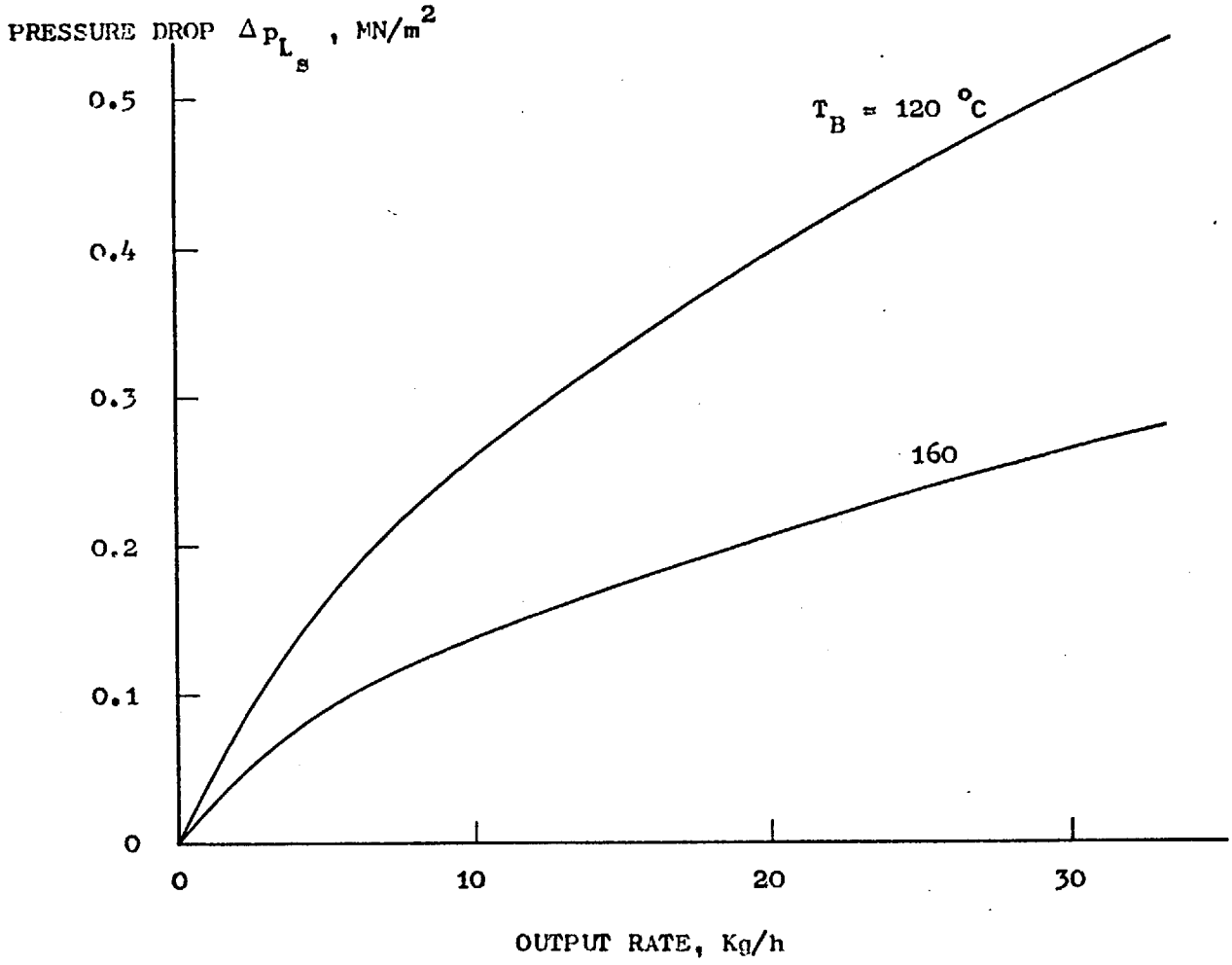

FIG. 3.24 - VARIATION OF PRESSURE DROP WITH OUTPUT RATE

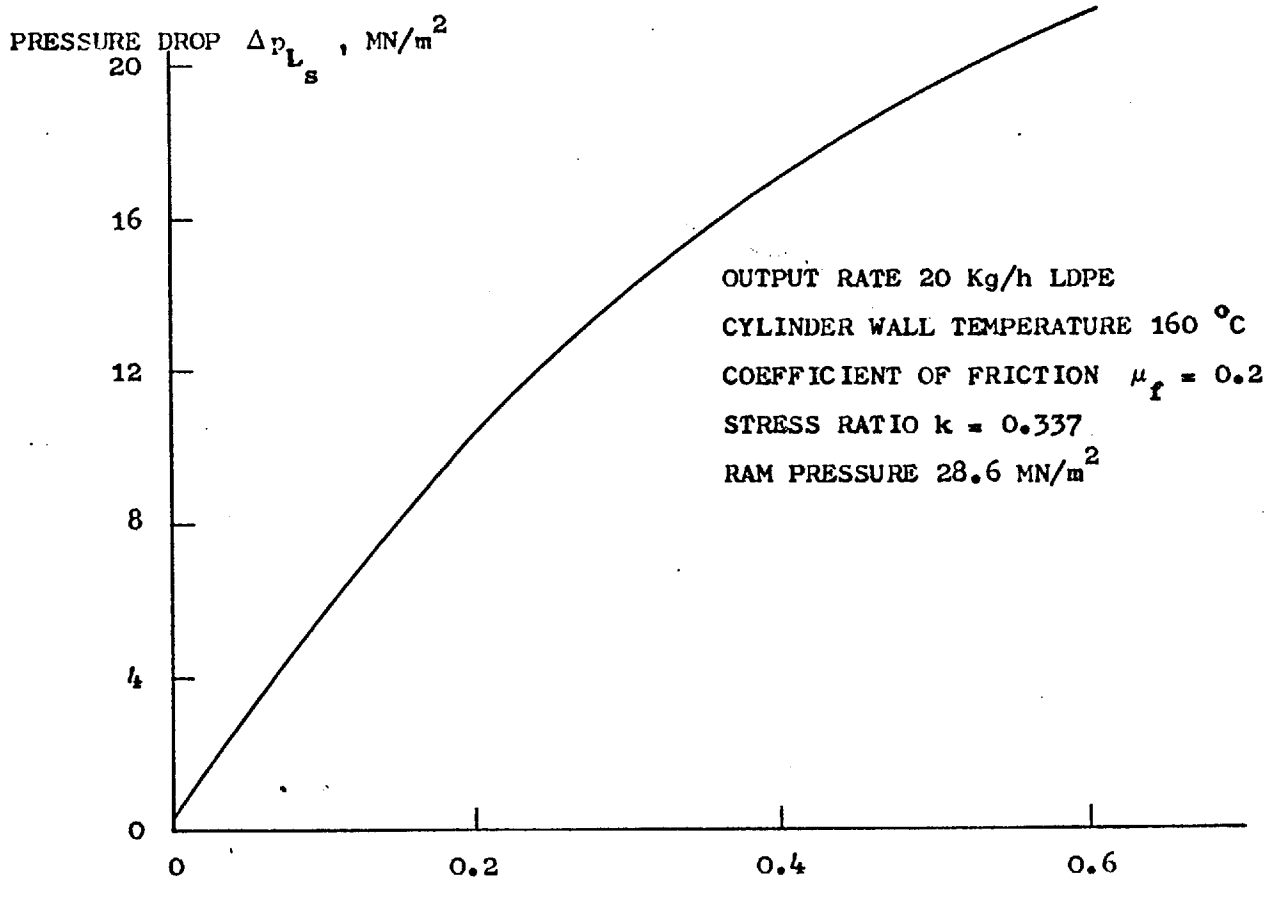

FIG. 3.25 - VARIATION OF PRESSURE DROP WITH DELAY ZONE LENGTH

CHAPTER 4

THEORETICAL MODEL FOR MELTING

4.1 Introduction

In chapter 3, melting of the feedstock as a result of heat conduction in the feed cylinders was considered when calculating pressure losses in the feeding zone. In this chapter, the main melting mechanism occurring in the annular channel of the extruder is examined.

Theoretical models for the melting process were developed to predict the length of the region required for complete melting to occur and to predict the pressure drop in this region of the extruder. Clearly, these are important factors in the operation of the machine since it is necessary to ensure that the material reaching the die is fully melted and that adequate pressures are maintained to provide the required output rates. Other parameters like power consumption and mean melt temperatures could also be obtained from the theoretical models.

Models with different degrees of assumptions were developed. Initially, a simple analytical solution was obtained by assuming the polymer melts to behave as Newtonian fluids with simple velocity and temperature fields in the melts and in the solid polymer. Later, several other factors, including the use of a power-law fluid model for the melts, were taken into account to allow for a more realistic model. Solutions for the different models were compared to assess the improvements by gradually developing more advanced models.

4.2 Melting in the Annular Channel

Figure 4.1 shows a diagram of the melting mechanism operating in a typical length of the annular channel. Melt films are formed between the

metal walls and the solid polymer. The films grow in thickness as more solid material melts until the flow channel is completely filled with melt.

The solid material moves downstream by virtue of the pressure forces exerted by the rams and therefore the polymer melt is dragged by the solid bed and it is also conveyed downstream by pressure forces in the melt itself.

Material melts by heat conducted through the melt and heat generated by viscous dissipation within the melt, this being more pronounced in the melt film adjacent to the shaft.

Though relatively little experimental evidence of the melting mechanism was available at the start of the work on the melting model, it was assumed that this was the most likely melting mechanism in operation in the ram extruder.

4.2.1 Geometry

For analytical purposes, the relatively thin annular films and solid bed were considered as contained in slits and hence rectangular coordinates used for deriving the relevant equations.

The overall error introduced by the assumption was small if $(\Delta R/R_a) \ll 1$, where ΔR is the annular gap and R_a is a mean radius of the annulus. In the existing extruder, $\Delta R/R_a \simeq 0.15$. It should be noted that this ratio becomes smaller if each melt film and the annular solid bed are treated individually, e.g. by considering H_1 and a mean radius for the annular film 1 in Figure 4.2 which shows the rectangular geometry.

Quantities referring to the melt film adjacent to the barrel will be subscripted by 1, adjacent to the shaft by 2 and by s for the solid phase (called the solid bed). Unsubscripted variables will in general

refer to both melt films unless otherwise specified.

The coordinates normal to the plates - y - were chosen to have their origin at the solid/melt interface. By doing this, the variation of the melt film thicknesses does not appear in the differential flow equations but are taken account of in the melting equations. This was permissible because in general H varied slowly with z, i.e. $\left|\frac{dH}{dz}\right| \ll 1$, which minimises the effect of the slight distortion of the coordinate system from the truly rectangular one. It will be seen later that this coordinate system can easily take care of any slowly varying channel taper. Also, since $\frac{dH}{dz} \ll 1$, the lubrication approximation was applied here to the velocities in the melt films, i.e. the velocity profiles are fully developed [4]. It was also applied to the temperature profiles initially, but was later relaxed.

The position of z = 0 was arbitrary and was conveniently chosen as the position where the melting mechanism started to operate. The x-direction is normal to the plane of Figure 4.2.

4.2.2 Melting rates

The mass conservation for an element of melt film adjacent to the barrel of length 2δz at a typical downstream position z as shown in Figure 4.3 gives

$$dW_1^* = 2 \frac{d\dot{m}_1}{dz} \delta z \qquad (4.1)$$

where $\dot{m}_1$ is the local mass flow rate of melt film 1 and dW_1^* is the local rate of melting.

Equation (4.1) was obtained assuming a steady state melting process in the plasticating zone. It was assumed that the cycling of the feed rams of the extruder, and their pressure were adjusted in such a way that

a continuous steady flow of material through the machine was maintained. Even if this was not obtained in practice, the equation should still be valid for the average melting rate over each cycle. Little progress would have been achieved if this assumption was not made. The problem therefore becomes time-independent and hence comparatively easier to solve.

The rate of melting dW_1^* can be expressed by an energy equation of the type:

Rate of melting x Change in enthalpy = Heat supplied to the melting interface - Heat conducted from the melting interface

$$\text{i.e.} \quad dW_1^* \, \Delta E_1 = C \left[km \left(\frac{\delta T_1}{\delta Y_1} \right)_{Y_1=0} - ks \left(\frac{\delta T_s}{\delta Y_s} \right)_{Y_s=H_s} \right] z \quad 2\delta z \qquad (4.2)$$

where ΔE_1 is the average change in enthalpy, C is the mean circumference of the annulus and the temperature gradients are evaluated locally. Combining equations (4.1) and (4.2) and taking the limit as $\delta z \rightarrow 0$,

$$\frac{d\dot{m}_1}{dz} = \frac{C}{\Delta E_1} \left[km \left(\frac{\delta T_1}{\delta Y_1} \right)_{Y_1=0} - ks \left(\frac{\delta T_s}{\delta Y_s} \right)_{Y_s=H_s} \right] z \qquad (4.3)$$

A similar equation can be derived for the other film:

$$\frac{d\dot{m}_2}{dz} = \frac{C}{\Delta E_2} \left[km \left(\frac{\delta T_2}{\delta Y_2} \right)_{Y_2=0} + ks \left(\frac{\delta T_s}{\delta Y_s} \right)_{Y_s=0} \right] z \qquad (4.4)$$

Equations (4.3) and (4.4) are the basic equations for the melting model. To solve these, it is necessary to evaluate the terms in the R.H.S. of these equations. The required terms are obtained by detailed analysis of the melt films flow behaviour in terms of velocity

and temperature distribution and also an analysis of the temperature distribution in the solid phase.

4.3 Brief Literature Survey

Before describing the relevant equations for the velocity and temperature profiles and presenting their solution, it is appropriate to consider some reported work on similar and other melting problems. It should be clear that in any problem concerning the melting of solids, it is usually necessary to consider the basic problems of heat transfer in the solid and also heat transfer in the resulting melt that is formed and its flow behaviour.

Ross [45] has discussed some design formulations for three commonly used types of industrial melters applying the respective methods of mix melting, contact melting and convection melting. Of these, contact melting is the most relevant one to polymer processing machinery. Ross obtained results for the coefficients of heat transfer for a melt film formed by the melting of a solid slab over an inclined hot plate [46]. The solution for the heat transfer problem in the melt and in the solid slab was simplified in his analysis by assuming a linear temperature distribution in the melt film and a uniform temperature in the solid slab. The analysis of the flow behaviour of the melt was also simplified by considering only Newtonian melts.

Skelland [47,48] solved the same problem, but unlike Ross, he confined his attention to the case in which the molten material was represented by a time-independent non-Newtonian fluid of the power-law type. The flow equations were accordingly modified and the same simplifications were made concerning the temperature distribution in the melt film and the solid slab.

Thermal convection effects in the melt film were included in the same problem by Griffin and Szewczyk [49,50] for Newtonian and non-Newtonian melts. This resulted in a more realistic temperature distribution within the melt but the problem was a mathematically more complex one. A suitable method for solving this was presented by Griffin [51]. In all these works, viscous dissipation in the melt film was neglected. With polymer processing machinery, and in particular the ram extruder, viscous dissipation in the polymer melt films may contribute a significant amount of heat used for melting and is the only source of heat when the machine operates under adiabatic conditions. To initiate the melting mechanism by viscous dissipation, however, either contact melting, i.e. melting by heat conducted from a hot metal wall to the solid polymer and/or frictional melting must occur. Frictional melting was examined by Mustafaev et al [24] who observed the formation of melt films under severe frictional forces during their measurement on frictional properties. Unfortunately, this type of work is not suitable for inclusion in a melting model.

Sundstrom and Young [52] calculated melting rates of crystalline polymers under shear conditions. In their studies, viscous dissipation contributed 5% to 25% of the total energy required to melt the polymer with the remaining energy derived from heat conduction.

The original model for melting in single screw extruders was presented by Tadmor [53] based on experimental investigations and qualitative proposals made by Maddock [54]. This simple model in which the melt was assumed to behave as a Newtonian fluid was soon superceded by others based on the same formulation but with more realistic assumptions. Tadmor et al [55] improved the original model by assuming the melt to behave as a non-Newtonian fluid of the power-law type and also by using

an effective latent heat of fusion which included the enthalpy change in heating the melt from the melting point to the average melt temperature to compensate for the omission of the relevant thermal convection term in the energy equation for the melt film.

One of the most accurate and complete models for melting in single screw extruders so far presented is the one developed by Edmondson [6] and Fenner and Edmondson [56]. Amongst the features in this model are the allowance for the solid bed velocity to vary in the downstream direction and the inclusion of melt films in all the metal boundaries of the screw channel when operating conditions give rise to these.

4.4 General Assumptions

In order to solve the present problem, it was necessary to make a number of assumptions. In this section some general ones are discussed. Other assumptions are introduced where appropriate in the derivation of the solution for each model. The following assumptions are common to all the melting models presented in this chapter:

1. There is no slip of the polymer melt at the metal walls.
2. Good thermal contact between polymer melt and metal surfaces exist, i.e. the temperature of the melt adjacent to the wall is the same as that of the wall.
3. The physical properties (thermal conductivity, density and specific heat) are not temperature nor pressure dependent.
4. The processed polymer exhibits a sharp melting point, T_m.
5. Forces other than viscous and pressure forces (e.g. inertia and body forces) in the melt films are negligible.

Assumption 1 should be suitable here though it may break down under severe shear rates and for certain materials. Relatively little is known about assumption 2, but it should be reasonable in view of the pressures involved. Assumption 3 in general is unsatisfactory for polymers, but within a limited range, it should be valid. Assumption 4 is also generally poor for polymers though it is reasonable for crystalline polymers. Finally, assumption 5 should be fairly accurate because the flow of polymer melts is highly viscous and are of low Reynolds number (laminar flow).

4.5 Analytical Solution

4.5.1 Melt film analyses

A simple analytical solution may be obtained by assuming linear velocity profiles in the melts corresponding to the case of constant viscosity Newtonian melts with negligible pressure gradient. The downstream velocities v_z and the x-component of the velocity due to the rotation of the shaft in film 2, v_x, are therefore

$$\left.\begin{aligned} v_{z_1} &= \left(1 - \frac{y_1}{H_1}\right) V_{sz} \\ v_{z_2} &= \left(1 - \frac{y_2}{H_2}\right) V_{sz} \end{aligned}\right\} \quad (4.5)$$

and

$$v_x = \frac{y_2}{H_2} V$$

where the velocity of the solid bed $V_{sz} = \frac{Q}{\Delta R.C}$ is assumed to be constant. It is also assumed that the solid bed does not rotate. The temperature distribution in the melt films, assuming fully developed temperature profiles, is given by

$$km \frac{d^2T}{dy^2} + \mu \left(\frac{U_r}{H}\right)^2 = 0 \qquad (4.6)$$

where U_r is the velocity of the wall relative to the melt interface and is given by

$$U_{r_1}^2 = V_{sz}^2$$

and

$$U_{r_2}^2 = V_{sz}^2 + V^2$$

with the boundary condition $T(y=0) = T_m$ and $T(y=H) = T_r$.

In general, the barrel temperature is set at a known value T_b and the assumption of good thermal contact between melt and metal leads to $T_{r_1} = T_b$. For the melt film 2 however, the temperature of the shaft is usually unknown. Martin [57] has evaluated the magnitude of heat fluxes in a problem relating heat transfer coupling effects between a dissipative fluid flow and its containing metal boundaries. Using his results, the plasticating shaft in the present extruder operating under typical conditions is most likely to behave as an insulated thermal boundary, i.e.

$$\left(\frac{dT_2}{dy_2}\right)_{y_2=H_2} = 0$$

Under these circumstances,

$$T_{r_2} = \frac{\mu_2 U_{r_2}^2}{2km} + T_m$$

If, however, the temperature of the shaft T_{shaft} is known, this can easily be incorporated in the solution by having $T_{r_2} = T_{shaft}$.

Integrating equation (4.6) with the appropriate boundary conditions,

the temperature profiles are

$$\frac{T - T_m}{T_r - T_m} = \frac{\mu U_r^2}{2km (T_r - T_m)} \left[\frac{Y}{H}\left(1 - \frac{Y}{H}\right)\right] + \frac{Y}{H} \qquad (4.7)$$

4.5.2 Solid bed profile

Whilst equation (4.3) and (4.4) can be integrated in their actual form to give the melting rates, it is more convenient to replace the mass flow rates as functions of film thicknesses in order to calculate directly the variation of the melt film thicknesses with downstream direction z.

The terms in equations (4.3) and (4.4) can now be evaluated using equations (4.5) and (4.7). The mass flow rates are

$$\left.\begin{aligned} \dot{m}_1 &= \rho_m \frac{V_{sz}}{2} H_1 C_1 \\ \text{and} \quad \dot{m}_2 &= \rho_m \frac{V_{sz}}{2} H_2 C_2 \end{aligned}\right\} \qquad (4.8)$$

where $C_1 = 2\pi (R_o - H_1/2)$ and $C_2 = 2\pi (R_i + H_2/2)$ are the local mean circumferences for each melt film. Although a mean circumference C can be used, it is possible in this simple analysis to use local mean circumferences for each phase of the material and also for each melt/solid interface without too much algebraic complexity. This helps to further reduce the error introduced by using cartesian coordinates for the cylindrical geometry.

The net heat supplied to the melt/solid interfaces for melting, neglecting any heat conducted into the solid, is evaluated using equation (4.7) which gives

$$km \left(\frac{dT}{dy}\right)_{y=0} = \frac{km\ (T_r - T_m)}{H} + \frac{\mu\ U_r^{\,2}}{2H} \qquad (4.9)$$

Substituting equations (4.8) and (4.9) into equations (4.3) and (4.4) and rearranging,

$$\left.\begin{aligned} &\frac{\rho_m\ V_{sz}\ \Delta E_1}{2km\ (T_b - T_m) + \mu_1\ U_{r_1}^{\,2}}\ \frac{dH_1}{dz} = \frac{1}{H_1} \\ \text{and}\quad &\frac{\rho_m\ V_{sz}\ \Delta E_2}{2km\ (T_{r_2} - T_m) + \mu_2\ U_{r_2}^{\,2}}\ \frac{dH_2}{dz} = \frac{1}{H_2} \end{aligned}\right\} \qquad (4.10)$$

where the enthalpy change ΔE includes the energy required to raise the temperature of the material from the bulk solid temperature $\overline{T}_s$ to the melting point, to melt the material (latent heat of fusion λ) and to raise the temperature of the newly melted material from the melting point to the bulk mean temperature of the melt film $\overline{T}$.

i.e. $$\Delta E = c_s\ (T_m - \overline{T}_s) + \lambda + c_m\ (\overline{T} - T_m) \qquad (4.11)$$

where $$\overline{T} = \frac{\int_0^H v_z\ T\ dy}{\int_0^H v_z\ dy} \qquad (4.12)$$

i.e. $$\overline{T} = \frac{(2\ T_r + T_m)}{3} + \frac{\mu\ U_r^{\,2}}{12km}$$

Equations (4.10) are integrated with the boundary conditions $H(z=0) = H_o$ to give the variation of the film thicknesses with downstream direction z. It is necessary that $H_o \neq 0$, otherwise the melting

mechanism could not operate.

The resulting equation for the film thicknesses is

$$H^2 = \frac{4z}{\Delta E \, \rho_m \, V_{sz}} \left[km \, (T_r - T_m) + \frac{\mu \, U_r^2}{2} \right] + H_o^2 \qquad (4.13)$$

i.e. the film thicknesses vary with the square root of z.

Equation (4.13) may be conveniently written in a dimensionless form as

$$X^2 = Z \, N + X_o^2 \qquad (4.14)$$

where $X = H/\Delta R$ is a dimensionless film thickness

$Z = z/\Delta R$ is a dimensionless downstream distance

$X_o = H_o/\Delta R$ is the dimensionless initial film thickness

and N is a dimensionless number expressing the ratio of the heat supplied for melting to the total enthalpy change of the material in the melting process.

i.e. $$N = \left[\frac{km(T_r - T_m)/\Delta R + \mu \, U_r^2/(2\Delta R)}{c_s(T_m - \overline{T}_s) + \lambda + c_m(\overline{T} - T_m)} \right] \frac{4}{\rho_m \, V_{sz}}$$

and contains the property data of the material, the geometry and the operating conditions.

4.5.3 Pressure losses in the melting zone

The melting zone is defined as that section of the annular channel in which melting of the material occurs. It is clear that its length varies according to operating conditions. In order to predict the pressure drop over the melting zone, it is necessary to consider a force balance on the solid bed. Figure 4.4 indicates the stresses acting on

an element of the solid material of length δz. The balance of forces acting on the element gives

$$- \frac{dp}{dz} (\Delta R - H_1 - H_2)\, 2\pi \left[R_i + H_2 + \tfrac{1}{2} (\Delta R - H_1 - H_2)\right] \delta z$$

$$= \left[\tau_1\, 2\pi\, (R_o - H_1) \;+\; \tau_2\, 2\pi\, (R_i + H_2)\right] \delta z$$

Using the velocity profiles to evaluate the shear stresses and taking the limit as $\delta z \to 0$,

$$\frac{dp}{dz} = \frac{- \mu_1 V_{sz} (R_o/H_1 - 1) - \mu_2 V_{sz} (R_i/H_2 + 1)}{(\Delta R - H_1 - H_2) \left[R_i + H_2 + \tfrac{1}{2} (\Delta R - H_1 - H_2)\right]} \qquad (4.15)$$

It is worth noting that the pressure gradient $\frac{dp}{dz}$ is always negative and the pressure will always drop along the region. The pressure drop Δp_L over a melting zone of length z_L is then obtained by integrating equation (4.15)

$$\Delta p_L = \int_0^{z_L} \frac{dp}{dz}\, dz \qquad (4.16)$$

where z_L is the solution of

$$1 = \left(\frac{N_1 z_L}{\Delta R} + X_{o_1}^2\right)^{\frac{1}{2}} + \left(\frac{N_2 z_L}{\Delta R} + X_{o_2}^2\right)^{\frac{1}{2}} \qquad (4.17)$$

4.5.4 Contribution of viscous dissipation to melting

The contribution of viscous dissipation towards melting can be expressed as a ratio of the shaft power to the total power supplied for melting. The shaft power $\dot{W}$ is given by

$$\dot{W} = 2\pi R_i V \int_0^{z_L} \mu_2 \left(\frac{dv_x}{dy_2}\right)_{y_2=H_2} dz$$

i.e. $$\dot{W} = 4\pi R_i \mu_2 V^2 \left(\frac{X_L - X_o}{N}\right)_2 \qquad (4.18)$$

and the net heat supplied to the melting zone is

$$\dot{q}_T = 2\pi km \int_0^{z_L} \left[R_o \left(\frac{dT_1}{dy_1}\right)_{y_1=H_1} + R_i \left(\frac{dT_2}{dy_2}\right)_{y_2=H_2}\right] dz$$

i.e. $$\dot{q}_T = 4\pi \left\{ R_o \left[km\,(T_b - T_m) - \frac{\mu_1 U_{r_1}^2}{2}\right] \left(\frac{X_L - X_o}{N}\right)_1 + R_i \left[km\,(T_{r_2} - T_m) - \frac{\mu_2 U_{r_2}^2}{2}\right] \left(\frac{X_L - X_o}{N}\right)_2 \right\} \qquad (4.19)$$

where X_L are the dimensionless thicknesses of the films at the end of the melting process and are obtained from equation (4.14) with $Z = z_L/\Delta R$. The total power input is therefore

$$\dot{W}_T = \dot{W} + \dot{q}_T \qquad (4.20)$$

4.5.5 Evaluation of constant viscosities

In the results presented in the following sections the material considered was a particular grade of low density polyethylene (LDPE) whose properties are presented in Table 4.1 and were originally measured by Pocklington [21]. The values for the apparent viscosity for each film were evaluated from the expression

$$\mu = \mu_o \left(\frac{\bar{\gamma}}{\gamma_o}\right)^{n-1}$$

which will be discussed in greater detail in the non-Newtonian analysis of section 4.7.1. For this material, the dependence of viscosity on temperature was small in comparison with the effects of shear rates and b has been neglected here. This was, however, included in the advanced models described later. The mean shear rates $\bar{\gamma}$ were

$$\bar{\gamma}_1 = V_{sz}/(\Delta R/4) \quad \text{and} \quad \bar{\gamma}_2 = \sqrt{V^2 + V_{sz}^2}/(\Delta R/4)$$

assuming the average thickness of each film in the melting zone to be $\Delta R/4$. The value for V_{sz} was obtained from

$$V_{sz} = \frac{Q}{\Delta R . C}$$

The dependence of the viscosity on shear rates was therefore taken into account in an overall sense.

4.5.6 Initial melt film thicknesses and solid bed temperature

In equations (4.13) there are uncertainties concerning the values of the initial melt film thicknesses H_o and the mean temperature of the solid bed used for evaluating ΔE. In general, experimental observations are a useful guide as to the likely values of H_o, whilst the mean temperature of the solid bed can only be determined by considering the complete heat transfer problem in the solid material from the moment the material is fed at room temperature into the machine. The analysis of the temperature in the solid material in chapter 3 can provide some

indications of temperatures in the solid material. Assuming that H_o is typically less than 0.5 mm, the values of H at large z become virtually unaffected by H_o in equation (4.13) and thus the choice of H_o may not be so critical.

The effect of these two variables H_o and $\overline{T}_s$ have been investigated by considering a typical operating condition - output rate 20 kg/h of LDPE, barrel temperature set at 200°C and shaft speed of 120 rpm. H_o was varied from 0.1 to 0.4 mm and $T_{room} < \overline{T}_s < T_m$. The results are presented in Table 4.2. They show that the variation of the melting zone length with the initial film thicknesses is small - cases 2, 4 and 5. The overall effect is that the larger the initial thicknesses the sooner melting reaches completion, but the differences are small. The effect on pressure drop predictions is, however, greater. Figure 4.5 shows the pressure profiles for cases 1, 3 and 5 where it can be noted that the pressure losses for cases 1 and 3 at the initial section of the melting zone are greater than for case 5. The rapid increase in pressure losses towards the end of melting is due to the presence of the term $H_s = \Delta R - H_1 - H_2$ in the denominator of the expression for $\frac{dp}{dz}$, in equation (4.15). As the material reaches its fully molten state, H_s becomes smaller and hence the very high pressure losses towards the end of melting.

The variation of the melting zone length with $\overline{T}_s$ is more significant, a change of about 25% when $\overline{T}_s$ is increased from 30 to 80°C. For the results presented below, initial melt film thicknesses of 0.1 mm and a mean solid temperature of 50°C were reasonable to use.

4.5.7 Results

The solid bed profiles for three illustrative cases have been

computed. These are plotted in Figure 4.6. The output rate for the three cases had a typical value of 20 kg/h. Graph A shows the length of the melting zone and the profile of the solid bed when both barrel temperature and the velocity of the shaft are relatively low. By increasing the barrel temperature, melting occurs quicker in the material adjacent to the barrel and melt film 1 grows quicker as shown in graph B. The overall length of the melting zone is therefore reduced and the rate of growth of melt film 2 remains as before since the conditions at the shaft have not been changed. Profile C shows the effect of increasing the shaft speed and hence of increased viscous dissipation in melt film 2. The barrel temperature is the same as case B and therefore the growth of film 1 is unchanged.

Figure 4.7 shows the temperature profiles at the end of the melting processes for the three cases. The bulk mean temperature for the melt film 1 was 137^{o}C for case A and 170^{o}C for cases B and C; and for melt film 2, 209^{o}C for case C and 130^{o}C for cases A and B.

The general effects of the operating variables, i.e. barrel temperature and shaft speed on the melting process, are summarised by the graphs of Figures 4.8 to 4.10. In Figure 4.8 the melting zone length is plotted against shaft speed with barrel temperature as a parameter. At low shaft speeds when melting occurs mainly by heat conducted from the barrel, an increase in the barrel temperature increases considerably the melting rate and therefore the melting zone length is accordingly reduced. At higher shaft speeds, change in barrel temperature hardly affects the melting zone length. At a fixed barrel temperature, increase in shaft speed results in higher overall melting rates and thus the melting zone length is reduced. In the cases considered, speeds above 300 rpm have little effect upon the overall

melting rate because further increase in viscous dissipation becomes negligible due to smaller melt viscosities in film 2. Complementary to these results are the ones shown in Figure 4.9 where the ratio of the shaft power to the total power consumption in the melting zone is plotted against the shaft speed. As expected, because the apparent viscosity of melt film 2 becomes lower at higher shaft speeds, the curve for the ratio of the shaft power to total power input tends to flatten out as shaft speed increases. At a given shaft speed, the proportion of shaft power decreases with increasing barrel temperatures. An additional effect of increasing the shaft speed is to increase the melt temperature. Figure 4.10 shows the mean temperature of the melt film 2 plotted against shaft speed. This indicates that the shaft speed can be used effectively to control stock temperature. Also shown is the shaft temperature when it behaves as an insulated boundary.

Finally, the channel length required to completely melt the material is plotted as a function of output rate for different operating conditions in Figure 4.11. The melting length is roughly proportional to output rate over a wide range for a given set of operating conditions. For the cases shown in Figure 4.11, reduction in melting zone length can be achieved more effectively by increasing the shaft speed than increasing the barrel temperature, underlying that in these conditions, melting occurs predominantly by viscous dissipation in the melt film adjacent to the shaft.

4.5.8 Discussions and conclusions

The analytical solid bed profile derived in this simple analysis was obtained from the combination of two independently growing melt films. The conditions prevailing in one film therefore did not affect the

development of the other. A fundamental error resulting from this was that by assuming linear velocity profiles in the melt films and the solid bed to move at uniform velocity a mass discontinuity occurred. This is best illustrated by considering the velocity profiles shown in Figure 4.12. Ignoring density variations between solid and molten polymer in this discussion, and considering a mean circumference for the annulus, the flow rates are proportional to the shaded areas in Figure 4.12. Thus, as melting proceeded, the analysis predicted a continuous loss of material, i.e. from diagram (i) to (ii). Clearly, if material was not to vanish, either the velocity of the solid bed must have increased or, more certainly, the velocity profiles must have been modified by the presence of a negative pressure gradient as shown in diagram (iii) of Figure 4.12.

In view of this, the model was only suitable for the initial length of the melting zone, where the films are still relatively thin. In these thin films, the presence of a pressure gradient would have not distorted significantly the linear velocity profiles and the errors in the mass conservation would have been small.

As melting proceeded, the linear velocity profiles would tend to give higher shear stresses acting on the solid bed than if a pressure gradient existed. Thus, it was anticipated that the pressure losses predicted would be on the excessive side. Also, it was pointed out previously that this model predicts excessive pressure losses in the final region of the melting zone as a result of the way in which these have been calculated - equations (4.15) and (4.16). This model was therefore not particularly suitable for predicting overall pressure losses.

The melting rates predicted by this model were also anticipated to

be excessive. There were two reasons for this. First, by ignoring any heat conducted away from the melting interface into the solid bed, the net heat available for melting was overestimated. Second, the omission of the negative pressure gradient could lead to higher temperature gradients in the melt films at the interface than if a pressure gradient existed. This again overestimates the amount of energy available for melting and hence the overall effect is that predicted melting would occur at a higher rate than in reality.

The results shown in the graphs of Figures 4.5 to 4.11 therefore cannot be considered quantitatively accurate, however, they serve to show qualitatively the general behaviour of the melting process in this type of plasticating extruder.

Clearly, a more advanced model is required if quantitative predictions are to be of any practical use. The major drawbacks in this simple analysis have been eliminated in an improved model in which pressure gradient effects were included and the solid bed was allowed to deform freely, thereby permitting its velocity to change naturally and hence to maintain mass conservation and equilibrium of forces. This model is described in the following section together with other general improvements.

4.6 Advanced Newtonian Model

In this section, the polymer melts are still assumed to behave as Newtonian fluids. The major improvements upon the previous model are, apart from the inclusion of a pressure gradient and the allowance for the solid bed velocity to vary, the improved analyses of the temperatures in the melt films and the solid bed. The temperatures are allowed to develop in the flow direction and hence more accurate melting rates

predicted.

4.6.1 Velocity and temperature analyses

The downstream velocity profiles for the combined drag and pressure flow due to a pressure gradient $P_z = \frac{dp}{dz}$ are given by

$$v_z = \frac{P_z H^2}{2\mu}\left(\frac{Y^2}{H^2} - \frac{Y}{H}\right) + V_{sz}\left(1 - \frac{Y}{H}\right) \qquad (4.21)$$

Equation (4.21) is for locally fully developed velocity profiles in flows between parallel plates. In this analysis, however, both P_z and V_{sz} will be allowed to vary with z and therefore v_z varies with z only because H, P_z and V_{sz} vary with z. The allowance for P_z and V_{sz} to vary with z makes the solution more complicated but the model becomes more versatile particularly when modifications are later introduced to allow for a tapering annular zone in which P_z and V_{sz} are very likely to vary with z.

For the melt film 2, the velocity component v_x is given as previously by

$$v_x = \frac{Y_2}{H_2} V \qquad (4.22)$$

The temperature distribution in the melt films is given by the solution of the energy conservation equation including terms for thermal convection in the downstream direction, thermal conduction through the thickness of the films and viscous dissipation

$$\text{i.e.} \qquad \rho_m c_m v_z \frac{\partial T}{\partial z} = km \frac{\partial^2 T}{\partial y^2} + \tau_{yz} \frac{dv_z}{dy} + \tau_{xy} \frac{dv_x}{dy} \qquad (4.23)$$

The improvement upon the analytical solution presented in section 4.5 is the inclusion of the convection term. Yates [58] has shown for similar

flows in screw extruder channels that downstream thermal convection is significant because of the high Peclet numbers

$$Pe = \frac{\rho_m V_{sz} H c_m}{km}$$

involved. For the present extruder, the Peclet number based on typical conditions is of the order of 20 - 300. Omission of this term would have resulted in excessive melt temperatures particularly in large extruders where Pe is of the order of 3000 - 4000.

The boundary conditions for equation (4.23) are

$$T(y=0) = T_m \text{ at any } z$$

$$T(y=H) = T_r(z) \quad \text{or} \quad \left(\frac{\partial T_2}{\partial y_2}\right)_{y_2=H_2} = 0 \text{ for film 2}$$

and $$T = T'(y) \text{ at } z = 0$$

Note that T_r may be a function of z.

The viscous dissipation terms in equation (4.23) are evaluated using the velocity profiles given by equations (4.21) and (4.22). The last term of equation (4.23) is omitted for melt film 1. The equation is rearranged as

$$v_z \frac{\partial T}{\partial z} = \alpha_m \frac{\partial^2 T}{\partial y^2} + G_v \qquad (4.24)$$

where

$$(G_v)_1 = \frac{\mu_1}{\rho_m c_m}\left[\frac{P_z}{2\mu_1}(2y_1 - H_1) - \frac{V_{sz}}{H_1}\right]^2$$

$$(G_v)_2 = \frac{\mu_2}{\rho_m c_m}\left\{\left(\frac{V}{H_2}\right)^2 + \left[\frac{P_z}{2\mu_2}(2y_2 - H_2) - \frac{V_{sz}}{H_2}\right]^2\right\}$$

and α_m is the thermal diffusivity. A simple analytical solution for this equation is not possible. It is of the parabolic type and a suitable numerical procedure of the marching type like the Crank-Nicholson method [59] is used to solve this equation. The procedure consists of replacing the partial derivatives in equation (4.24) by finite difference expressions and solving the resulting matrix equation. Given the velocity and temperature distribution at any section z, the method allows the temperature distribution at $z + \Delta z$ to be evaluated provided Δz is a suitable increment in z. By using a numerical method, the boundary temperatures could be specified as functions of z, e.g. the barrel temperature. The basic numerical procedure is outlined in Appendix B.

The temperature distribution in the solid is given by

$$\rho_s \, c_s \, V_{sz} \, \frac{\partial T_s}{\partial z} = ks \, \frac{\partial^2 T_s}{\partial y_s} \qquad (4.25)$$

with the boundary conditions

$$T_s(y_s=0) = T_m$$

$$T_s(y_s=H_s) = T_m$$

and $$T_s = T_s'(y_s) \text{ at } z = 0$$

This equation was also solved numerically by the Crank-Nicholson method. The first term in equation (4.25) accounts for the axial change in temperature as the solid bed moves downstream and the second term the heat conducted into the solid from the melting interfaces.

4.6.2 Variation of melt film thicknesses

The equations of melting will again be rearranged to give the variation of film thicknesses with z rather than the melting rates. Integrating the velocity profiles given by equations (4.21) over the thicknesses H, the mass flow rate for each film is

$$\dot{m} = \left(- \frac{H^2 P_z}{12\mu} + \frac{V_{sz}}{2} \right) H \rho_m C \qquad (4.26)$$

Substituting these into equations (4.3) and (4.4) and rearranging,

$$\left(- \frac{P_z H^2}{4\mu} + \frac{V_{sz}}{2} \right) \frac{dH}{dz} + \frac{H}{2} \frac{dV_{sz}}{dz} - \frac{H^3}{12\mu} \frac{dP_z}{dz}$$

$$= \frac{1}{\rho_m \Delta E} \left[km \left(\frac{\partial T}{\partial y} \right)_{y=0} \pm ks \left(\frac{\partial T_s}{\partial y_s} \right)_{y_s = H_s} \right] \qquad (4.27)$$

In equation (4.27), it is necessary to obtain expressions for $\frac{dV_{sz}}{dz}$ and $\frac{dP_z}{dz}$ before solving it. These are derived from an overall mass balance equation and an equation for the balance of forces on the solid bed.

4.6.3 Overall mass balance and equilibrium of forces on the solid bed

The total mass of material flowing through the channel is $\dot{M} = \dot{m}_1 + \dot{m}_2 + \dot{m}_s$ and remains constant, i.e. $\dot{M} \neq \dot{M}(z)$. Using equation (4.26) for the mass flow rates of the films and $\dot{m}_s = \rho_s H_s V_{sz} C$,

$$\dot{M} = V_{sz} C \left[\rho_m \frac{(H_1 + H_2)}{2} + H_s \rho_s \right] - \frac{\rho_m C}{12} P_z \left[\frac{H_1^3}{\mu_1} + \frac{H_2^3}{\mu_2} \right] \qquad (4.28)$$

The balance of forces on a typical solid element of length δz surrounded by melt films on both sides (Figure 4.4) gives

$$\tau_1 \, C \, \delta z \; + \; \tau_2 \, C \, \delta z \; = \; - \frac{dp}{dz} \; H_s \, C \, \delta z$$

Using the velocity profiles given by equation (4.21) to evaluate the shear stresses

$$\tau \; = \; \mu \left(\frac{dv_z}{dy} \right)_{y=0}$$

and taking the limit as $\delta z \rightarrow 0$,

$$P_z \left(H_s + \frac{H_1 + H_2}{2} \right) \; = \; - V_{sz} \left(\frac{\mu_1}{H_1} + \frac{\mu_2}{H_2} \right) \qquad (4.29)$$

Equations (4.28) and (4.29) are used to solve for P_z and V_{sz} and these can be expressed explicitly as

$$\left.\begin{aligned} V_{sz} &= V_{sz} \{H_1, H_2\} \\ \text{and} \qquad P_z &= P_z \{H_1, H_2\} \end{aligned}\right\} \qquad (4.30)$$

The full expressions are given in Table 4.3.

4.6.4 Differential equations for the film growth

Differentiating expressions (4.30) with respect to z,

$$\left.\begin{aligned} \frac{dP_z}{dz} &= f_1 \frac{dH_1}{dz} + f_2 \frac{dH_2}{dz} \\ \text{and} \qquad \frac{dV_{sz}}{dz} &= f_3 \frac{dH_1}{dz} + f_4 \frac{dH_2}{dz} \end{aligned}\right\} \qquad (4.31)$$

where f_{1-4} are expressions containing H_1 and H_2 and are presented in Table 4.3.

Substituting these expressions for

$$\frac{dP_z}{dz} \quad \text{and} \quad \frac{dV_{sz}}{dz}$$

in equations (4.27) and after some rearrangement, the following pair of simultaneous differential equations is obtained:

$$\left.\begin{aligned} F_{11}\frac{dH_1}{dz} + F_{12}\frac{dH_2}{dz} &= F_{13} \\ \text{and} \quad F_{21}\frac{dH_1}{dz} + F_{22}\frac{dH_2}{dz} &= F_{23} \end{aligned}\right\} \quad (4.32)$$

where functions F contain terms with H_1 and H_2 and are detailed in Table 4.3

Finally, from equations (4.32),

$$\frac{dH_1}{dz} \quad \text{and} \quad \frac{dH_2}{dz}$$

can be expressed explicitly and hence obtain the differential equations for the growth of the films thicknesses.

$$\left.\begin{aligned} \text{i.e.} \quad \frac{dH_1}{dz} &= \frac{F_{22}F_{13} - F_{23}F_{12}}{F_{11}F_{22} - F_{21}F_{12}} = F'_1 \\ \text{and} \quad \frac{dH_2}{dz} &= \frac{F_{11}F_{23} - F_{13}F_{21}}{F_{11}F_{22} - F_{21}F_{12}} = F'_2 \end{aligned}\right\} \quad (4.33)$$

Equations (4.33) are then numerically solved using Euler's method to give

the variation of H_1 and H_2 with z, starting with suitable initial film thicknesses, i.e. $H_1(z=0) = H_{o_1}$ and $H_2(z=0) = H_{o_2}$. The numerical method is described in Appendix B.

4.6.5 Overall energy balance

A procedure to test the accuracy of the numerical solution was to perform an overall energy balance on the melting zone. Figure 4.13 shows the energy exchanges between the control volume and its surroundings. Energy conservation requires that

Rate of work done by shaft + Rate of heat conducted to the melting zone = Rate of storage of pressure energy + Rate of storage of thermal energy.

The rate of work done by the shaft is given by

$$\dot{W} = \int_o^{z_L} \mu_2 \left(\frac{dv_x}{dy_2}\right)_{y_2=H_2} V\, C\, dz \qquad (4.34)$$

and the net rate of heat conducted from the boundaries into the melting zone is

$$\dot{q}_T = \int_o^{z_L} km \left(\frac{\partial T_1}{\partial y_1}\right)_{y_1=H_1} C\, dz + \int_o^{z_L} km \left(\frac{\partial T_2}{\partial y_2}\right)_{y_2=H_2} C\, dz \qquad (4.35)$$

The rate of storage of pressure energy is obtained from

$$E_p = \int_o^{z_L} \frac{d}{dz}(pQ)\, dz \simeq \Delta p_L\, \overline{Q} \qquad (4.36)$$

where $\overline{Q} = [(Q)_{z=0} + (Q)_{z=z_L}]/2$ is a mean volumetric flow rate of the

material through the channel. It is necessary to take an average value because the volumetric flow rate changes due to differences in the density of solid and melt. The error introduced by taking an approximate value for E_p in the energy balance equation is very small because the pressure energy term itself is very small compared with the other terms in the equation. It is typically less than 0.5% of the total power input.

The rate of storage of thermal energy is the difference between the rate of convection of thermal energy into the melting region and the rate of thermal energy flowing out of it. The rate of thermal energy convected is

$$E = \dot{m}_1 h_1 + \dot{m}_s h_s + \dot{m}_2 h_2$$

where h's are the specific enthalpies for the three phases evaluated relative to an arbitrary reference temperature $T_{ref} < \overline{T}_s$. Assuming linear relationships between enthalpy and temperature,

$$h_1 = c_m (\overline{T}_1 - T_m) + \lambda + c_s (T_m - T_{ref})$$

$$h_s = c_s (\overline{T}_s - T_{ref})$$

and $$h_2 = c_m (\overline{T}_s - T_m) + \lambda + c_s (T_m - T_{ref})$$

The rate of storage of thermal energy is

$$E_T = E_{out} - E_{in} \qquad (4.37)$$

The quantities given by equations (4.34) and (4.35) were evaluated

numerically using Simpson's rule for integration. The difference between the L.H.S. and the R.H.S. of the overall energy balance equation was expressed as a percentage of the total power input and this gave an indication of the accuracy of the numerical solution for the melting problem.

4.6.6 Computational procedure

The analysis described in the section was programmed and solved on a digital computer.

The procedure to obtain a solution consisted basically of the following steps:

1. The geometry, operating conditions (output rate, barrel temperature and shaft speed) and the material properties were specified. The apparent viscosity for each film was evaluated as described in section 4.5.5.
2. The initial melt film thicknesses were specified. These were usually very thin at the initiation of melting and typical values used were H_o = 0.0001 m.
3. Using the specifications above, P_z and V_{sz} (Table 4.3) were evaluated at the initial section and also the velocity profiles given by equations (4.21) and (4.22) were determined.
4. The initial temperature profiles in the melt films, T'(y) at z = 0 were determined by assuming them to be fully developed (i.e. solution of equation (4.23) with $\frac{\partial T}{\partial z} = 0$) for which an analytical expression is available and given in Table 4.4. A linear temperature distribution was assumed for the solid at z = 0 with the temperature in the middle at some value T_R, and

T_m at the interfaces with the melt films.

5. With the quantities so far obtained, the functions F'_1 and F'_2 in equations (4.33) were evaluated (Table 4.3) and using Euler's method on equations (4.33) H_1 and H_2 at the following step at distance Δz were calculated.

6. P_z, V_{sz} and the velocity profiles v_{z_1} and v_{z_2} were now evaluated at the new step using the thicknesses obtained in step 5.

7. The temperature profiles at the new step were also obtained by solving equations (4.24) and (4.25) using the Crank-Nicholson numerical method.

8. Functions F'_1 and F'_2 at the new step were evaluated and hence the melt film thicknesses at the following step were calculated.

9. The procedure was carried out until the sum of the thicknesses of the two melt films reached the value of ΔR.

10. Finally, all the terms in the overall energy balance described in section 4.6.5 were evaluated and, hence a check on the accuracy of the solution made. The bulk mean temperatures used in ΔE and the temperature gradients in equation (4.27) were all evaluated numerically.

The output of the computer program was a comprehensive set of results giving amongst other information, the variations of thicknesses H_1 and H_2, pressure gradient P_z and velocity of the solid bed V_{sz} with z, local velocity and temperature profile, melting rates, bulk mean temperatures, pressure profile of the melting zone (obtained from $\int_0^z P_z \, dz$), mechanical power consumption, heat conducted from the boundaries, and other secondary parameters.

4.6.7 Discussion of starting conditions and numerical method

To initiate the numerical solution, it was necessary to specify the temperature profiles in the material and also the initial film thicknesses.

Regarding the initial temperature profiles, the fully developed temperature profiles in the melt films at the start were suitable since the films were very thin here (small Peclet numbers). The initially linear temperature profile assumed for the solid was also reasonable provided that the temperature T_R in the middle of the solid ($y_s = \frac{H_s}{2}$) was at some temperature between T_m and room temperature.

Specification of the initial thicknesses of the films was, however, more critical. If the films were too thin initially, the temperature gradients in the melt films near the solid/melt interfaces were so high that exaggerated melting rates were predicted, resulting in a very fast growth of film thicknesses. The other variables also changed abruptly as a result of this. Thereafter, the computed variables changed at a fairly steady rate downstream. Taking the conditions of case B in Figure 4.6 as an example, the temperature at the first two steps, spaced at Δz = 2.5 mm apart, were 122.6 and 158.5°C in melt film 2, and the film 1 thickness grew by about three times in the first downstream step. Table 4.5(i) shows the computed values for several variables for the first few downstream steps.

Clearly, to avoid the very large change in the values of the variables it was necessary to prescribe thicker initial films. By doubling the initial thicknesses the changes in the values of the variables in the initial few sections were less abrupt - Table 4.5(ii). On the other hand, if the films were initially too thick, the net heat supplied to the solid/melt interfaces could be negative and consequently

negative melting rates were computed. This clearly was unrealistic and unacceptable - Table 4.5(iii).

By varying T_R from 30°C to 50°C, the difference in the predicted melting zone lengths was only 4.5%.

A guide to the selection of the initial thicknesses for the melt films was found in the error in the energy balance. For the example presented in Table 4.5(i), an error of 7.0% was computed. By doubling the initial film thicknesses, the error was reduced to 1.7% - Table 4.5(ii). The change in the melting zone length was only 1.5%, and 1% in the overall pressure drop.

When using the model for simulations, a trial and error method was used to estimate suitable values for the film thicknesses. It was found that not more than 2 attempts were required to select suitable values to give errors less than 5% in the energy balance equation.

Another factor that influenced the error in the numerical procedure was the selection of suitable downstream step sizes Δz and the number of steps in the y-direction for the developing temperature profiles in the films and the solid bed. Analytical procedures exist for predicting instabilities in idealised numerical techniques as a result of inadequate selection of step sizes [59], but these are not suitable for the present numerical technique.

Again, a trial and error method was used here. In general, no instability was detected and the step sizes were chosen as a compromise between computational times and accuracy required. It was found that 10 steps in the y-direction in each phase of the material and not more than 200 downstream steps were adequate for most cases. Under extreme cases the initial downstream steps were made smaller and gradually increased once the variables changed at a slower rate.

4.6.8 Results, discussions and conclusions

Results obtained with this advanced Newtonian model are presented below. Figure 4.14 shows the solid bed profile (B) predicted for an output rate of 20 kg/h with the barrel set at 200°C and a shaft speed of 120 rpm. This profile was compared with that obtained from the simple analytical solution (A). In both melt films, the advanced model predicted lower melting rates except at the initial region ($z < 20$ mm) where both models predicted about the same melting rates and hence very little difference in the solid bed profile. As discussed previously, in this region, the effects of pressure gradients on the flow are small compared with the drag flow component and therefore both analyses would predict close results. As z increases, the effect becomes more marked and hence the differences.

Figure 4.15 compares the pressure profiles predicted by the two models. Both models predicted high pressure drops initially. The advanced model thereafter predicted a fairly uniform pressure drop whilst the simple analytical model predicted exaggerated pressure losses.

The computed mean temperatures of the polymer at the end of melting were close for both models. Figure 4.16 compares the two temperature profiles at the end of melting. These are not at the same downstream position z since the models predicted different melting zone lengths. The difference between the two profiles (A and B) is small.

Thermal convection in the melt films for the present size of extruder and operating conditions had only a small effect as shown by the slight changes in $\overline{T}_1$ and $\overline{T}_2$ with z in Tables 4.5. This was because the Peclet numbers were in the range of 20 - 300 only, not insignificant, but simply not large enough to demonstrate the full effects of thermal convection. The relevant term should, however, be retained in the

analysis bearing in mind that Peclet numbers can be considerably higher in larger machines. On the other hand, the downstream variation of the solid bed temperature was more pronounced. The final 25% of the length of the solid bed was at a uniform temperature equal to T_m, having started with a mean temperature of about 70°C.

Figures 4.17 to 4.19 show some predictions for a range of conditions (full lines). Qualitatively, the general behaviour is the same as that predicted by the simple analytical model. Quantitatively, comparing Figure 4.17 with Figure 4.8 and Figure 4.19 with Figure 4.11, the melting zone lengths predicted by the simple model were shorter than the ones predicted by the advanced model as expected.

The ratios of mechanical power supplied by the shaft to the total power input differed only slightly. The advanced model predicted slightly higher values - Figures 4.18 and 4.9.

It was concluded that in general the advanced model was a better one both for predicting pressure drops and melting zone lengths.

The velocity of the solid bed changed only slightly. The difference between the highest and the lowest velocites attained was only 7%, and therefore the difference between the two models were mainly due to the effects of pressure gradient in the melt films and the improved thermal analyses. In spite of this small variation in the solid bed velocity and hence its negligible effects on the predictions, the analysis was maintained in the present form so that when modified for tapered channels it could easily allow for large changes in the solid bed velocity.

Since a modification of the linear velocity profiles in the simple analysis by the action of a pressure gradient could result in considerable differences between the predictions by the two models, it was decided to analyse other important factors which could affect

significantly the velocity profiles. These were the non-Newtonian characteristic of polymer melts and the dependence of their viscosity on temperature. The effect of these on the melting performance was investigated in a more comprehensive model described in the following section.

4.7 Advanced Non-Newtonian Model

4.7.1 Power-law polymer melt

The major improvement of this analysis over the previous one described in section 4.6 is the use of a more realistic rheological model for the melt films. In particular, the polymer melt is assumed to behave as a non-Newtonian fluid.

Several non-Newtonian constitutive equations relating shear stresses to shear rates have been proposed and used in the literature. A discussion of the relative merits of each is outside the scope of the present work but valuable discussions on rheological models can be found in Fredrickson [60] and Lodge [61].

In most literature and work on flows of polymer melts, the power-law model is the most favoured one. The main reasons for its wide usage are that the model describes fairly accurately the behaviour of most polymer melts and that only a few constants are required to characterise the non-Newtonian behaviour of the fluid, and these can be obtained comparatively easily in the laboratory. For these reasons this model was used in the present analysis apart from the fact that it was also mathematically simpler to handle.

In effect, the power-law model states that

$$\mu = \mu_o \left| \frac{\sqrt{4I_2}}{\gamma_o} \right|^{n-1} \qquad (4.38)$$

where I_2 is the second invariant of the rate of strain tensor and in the present problem

$$4I_2 = \left(\frac{dv_z}{dy}\right)^2 + \left(\frac{dv_x}{dy}\right)^2$$

For simple one-dimensional flows, $\sqrt{4I_2}$ is the local shear rate.

In general, the apparent viscosity of polymer melts varies also with temperature and equation (4.38) was modified to include this effect [4]

i.e. $$\mu = \mu_o \left|\frac{\sqrt{4I_2}}{\gamma_o}\right|^{n-1} \exp\left[-b\,(T - T_o)\right] \qquad (4.39)$$

The constant μ_o, n and b can be determined experimentally by a series of viscometric tests on a standard capillary rheometer at different flow rates and a range of temperatures, and curve fitting of the results to equation (4.39) [4]. For convenience, γ_o is usually chosen to be 1 s^{-1}.

4.7.2 Melt film analyses

The relevant equations of motion for the flow behaviour of the melt films are

$$\frac{d}{dy}(\tau_{xy}) = \frac{d}{dy}\left(\mu \frac{dv_x}{dy}\right) = 0 \qquad (4.40)$$

and $$\frac{d}{dy}(\tau_{yz}) = \frac{d}{dy}\left(\mu \frac{dv_z}{dy}\right) = \frac{dp}{dz} = P_z \qquad (4.41)$$

with the boundary conditions

$$v_x\,(y=0) = 0 \qquad \text{and} \qquad v_z\,(y=0) = V_{sz}$$
$$v_x\,(y=H) = V \qquad\qquad v_z\,(y=H) = 0$$

and μ given by equation (4.39). The energy conservation equation is the

same as the one used in the previous section 4.6, i.e. equation (4.23) with the same boundary conditions.

The equations of motion and the energy conservation equation are coupled in this case by the presence of T in the viscosity equation (4.39) and therefore these should be solved simultaneously. However, by using the Crank-Nicholson method for the numerical solution of the energy equation described in Appendix B, the equations are effectively uncoupled at each downstream section and they can be solved independently of each other. The physical implication of this is that velocity profiles reach the fully developed state infinitely faster than the temperature profiles. This is reasonable in the present analysis in view of the possible large Peclet numbers associated with the flow of the melt films. Thus, as long as the temperatures are known at any downstream section, these can be substituted into equation (4.39) and hence the momentum equations (4.40) and (4.41) solved independently of the energy equation.

The procedure adopted for solving the momentum equations was based on one developed previously for studies of polymer melt flows in annular channels [62]. The procedure was modified for the present analysis where the boundary conditions are different, and in addition, the solutions have also to satisfy a force balance on the solid bed and to maintain overall mass continuity.

The equations of motion (4.40) and (4.41) are non-dimensionalised using the following variables:

$$\left.\begin{aligned} W &= \frac{v_z}{V_{sz}}\ , \quad \pi_P = \frac{P_z H}{\bar{\tau}}\ , \quad Y = \frac{y}{H} \\ U &= \frac{v_x}{V_{sz}} \quad \text{and} \quad T^* = b\,(T - T_m) \end{aligned}\right\} \qquad (4.42)$$

where $\bar{\tau}$ is the shear stress evaluated at $T = T_m$ and at a mean shear rate V_{sz}/H.

Equations (4.40) and (4.41) become, after some rearrangement,

$$\frac{dW}{dY} = \pi_p (Y - Y_o) G \qquad (4.43)$$

$$\frac{dU}{dY} = \Phi G \qquad (4.44)$$

where Y_o is the distance of the stress neutral surface, i.e. $\frac{dW}{dY} = 0$ at Y_o

Φ is a constant independent of Y

and $$G = G\{Y\} = \left\{\left[\pi_p (Y - Y_o)\right]^2 + \Phi^2\right\}^{\frac{1-n}{2n}} \exp\left(\frac{T^*}{n}\right) \qquad (4.45)$$

Equation (4.43) is integrated with the boundary conditions W(Y=0) = 1 and W(Y=1) = 0 to give the dimensionless velocity profile as

$$W = \pi_p \int_o^Y (\alpha_v - Y_o) G\{\alpha_v\} d\alpha_v + 1 \qquad (4.46)$$

and also $$0 = 1 + \pi_p (J_1 - Y_o J_o) \qquad (4.47)$$

and equation (4.44) is integrated with the boundary conditions U(Y=1) = V/V_{sz} and U(Y=0) = 0 to give

$$U = \Phi \int_o^Y G\{\alpha_v\} d\alpha_v \qquad (4.48)$$

and $$\frac{V}{V_{sz}} = \Phi J_o \qquad (4.49)$$

where $$J_m = \int_o^1 \alpha_v^m G\{\alpha\} d\alpha_v \qquad (4.50)$$

and α_v is a dummy variable used in the integrations.

The local dimensionless volumetric flow rate π_Q is obtained from

$$\pi_Q = \int_0^1 W \, dY$$

i.e. $$\pi_Q = 1 + \pi_P \left[(1 + Y_o) J_1 - J_2 - Y_o J_o\right] \qquad (4.51)$$

For melt film 1, equation (4.40) is modified with $v_x = 0$ or $U = \Phi = 0$ in equations (4.44), (4.45), (4.48) and (4.49). Equations (4.47), (4.49) and (4.51) can now be written for each film individually and the resulting five equations are obtained:

$$\left.\begin{aligned} 0 &= 1 + \pi_{P_1} \left[(J_1)_1 - Y_{o_1} (J_o)_1\right] \\ 0 &= 1 + \pi_{P_2} \left[(J_1)_2 - Y_{o_2} (J_o)_2\right] \\ \frac{V}{V_{sz}} &= \Phi (J_o)_2 \\ \pi_{Q_1} &= 1 + \pi_{P_1} \left[(1 + Y_{o_1})(J_1)_1 - (J_2)_1 - Y_{o_1} (J_o)_1\right] \end{aligned}\right\} \qquad (4.52)$$

and $$\pi_{Q_2} = 1 + \pi_{P_2} \left[(1 + Y_{o_2})(J_1)_2 - (J_2)_2 - Y_{o_2} (J_o)_2\right]$$

If the local temperature profile is known, the five unknowns π_{P_1}, π_{P_2}, Y_{o_1}, Y_{o_2} and Φ which constitute the solution for the flow analysis can be obtained from equations (4.52) given the dimensionless volumetric flow rates π_{Q_1} and π_{Q_2}.

4.7.3 Equations for melt film thicknesses

There are, however, additional conditions which the solution must satisfy. These are that the pressure gradient must be the same in both films at the same position z and that the forces acting on the solid bed should balance. The former results in, using definitions (4.42),

$$\frac{\pi_{P_1}}{\pi_{P_2}} = \left(\frac{H_1}{H_2}\right)^{n+1} \qquad (4.53)$$

and the latter in

$$(\Delta R - H_1 - H_2) + H_1 Y_{o_1} + H_2 Y_{o_2} = 0 \qquad (4.54)$$

Apparently, there are seven equations, (4.52), (4.53) and (4.54) and only five unknowns. This is not so, however, because in equations (4.53) and (4.54) the films thicknesses are introduced and the solution is such that the flow rates and H_1 and H_2 must be compatible and satisfy the seven equations. In other words, given the flow rates, H_1 and H_2 are also unknowns in the problem. Equations (4.53) and (4.54) are used to eliminate π_{P_2} and Y_{o_2} from the other five equations (4.52) and the mathematical statement of the problem is reduced back to five equations with the following unknowns: π_{P_1}, Y_{o_1}, Φ, H_1 and H_2. Using $\dot{m}_s = \rho_s C H_s V_{sz}$ and $\pi_Q = \dot{m}/\rho_m C H V_{sz}$, the dimensionless volumetric flow rates π_Q can be replaced and the resulting equations are:

$$0 = F_1 = 1 + \pi_{P_1}\left[(J_1)_1 - (J_o)_1 Y_{o_1}\right]$$

$$0 = F_2 = 1 + \pi_{P_2}\left(\frac{H_2}{H_1}\right)^{n+1}\left[(J_1)_2 - \frac{(J_o)_2(H_s + H_1 Y_{o_1})}{H_2}\right]$$

$$0 = F_3 = \Phi - \frac{V C \rho_s H_s}{(J_o)_2 \dot{m}_s} \qquad (4.55)$$

$$0 = F_4 = \frac{\dot{m}_1}{\dot{m}_s}\frac{\rho_s}{\rho_m}\frac{H_s}{H_1} - 1 - \pi_{P_1}\left[(1 + Y_{o_1})(J_1)_1 - (J_2)_1 - Y_{o_1}(J_o)_1\right]$$

$$0 = F_5 = \frac{\dot{m}_2}{\dot{m}_s}\frac{\rho_s}{\rho_m}\frac{H_s}{H_2} - 1 - \pi_{P_1}\left(\frac{H_2}{H_1}\right)^{n+1}\left\{(J_1)_2 - (J_2)_2 + \left[(J_o)_2 - (J_1)_2\right]\frac{H_s + H_1 Y_{o_1}}{H_2}\right\}$$

Whilst in the previous Newtonian analysis the flow rates could be easily expressed in terms of the film thicknesses and then replaced in equations (4.3) and (4.4) to obtain the variation of H with z directly, here it is not possible to express $\dot{m}_1$ and $\dot{m}_2$ explicitly as functions of H_1 and H_2 because of the nature of equations (4.55). Equations (4.3) and (4.4) are therefore used in their actual form. Thus, given $\dot{m}_1$, $\dot{m}_2$ and $\dot{M}$ (hence $\dot{m}_s = \dot{M} - \dot{m}_1 - \dot{m}_2$), the required five parameters are the solutions of

$$F_i\{x_i\} = 0 \quad \text{for } i = 1 \text{ to } 5 \qquad (4.56)$$

where $x_1 = \pi_{P_1}$, $x_2 = Y_{o_1}$, $x_3 = \Phi$, $x_4 = H_1/\Delta R$ and $x_5 = H_2/\Delta R$.

Equations (4.56) were solved numerically using a Newton-Raphson

iterative method as described in Appendix B. This method required initial guessed values for x_i. To start the iterative process at z = 0, Newtonian results were used to provide the initial estimates - Table 4.6. Thereafter, the results obtained at the preceding step were used as initial values for x_i at the following step.

4.7.4 Initiation of the numerical solution

Unlike the advanced Newtonian analysis, the numerical method used here was more complicated. It posed particular problems in starting the computational cycle.

The solution for the velocity profiles in the melt films at each downstream position required the specification of the local flow rates of the melt. It was, however, easier at the start to estimate the thicknesses of the films rather than the flow rates in each film. Thus, given estimates for H_{o_1} and H_{o_2}, and also the overall flow rate of material an estimated velocity for the solid bed was obtained assuming linear velocity profiles. This solid bed velocity was used only to evaluate the local shear rates and hence to obtain the apparent viscosity for each film as in 4.5.5. The pressure gradient and an improved solid bed velocity were then obtained using the advanced Newtonian analysis (Table 4.3). The local flow rates $\dot{m}_1$ and $\dot{m}_2$ at the start were then evaluated using equation (4.26). These were then used as the initial values to start the numerical integration of equations (4.3) and (4.4).

Also, with developing temperature profiles, it was necessary to specify an initial temperature profile in the material. For the melt films, the temperature profiles specified were those for the fully developed Newtonian case - Table 4.4 - and for the solid, a linear

profile as the one assumed in section 4.6.6 was used. In this analysis, however, the thicknesses of the films at the start are not known. The values taken for H in the equations of Table 4.4 were therefore the estimated ones and it was assumed that the actual profile was geometrically similar to the specified one provided that the estimated film thicknesses did not differ very much from the computed ones at the start.

Once these initial conditions were specified, the numerical procedure proceeded as described below.

4.7.5 Computational procedure

A suitable computer program was written to solve the non-Newtonian melting problem. The procedure consisted essentially of the following steps:

1. The geometry, operating conditions and the material properties were specified.
2. Suitable step sizes in the numerical methods were selected.
3. The starting conditions were obtained as described above.
4. The initial estimates for the variables x_i in equations (4.56) were set.
5. The variables x_i were obtained by the Newton-Raphson iterative method.
6. The relevant local parameters, e.g. pressure gradient, shear stresses, bulk mean temperatures, temperature gradients, etc., were evaluated.
7. The temperature profiles at the following downstream position were evaluated by the method described in Appendix B for the

energy conservation equation.

[Note: The mean step size $\overline{\Delta y}$ (Appendix B) in this case could not be used since the film thicknesses at the following step were not known yet. Instead the local Δy was used. This was acceptable since H did not change abruptly.]

8. The mass flow rates at the following downstream position were evaluated by integrating numerically equations (4.3) and (4.4).

9. Having obtained the flow rates at the following position, steps 4 to 8 were repeated and the solution marched out until melting was completed, i.e. $H_1 + H_2 = \Delta R$.

10. The terms in the overall energy balance were evaluated and a check on the accuracy of the solution was made. Other secondary parameters were also evaluated.

This computational procedure was very similar to the one used in the advanced Newtonian analysis. The previous discussion on step sizes Δz, Δy and about the numerical method in general is therefore applicable here. The major difference was the application of an iterative technique to solve the melt flow equations at each downstream position.

The initial estimates for the iterations, obtained from considerations of Newtonian melt films - Table 4.6 - were found in general to be satisfactory. Convergence occurred in all cases tested without serious difficulties. Usually at the start, the number of iterations required was larger than for the solution at following downstream positions. However, less than 10 iterations were required for the values of the variables x_i to converge within a tolerance of 0.001%, i.e. the largest change in any of the five variables at two consecutive iterations was less than 0.001%. Thereafter, using the results at the previous section

as initial estimates of x_i at the new section, less than four iterations were required to achieve the same degree of convergence.

The errors in the overall energy balance were of the same order as those for the advanced Newtonian analysis.

4.7.6 Results and discussion

Results for the typical case of output rate of 20 kg/h of LDPE with the barrel temperature at 200°C and a shaft speed of 120 rpm obtained with this model were compared with those obtained from the previous model.

It is worth remembering in the following discussion that in the advanced Newtonian model mean values for the apparent viscosities were used for each film and these were assumed to remain constant throughout the films.

In Figure 4.14 the solid bed profiles are plotted and compared (B and D). The non-Newtonian model predicted a slightly longer profile, a difference of about 4%. Confining attention to melt film 2 where considerable shear rates are imparted by the rotating shaft, initially the melting rates are lower for the non-Newtonian model than for the advanced Newtonian model. This was because the mean viscosity was lower due to high shear rates in the very thin films at the start and hence less heat was generated by viscous dissipation in the non-Newtonian model. Thus, the film thickness grows at a slower rate. As the film thickness increases, the shear rate imposed by the shaft reduces and the viscosity increases. The amount of heat generated is consequently higher in this model than for the advanced Newtonian model and hence higher melting rates are predicted. Thus, in Figure 4.14 the melting interfaces 2 for the two models cross each other.

In melt film 1, however, this behaviour does not occur because the

effect of shear rates on viscosity and hence viscous dissipation are not as pronounced since there are no transverse shear rates. The non-Newtonian model predicted lower melting rates throughout. Full explanation for this is not possible without analysing in detail the changes introduced by the shear rate and temperature dependence of viscosity to the local velocity and temperature profiles and bulk mean temperatures, the combination of all these factors leading to slightly lower melting rates. Note that the initial film thicknesses for the different models are not the same. This was the result of the method used for initiating the non-Newtonian solution as described in section 4.7.4.

In Figure 4.15 the pressure profiles are plotted and compared. The non-Newtonian model predicted lower pressure losses. The reason for this was that at the start of melting, shear stresses adjacent to the melting interfaces used for calculating pressure gradients were lower in this model due to lower viscosities. Therefore the pressure drop in the initial region was not so high in this model. Thereafter, the pressure gradients are roughly the same, i.e. the two lines are nearly parallel in Figure 4.15. Thus, the difference between the two pressure profiles is attributed mainly to the quick change in the pressure gradients predicted by the advanced Newtonian analysis due to unrealistic high viscosities for the initially thin melt films. Since the melting process initiates gradually it is likely that no such large changes occur initially and hence the non-Newtonian results which exhibit a smaller change initially should be more reliable.

Figure 4.16 shows the melt temperature profiles at the end of melting. These are not at the same axial position since completion of melting occurs at different positions in the different models. The

non-Newtonian model predicted slightly higher bulk mean temperatures for each melt film. This was more in evidence in melt film 2 where viscous dissipation was more significant.

General results for the non-Newtonian model are also plotted in the graphs of Figures 4.17 to 4.19. In Figure 4.17, at low shaft speeds both models predicted about the same melting zone lengths. The difference between the results corresponding to each barrel temperature setting becomes increasingly larger at higher shaft speeds. This behaviour is attributed to the non-Newtonian character of the melts and also to the temperature effects on viscosity which are more pronounced at higher shaft speeds. Similarly, the shaft power to the total power input ratio also showed differences. Figure 4.18 shows that again the differences become larger at higher shaft speeds. The same effect is reflected on the graphs of Figure 4.19 where the non-Newtonian melting model predicted longer melting zones than the advanced Newtonian model, the discrepancies again being larger for curves C and D than for A and B corresponding respectively to a high and a low shaft speed.

Because the two models were similar except for the dependence of viscosity on shear rates and temperature, and since the Newtonian model took account of the dependence of viscosity on shear rates already in an overall sense, the discrepancies between the two models could be mainly attributed to the dependence of viscosity on temperature. The viscosities for the Newtonian models were evaluated as indicated in section 4.5.5 and it took no account of its dependence on the temperature whilst in the non-Newtonian analysis this was included in equation (4.39) where the apparent viscosity varied exponentially with temperature.

The viscosities evaluated with the expression in section 4.5.5 are strictly valid only if the mean melt temperature is $\overline{T} = T_o$. Thus, if

the local melt temperature was above T_o, the values used for the viscosities in the Newtonian models were overestimated and hence both mechanical power consumption and melting rates predicted were excessive. The opposite occurring when the temperatures were below T_o.

In view of this, the advanced Newtonian melting model was modified to include some means of correcting for this. Instead of using the expression in section 4.5.5, the viscosities were evaluated from

$$\mu_1 = \mu_o (\bar{\gamma}_1)^{n-1} \exp\left[-b\left(\frac{T_b + T_m}{2} - T_o\right)\right] \qquad (4.57)$$

and

$$\mu_2 = \mu_o (\bar{\gamma}_2)^{n-1} \exp\left[-b\left(\frac{T_{shaft} + T_m}{2} - T_o\right)\right] \qquad (4.58)$$

thus introducing some degree of dependence of apparent viscosities on algebraic mean temperatures.

In equation (4.58), however, T_{shaft} is not known when the shaft behaves as an insulated boundary. For the purposes of evaluating the viscosity at a mean temperature, an estimate given by

$$T_{shaft} = \mu_2 \frac{U_{r_2}^2}{2km} + T_m \qquad (4.59)$$

was adequate.

A systematic trial and error method was used to select the correct value of T_{shaft} to satisfy both equations (4.58) and (4.59). Starting with an estimated value for T_{shaft}, μ_2 was evaluated from equation (4.58) and substituted into equation (4.59). The value of T_{shaft} thus obtained was compared with the estimated one. If necessary, a new estimate was used and the evaluations repeated until a difference of less than 1% between the estimated and the finally computed values for T_{shaft} was

achieved. In this way the viscosity for melt film 2 was obtained.

With this correction introduced into the advanced Newtonian model, results were obtained and plotted on the same graphs of Figure 4.17 to 4.19. In general, the correction proved to be effective and improved the Newtonian results considerably and these are now much closer to the more realistic non-Newtonian results.

Note that with the conditions considered for the present case studies, in Figure 4.17 the Newtonian model without the correction appears to predict better agreement with the non-Newtonian results, at low shaft speeds, than if the correction was made. This better agreement actually originates more from the errors in estimating the values for the viscosities by neglecting their dependence on temperature rather than from the superiority of the model without the correction. For if the results were extrapolated to lower shaft speeds, the discrepancies between the results would again increase whilst if the correction was included, results close to the non-Newtonian ones would still be predicted.

4.8 Conclusions

In this chapter a theoretical study of the melting process in the annular shear cell of the machine where most of the melting was expected to take place was carried out. The aim was to derive an adequate theoretical model from which the results for different operating conditions, materials and geometry could be obtained by theoretical simulations.

The melting mechanism was postulated with relatively little experimental evidence but should be the most likely one in practice.

A simple analytical solution was obtained for a model in which many unrealistic assumptions were made. It served the purpose to illustrate

qualitatively the effect of the dominant parameters on the melting process. Two other more advanced models were developed for predicting reliable quantitative results. One was based on flow of Newtonian melt films and the other one based on flow of non-Newtonian power-law type of polymer melts. On the grounds of theoretical results only, the non-Newtonian model proved to be a more reliable model, though with adequate choice of values for the mean apparent viscosities, the advanced Newtonian model predicted results close to those for the non-Newtonian model. The non-Newtonian model was clearly preferable for materials whose melts viscosities exhibited a high degree of dependence on shear rates and temperature.

The penalty for using the non-Newtonian model was the higher cost of computation. In the cases considered here, computational costs for the non-Newtonian model could be as much as five times that for the advanced Newtonian model.

Although the dependence of viscosity on temperature for the material considered was small (small b), when this was included in the advanced Newtonian model considerable improvements were obtained. Provided local quantities were not required this model could be used for predicting overall melting performance at a considerably lower cost than the non-Newtonian model.

Table 4.1

Property Data used for Simulations

Material: LDPE granules - ICI 'Alkathene' WNC71

Viscosity: $\mu = 6274 \left(\frac{\dot{\gamma}}{\dot{\gamma}_o}\right)^{-0.577} \exp\left[-0.00537\ (T - 145)\right]$ Ns/m^2

measured at $\dot{\gamma}$ = 145.7 to 1457.1 s^{-1}

and T = 140 to 150°C

$\dot{\gamma}_o$ = 1 s^{-1}

Thermal Properties: km = ks = 0.268 J/m s deg C

c_m = 2428.5 J/kg deg C

c_s = 2512.2 J/kg deg C

λ = 209.35 kJ/kg

Densities: ρ_m = 780 kg/m^3

ρ_s = 880 kg/m^3

ρ_B = 570 kg/m^3

Table 4.2

Effects of Initial Film Thicknesses and

Mean Solid Bed Temperature on the Analytical Solution

Case Number	H_{o_1} (mm)	H_{o_2} (mm)	$\bar{T}_s$ ^{o}C	N_1	N_2	Melting Zone Length (mm)
1	0.1	0.1	30.0	0.0046	0.0031	208.8
2	0.1	0.1	50.0	0.0050	0.0034	188.1
3	0.1	0.1	80.0	0.0059	0.0042	157.2
4	0.2	0.2	50.0	0.0050	0.0034	185.9
5	0.4	0.4	50.0	0.0050	0.0034	176.8

Table 4.3

Expressions Used in Section 4.6

$$V_{sz} = \dot{M}\left(H_s + \frac{H_1 + H_2}{2}\right) / D_n$$

$$P_z = -\dot{M}\left(\mu_1/H_1 + \mu_2/H_2\right) / D_n$$

$$f_1 = \frac{\dot{M}}{D_n^2}\left[D_n \frac{\mu_1}{H_1^2} + \left(\frac{\mu_1}{H_1} + \frac{\mu_2}{H_2}\right) D_1\right]$$

$$f_2 = \frac{\dot{M}}{D_n^2}\left[D_n \frac{\mu_2}{H_2^2} + \left(\frac{\mu_1}{H_1} + \frac{\mu_2}{H_2}\right) D_2\right]$$

$$f_3 = \frac{\dot{M}}{D_n^2}\left[-\frac{D_n}{2} - \left(H_s + \frac{H_1 + H_2}{2}\right) D_1\right]$$

$$f_4 = \frac{\dot{M}}{D_n^2}\left[-\frac{D_n}{2} - \left(H_s + \frac{H_1 + H_2}{2}\right) D_2\right]$$

$$F_{11} = -\frac{P_z H_1^2}{4\mu_1} - \frac{f_1 H_1^3}{12\mu_1} + \frac{V_{sz}}{2} + \frac{H_1}{2} f_3$$

$$F_{12} = -\frac{f_2 H_1^3}{12\mu_1} + \frac{H_1}{2} f_4$$

$$F_{13} = \frac{1}{\rho_m \Delta E_1} \left[km \left(\frac{\partial T_1}{\partial y_1} \right)_{y_1=0} - ks \left(\frac{\partial T_s}{\partial y_s} \right)_{y_s=H_s} \right]$$

$$F_{21} = - \frac{f_1 H_2^3}{12\mu_2} + \frac{H_2}{2} f_3$$

$$F_{22} = - \frac{P_z H_2^2}{4\mu_2} - \frac{f_2 H_2^3}{12\mu_2} + \frac{V_{sz}}{2} + \frac{H_2}{2} f_4$$

$$F_{23} = \frac{1}{\rho_m \Delta E_2} \left[km \left(\frac{\partial T_2}{\partial y_2} \right)_{y_2=0} + ks \left(\frac{\partial T_s}{\partial y_s} \right)_{y_s=0} \right]$$

where:

$$D_n = \rho_m C \left(\frac{H_1^3}{12\mu_1} + \frac{H_2^3}{12\mu_2} \right) \left(\frac{\mu_1}{H_1} + \frac{\mu_2}{H_2} \right) + C \left[\rho_m \frac{(H_1 + H_2)}{2} + H_s \rho_s \right] \left(H_s + \frac{H_1 + H_2}{2} \right)$$

$$D_1 = C \left[- \frac{\rho_m}{12} \frac{\mu_1}{H_1} \left(\frac{H_1^3}{\mu_1} + \frac{H_2^3}{\mu_2} \right) + \frac{\rho_m H_1^2}{4\mu_1} \left(\frac{\mu_1}{H_1} + \frac{\mu_2}{H_2} \right) + \frac{H_s}{2} (\rho_m - \rho_s) - \rho_s \left(H_s + \frac{H_1 + H_2}{2} \right) \right]$$

$$D_2 = C \left[- \frac{\rho_m}{12} \frac{\mu_2}{H_2} \left(\frac{H_1^3}{\mu_1} + \frac{H_2^3}{\mu_2} \right) + \frac{\rho_m H_2^2}{4\mu_2} \left(\frac{\mu_1}{H_1} + \frac{\mu_2}{H_2} \right) + \frac{H_s}{2} (\rho_m - \rho_s) - \rho_s \left(H_s + \frac{H_1 + H_2}{2} \right) \right]$$

and:

$$H_s = \Delta R - H_1 - H_2$$

Table 4.4

Fully Developed Temperature Profile for Melt Films

$$T = \frac{\mu U_r^2}{2km}\frac{y}{H}\left(1-\frac{y}{H}\right) + \frac{H^4 P_z^2}{\mu km}\left[\frac{y}{24H} - \frac{1}{8}\left(\frac{y}{H}\right)^2 + \frac{1}{6}\left(\frac{y}{H}\right)^3 - \frac{1}{12}\left(\frac{y}{H}\right)^4\right]$$

$$+ \frac{H^2 P_z V_{sz}}{km}\left[\frac{y}{6H} - \frac{1}{2}\left(\frac{y}{H}\right)^2 + \frac{1}{3}\left(\frac{y}{H}\right)^3\right] + (T_r - T_m)\frac{y}{H} + T_m$$

where $T_{r_1} = T_b$

and $T_{r_2} = \frac{\mu_2 U_{r_2}^2}{2km} + \frac{P_z^2 H_2^4}{24\mu_2 km} - \frac{P_z H_2^2 V_{sz}}{6km} + T_m$

for an insulated shaft.

Table 4.5

Effects of H_{o_1} and H_{o_2} on the Numerical Solution for the Advanced Newtonian Model

(i)

z (mm)	$H_1/\Delta R$	$H_2/\Delta R$	dp/dz ($MN/m^2/m$)	$d\dot{m}_1/dz$ (kg/h/m)	$d\dot{m}_2/dz$ (kg/h/m)	$\overline{T}_1$ (^oC)	$\overline{T}_2$ (^oC)
0.0	0.0315	0.0315	- 65.67	298.0	175.5	140.17	122.63
2.5	0.1094	0.0751	- 23.30	72.68	232.8	140.96	158.50
5.0	0.1235	0.1237	- 20.50	57.68	65.18	140.41	136.38
7.5	0.1353	0.1347	- 19.22	50.72	42.50	140.57	126.61
10.0	0.1456	0.1417	- 18.30	44.82	23.75	140.59	125.15
12.5	0.1545	0.1454	- 17.60	40.89	23.75	140.64	124.38
15.0	0.1625	0.1491	- 17.02	37.52	15.18	140.70	123.69
20.0	0.1765	0.1539	- 16.04	33.21	13.21	140.73	123.69
40.0	0.2195	0.1696	- 14.33	27.68	15.18	140.92	123.34
60.0	0.2556	0.1874	- 13.27	27.86	19.10	141.09	123.40
330.0	0.5914	0.4059	- 11.37	22.32	20.71	143.04	123.60

Error in energy balance = 7.0%; z_L = 330.0 mm; Δp_L = 4.15 MN/m^2

(ii)

z (mm)	$H_1/\Delta R$	$H_2/\Delta R$	dp/dz ($MN/m^2/m$)	$d\dot{m}_1/dz$ (kg/h/m)	$d\dot{m}_2/dz$ (kg/h/m)	$\overline{T}_1$ (^oC)	$\overline{T}_2$ (^oC)
0.0	0.0630	0.0630	- 35.15	138.2	75.54	140.28	122.79
2.5	0.0965	0.0796	- 25.14	82.86	78.75	140.48	127.18
5.0	0.1149	0.0955	- 21.90	65.18	52.50	140.48	125.63
7.5	0.1289	0.1054	- 20.14	55.53	40.89	140.55	124.52
10.0	0.1502	0.1128	- 18.95	48.75	33.04	140.59	124.06
20.0	0.1737	0.1319	- 16.47	34.82	21.96	140.72	123.48
30.0	0.1977	0.1449	- 15.23	29.64	19.28	140.83	123.37
335.0	0.5936	0.4062	- 11.40	22.32	17.86	143.06	123.60

Error in energy balance = 1.7%; z_L = 335.0 mm; Δp_L = 4.19 MN/m^2

(iii)

z (mm)	$H_1/\Delta R$	$H_2/\Delta R$	dp/dz ($MN/m^2/m$)	$d\dot{m}_1/dz$ (kg/h/m)	$d\dot{m}_2/dz$ (kg/h/m)	$\overline{T}_1$ (^oC)	$\overline{T}_2$ (^oC)
0.0	0.3150	0.3150	- 12.35	-15.71	-33.40	141.40	124.18
2.5	0.3128	0.3121	- 12.37	-15.36	-33.57	141.39	124.11
5.0	0.3106	0.3093	- 12.40	-14.11	-32.68	141.37	124.05
7.5	0.3087	0.3064	- 12.43	-11.07	-29.82	141.36	123.99
10.0	0.3071	0.3038	- 12.46	- 6.96	-25.74	141.34	123.93
20.0	0.3064	0.2967	- 12.46	7.32	-10.54	141.34	123.76
30.0	0.3127	0.2942	- 12.35	16.78	0.536	141.37	123.67
40.0	0.3233	0.2951	- 12.21	23.04	8.57	141.42	123.63
252.0	0.5789	0.4183	- 11.35	22.86	20.00	142.98	123.54

Error in energy balance = 2.9%; z_L = 252.0 mm; Δp_L = 2.94 MN/m^2

Table 4.6

Initial Estimates for the Newton-Raphson Iterative Method

$$x_1 = \pi_{P_1} = 2\frac{H_1}{\Delta R}\left(1 + \frac{\mu_1}{\mu_2}\frac{H_1}{H_2}\right) \Big/ \left(\frac{H_1}{\Delta R} + \frac{H_2}{\Delta R} - 2\right)$$

$$x_2 = Y_{o_1} = \frac{1}{2}\left[\frac{\frac{H_1}{\Delta R} + \frac{H_2}{\Delta R} - 2}{\frac{H_1}{\Delta R}\left(1 + \frac{\mu_2 H_1}{\mu_1 H_2}\right)}\right]$$

$$x_3 = \Phi = \frac{V}{V_{sz}}$$

$$x_4 = \frac{H_1}{\Delta R} = \frac{H_{o_1}}{\Delta R}$$

$$x_5 = \frac{H_2}{\Delta R} = \frac{H_{o_2}}{\Delta R}$$

An alternative improved x_3 was obtained as

$$x_3 = \Phi = \left(\frac{V}{V_{sz}}\right)^n \exp\left[-b\left(\frac{T_m + T_{r_2}}{2} - T_m\right)\right]$$

from the definition of Φ in equation (4.44) and using a mean temperature $(T_m + T_r)/2$.

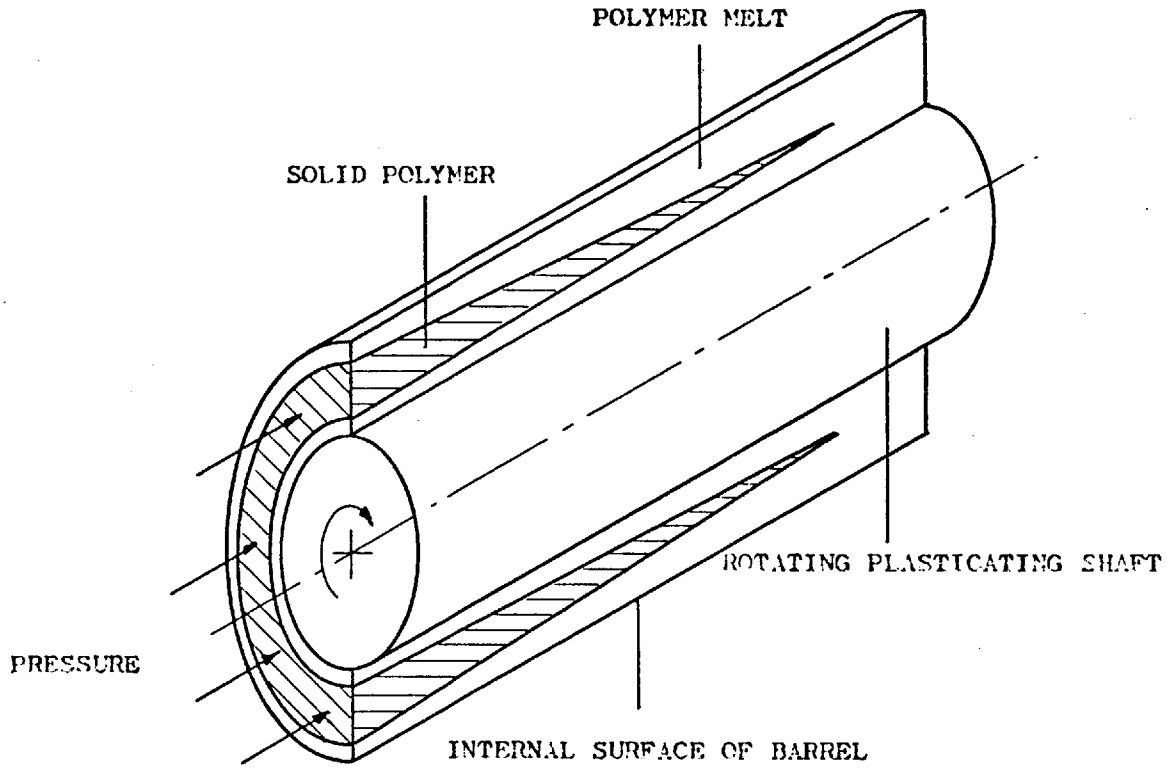

FIG. 4.1 - MELTING MECHANISM IN THE ANNULAR FLOW CHANNEL

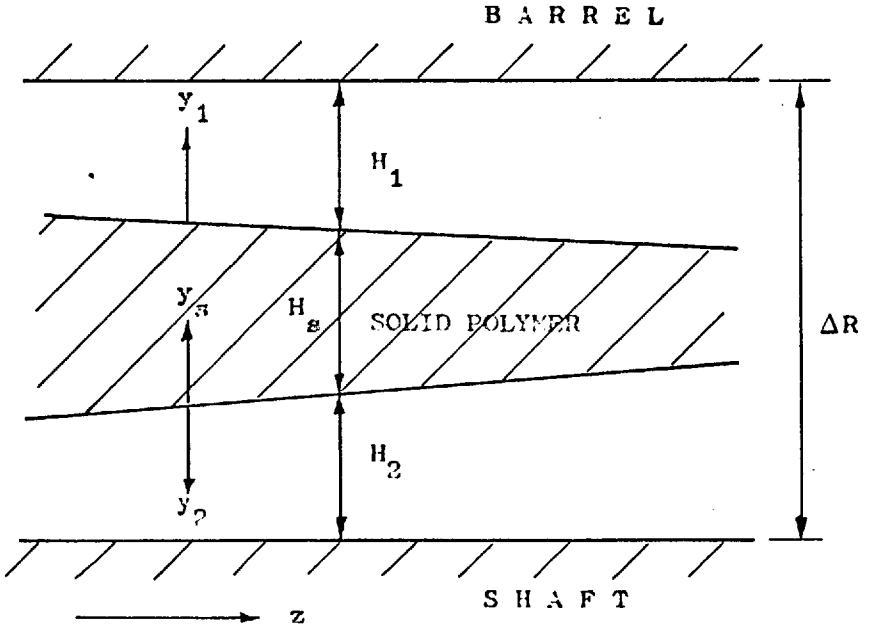

FIG. 4.2 - GEOMETRY FOR MELTING ANALYSIS

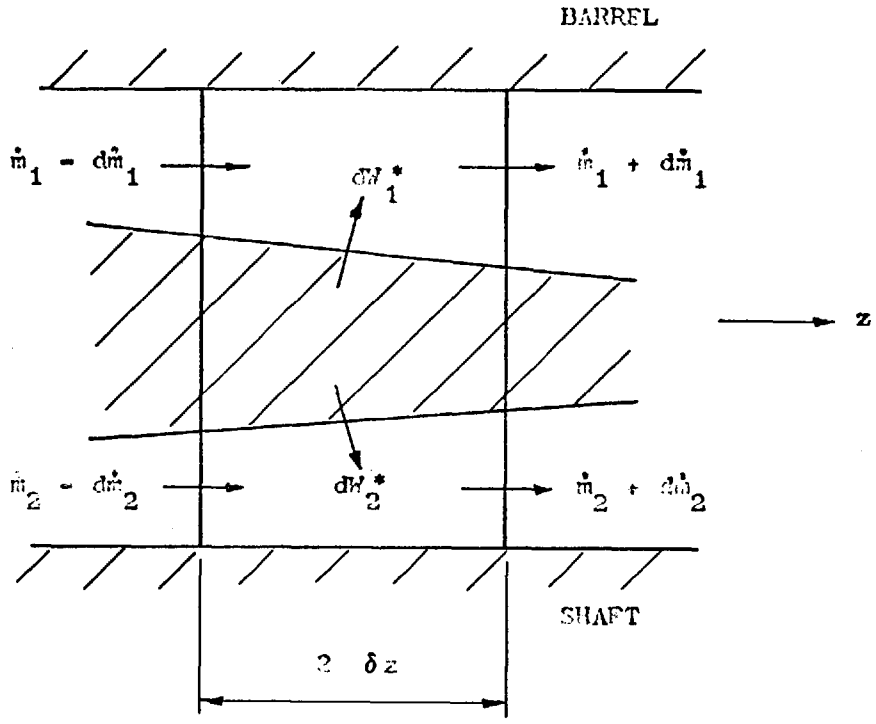

FIG. 4.3 - MASS FLOW RATES IN MELT FILMS

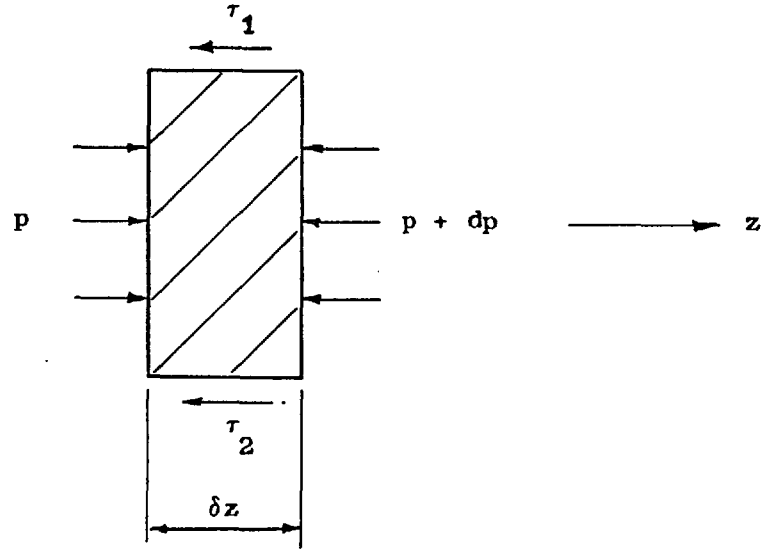

FIG. 4.4 - STRESSES ACTING ON AN ELEMENT OF SOLID MATERIAL

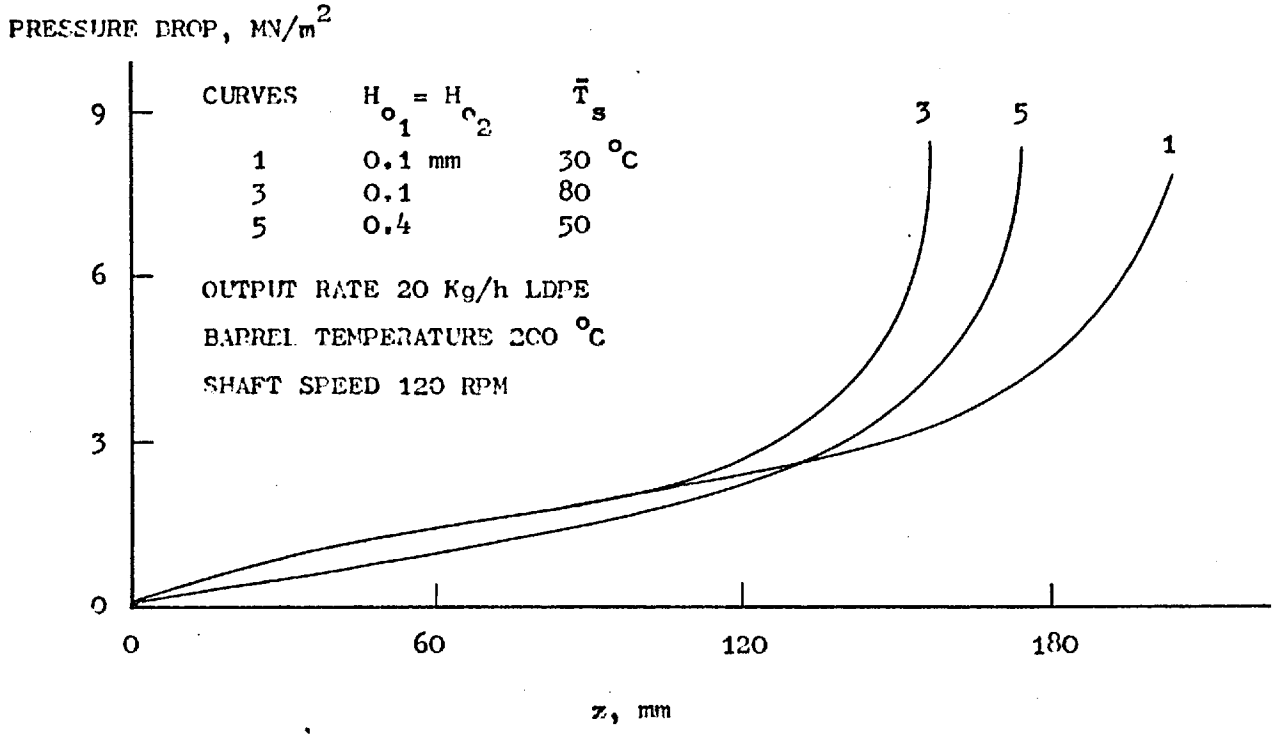

FIG. 4.5 - PRESSURE PROFILES

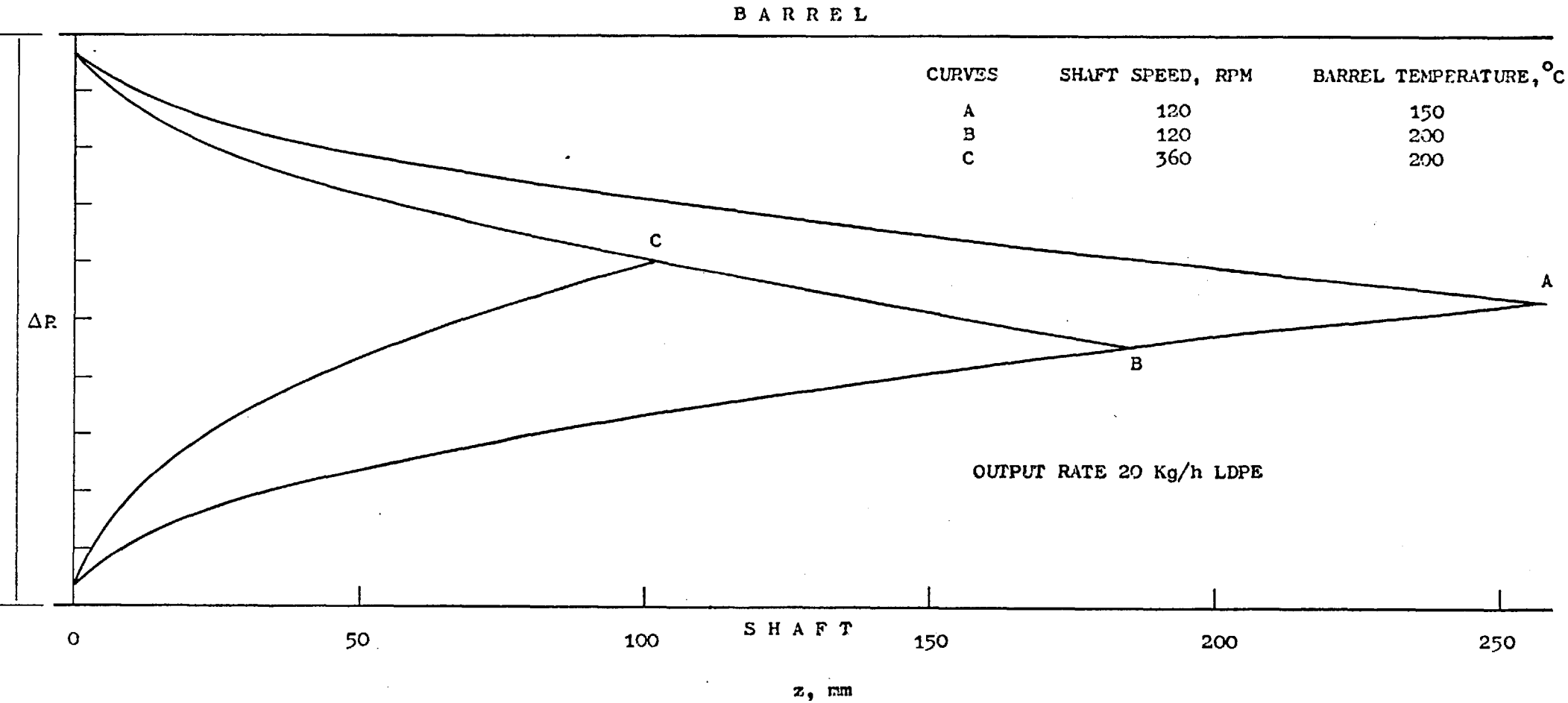

FIG. 4.6 - SOLID BED PROFILES

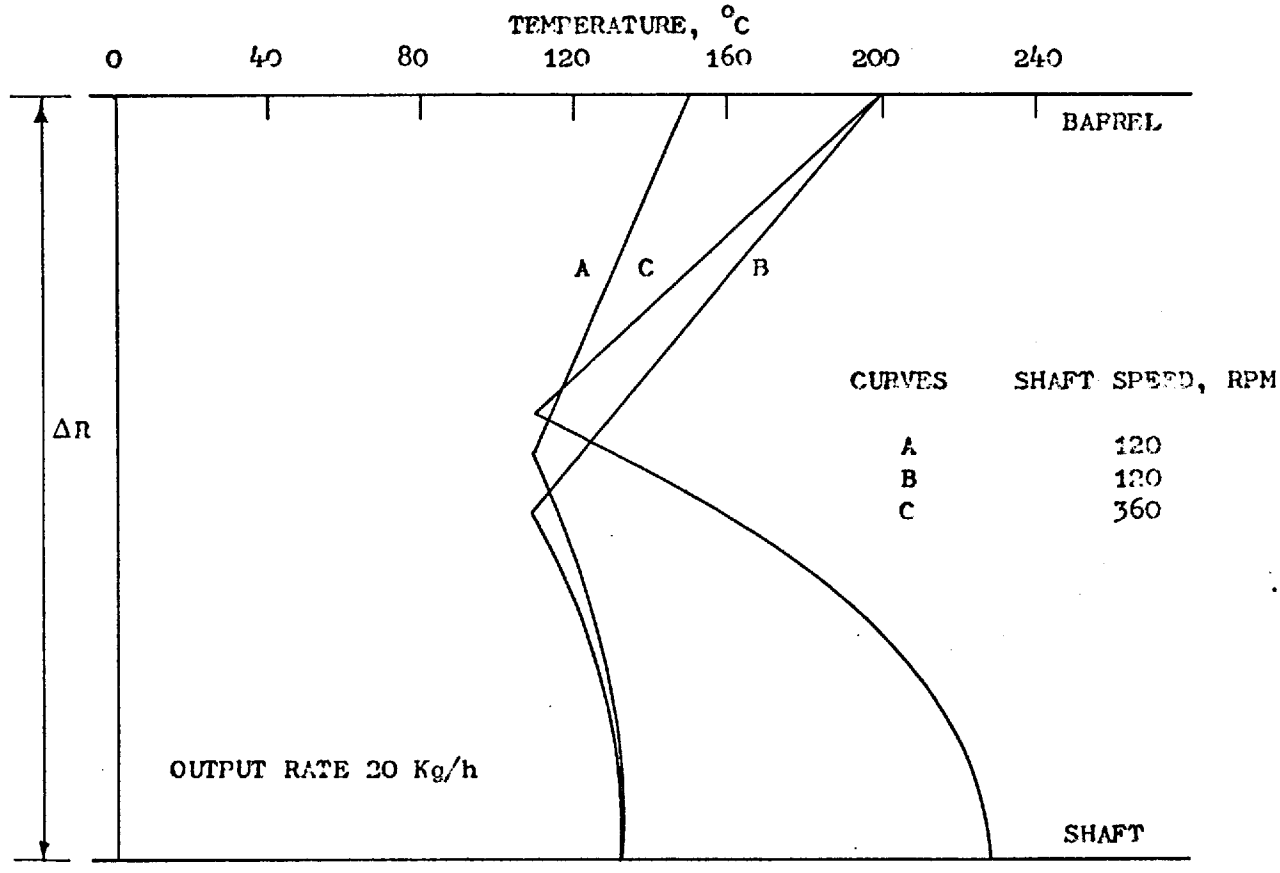

FIG. 4.7 - TEMPERATURE PROFILES AT COMPLETION OF MELTING

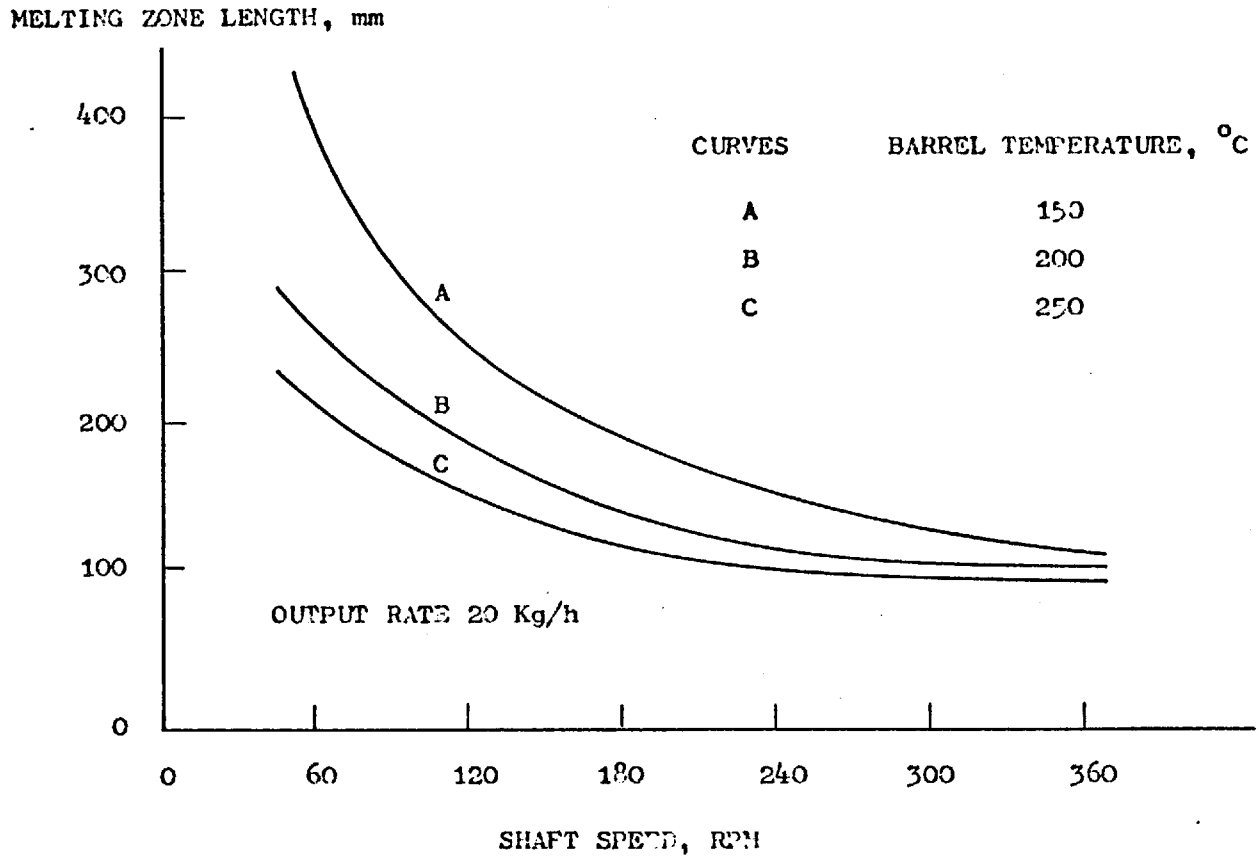

FIG. 4.8 - MELTING ZONE LENGTH PLOTTED AGAINST SHAFT SPEED

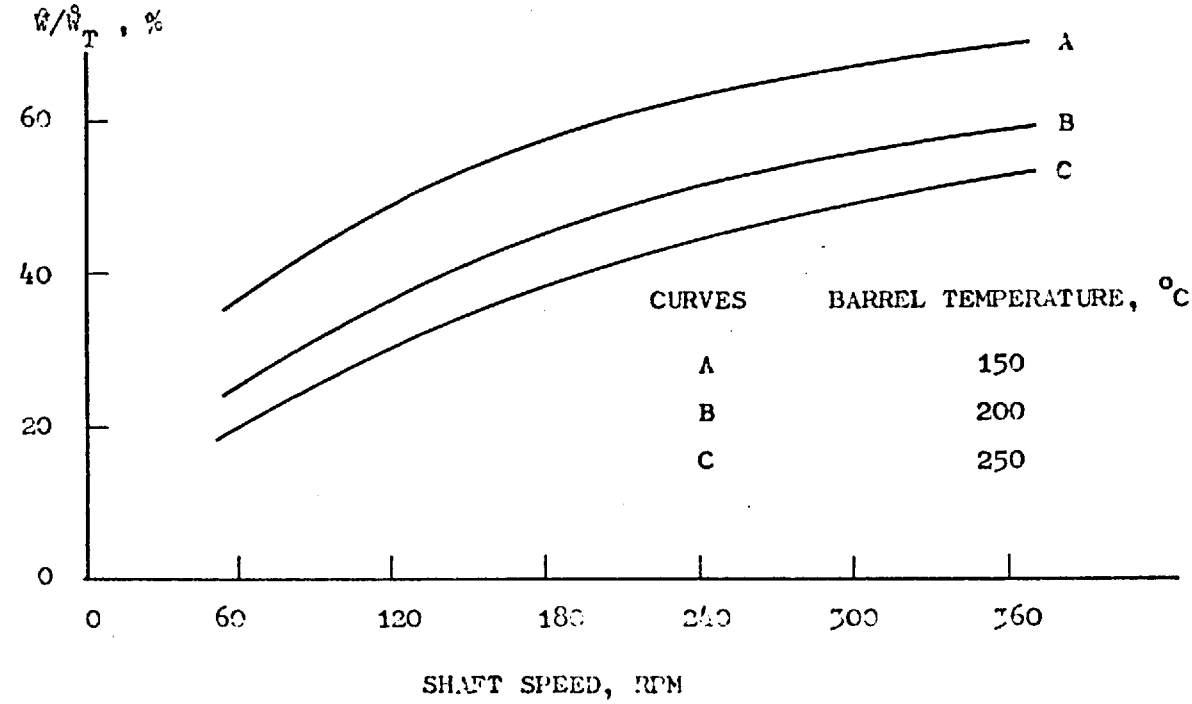

FIG. 4.9 - RATIO OF MECHANICAL POWER TO TOTAL POWER CONSUMPTION IN THE MELTING ZONE PLOTTED AGAINST SHAFT SPEED

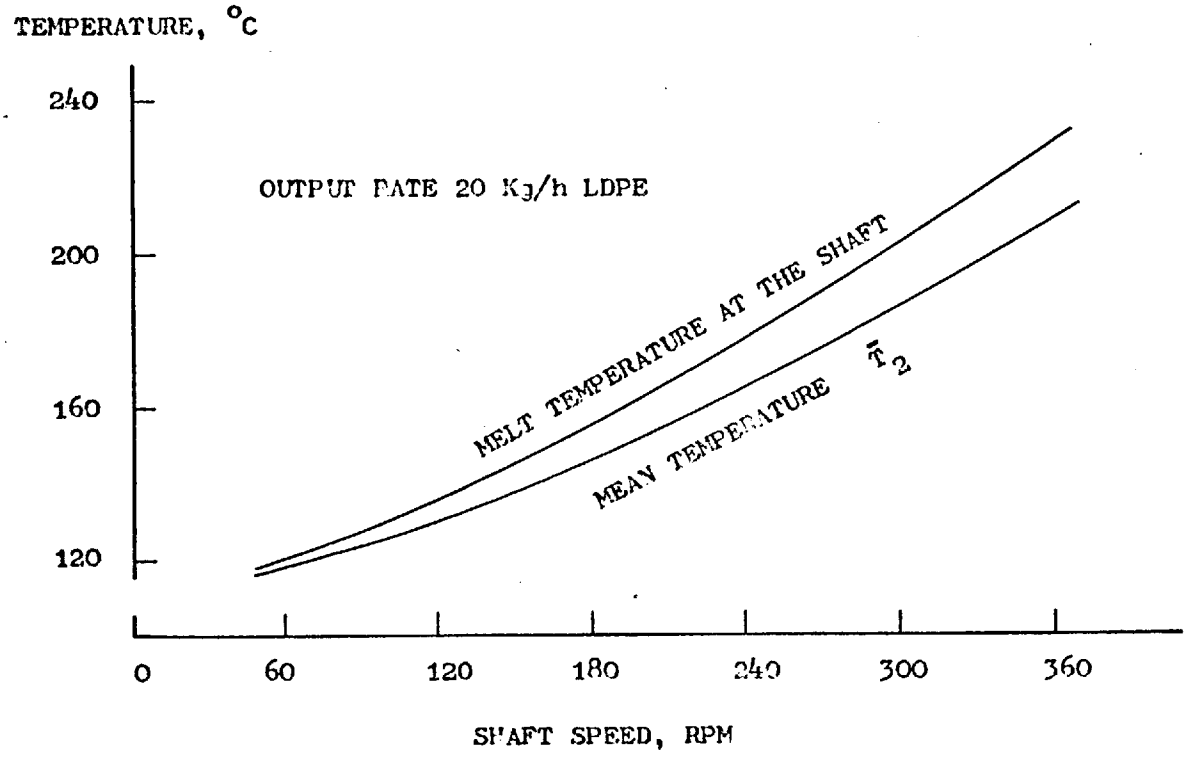

FIG. 4.10 - VARIATION OF MELT TEMPERATURES WITH SHAFT SPEED

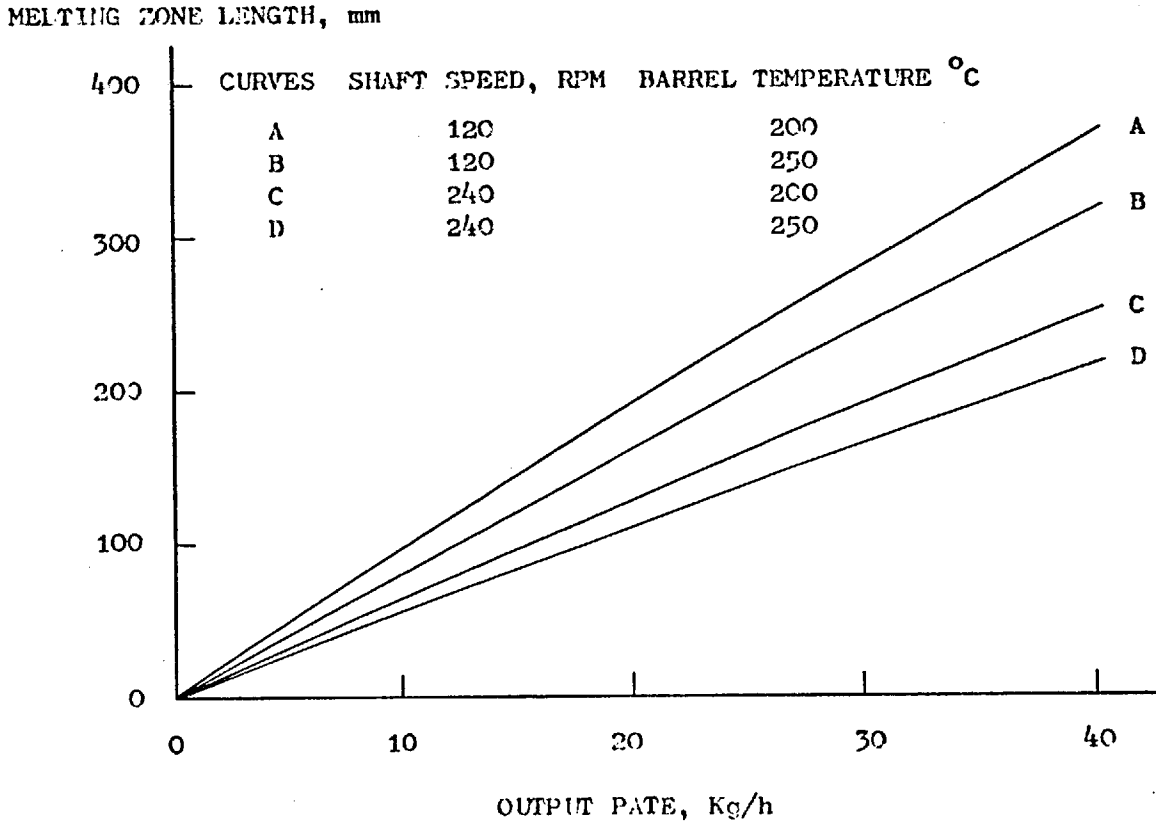

FIG. 4.11 - VARIATION OF MELTING ZONE LENGTH WITH OUTPUT RATE FOR A RANGE OF OPERATING CONDITIONS

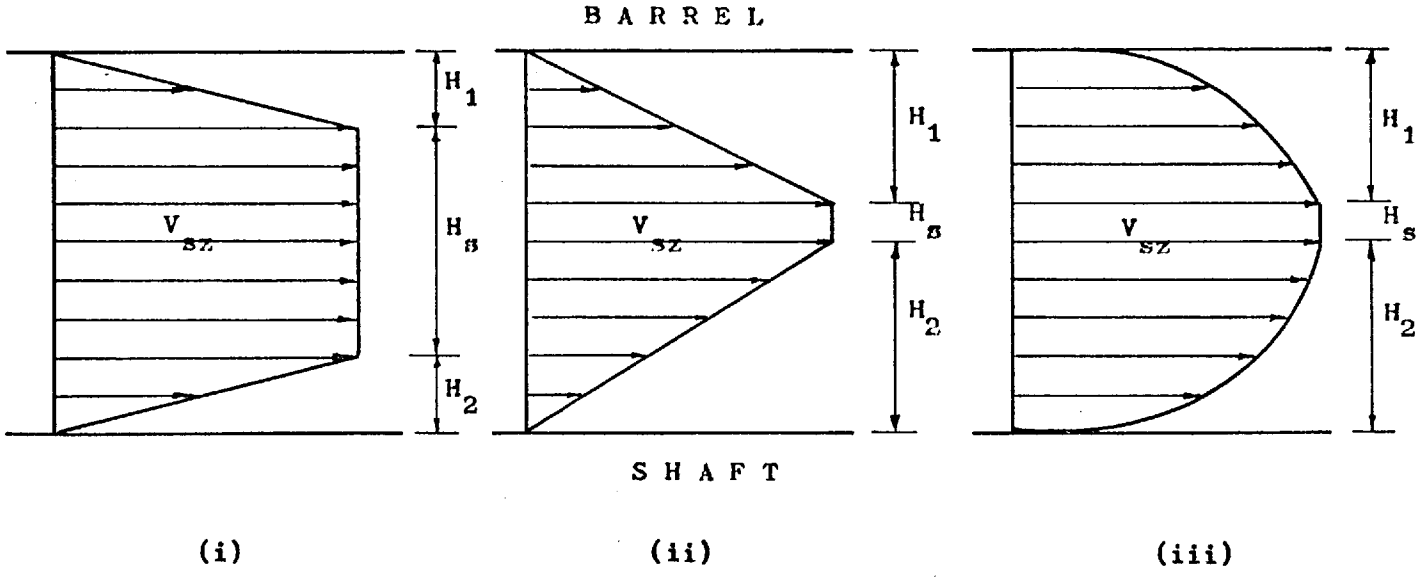

FIG. 4.12 - DOWNSTREAM VELOCITY PROFILES

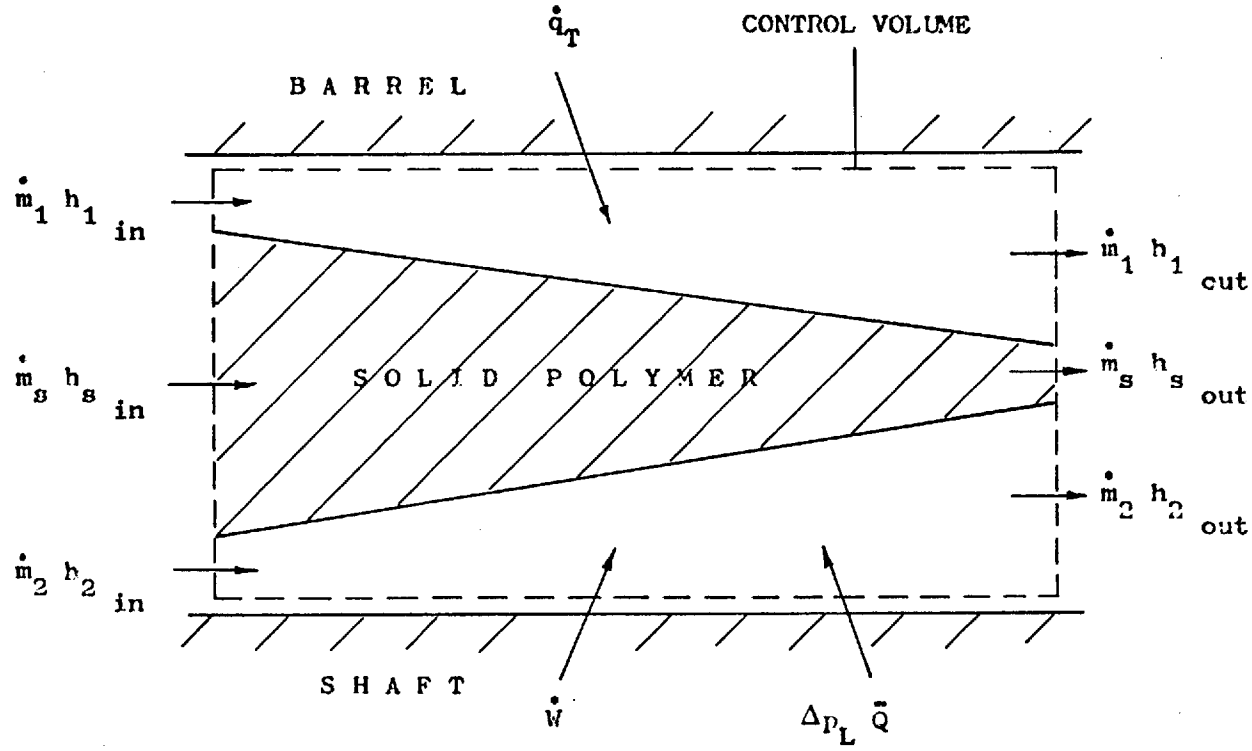

FIG. 4.13 - ENERGY FLUXES IN THE MELTING ZONE

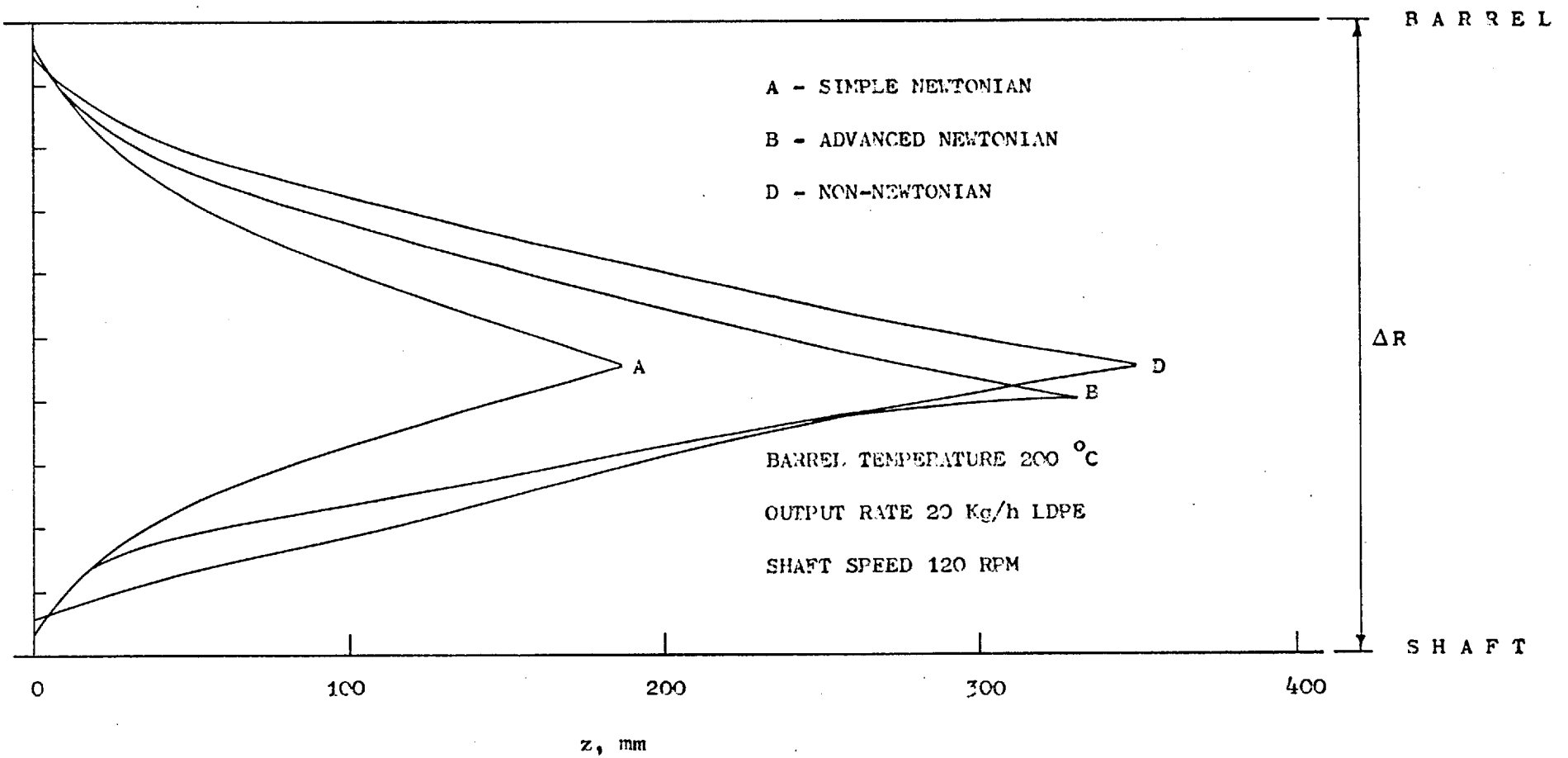

FIG. 4.14 - SOLID BED PROFILES FOR DIFFERENT MODELS

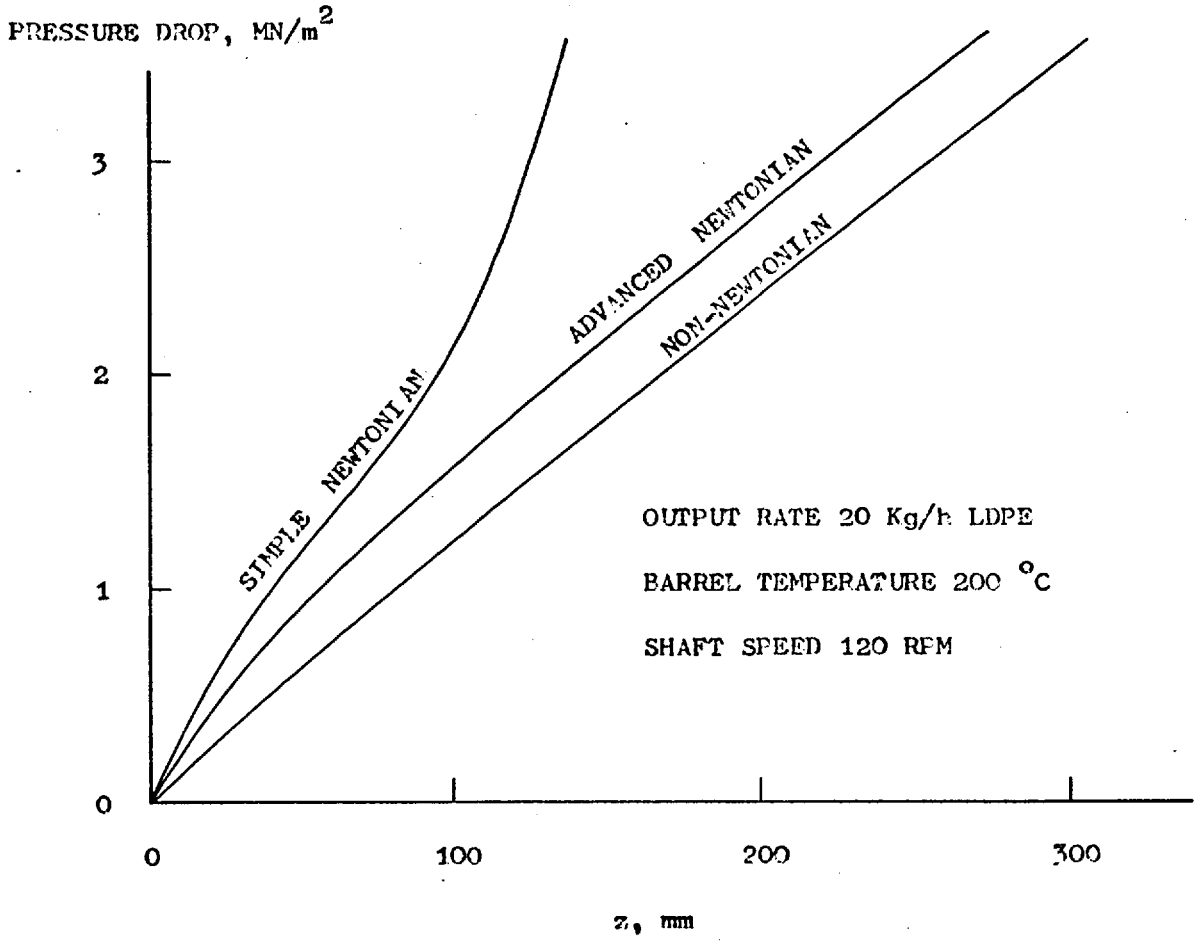

FIG. 4.15 - PRESSURE PROFILES

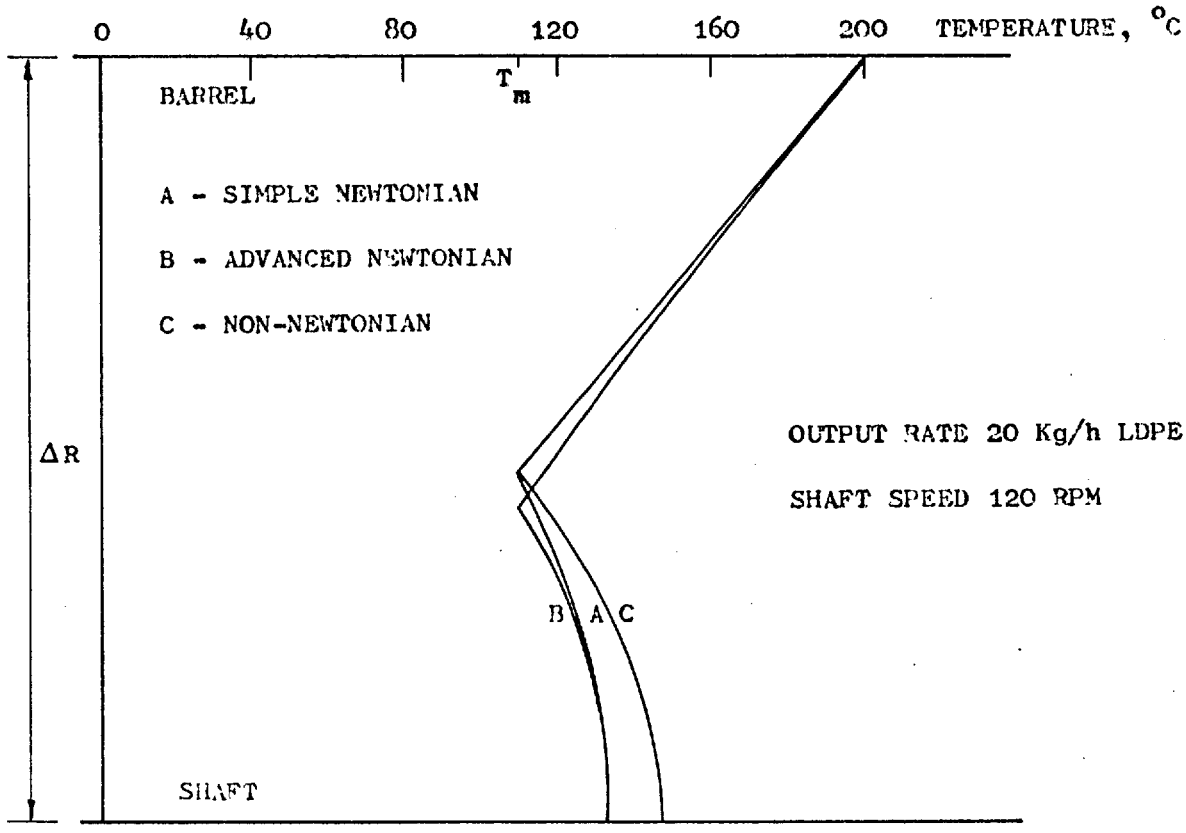

FIG. 4.16 - TEMPERATURE PROFILES AT END OF MELTING

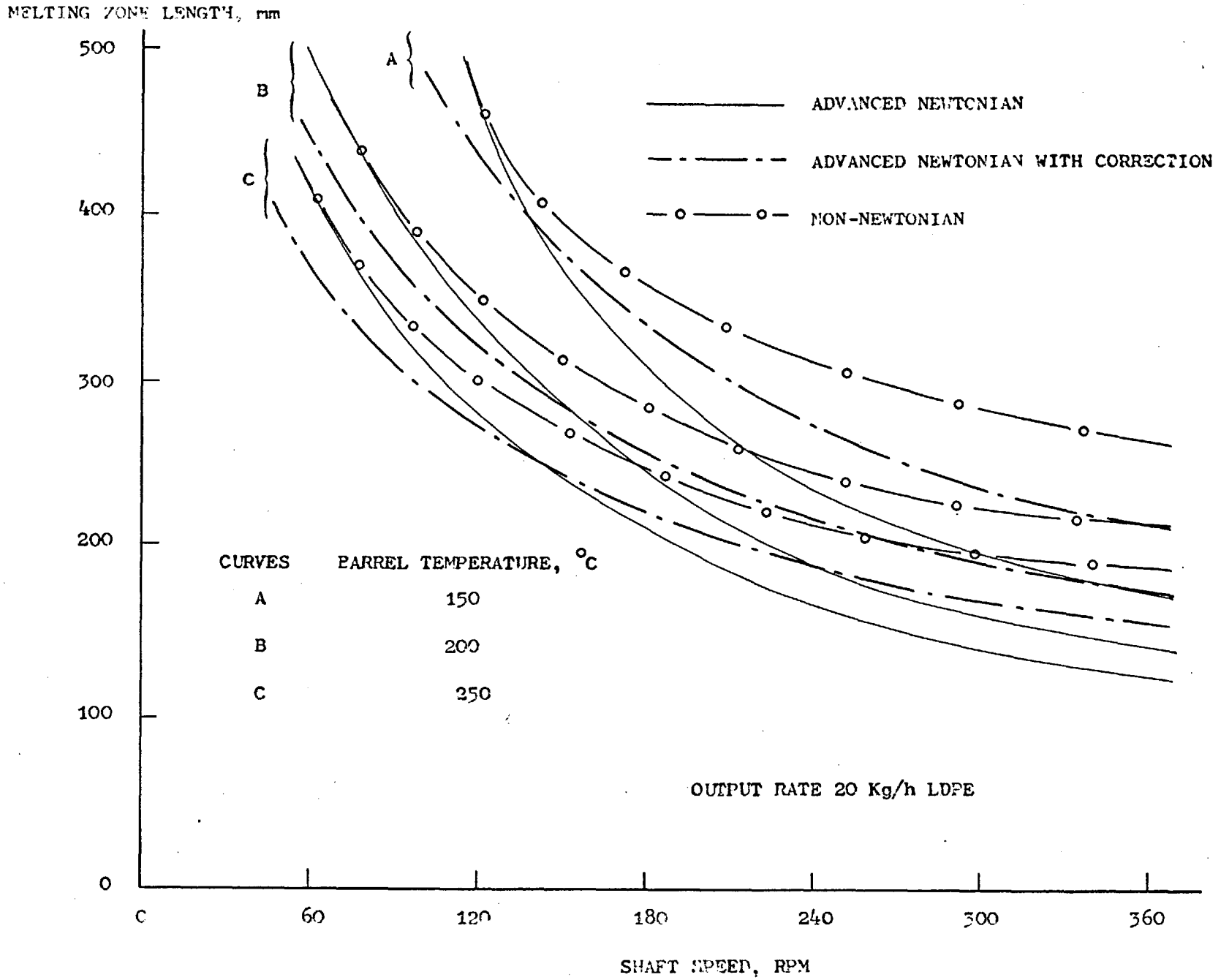

FIG. 4.17 - VARIATION OF MELTING ZONE LENGTH WITH SHAFT SPEED

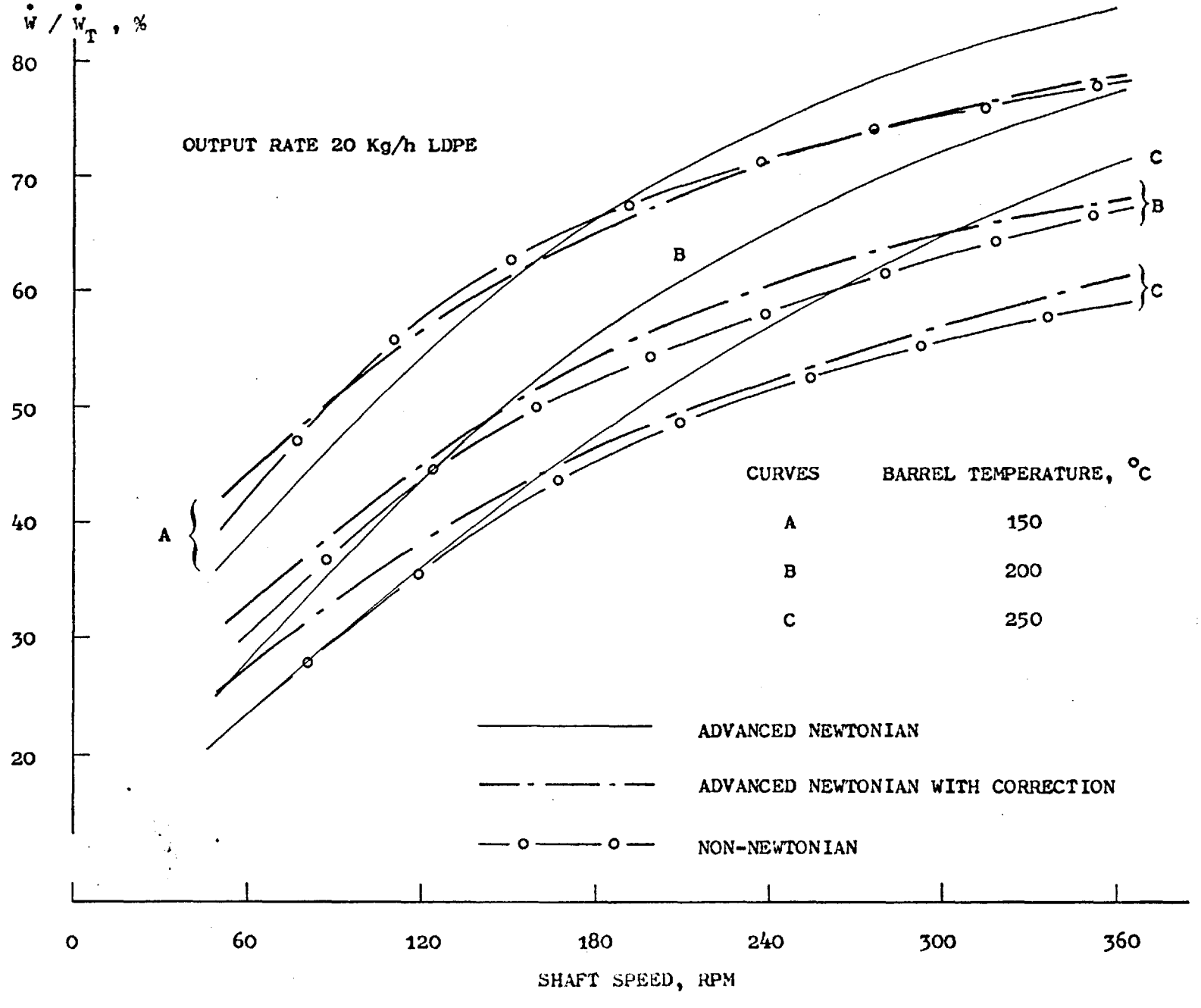

FIG. 4.18 - EFFECT OF SHAFT SPEED ON $\dot{W} / \dot{W}_T$

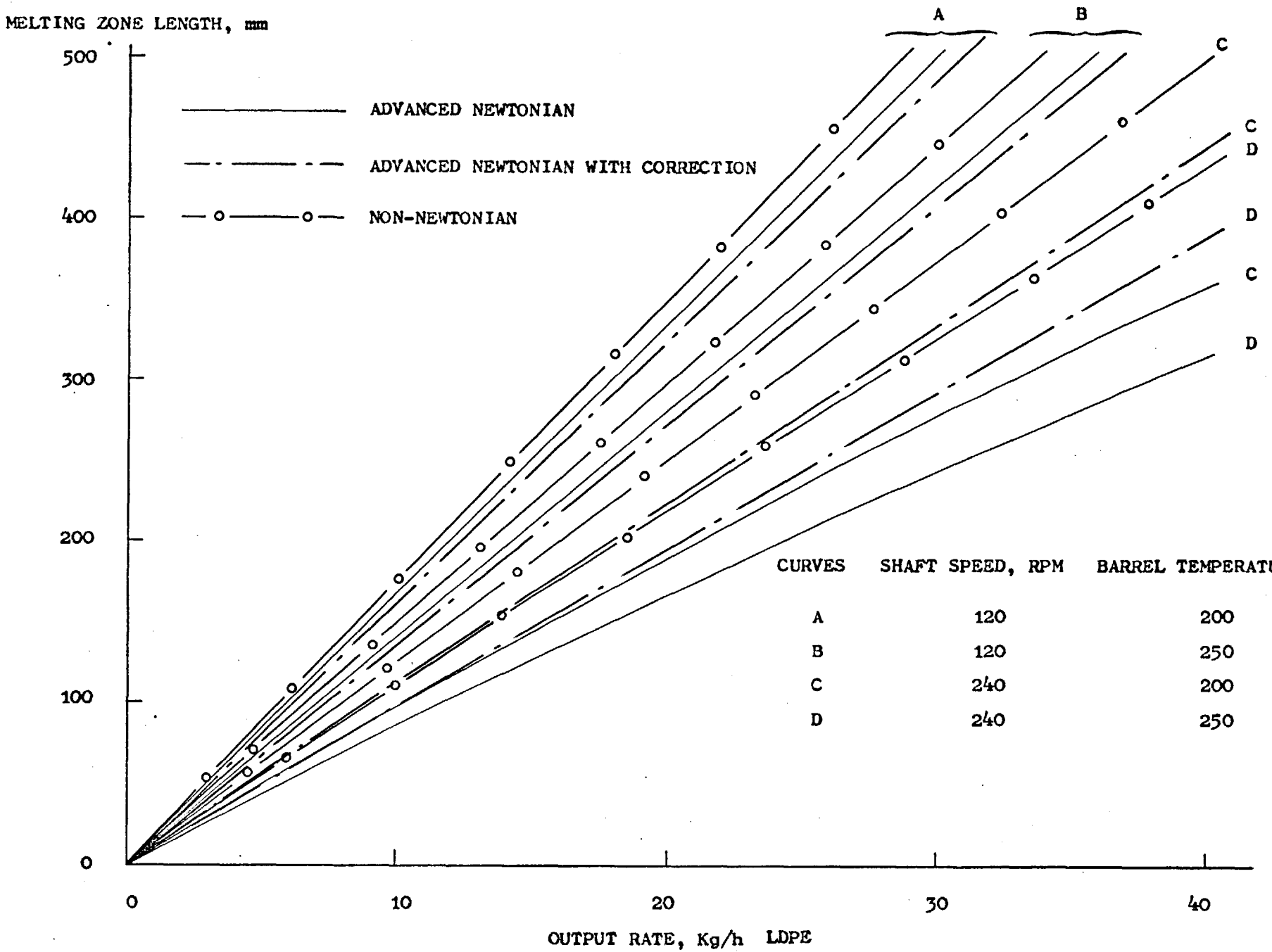

FIG. 4.19 - VARIATION OF MELTING ZONE LENGTH WITH OUTPUT RATE

CHAPTER 5

THEORETICAL MODEL FOR THE CONTINUOUS RAM EXTRUDER

5.1 Introduction

In chapters 3 and 4, theoretical models were developed to describe the processes occurring in the feeding and melting zones respectively. Melt flow through the remaining section of the annular channel has been studied previously [62] and the flow behaviour of the melt through the die is relatively simple to analyse. In this chapter an overall model for the continuous ram extrusion method is considered. It is a combination of the individual models referred to above.

In general, the end conditions predicted by each model served as starting conditions for the model of the following section of the extruder. For example, if the pressure profile along the flow channel was required for a given set of operating conditions, the pressure transmitted through the feeding zone was used as the starting pressure for the melting zone. Having computed the pressure drop across the melting zone and the remainder of the annular channel, the melt pressure at the entry to the die was obtained. Similarly the material temperature along the extruder and other parameters could be determined.

A summary of the previous work on flow of polymer melts through the annular channel [62] is given in Appendix C, and the die characteristic is briefly considered here.

In order to assess the validity of the theoretical model, predictions were compared with experimental results whenever possible. Before this could be done, however, minor modifications were introduced to the analysis presented in the previous chapter to conform with the experimental extruder's geometry.

Theoretical simulations were obtained using the model to study the effects of operating conditions, different material properties and extruder geometry on the overall process. Also, scaling up of the process in terms of output rates has been considered.

Some theoretical aspects of the mixing performance of the extruder are also considered.

5.2 Modifications to the Melting Model

In chapter 4, melting in an annular channel was studied. The channel was assumed to be a rectangular slit of width $C = \pi (R_i + R_o)$ and height $\Delta R = R_o - R_i$ and since the annulus was cylindrical, C and ΔR were constant. In the actual extruder, the annular channel converges in the initial region as shown in Figure 5.1. Assuming that the convergence is sufficiently small for the lubrication approximation to be valid, the equations remain unchanged except where C and ΔR appear. The analysis was therefore modified by replacing ΔR and C by $\Delta R'(z) = R_o'(z) - R_i$ and $C'(z) = \pi (R_i + R_o') - 2 W_k$ respectively. The quantity W_k is the width of each metal key used to create the separate feed chambers as shown in Figure 5.2. These modifications were easily carried out in the numerical solutions by specifying the variation of R_o' with z and hence defining $\Delta R'$ and C' at each axial position. It was assumed that the presence of the keys did not affect the melting mechanism postulated and that the solid material was strong enough not to break off and hence rotate when it entered into the barrel where the keys terminate.

The presence of melt films adjacent to the keys was also ignored on the assumption that the effect of these on the melting process was negligible. Another effect that the keys could have was to promote the accumulation of melt into two pools as suggested in Figure 5.2(b).

This, however, was not expected to happen in view of the convergence of the channel and the reduced scraping action of the keys due to large clearances between these and the shaft. The validity of this assumption was later confirmed experimentally.

In general, the block remained at a temperature different from that of the barrel. In the computed solutions below, the relevant thermal boundary condition was changed to allow for a linear temperature variation along the barrel reducer plate as indicated in Figure 5.1.

5.3 Melt Flow in Breaker Plate and Die

At the front end of the barrel, before the extrusion die, a breaker plate was used to, amongst other functions, break up the helical flow pattern of the melt as it emerged from the annular region, and to hold back any unmelted polymer. Figure 5.3 shows details of the region in question. The breaker plate consisted essentially of a perforated thick disc. The perforations were cylindrical holes whose dimensions are given in Table 2.1. Assuming the flow rate through each of the n_h holes to be the same, the relationship between the overall mass flow rate, $\dot{M}$, and the pressure drop Δp_{BP} across the breaker plate is given by (see, for example, McKelvey [2])

$$\frac{\dot{M}}{\rho_m \, n_h} = \left(\frac{\gamma_o \, n \, \pi \, R_h^{\,3}}{3n + 1} \right) \left(\frac{R_h \, \Delta p_{BP}}{2\mu_o' \, \gamma_o \, L_{BP}} \right)^{\frac{1}{n}} \qquad (5.1)$$

where R_h is the radius of each hole in the breaker plate,

L_{BP} is the length of the breaker plate, and

$\mu_o' = \mu_o \exp \left[- b \, (\bar{T} - T_o) \right]$ with $\bar{T}$ as the mean temperature of the melt emerging from the annular channel.

Similarly the pressure drop Δp_D across the cylindrical die is given by

$$\frac{\dot{M}}{\rho_m} = \left(\frac{\gamma_o \, n \, \pi \, R_D^{\,3}}{3n + 1}\right)\left(\frac{R_D \, \Delta p_D}{2\mu_o' \, \gamma_o \, L_D}\right)^{\frac{1}{n}} \qquad (5.2)$$

where R_D and L_D are respectively the radius and the length of the lace die. Entry effects are ignored in both cases. Assuming that the pressure drops across sections a and b in Figure 5.3 are negligible compared with Δp_D and Δp_{BP}, the overall pressure drop from the end of the annular region to the exit of the die is

$$\Delta p \simeq \Delta p_D + \Delta p_{BP} = 2\mu_o' \gamma_o \left[\frac{\dot{M}(3n + 1)}{\rho_m \, n \, \pi \, \gamma_o}\right]^n \left(\frac{L_D}{R_D^{\,3n+1}} + \frac{L_{BP}}{n_h^{\,n} \, R_{BP}^{\,3n+1}}\right) \qquad (5.3)$$

Thus, given the output rate of the extruder, the pressure drop in this region could be evaluated using equation (5.3).

5.4 Procedure for Theoretical Simulations

This section outlines briefly the general procedure for obtaining overall performance predictions using the theoretical models.

Figure 5.4 shows a diagram of the extruder divided into a number of regions. The initial part consists of a cylindrical solids feeding zone (CFZ) followed by an angled feeding zone (AFZ). The material melts in the melting zone (MZ), flows through the remaining annular region (MF) and finally out of the extruder through the breaker plate and the die (DF). The procedure consisted of the following steps:

i) The operating conditions and material properties were specified as input data.

ii) The pressure losses through CFZ were calculated using the appropriate model derived in chapter 3 for Coulomb and/or

viscous friction depending on operating conditions. The temperature of the solid plug was also evaluated.

iii) The pressure transmitted through AFZ was computed and hence the overall pressure drop in the solids feeding zone evaluated.

iv) The non-Newtonian melting model was applied to MZ with the modifications introduced in section 5.2. The length of this zone was determined amongst other parameters and hence the length of the following region MF obtained.

v) The thermally developing flow of polymer melt through MF was then considered, applying the analysis described in Appendix C.

vi) Finally, the pressure drop across region DF was calculated using equation (5.3).

The outcome of these computer simulations were results relating the dependent variables such as output rates, melt temperatures, power consumption and degree of mixing to the operating conditions, for specified material properties and extruder geometry.

5.5 Comparison of Theoretical Predictions with Experimental Results

If computer simulations are to be of any use, it is necessary first to compare predictions with experimental results in order to assess their validity and accuracy. It has already been pointed out that the process is not a truly steady state one, though theoretical analyses were based on the assumption of steady state conditions. In the following comparisons, where fluctuations in a variable were sufficiently large and measurable, e.g. melt pressures, the mean of the maximum and minimum values was used. Other parameters like output rates were already averaged during the measurement. Because the number of performance

parameters and independent variables is large and little advantage was gained by using dimensionless variables, the number of comparisons presented can only be a fraction of all the results obtained. However, results have been chosen to include a representative range of conditions rather than to show best agreement between theory and experiment. All the results presented are related to extrusion of LDPE.

5.5.1 Flow through breaker plate and die

Figure 5.5 shows the variation of the pressure drop across zone DF with the output rate. The experimental values for the pressure drop was measured at the tapping shown in Figure 5.3 and the theoretical values calculated using equation (5.3), assuming mean melt temperatures. The agreement was considered to be satisfactory and therefore equation (5.3) could be used confidently for relating flow rates and pressure drops in this region.

5.5.2 Pressure profiles

Pressure readings were taken along the extruder. Two transducers giving a continuous recording of the pressure were employed. Figures 5.6 and 5.7 show the mean pressures compared with the steady state predictions for a high and a low output rate respectively. As an indication of the fluctuation of the pressure recordings, the peak pressure at each position is also shown. In the predicted profiles, a straight line was drawn from the pressure just before the breaker plate to zero atmospheric pressure (gauge). These profiles were determined backwards from zero pressure at the exit of the die. Agreement between computed and experimental results is good, admittedly for very few pressure measurements. Only two cases have been presented, but

similarly good agreement has been obtained for other cases.

Pressures along the barrel only have been considered. In general, all the relevant data are accurately ($\pm$ 5%) known in this region, whilst predictions of pressure drops along the feeding zone depend to a large extent on the accuracy of frictional data and on the type of friction. Because very little information is available on this, and measurement of pressures in the feeding zone was not possible, comparisons of results in this region were not carried out. However, the ram pressures were known in both cases and an indication of the pressure drop through the solids feeding zone was obtained. These were 20.0 MN/m^2 for the case shown in Figure 5.6 and 17.2 MN/m^2 for the other case. These agree, at least in order of magnitude, with the results predicted in chapter 3 and also suggest that melt films must have been formed in the feeding zone.

5.5.3. Power consumption

The specific shaft power consumption has been plotted in Figure 5.8 for a range of output rates. It can be seen that the experimentally measured values are considerably higher than those predicted (full line). The reason for this is that the predicted values are those for the power consumption in the MZ and MF zones only, whilst the measured values include the bearing losses and the power consumed in AFZ as the shaft rotates against the solid polymer. If the predicted results are corrected to include these power losses agreement in the results is improved. For the case considered, a reasonable estimate of an extra 3 kW consumption produces the broken line shown in Figure 5.8 giving good agreement between theoretical and experimental results.

5.5.4 Melt temperatures

An attempt to compare experimentally measured melt temperatures with theoretically computed bulk mean temperatures is shown in Figure 5.9. The predictions at high output rates were found to give values considerably lower than the experimentally measured ones. Above 27.5 kg/h the melting model predicted the presence of solid polymer and the bulk mean temperature of the melt film adjacent to the barrel was plotted instead. In the results shown, the shaft speeds ranged from 60 to 240 rpm for the experimental results and the computed values were based on a shaft speed of 180 rpm. It is worth noting that the band of temperatures measured lies around 200^{o}C which was the temperature set for the barrel. Clearly the readings were strongly influenced by the barrel temperature and therefore the comparison cannot be conclusive.

5.5.5 Melting mechanism

One of the major processes occurring in the extruder channel is the melting of the solid polymer. Ideally the accuracy of the melting model should have been checked by a series of experiments with measurements of film thicknesses and amount of solid polymer present. The existing extruder is not suitable for such experimental work but further qualitative support for the validity of the theoretical model was obtained. The machine was run for a reasonable period of time for steady state conditions to be reached. The shaft and rams were then stopped and immediate cooling of the barrel and main block started. When the temperature of the polymer was sufficiently low, the barrel was removed. The 'frozen' polymer was then inspected. In order to aid visual distinction of the original solid polymer granules from the melt, a coloured dye powder was dispersed into the granules prior to feeding

into the hoppers. The unmelted polymer could thus be detected by the presence of a coloured layer on the surface of the granules. It was observed that initially the presence of the keys tended to create small melt pools as suggested in Figure 5.2(b) but as the annular channel converged, the deformed solid bed spread into the pools and these were reduced into an insignificant amount. The film thicknesses, adjacent to barrel and shaft were of the same order of magnitude but at lower barrel temperatures the film adjacent to barrel was thinner than that adjacent to the shaft. In spite of the rapid deformation of the solid bed in the converging channel, it remained intact and was sufficiently rigid not to be broken up by the rotation of the shaft. Thus, most of the assumptions adopted in the derivation of the theoretical model can be considered to be valid and as such the model should be acceptable, though it has not been verified quantitatively except for some measurement of pressures as presented in section 5.5.2.

5.6 Distributive Mixing in the Extruder

An important requirement from the extruder is the production of a homogeneous extrudate. Fenner [4] has discussed briefly different types of mixing with relevance to screw extruders. In the present work only distributive mixing is considered. This is the more important type of mixing in the laminar flow of polymer melt in the extruder. Distributive mixing depends on the total deformation of the system, which spreads the clumps of material and so reduces the average distance between them. The degree of mixing produced by this process can be expressed in terms of a ratio of initial to final striation thicknesses. The concept of striation thicknesses has been extended to three-dimensional flows by Fenner [4] and the degree of mixing M is given by

$$\frac{dM}{dt} = (4I_2)^{\frac{1}{2}} \qquad (5.4)$$

where t is time, and I_2 is obtained from the velocity profiles of the melt flow. Equation (5.4) was integrated along the path taken by a typical element of material and gave results for degree of mixing as a function of the initial position of the element in the flow channel. Figure 5.10 shows the variation of the degree of mixing across the annular gap at the completion of melting. The path of each particle of melt started where it first joined the melt stream as it changed from solid to melt. Whilst such a result is useful for investigating the local variation of degree of mixing, for example in Figure 5.10 the degree of mixing for particles adjacent to the boundaries tends to infinity since their downstream velocity is zero and that for the particle which has just melted is zero, it is not very convenient to use in practice. Instead, a bulk mean mixing parameter $\bar{M}$ has been defined by Fenner [4] as

$$\frac{d\bar{M}}{dz} = \frac{1}{v_z H} \int_0^H (4I_2)^{\frac{1}{2}} \, dy \qquad (5.5)$$

Equation (5.5) was integrated from z = 0 to the end of the annular channel and hence an overall degree of mixing $\bar{M}$ of the extrudate obtained.

It is worth noting that this value depends on the solution of the flow equations which were solved assuming the melt to be homogeneous. On the other hand, mixing is a homogenising process. In general, the assumption of homogeneity must be retained if any progress is to be made at all. Where materials with different viscous properties are mixed

difficulties could arise in obtaining a solution. Though $\overline{M}$ has a purely theoretical meaning, it should be a practical basis on which the mixing performance of homogenisers can be compared. As a reference, in single screw homogenisers it has a typical value of 4000.

5.7 Theoretical Simulations

Because of the nature of the process and the interaction of different parameters, a considerable amount of theoretical results could be presented. Accepting the fact that the main result is the computer program which can be used to simulate the operation of the extruder, a limited amount of sample results is presented to illustrate the usefulness of the analysis and at the same time to study the process in greater detail.

5.7.1 Simulations concerning operating conditions

For the results presented below, an extruder of the same dimensions as the existing one was considered. Also the parameters varied are in the practical range possible with the existing machine.

Assuming that the ram pressures are adjusted accordingly to give a fixed output rate, the effect of varying the other major operating parameters namely the shaft speed and barrel temperature was studied. In chapter 4, the effect of these two variables on melting has already been investigated. Here it remains to summarise their influence on the quality of the extrudate in terms of the bulk mean melt temperature and mixing. Figure 5.11 shows the bulk mean melt temperature at the end of the annular channel plotted against bulk mean mixing with the shaft speed and barrel temperature as parameters. With the barrel set at a given temperature, mixing can be increased by increasing shaft speed. This,

however, leads also to an increase in melt temperature. In the relatively small size extruder considered, melt temperature can to some extent be reduced by lowering the barrel temperature without affecting mixing.

The pressure gradient required to maintain a given output rate decreases with increasing shaft speed and barrel temperature as shown in Figure 5.12. The pressure drop plotted refers to the pressure drop across the annular channel only, i.e. zones MZ and MF. Given the die characteristics and reliable values of the coefficient of friction in the feeding zone, the pressure required at the rams could be predicted. Figure 5.13 shows the variation of the shaft power (consumed in zones MZ and MF only) with shaft speed. The effect of barrel temperature on shaft power is relatively small. The extra power consumed at higher shaft speeds is used for raising the melt temperature and increasing $\overline{M}$.

Figure 5.14 shows the variation of shaft power and bulk mean mixing with output rate when both shaft speed and barrel temperature are fixed. Whilst the mean melt temperature decreases with increasing output rate - shown previously in Figure 5.9 - which is beneficial, mixing becomes poorer. This is because the residence time of the material in the extruder decreases and hence is subjected to less shearing. The shaft power increases with output rate, but the specific power consumption decreases as shown in Figure 5.8.

5.7.2 Simulations concerning some material properties

The effects of some important physical properties of the material on the process was analysed. The physical properties varied were the viscosity in terms of the constants in equation (4.39) and the thermal conductivity of the polymer melt. Each parameter was varied whilst

the others were held constant for a typical set of operating conditions, i.e. barrel temperature and shaft speed. The properties which were held constant during each simulation were given the values shown in Table 4.1. Figure 5.15 shows the effect of varying the coefficient b which characterises the temperature dependence of viscosity. For the cases considered, an increase in b corresponds to a reduction in viscosity. Thus, the pressure drop across the annular channel to maintain an output rate of 20 kg/h decreases; mixing decreases slightly; the output melt temperature also decreases slightly; complete melting of the material occurs further downstream; and the shaft power consumption also decreases. In general, the changes are relatively small and thus variations in the viscosity temperature coefficient b have minor effects on the performance. Figure 5.16 shows the effect of varying the power-law index n. Here, an increase in n is equivalent to an increase in the apparent viscosity. Thus, the trend of the results is opposite to those shown in Figure 5.15, with the exception of mixing which decreases slightly with increasing n. The variation of the parameters plotted in Figure 5.16 with n, are, however, more significant. Similar results have been obtained in Figure 5.17 where the datum viscosity μ_o has been varied. Again, the variation in mixing is small. In general, mixing is dependent on shear rates and residence time. Since both shaft speed and output rate were assumed constant the variation of mixing in Figures 5.15 to 5.17 was expected to be small. The variations in mixing were in fact due to small changes in the velocity profiles from which I_2 was obtained for use in equation (5.5). In Figure 5.18 the effects of the thermal conductivity of the polymer melt is shown. The melting length decreases as conductivity increases due to better heat transfer. The effect of this is to reduce the pressure gradient required to maintain

the same level of output rate. Mixing and shaft power consumption remain fairly constant, whilst melt temperatures increase slightly.

5.7.3 Simulations concerning geometry

The theoretical models have also been applied to studies on the effects of varying the physical dimensions of the existing extruder within a suitable range. In particular, the feed cylinder/barrel axis angle has been varied to study the effect of this on the pressure propagation through the granules in this region, and the length of the barrel and the shaft diameter have also been varied to assess their influence on the performance of the extruder.

Figure 3.1 shows in detail the angled solids feeding zone extending from plane CC to BB characterised by an angle β and a mean length L_{BC}. Figure 5.19 demonstrates the effect of varying the angle β on the ratio of the pressure at BB to that at CC. The cross-sectional areas at CC and BB were assumed to be constant, i.e. fixed feed cylinder and annulus sizes. The model used is that for flat plates presented in section 3.5 and the internal coefficient of friction μ_i was assumed to be the same as that for the polymer/melt interface μ_f. Figure 5.19 shows the results obtained for three values of the coefficient of friction. A maximum pressure ratio occurs in each curve. This is explained by the fact that as the angle increases, the length L_{BC} reduces and hence the pressure transmitted to BB increases, but when the angle becomes excessive, the pressure transmitted to BB decreases due to the sharpness of the bend and hence the maximum pressure ratio occurs. It should now be clear that the conical geometry model presented in section 3.6 cannot predict these maximum points since a change in β would merely affect the separation of planes bb and cc in Figure 3.18 with D_b and D_c constant.

For convenience, the coefficients of friction were chosen to be the same. This may not necessarily correspond to the practical case, but the results illustrate clearly the usefulness of the analysis for design applications.

Figure 5.20 shows the effect of increasing the annular channel length. The pressure drop, mixing, melt temperature and shaft power consumption all increase with the length of the channel. Once the material is completely melted, the remaining length of the channel is merely used to impart additional mixing. All the quantities plotted increase approximately in direct proportion with the channel length with the exception of melt temperature. As the material flows along the channel, its temperature increases gradually until the flow becomes thermally fully developed when no further change in temperature occurs. The curve for melt temperature therefore tends to flatten out. In Figure 5.20 fully developed flow is by no means achieved. Figure 5.21 shows developing temperature profiles in the material from z = 334 mm (where the material is fully melted). By selecting a suitable channel length, the melt temperature variation across the annular gap can be minimised.

Figure 5.22 shows the effect of using shafts of different diameter. A change in the shaft diameter alters the size of the annular gap. A reduction in the annular gap due to the use of larger shafts leads to greater flow resistance and hence the pressure drop along the annular channel must increase in order to maintain the same level of output rate. The higher shear rates produced in the smaller annular gap also result in a slight increase in mixing whilst both melt temperature and shaft power consumption increase significantly. Complete melting also occurs considerably earlier as the shaft diameter is increased.

5.8 Scaling-Up

This section considers the application of the theory to the problem of predicting the performance of scaled-up versions of the continuous ram extruder. Of particular interest is the maximum output rate obtainable from a particular size of the extruder.

It has already been shown that when extruding a given material under a given set of operating conditions, the higher the output rate the further the unmelted polymer extends into the extruder channel. Clearly a major requirement is that the material reaches the die in a fully molten state. Thus, scaling-up has been considered in this work in terms of the melting performance of the extruder. For a given size of machine and set of operating conditions, the maximum output rate was that at which fully melting was just achieved before the polymer reached the die. Initially all the extruders considered were geometrically similar to the existing one. All the physical dimensions were varied in proportion with the internal barrel diameter D. Figure 5.23 shows the maximum output rate for a range of extruder sizes characterised by the diameter D operated at different shaft speeds. At a shaft speed of 240 rpm, the output rate is approximately proportional to $D^{1.25}$. The length of the extruders considered were taken as 12 times the barrel diameter. Clearly, higher output rates could be achieved if the length of the extruder was larger and/or if the shaft speed was increased. This, however, could lead to mechanical problems such as whirling.

Melting rate can also be improved by reducing the annular gap. An empirical rule of allowing the annular gap to vary with the square root of barrel diameter has been tried here and it has been found that higher output rates are possible even allowing the shaft speed to vary inversely proportionally with the square root of the barrel diameter. This square

root law has been successfully applied by other workers to scaling-up of single screw extruders [63,64]. Figure 5.24 shows the results obtained using this method for scaling-up. The barrel diameter of the existing extruder has been selected as the basis for scaling up and a reference shaft speed of 240 rpm was taken. For a barrel length to diameter ratio (L/D) of 12:1, the maximum output rates are approximately proportional to $D^{1.7}$, showing a considerable improvement over the previous method of scaling-up. Also shown in Figure 5.24 are the expected maximum output rates for longer versions of the extruder with an L/D ratio of 20:1. The output rates were found to be approximately proportional to $D^{2.1}$, suggesting that longer machines are preferable for higher production rates. Typical performance data for a short and a long extruder, with a barrel diameter of 200 mm, operating at T_b = 200°C and shaft speed of 113 rpm are:

	L/D = 12:1	L/D = 20:1
Maximum output rate (LDPE):	620 kg/h	1200 kg/h
Bulk mean mixing $\bar{M}$:	8700	8600
Bulk mean melt temperature:	193°C	192°C
Specific shaft power consumption:	0.151 kWh/kg	0.123 kWh/kg
Pressure drop along barrel:	13.1 MN/m^2	27.5 MN/m^2

In terms of extrudate quality (bulk mean mixing and temperature) there is little difference between the two extruders. The longer version is, however, more economical in terms of specific power consumption. The hydraulic rams would have to be considerably more powerful in the long extruder in order to maintain the higher output rate through the longer

barrel.

In general, maximum output rates also depend on other factors such as barrel temperature and limitations to the capacities of auxiliary equipment.

5.9 Discussions and Conclusions

In this chapter is was shown how the individual pieces of theoretical analysis can be used in an overall model for the continuous ram extruder. Though only relatively few experimental results have been compared with theoretical ones, these were conclusive enough to confirm the validity of the theory. The agreement between theory and experiment was found to be good in general. There is, however, plenty of room for improvement both on the theoretical and experimental aspects. For example, it was necessary to allow for additional shaft power consumption in the theory, and temperature measurements should be improved. It was unfortunate that the melting predictions could not be verified more quantitatively, but at least qualitative results proved the relevant assumptions to be valid.

Similarly, relatively little attention has been paid to the solids feeding process in this chapter mainly due to the lack of knowledge and data on frictional behaviour. However, the analysis is available and has been shown to be valuable for at least estimating pressure losses. It should also be useful for design applications in selecting the appropriate ram capacity.

It was not intended to present large amounts of theoretically simulated results, but rather to present comparatively few in order to illustrate typical applications of the theory and also to study the process in greater detail. Thus, the effects of some major factors

affecting the operation of the extruder namely the operating conditions, material properties and extruder geometry, have been investigated. Because of the large number of variables involved and their interaction it is not possible to state what is an optimum set of operating conditions or extruder design. In general, compromise solutions must be accepted. For example, at a given output rate, melt quality can be improved by operating at a low barrel temperature and high shaft speed (see Figure 5.11) but power consumption increases (Figure 5.13). Though not directly apparent, it should be noted that neither of these changes (shaft speed and barrel temperature) affects the output rate as long as the pressure gradient maintained along the extruder is accordingly adjusted, in practice, by altering the ram pressure. The advantage of separating plasticating functions from the output rate is thus clearly demonstrated.

The square root law for scaling-up was shown to be a better one than by just allowing the extruder size to vary in proportion with that of the existing model. It was also shown that considerably higher output rates can be obtained by using longer machines, but their physical size would be limited by mechanical restrictions.

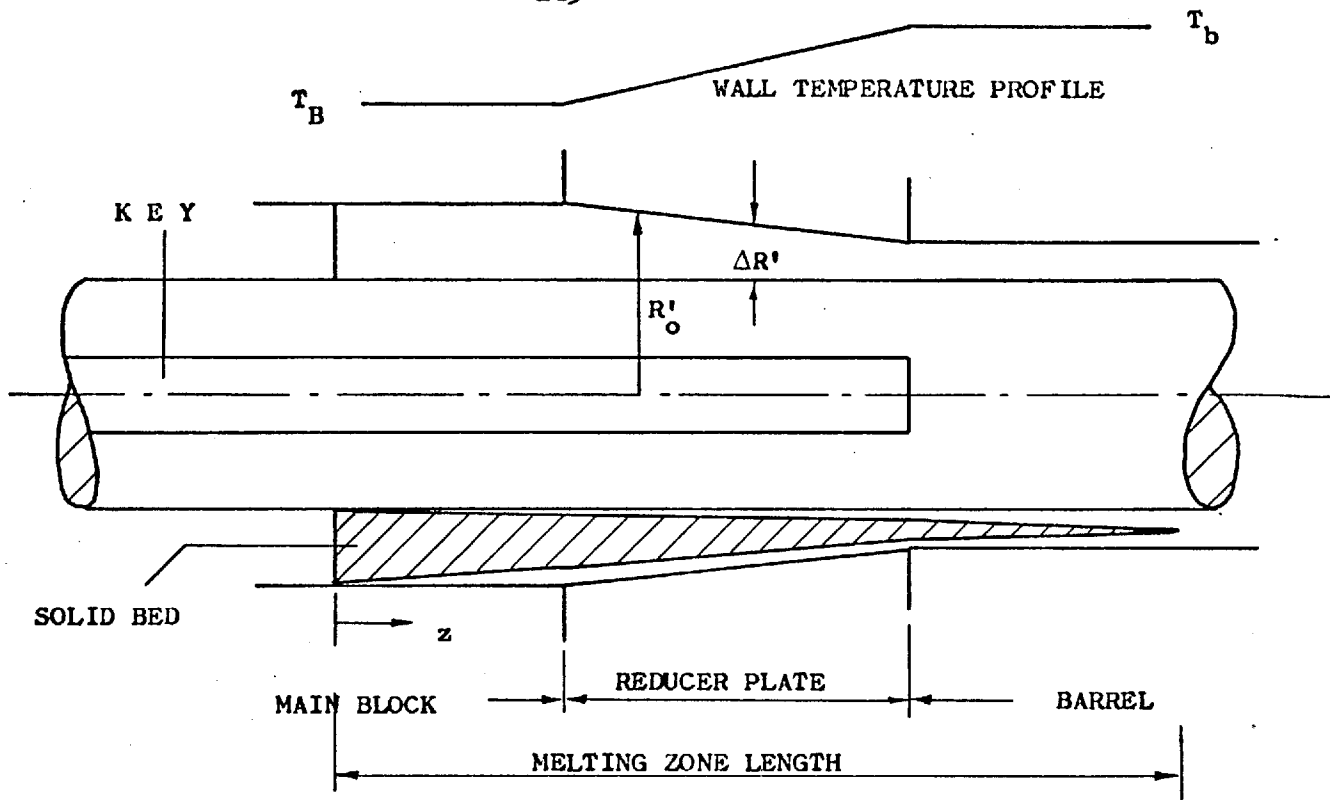

FIG. 5.1 - CONVERGING MELTING ZONE

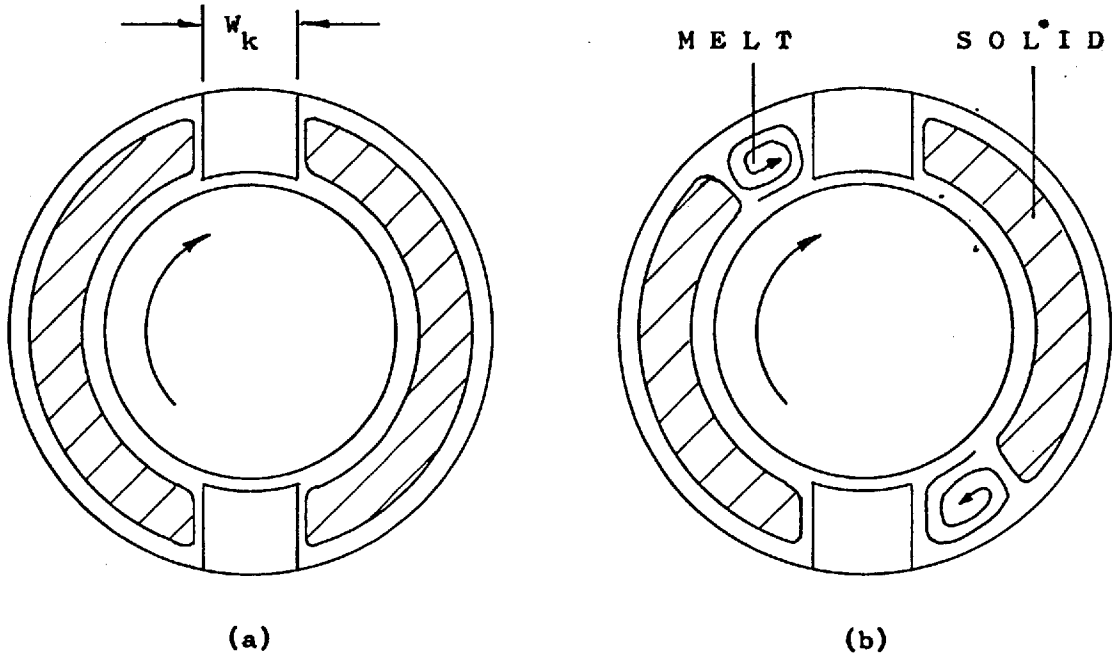

FIG. 5.2 - CROSS-SECTIONAL VIEWS OF THE ANNULAR CHANNEL WITH KEYS

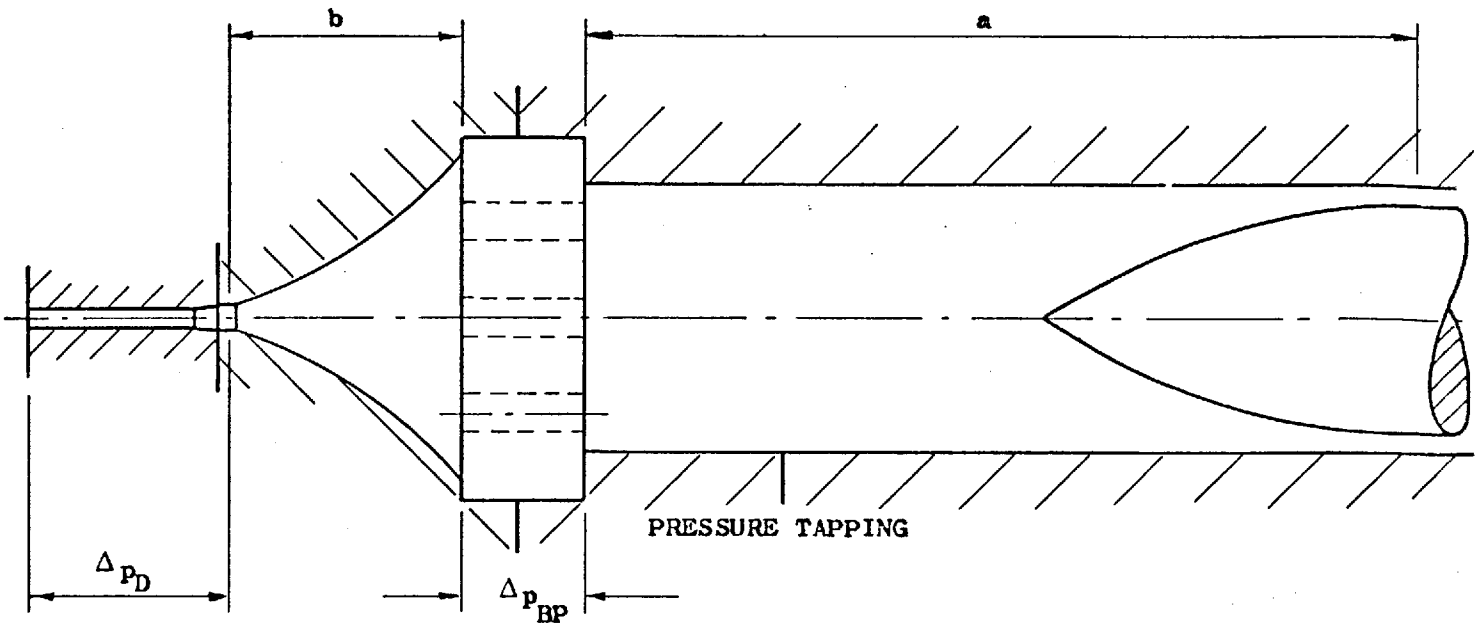

FIG. 5.3 - DETAILS OF THE FRONT END OF THE EXTRUDER

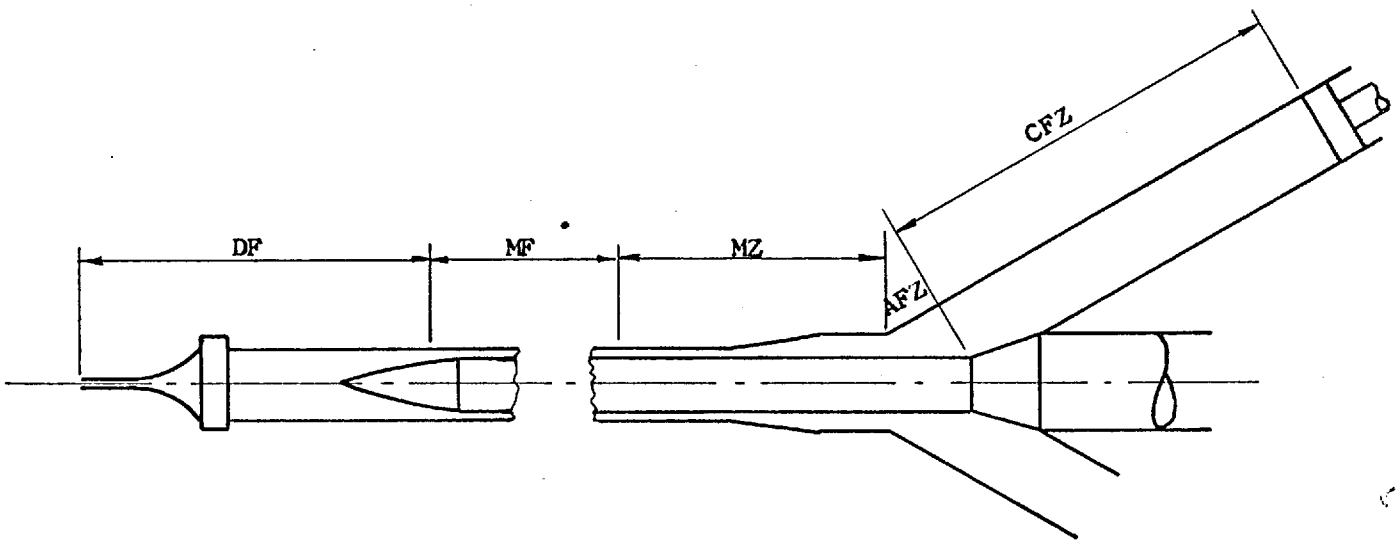

FIG. 5.4 - ZONES FOR THE THEORETICAL MODEL

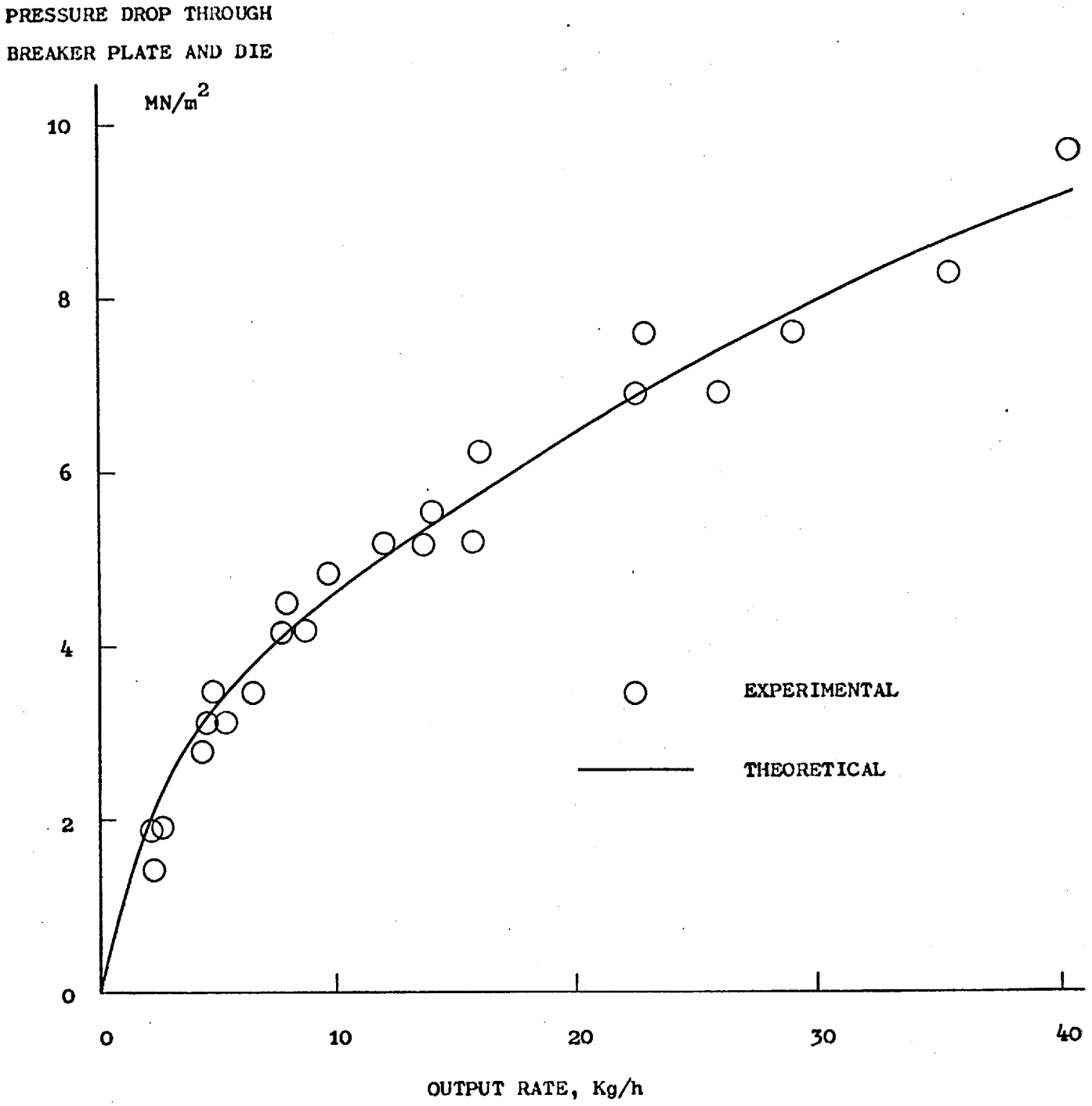

FIG. 5.5 - COMPARISON OF EXPERIMENTAL RESULTS WITH THEORETICAL PREDICTIONS FOR THE FLOW THROUGH THE BREAKER PLATE AND DIE

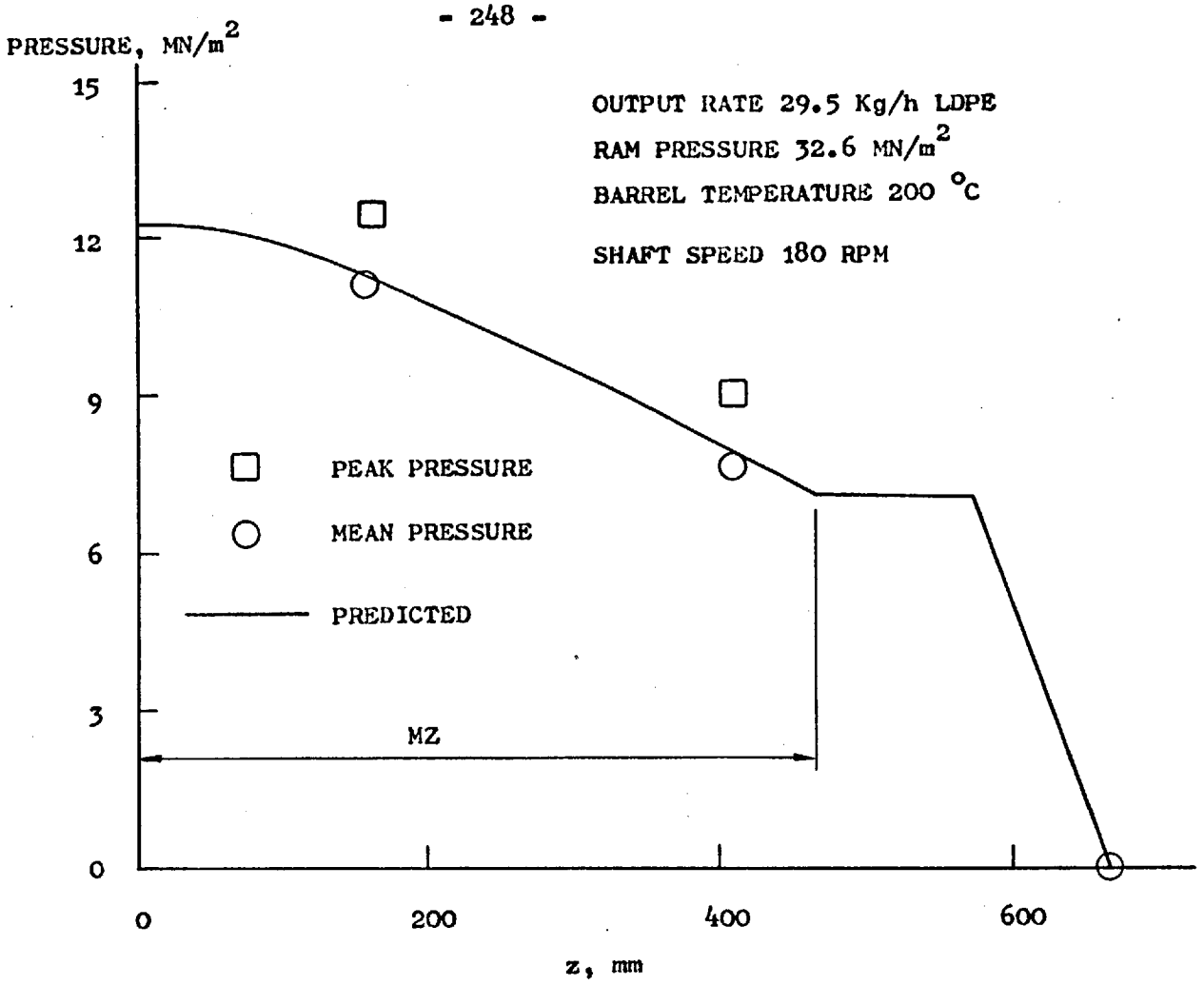

FIG. 5.6 - COMPARISON OF MEASURED AND PREDICTED PRESSURE PROFILES

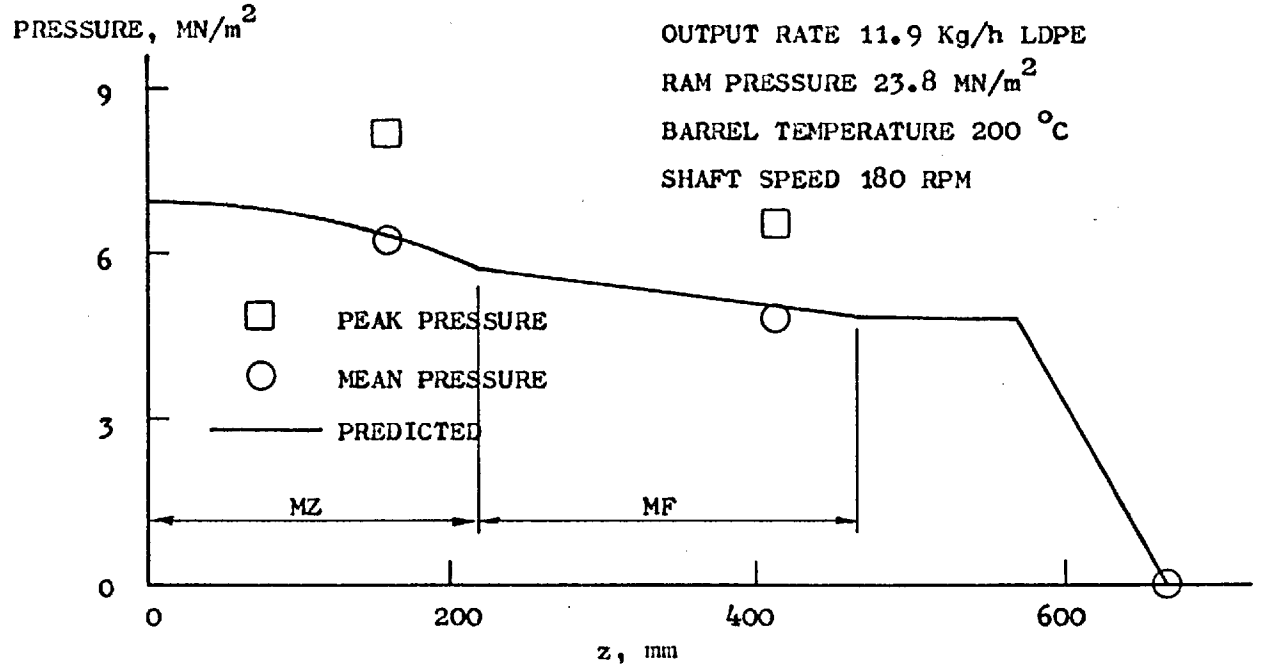

FIG. 5.7 - COMPARISON OF MEASURED AND PREDICTED PRESSURE PROFILES

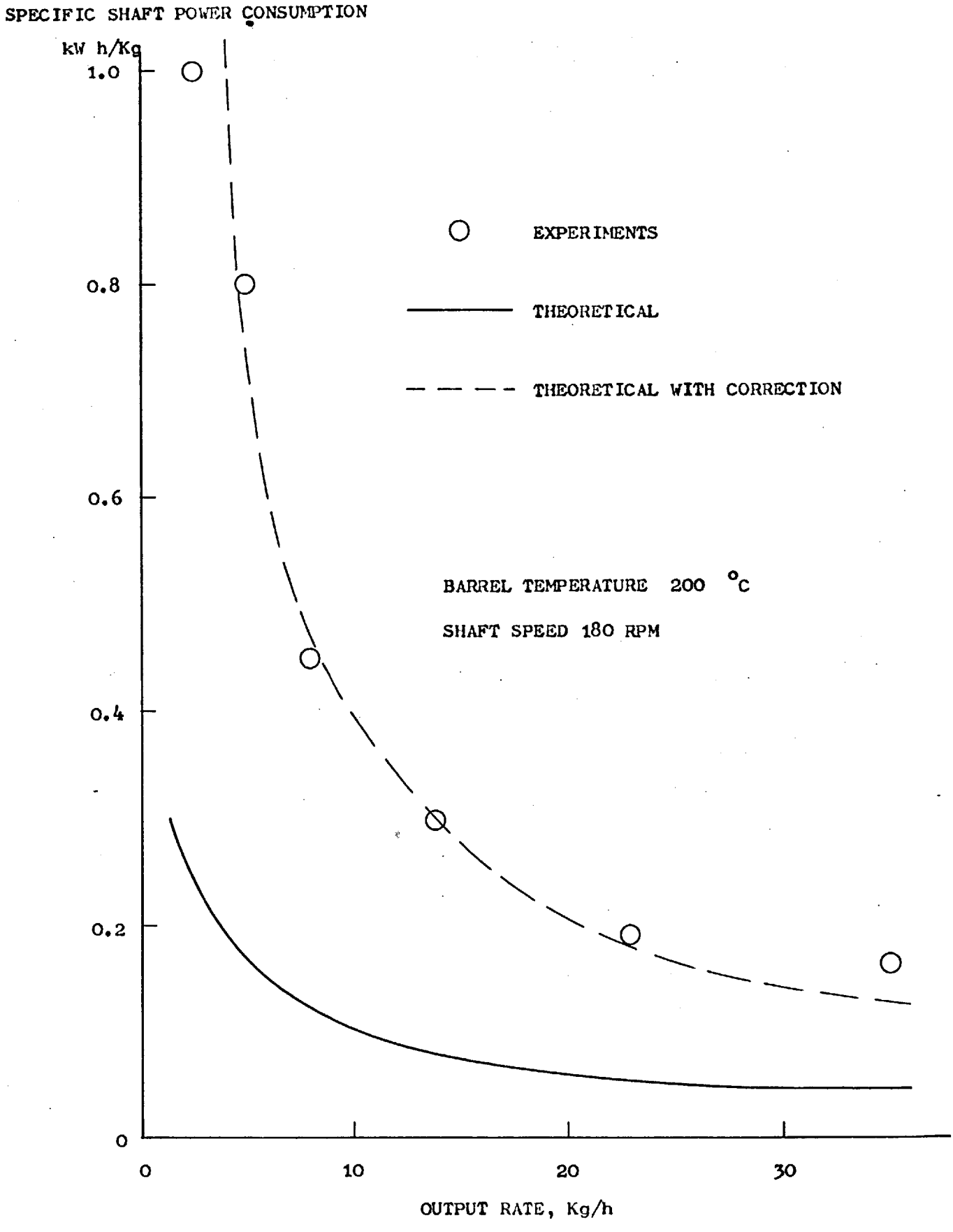

FIG. 5.8 - COMPARISON OF MEASURED SPECIFIC SHAFT POWER CONSUMPTION AS FUNCTION OF OUTPUT RATE WITH THEORETICAL RESULTS

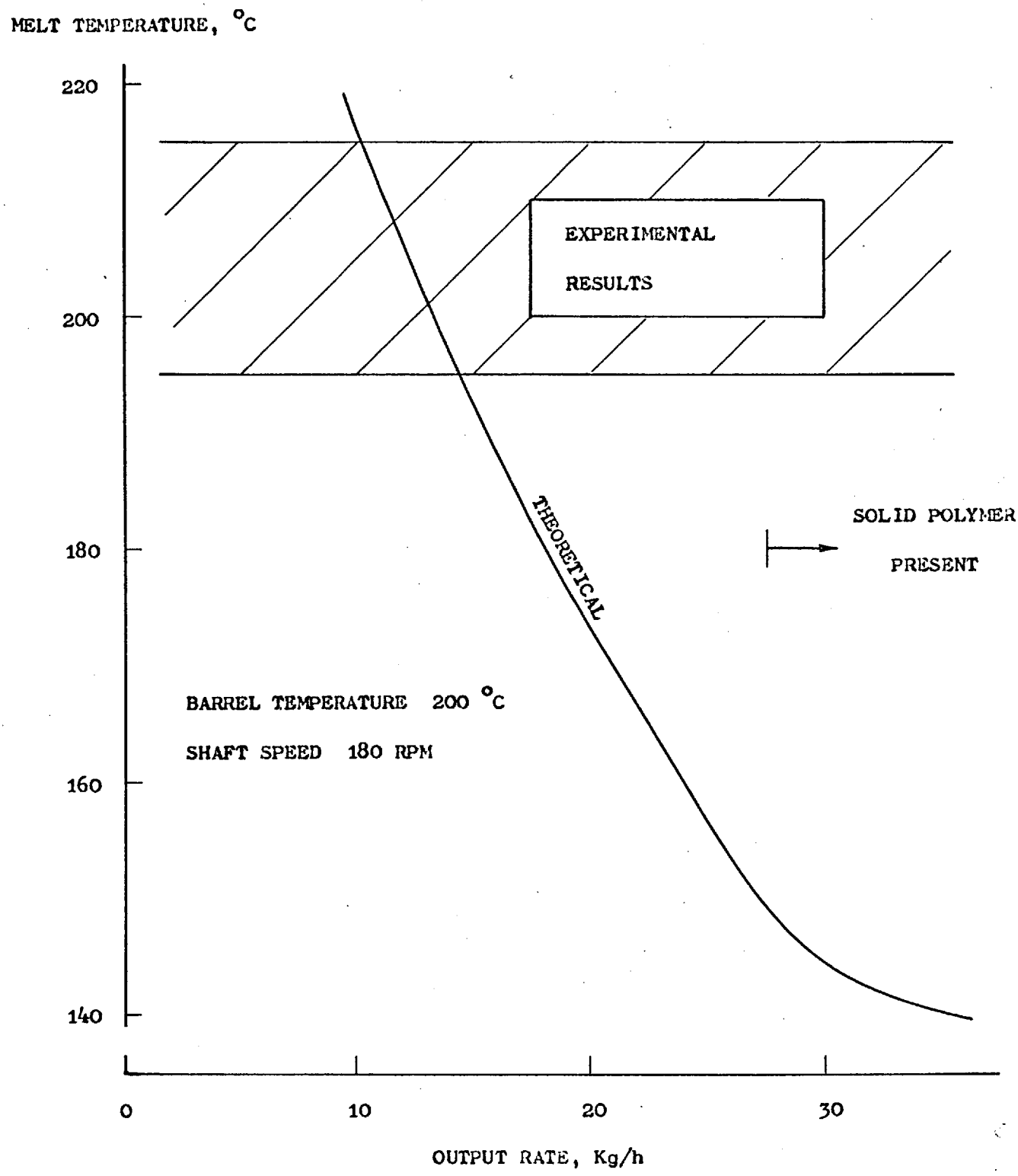

FIG. 5.9 - COMPARISON OF RESULTS FOR OUTPUT MELT TEMPERATURE AS FUNCTION OF OUTPUT RATE

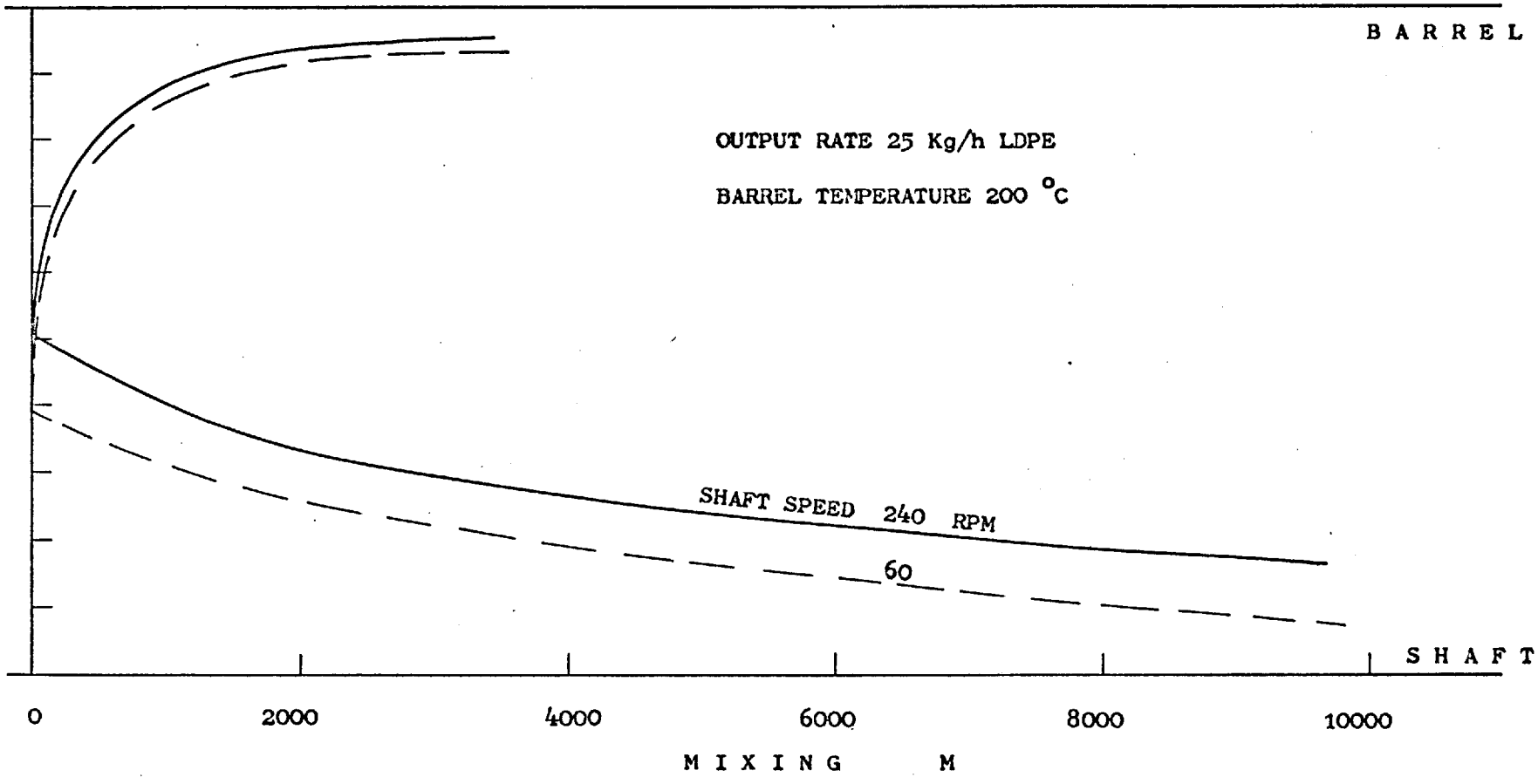

FIG. 5.10 - VARIATION OF MIXING ACROSS THE ANNULAR GAP AT THE COMPLETION OF MELTING

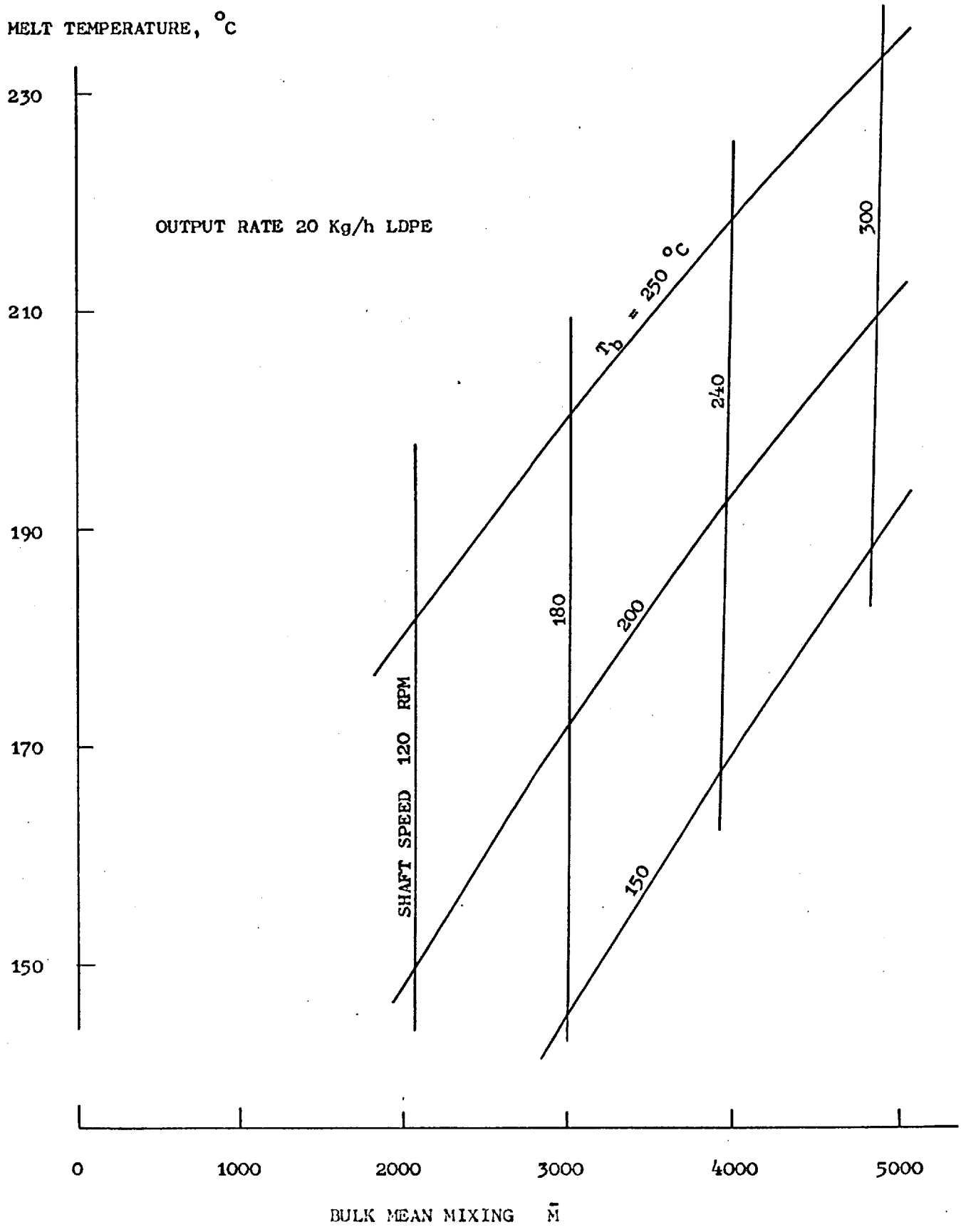

FIG. 5.11 - EFFECT OF OPERATING CONDITIONS ON EXTRUDATE QUALITY (BULK MEAN MELT TEMPERATURE AND MIXING)

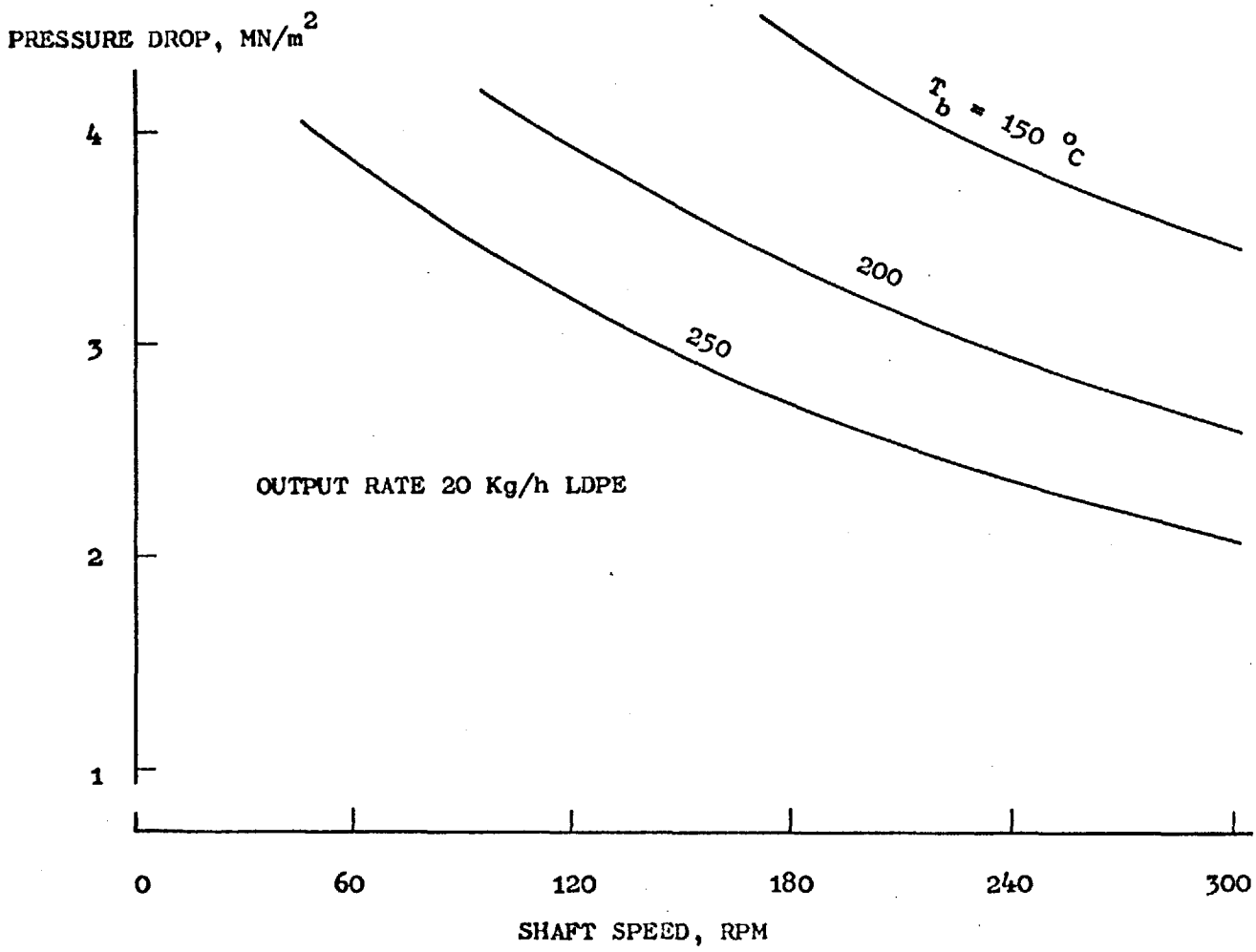

FIG. 5.12 - EFFECT OF OPERATING CONDITIONS ON THE PRESSURE DROP ALONG THE ANNULAR CHANNEL TO MAINTAIN CONSTANT OUTPUT RATE

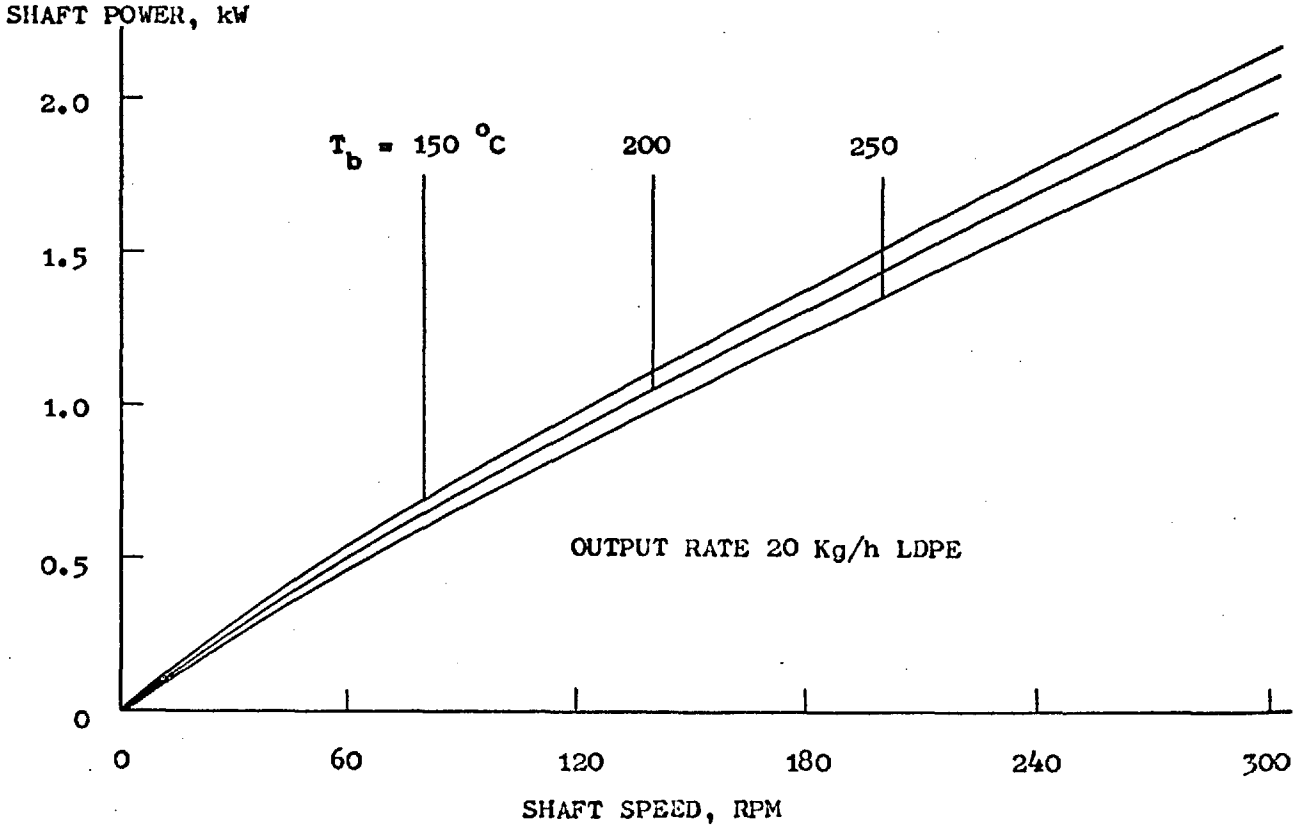

FIG. 5.13 - EFFECT OF OPERATING CONDITIONS ON SHAFT POWER CONSUMPTION

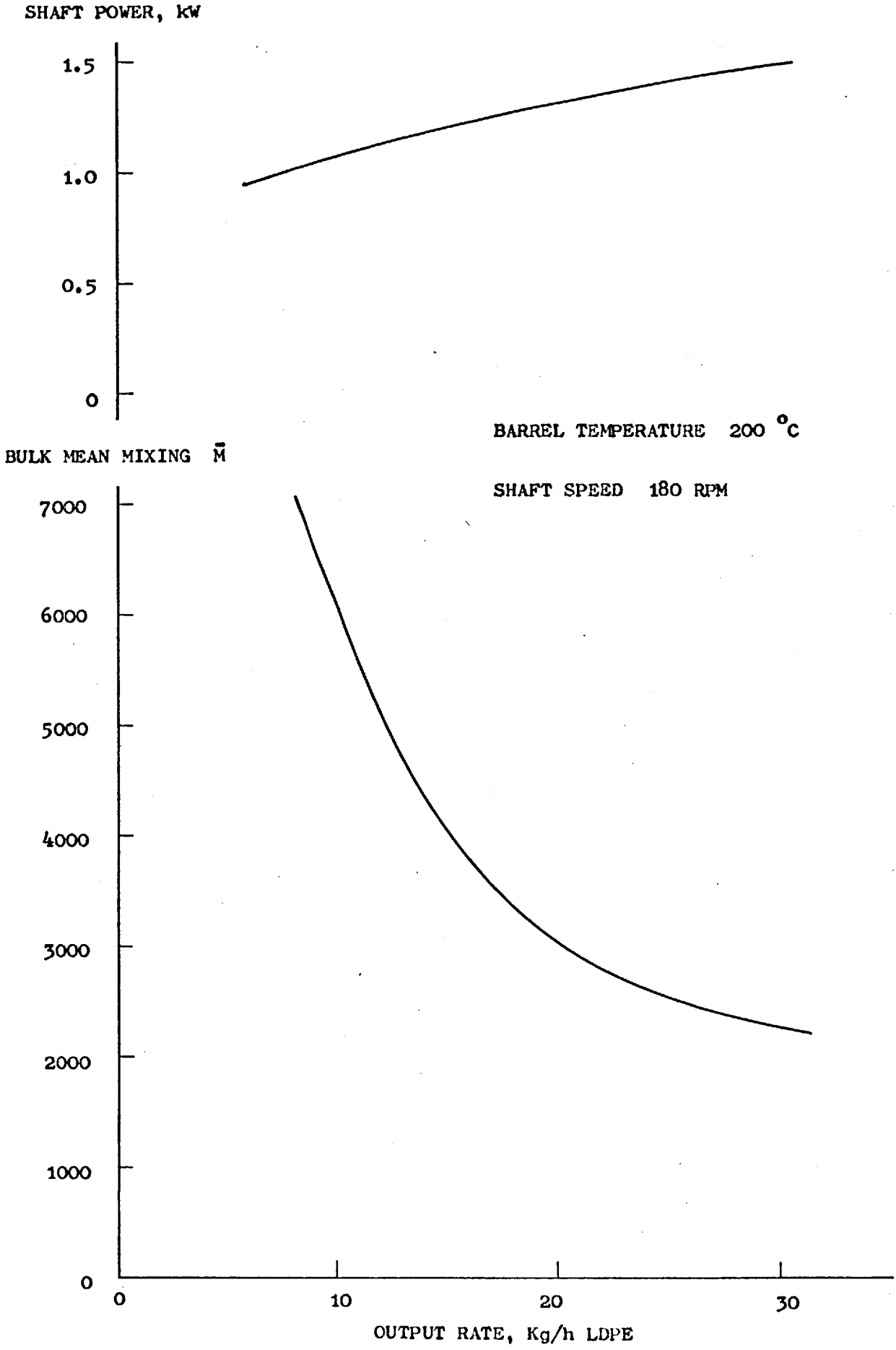

FIG. 5.14 - VARIATION OF SHAFT POWER AND BULK MEAN MIXING WITH OUTPUT RATE

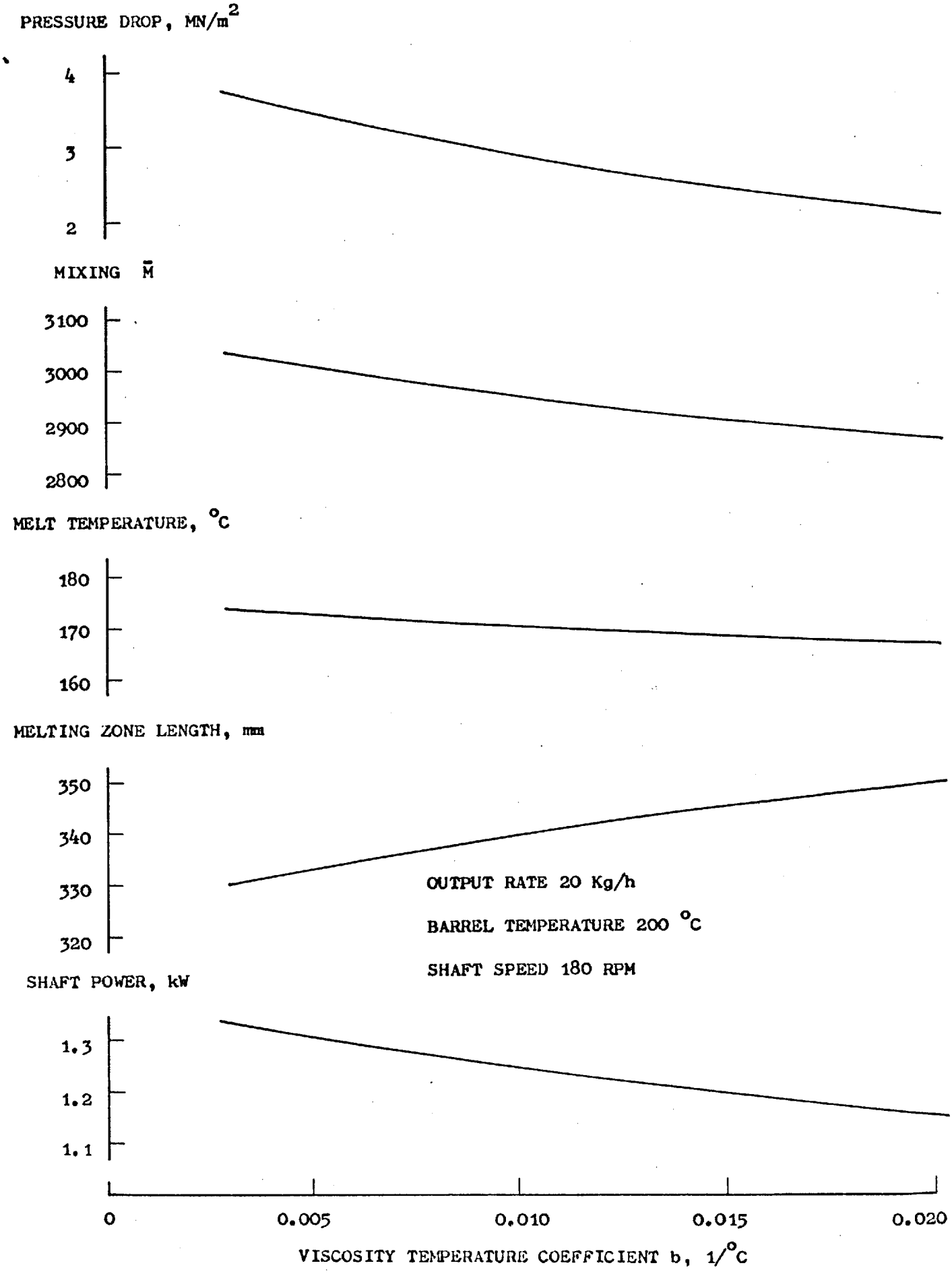

FIG. 5.15 - RESULTS FOR SIMULATIONS CONCERNING THE DEPENDENCE OF VISCOSITY ON TEMPERATURE

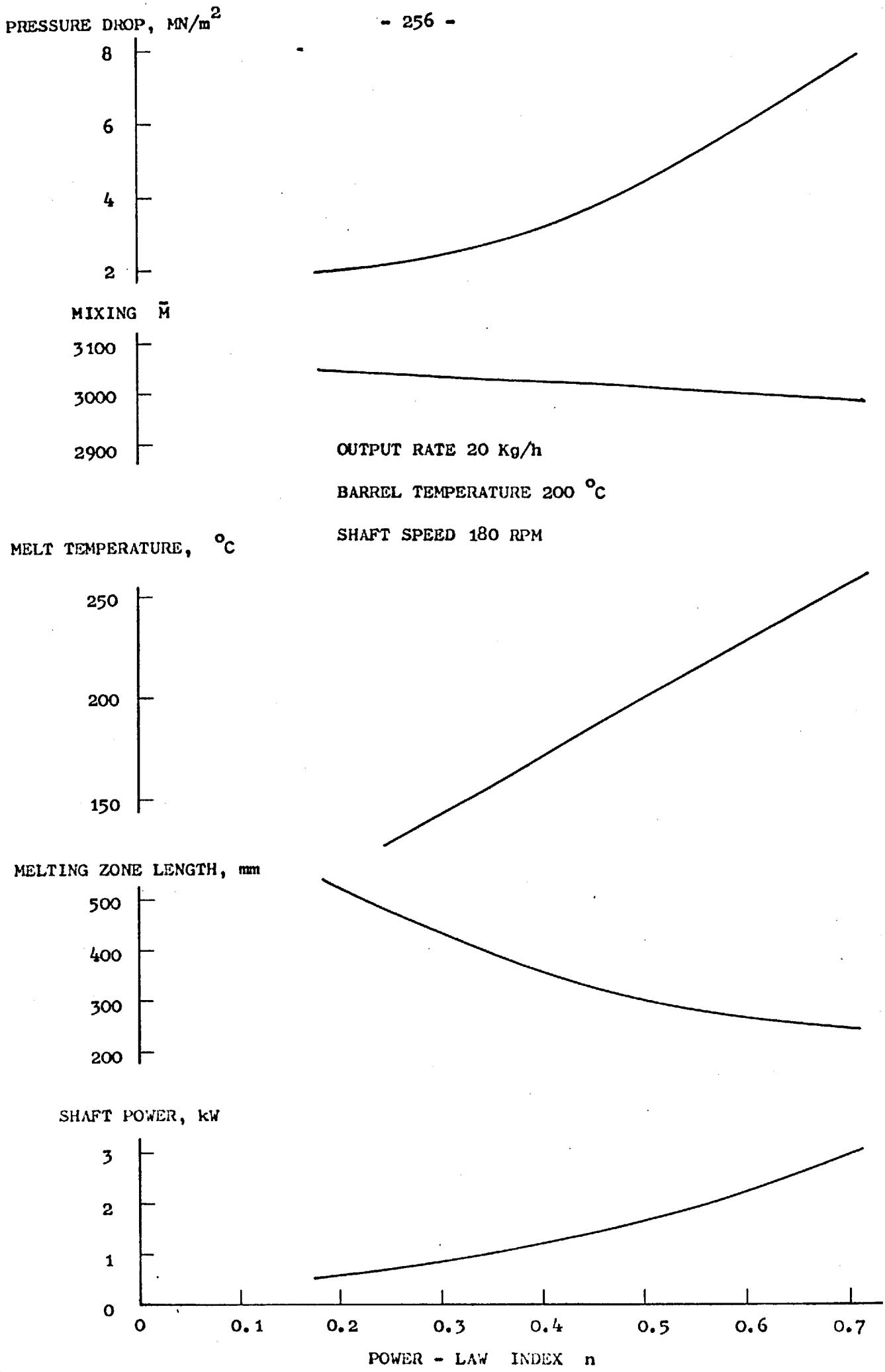

FIG. 5.16 - RESULTS FOR SIMULATIONS CONCERNING THE DEPENDENCE OF VISCOSITY ON SHEAR RATES

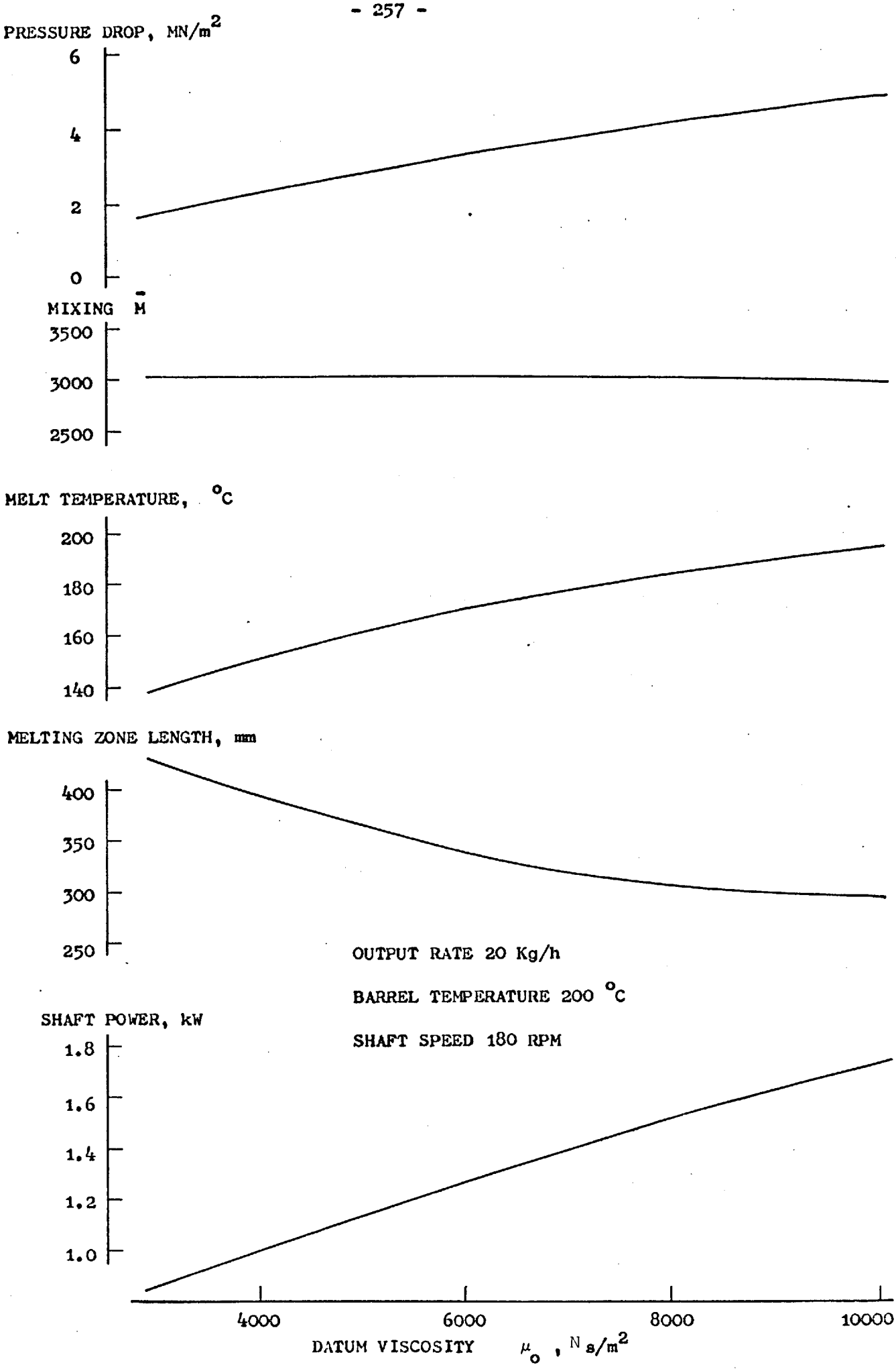

FIG. 5.17 - RESULTS FOR SIMULATIONS CONCERNING THE DATUM VISCOSITY

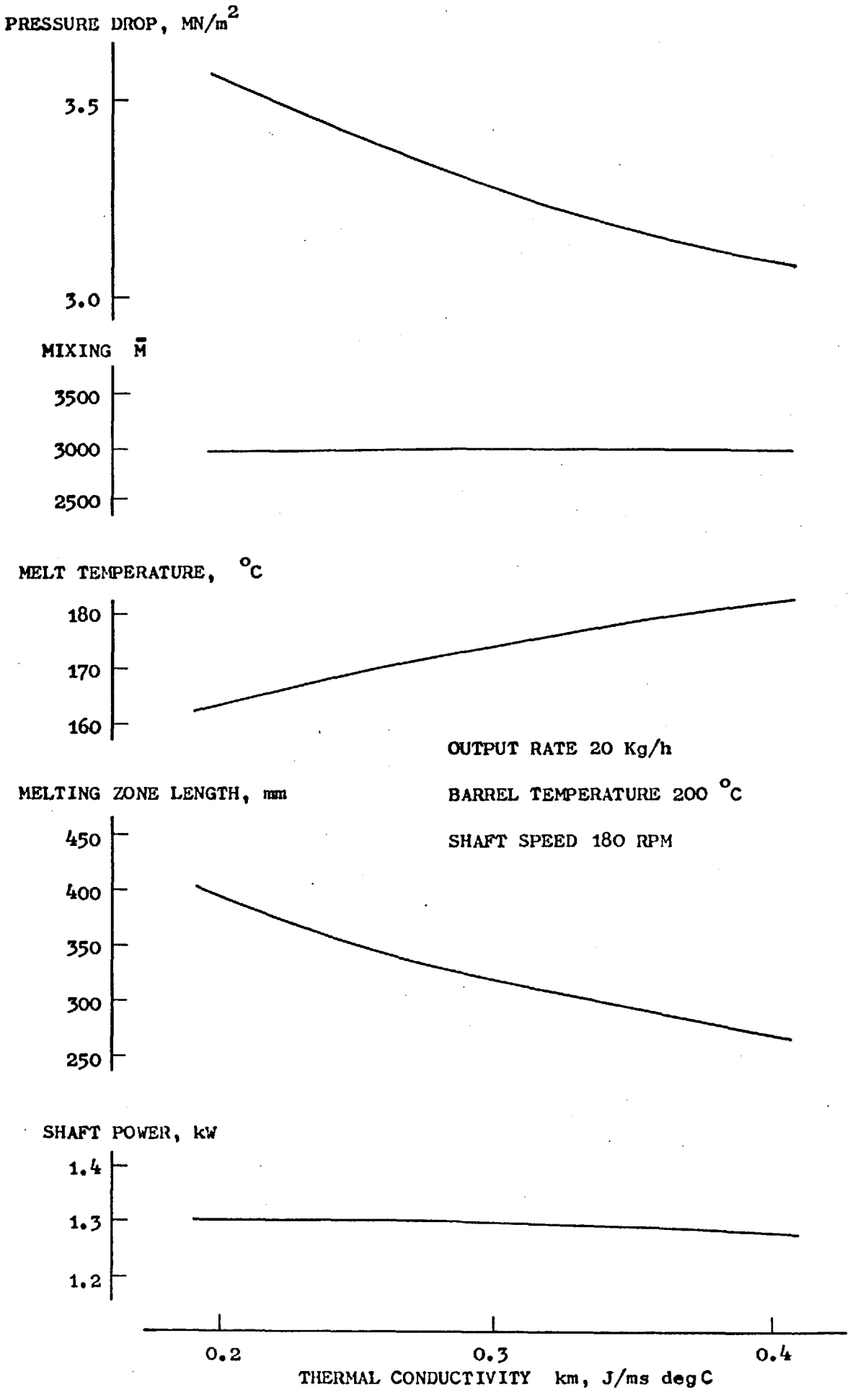

FIG. 5.18 - RESULTS FOR SIMULATIONS CONCERNING THE THERMAL CONDUCTIVITY OF THE POLYMER MELT

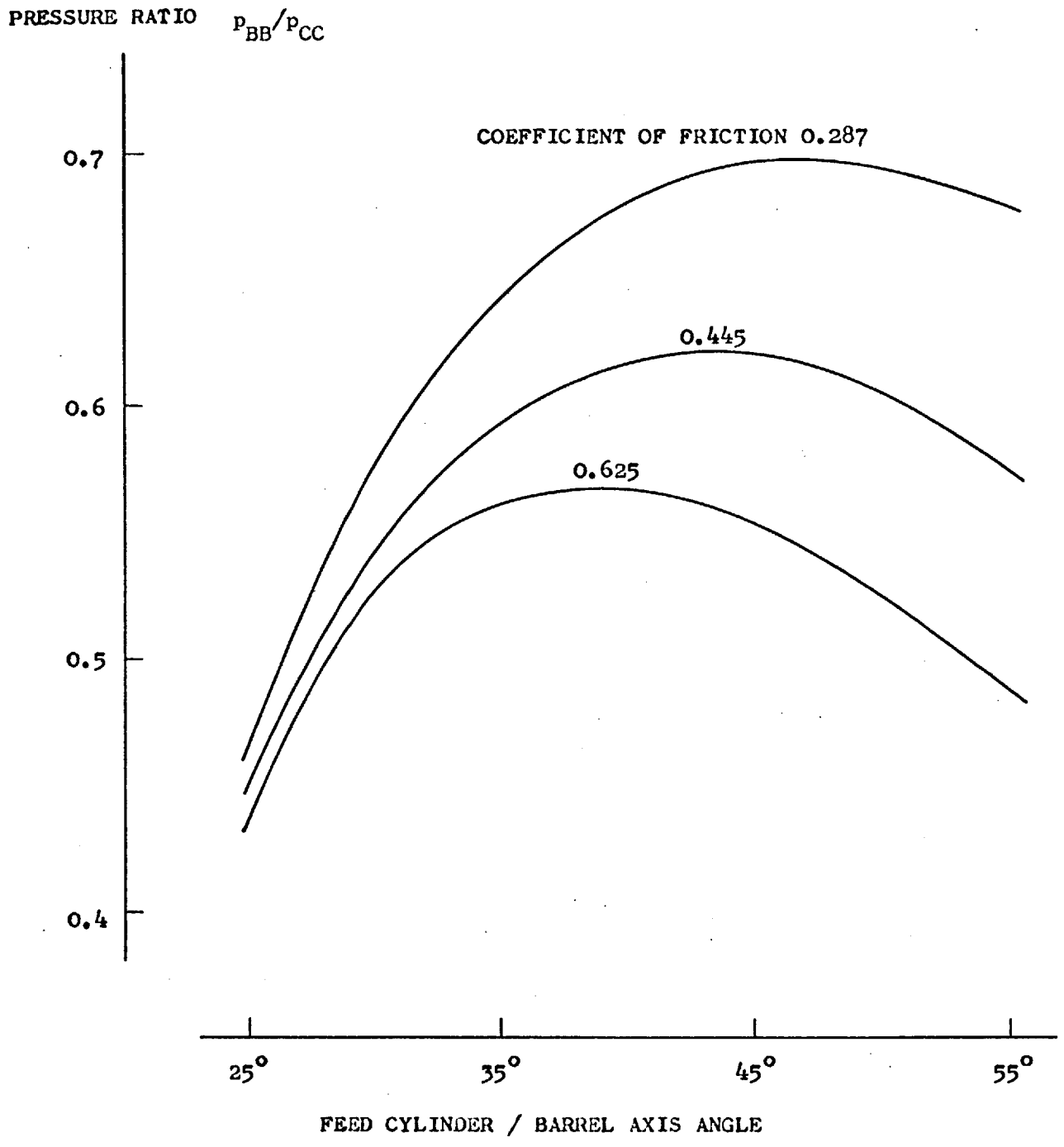

FIG. 5.19 - INFLUENCE OF THE FEED CYLINDER / BARREL AXIS ANGLE ON THE PRESSURE TRANSMISSION IN THE ANGLED FEEDING ZONE

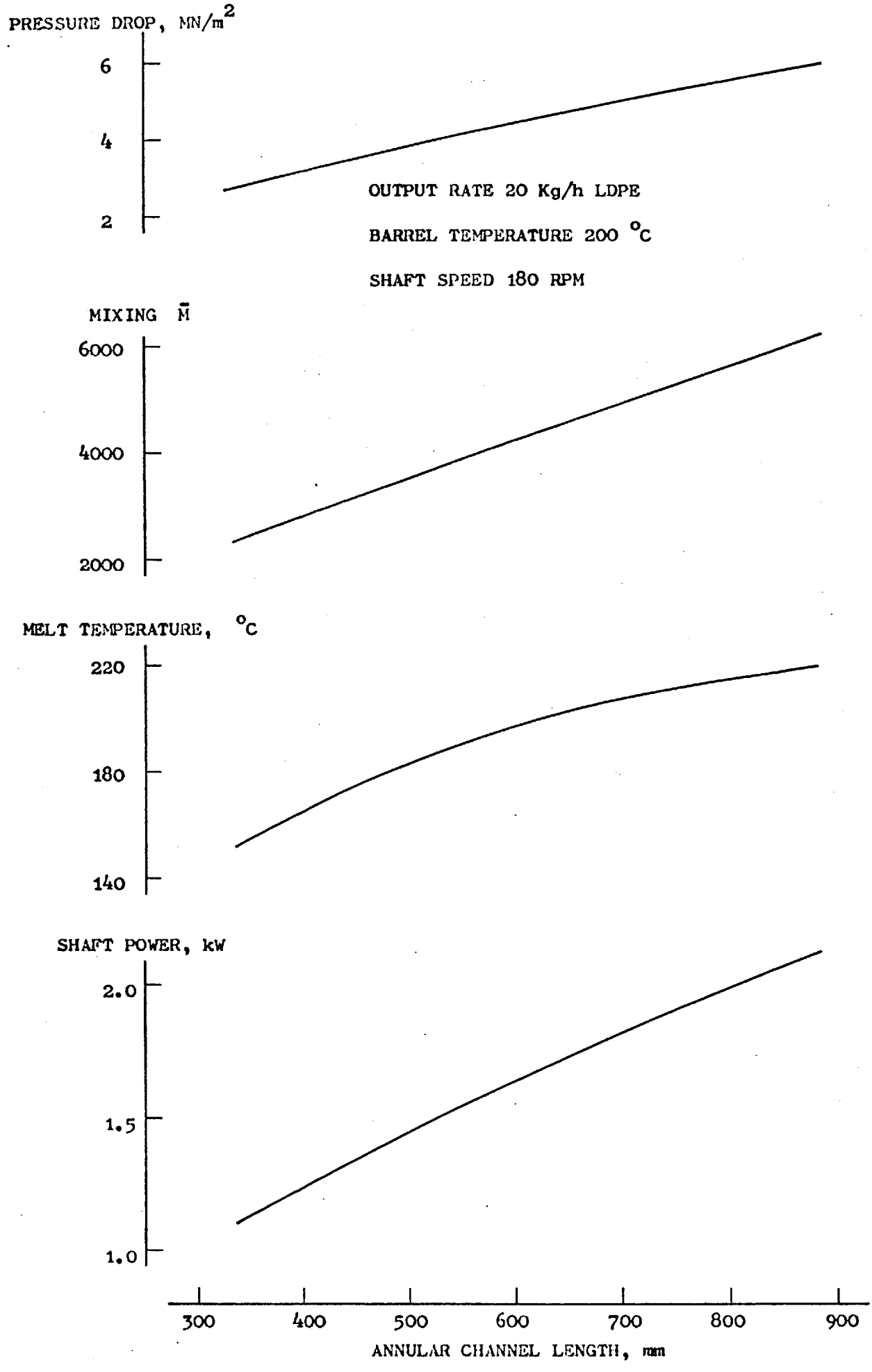

FIG. 5.20 - RESULTS FOR SIMULATIONS CONCERNING THE LENGTH OF THE ANNULAR FLOW CHANNEL

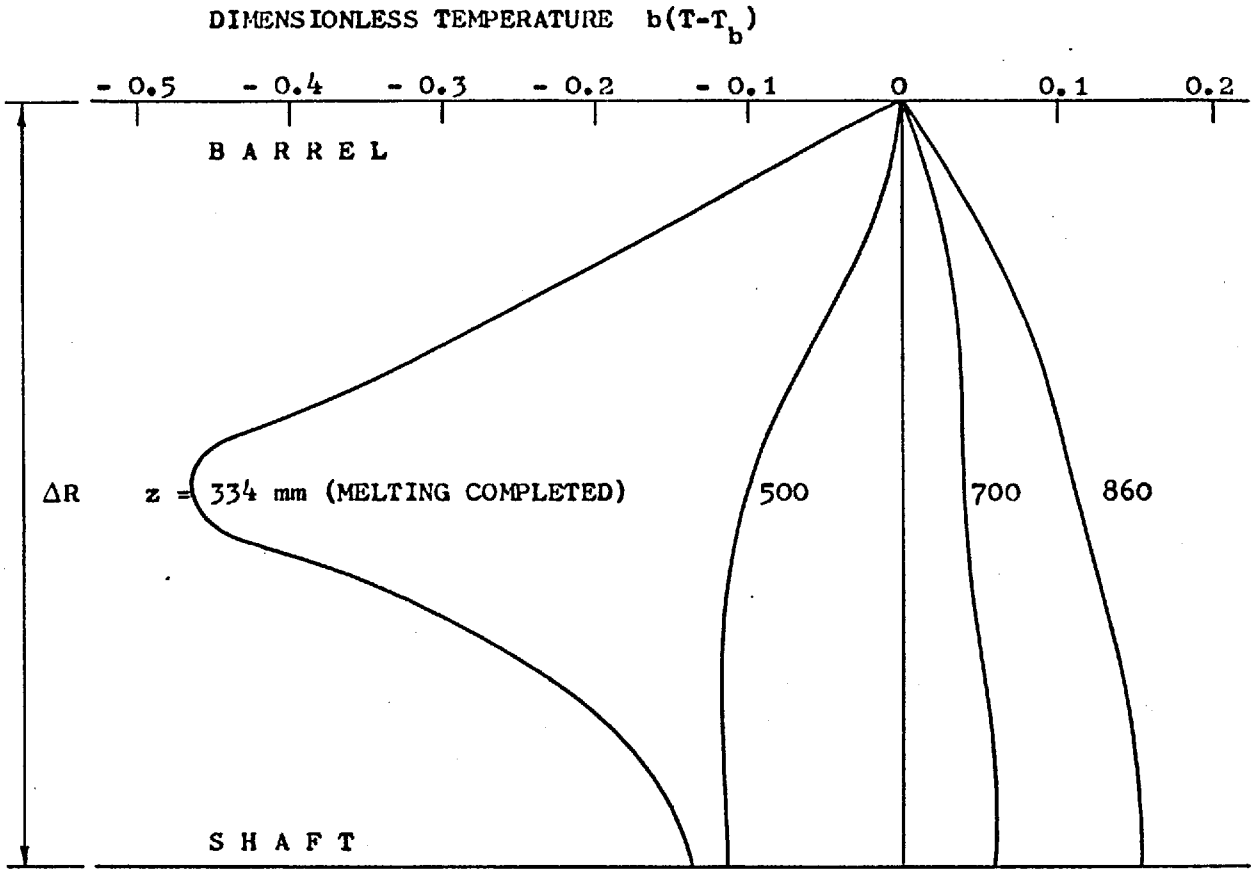

OUTPUT RATE 20 Kg/h LDPE

BARREL TEMPERATURE 200 °C

SHAFT SPEED 180 RPM

FIG. 5.21 - DEVELOPMENT OF MELT TEMPERATURE PROFILES ALONG THE FLOW CHANNEL

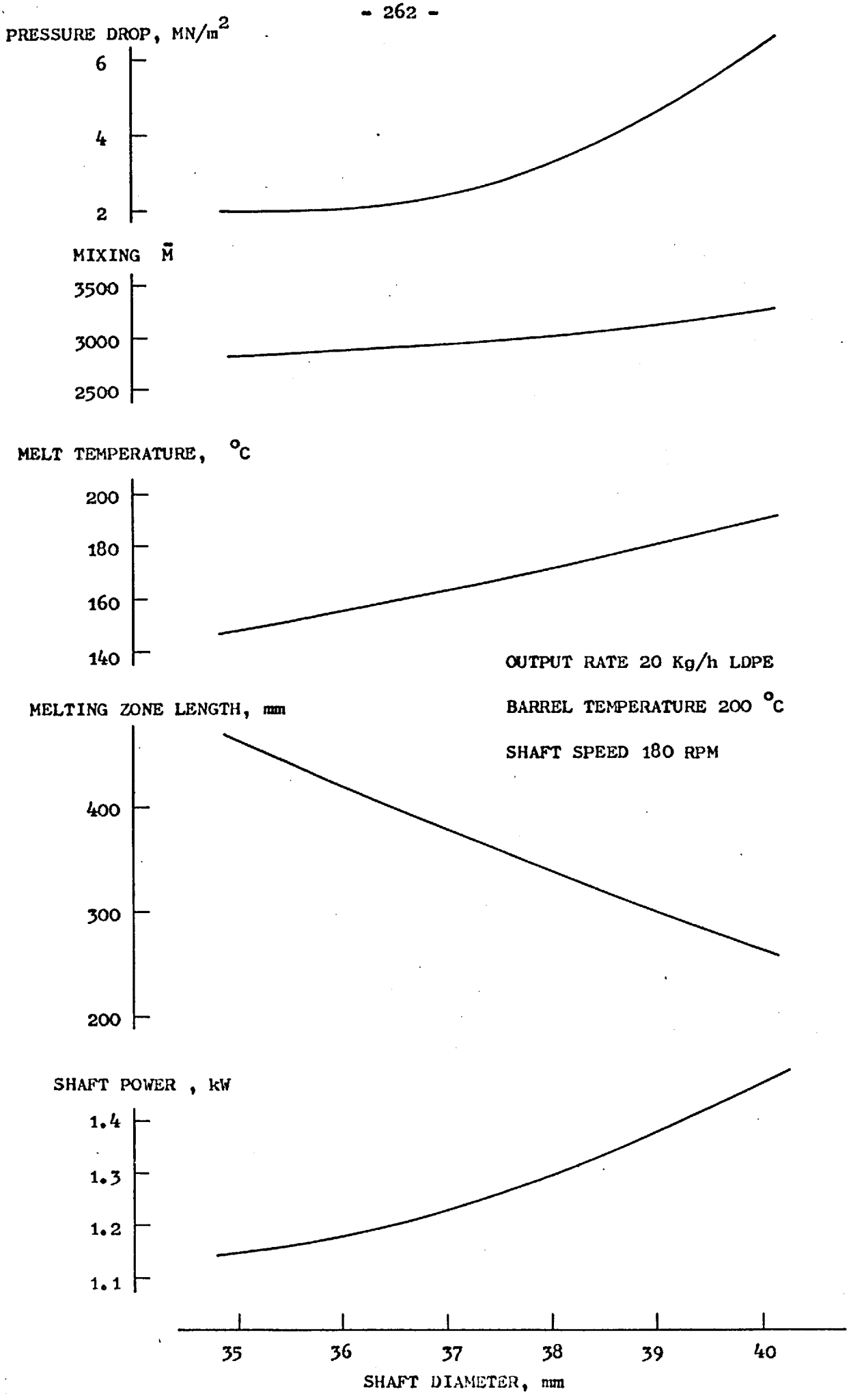

FIG. 5.22 - RESULTS FOR SIMULATIONS CONCERNING THE DIAMETER OF THE SHAFT

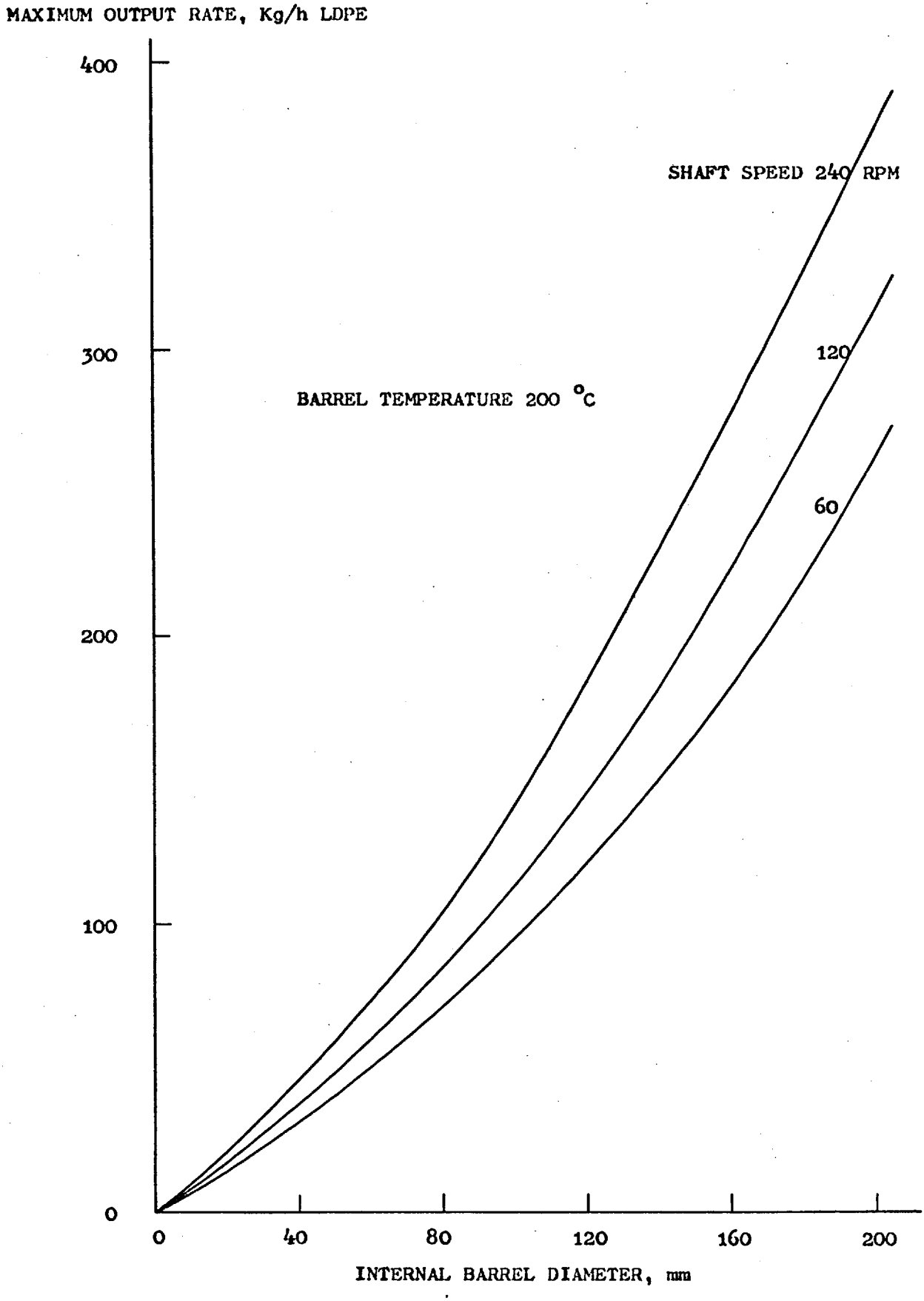

FIG. 5.23 - PREDICTIONS FOR MAXIMUM OUTPUT RATES FOR GEOMETRICALLY SIMILAR EXTRUDERS

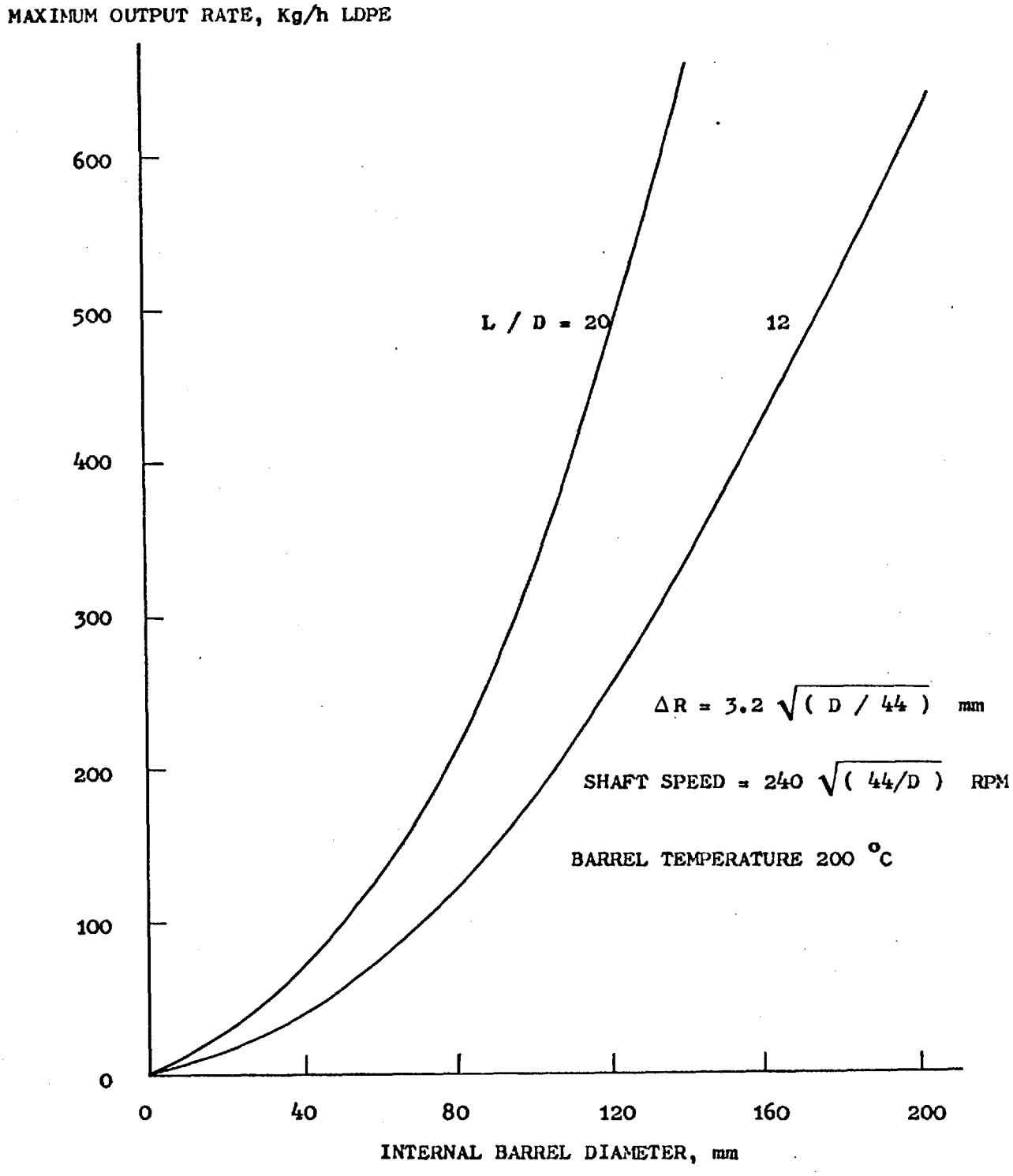

FIG. 5.24 - RESULTS FOR SCALING-UP USING A SQUARE ROOT LAW FOR VARYING THE SIZE OF THE ANNULAR GAP AND THE SHAFT SPEED

CHAPTER 6

GENERAL CONCLUSIONS

6.1 Some Economical Considerations

It is appropriate at this stage to consider some economical aspects of the process. The single screw extruder has been selected as a basis for comparison since this is the most widely available machine performing similar functions. A complete economical comparison is not possible as this would have to include amongst other factors, the running costs, ability to process different materials and the flexibility of the process, all of which are difficult to quantify. The comparison presented below is thus limited to capital costs only which are relatively simple to estimate.

The cost of manufacture of the existing extruder has been estimated at £4000 (at 1972 prices). The details of this estimate are given in Table 6.1. In order to extrapolate the costs of similar machines of different sizes, a simple formula applicable to the machinery manufacturing industry has been used. This states that the costs of similar types of machinery rise according to the volume of the machine raised to the power 0.6. The volume of the machine in the present case has been taken as proportional to D^2L. Table 6.2 shows the cost of different extruders obtained using this rule. Also shown in the Table, for comparison, are the costs of typical commercially available single screw extruders. These apply to fully equipped extruders with a length to diameter ratio of 25:1 but do not include any specialist equipment. For certain applications, additional equipment costs might upset considerably these figures. It is worth noting that these cost figures fit closely the extrapolation formula used above. The performance

figures for the ram extruder have been taken from the results presented in Figure 5.24 and the longer version of the machine has been assumed.

It can be seen that the capital costs for extruders tend to be higher than those for single screw extruders. It should, however, be pointed out that the output rates considered are comparatively modest in that the shaft speed was relatively low and that higher output rates could be obtained from each machine if the shaft speed was increased. Also, against the capital costs must be offset other factors. For example, considering the output quality in terms of mixing, an L/D = 12, D = 200 mm ram extruder giving an output rate of 620 kg/h would yield $\overline{M}$ = 8700 whilst a screw extruder would impart about half the mixing only.

6.2 Conclusions and Suggestions for Further Work

Throughout this thesis, where appropriate, discussions and conclusions have been presented at the end of each individual section and chapter. It remains now to summarise some general conclusions about the work done.

The major aim of the project in developing a process in which control of plasticating functions could be isolated from that of output rate was successfully achieved in the form of the continuous ram extruder.

In its present state, minor improvements to the extruder are necessary before it may be used commercially for product extrusion, in particular the output uniformity must be improved. Further work on this aspect could involve an assessment of likely improvements by the use of multiple feed rams. However, lack of output uniformity should not limit its application to operations such as plastication in moulding machines and homogenisation during polymer manufacture. Another forseeable application for the ram extruder is in the reprocessing of

scrap polymeric material largely due to its ability to accept feedstock under the most varied form. Its versatility should also make it ideally suited to other 'difficult to process' materials. A suggestion for further experimental work would be to investigate its suitability for processing thermosets (the extruder would have to be cleared with an adequate material at the end of each run).

A simple economical comparison with screw extruders based on capital costs only has shown that the ram extruder tends to be more costly than a comparable screw extruder. However, capital costs are not the only costs in which comparisons should be based. For example, it has been pointed out that the ram extruder can be more economical in terms of specific power consumption. In fact, capital costs may only be a minor fraction of the total cost involved in processing unit mass of material.

In conclusion, the prospects of commercial success for the process are high, at least in applications where the screw extruder has been proved to be unsuitable.

The bulk of this thesis was devoted to theoretical studies of the processes occurring in the ram extruder. This was a necessary part of the development work if further progress was to be made. It gave an insight to the method and the outcome of this was a model by which the operation of the machine could be simulated. The usefulness of the theoretical model for predicting performance and for design applications was demonstrated by the selected set of examples.

Though the theory was derived mainly related to the ram extruder, it is thought that some of the ideas formulated and methods used are of use to other workers in related fields of study. In particular, some aspects of the analyses of pressures in granular material and melting of

polymers should be relevant to other polymer processing equipment.

Further work on frictional behaviour is suggested here. It has been seen that frictional losses are very critical on the coefficients of friction. Measurements of these have been proved to be unreliable in that under similar conditions their values can vary by a factor of 2 to 3.

The theoretical analyses can be further improved by relaxing some of the assumptions in the models, for example, the geometrical and other simplifications introduced in the solids feeding analysis.

The initiation of the melting mechanism should also be investigated in future. This will not only be valuable to the present work but also to work related to melting in screw extruders and other processing machinery.

Table 6.1

Estimated Cost of the Prototype Continuous Ram Extruder (1972)

Materials and components		£1,000
Hydraulic system		£1,000
Manufacturing costs		£2,500
	Total	£4,500

This does not include instrumentation other than that required for control functions. Manufacturing costs are a considerable proportion of the total cost of the prototype. It includes the labour costs at the College workshop and also overheads. Under commercial production conditions, a reasonable manufacturing cost saving of about £500 is estimated and hence a final cost of about £4000 is derived (at 1972 prices).

Table 6.2

Capital Costs of Single Screw Extruders and Ram Extruders

Output Rate (kg/h) LDPE	SCREW EXTRUDERS			RAM EXTRUDERS		
	Screw Diameter (mm)	Length (m)	Cost £ x 1000	Barrel Diameter (mm)	Length (m)	Cost £ x 1000
80	65	1.6	6	50	1.0	6.7
250	115	2.9	12	90	1.8	19
500	150	3.8	18	120	2.4	32
1000	210	5.3	40	170	3.4	58

REFERENCES

[1] FENNER, R.T.

'The Design of Large Hot Melt Extruders',

Paper 13, Conference on Engineering Design of Plastics Processing Machinery, University of Bradford, 1974.

[2] McKELVEY, J.M.

'Polymer Processing',

John Wiley, New York, 1962.

[3] PEARSON, J.R.A.

'Mechanical Principles of Polymer Melt Processing',

Pergamon, Oxford, 1966.

[4] FENNER, R.T.

'Extruder Screw Design',

Iliffe, London, 1970.

[5] TADMOR, Z., and KLEIN, I.

'Principles of Plasticating Extrusion',

Van Nostrand Reinhold, New York, 1970.

[6] EDMONDSON, I.R.

'Melting in Single Screw Extruders',

Ph.D. Thesis, University of London, 1973.

[7] SCHNEIDER, K.

'Processes in the Feeding Zone of an Extruder',

IKV, TH Aachen, 1969.

[8] LOVEGROVE, J.G.A.

'Solids Flow in a Polymer Extruder',

Ph.D. Thesis, University of London, 1972.

[9] WESTOVER, R.F.

'New Views of Extrusion',

SPE Jl., 21, (5), 455, 1965.

[10] GOPPEL, J.M.

'New Concepts in Processing',

Plast. Polym., 37, (131), 449, 1969.

[11] ENGEL, T.

'The Melting Plate Extruder-Rotomelter',

Kunststoffe, 53, (4), 255, 1963.

[12] MAILLEFER, C.

'A Two-Channel Extruder Screw',

Mod. Plast., 40, (5), 132, 1963.

[13] MAXWELL, B., and SCALORA, A.J.

'The Elastic Melt Extruder Works Without Screw',

Mod. Plast., 37, (2), 107, 1959.

[14] WESTOVER, R.F.

'A Hydrodynamic Screwless Extruder',

SPE Jl., 18, (12), 1473, 1962.

[15] MINER, R.V.

US Patent No. 3 032 814, 1962.

[16] MAXWELL, B.

'A New Twist in Mixing Extruders',

Plast. Engng, 30, (5), 40, 1974.

[17] BORG-WARNER

'Une Nouvelle Unité d'Injection à Cône Rotatif Équipe les Presses Bliss/Borg-Warner',

Plast. Mod. et Elast., 20, (3), 97, 1968.

[18] BORG-WARNER

'Rotary Shear Cone Plasticating',

Rubber Age, 102, (6), 68, 1970.

[19] MENGES, G., et al

'Ultra-High Pressure Plastification of Plastics - Significance and Application',

Kunststoffe, 60, (2), 85, 1970.

[20] ENGEL, T.

'Injection Moulding by Compression Melting',

Mod. Plast., 47, (8), 96, 1970.

[21] POCKLINGTON, A.R.

'The Melting of Plastics by the Use of Rollers',

Ph.D. Thesis, University of London, 1972.

[22] WESTOVER, R.F.

'Continuous Flow Ram Type Extruder',

Mod. Plast., 40, (7), 130, 1963.

[23] FENNER, R.T., and WATTS, S.G.W.G.

'Continuous Ram Extrusion of Polymers: Preliminary Investigations',

Plast. Polym., 40, (184), 199, 1972.

[24] MUSTAFAEV, V.A., et al

'Cold Flow and Melting of Plastics under Severe Friction Conditions',

Mekh. Polim., 1, (5), 95, 1965.

[25] COHEN, S.C., and TABOR, D.

'The Friction and Lubrication of Polymers',

Proc. R. Soc., A291, 186, 1966.

[26] HACHMANN, H., and STRIKLE, E.

'Friction and Wear of Unlubricated Systems of Plastics Paired with Steel',

Kunststoffe, 59, (1), 45, 1969.

[27] McLAREN, K.G., and TABOR, D.
'Viscoelastic Properties and the Friction of Solids - Friction of Polymers: Influence of Speed and Temperature',
Nature, 197, (4870), 856, 1963.

[28] HARR, H.E.
'Foundations of Theoretical Soil Mechanics',
McGraw-Hill, New York, 1966.

[29] SCHOFIELD, A., and WROTH, P.
'Critical State Soil Mechanics',
McGraw-Hill, London, 1968.

[30] TERZAGHI, K.
'Theoretical Soil Mechanics',
John Wiley, New York, 1943.

[31] NADAI, A.L.
'Theory of Flow and Fracture of Solids - Volume 2',
McGraw-Hill, New York, 1963.

[32] KAWAKITA, K., and TSUTSUMI, Y.
'An Empirical Equation of State for Powder Compression',
Japan. J. Appl. Phys., 4, (1), 56, 1965.

[33] GLASTONBURY, J.R., and BRATEL, P.G.
'Pressures in Contained Particle Beds from a Two-Dimensional Model',
Trans. Instit. Chem. Engrs., 44, 128, 1966.

[34] STEPANOFF, A.J.
'Gravity Flow of Bulk Solids and Transport of Solids in Suspension',
John Wiley, New York, 1969.

[35] SPENCER, R.S., GILMORE, G.D., and WILEY, R.M.
'Behaviour of Granulated Polymers under Pressure',
J. Appl. Phys., 21, (6), 527, 1950.

[36] TOOR, H.L., and EAGLETON, S.D.
'Plug Flow and Lubrication of Polymer Particles',
Indust. Engng Chem., 48, (10), 1825, 1956.

[37] FORD, H.
'Advanced Mechanics of Materials',
Longmans, London, 1963.

[38] SOKOLOVSKII, V.V.
'Statics of Soil Media',
Butterworths, London, 1960.

[39] CRANDALL, S.H.
'Engineering Analysis - A Survey of Numerical Procedures',
McGraw-Hill, New York, 1956.

[40] COLLATZ, L.
'The Numerical Treatment of Differential Equations',
Translation of 2nd edition, Springer-Verlag, Berlin, 1966.

[41] GARABEDIAN, P.R.
'Partial Differential Equations',
John Wiley, New York, 1967.

[42] COURANT, R., and FRIEDRICHS, K.O.
'Supersonic Flow and Shock Waves',
Interscience, New York, 1948.

[43] THOMSON, E.G., YANG, C.T., and KOBAYASHI, S.
'Mechanics of Plastic Deformation in Metal Processing',
McMillan, New York, 1965.

[44] ARPACI, V.S.
'Conduction Heat Transfer',
Addison-Wesley, Reading, Massachusetts, 1966.

[45] ROSS, T.K.

'Heat Transfer to Fusible Solids',

Chem. Engng Sci., 1, (5), 212, 1952.

[46] ROSS, T.K.

'Melting of Solids',

Chem. Engng Prog. Symp. Series, 51, (17), 67, 1955.

[47] SKELLAND, A.H.P.

'Heat Transfer in the Melting of Solids to Non-Newtonian Liquids',

Can. J. Chem. Engng, 44, (2), 64, 1966.

[48] SKELLAND, A.H.P.

'Non-Newtonian Flow and Heat Transfer',

John Wiley, New York, 1967.

[49] GRIFFIN, O.M., and SZEWCZYK, A.A.

'An Analytical and Experimental Study of the Melting of Bulk Solids on Inclined Plane Heated Surface',

Proc. of 4th Int. Heat Transfer Conf., 1, Paris, 1970.

[50] GRIFFIN, O.M.

'On the Melting of Solids to Non-Newtonian Fluids',

Chem. Engng Sci., 25, (1), 109, 1970.

[51] GRIFFIN, O.M.

'Thermal Transport in the Contact Melting of Solids',

Polym. Engng Sci., 12, (4), 265, 1972.

[52] SUNDSTROM, D.M., and YOUNG, C.C.

'Melting Rates of Crystalline Polymers under Shear Conditions',

Polym. Engng Sci., 12, (1), 59, 1972.

[53] TADMOR, Z.

'Fundamentals of Plasticating Extrusion - I. A Theoretical Model for Melting',

Polym. Engng Sci., 6, (3), 185, 1966.

[54] MADDOCK, B.H.
'A Visual Analysis of Flow and Mixing in Extruder Screws',
SPE Jl., 15, (5), 383, 1959.

[55] TADMOR, Z., DUVDEVANI, I.J., and KLEIN, I.
'Melting in Plasticating Extruders - Theory and Experiments',
Polym. Engng Sci., 7, (3), 198, 1967.

[56] FENNER, R.T., and EDMONDSON, I.R.
Polymer Processing Report No. 3, Mechanical Engineering Department,
Imperial College, 1974.

[57] MARTIN, B.
'Heat Transfer Coupling Effects Between a Dissipative Fluid Flow
and Its Containing Metal Boundaries',
Report for the European Working Party on Polymer Processing, 1970.

[58] YATES, B.
'Temperature Development in Single Screw Extruders',
Ph.D. Thesis, University of Cambridge, 1968.

[59] SMITH, G.D.
'Numerical Solution of Partial Differential Equations',
Oxford University Press, London, 1965.

[60] FREDRICKSON, A.G.
'Theory and Applications of Rheology',
Prentice-Hall, New Jersey, 1964.

[61] LODGE, A.S.
'Elastic Liquids',
Academic Press, New York, 1964.

[62] YI, B.
'Polymer Melt Flow in a Continuous Ram Extruder',
M.Sc. Thesis, Mech. Eng. Dept., Imperial Collge, London, 1972.

[63] MADDOCK, B.H.

'Extruder Scale-Up Theory',

SPE Jl., 15, (11), 983, 1959.

[64] FENNER, R.T., and WILLIAMS, J.G.

'Some Melt Flow and Mechanical Design Aspects of Large Extruders',

Polym. Engng Sci., 11, (6), 474, 1971.

APPENDIX A

EQUATIONS FOR PLANE EQUILIBRIUM OF A GRANULAR MEDIUM IN CRITICAL STATE

This appendix describes the derivation of the set of hyperbolic partial differential equations (3.10) used in chapter 3.

The equations for equilibrium are:

$$\left.\begin{aligned} \frac{\partial \sigma_x}{\partial x} + \frac{\partial \tau_{xy}}{\partial y} &= 0 \\ \frac{\partial \tau_{xy}}{\partial x} + \frac{\partial \sigma_y}{\partial y} &= 0 \end{aligned}\right\} \quad (A.1)$$

and the critical state condition gives:

$$\frac{1}{4}(\sigma_x - \sigma_y)^2 + \tau_{xy}^2 = \frac{\sin^2 \delta_i}{4}(\sigma_x + \sigma_y)^2 \quad (A.2)$$

or $$(\sigma_1 - \sigma_2) = (\sigma_1 + \sigma_2) \sin \delta_i \quad (A.3)$$

where $$\begin{matrix}\sigma_1 \\ \sigma_2\end{matrix} = \frac{1}{2}(\sigma_x + \sigma_y) \pm \sqrt{\left[\frac{1}{4}(\sigma_x - \sigma_y)^2 + \tau_{xy}^2\right]} \quad (A.4)$$

$$\left.\begin{aligned} \text{or} \quad \begin{matrix}\sigma_x \\ \sigma_y\end{matrix} &= \frac{1}{2}(\sigma_1 + \sigma_2) \pm \frac{1}{2}(\sigma_1 - \sigma_2) \cos 2\emptyset \\ \text{and} \quad \tau_{xy} &= \frac{1}{2}(\sigma_1 - \sigma_2) \sin 2\emptyset \end{aligned}\right\} \quad (A.5)$$

where $\emptyset$ is the angle between the direction of the major principal stress σ_1 and the x-axis. A new variable σ is introduced and is defined as:

$$\sigma = \frac{1}{2}(\sigma_1 + \sigma_2) \quad (A.6)$$

From equation (A.3), and using the definition for σ,

$$(\sigma_1 - \sigma_2) = 2\,\sigma \sin \delta_i \qquad (A.7)$$

Substituting equations (A.6) and (A.7) into expressions (A.5),

$$\left.\begin{aligned} \sigma_x \\ \sigma_y \end{aligned}\right\} = \sigma\,(1 \pm \sin \delta_i \cos 2\emptyset)$$

and $$\tau_{xy} = \sigma \sin \delta_i \sin 2\emptyset \qquad (A.8)$$

Note that the three stress components σ_x, σ_y and τ_{xy} are now expressed in terms of two variables, σ and $\emptyset$ in equations (A.8). Also, equations (A.8) identically satisfy equation (A.2). The two equations are obtained by substituting equations (A.8) into the set (A.1),

$$\left.\begin{aligned} &(1 + \sin \delta_i \cos 2\emptyset)\frac{\partial \chi}{\partial x} + \sin \delta_i \sin 2\emptyset \frac{\partial \chi}{\partial y} - \cos \delta_i \\ &\left(\sin 2\emptyset \frac{\partial \emptyset}{\partial x} - \cos 2\emptyset \frac{\partial \emptyset}{\partial y}\right) = 0 \\ &\sin \delta_i \sin 2\emptyset \frac{\partial \chi}{\partial x} + (1 - \sin \delta_i \cos 2\emptyset)\frac{\partial \chi}{\partial y} + \cos \delta_i \\ &\left(\cos 2\emptyset \frac{\partial \emptyset}{\partial x} + \sin 2\emptyset \frac{\partial \emptyset}{\partial y}\right) = 0 \end{aligned}\right\} \qquad (A.9)$$

where $\chi = \dfrac{\cot \delta_i}{2} \ell n \dfrac{\sigma}{\sigma_o}$ and σ_o is an arbitrary constant quantity with units of stress. Equations (A.9) are still complicated and further simplifications are made by defining the following variables:

$$\alpha = \frac{\pi}{4} - \frac{\delta_i}{2}$$

and $\xi = \chi + \phi \quad , \quad \eta = \chi - \phi$ (A.10)

or $2\chi = \xi + \eta \quad , \quad 2\phi = \xi - \eta$

Substituting these definitions into equations (A.9) and multiplying the first one by sin $(\phi-\alpha)$ or sin $(\phi+\alpha)$, the second one by -cos $(\phi-\alpha)$ or -cos $(\phi+\alpha)$, and adding,

$$\left.\begin{aligned} \frac{\partial \eta}{\partial x} + \tan(\phi - \alpha)\frac{\partial \eta}{\partial y} &= 0 \\ \frac{\partial \xi}{\partial x} + \tan(\phi + \alpha)\frac{\partial \xi}{\partial y} &= 0 \end{aligned}\right\} \quad \text{(A.11)}$$

APPENDIX B

NUMERICAL METHODS

B.1 Solution of the Energy Conservation Equation

The energy conservation equation is of the form:

$$v_z \frac{\partial T}{\partial z} = \alpha_m \frac{\partial^2 T}{\partial y^2} + G$$

The solution domain is divided into a grid as shown in Figure B.1. Note that the two boundaries need not be parallel and the error introduced as a consequence of using the distorted grid from the truly rectangular one is small as long as the taper is slowly varying. The partial derivatives in the energy equation are replaced by the following finite difference expressions:

$$\left(\frac{\partial T}{\partial z}\right)_{i,j} \simeq \frac{1}{\Delta z} \left(T_{i+1,j} - T_{i,j}\right) \qquad (B.1)$$

and

$$\left(\frac{\partial^2 T}{\partial y^2}\right)_{i,j} \simeq \frac{1}{2(\overline{\Delta y})^2} \left[\left(T_{i+1,j+1} - 2T_{i+1,j} + T_{i+1,j-1}\right) + \left(T_{i,j+1} - 2T_{i,j} + T_{i,j-1}\right)\right] \qquad (B.2)$$

where i,j, etc., refer to the grid points as shown in Figure B.1. The truncation errors in expression (B.1) and (B.2) are of the order of (Δz) and $(\overline{\Delta y})^2$ respectively. Equation (B.2) is commonly known as the Crank-Nicholson average and is used for stepping downstream to evaluate the temperatures at i+1. Because Δy changes with z, a mean value $\overline{\Delta y} = (\Delta y_i + \Delta y_{i+1})/2$ is used in equation (B.2). Substituting the expressions (B.1) and (B.2) for the partial derivatives, the energy

conservation equation becomes

$$v_{z\,i,j}\,\frac{(T_{i+1,j} - T_{i,j})}{\Delta z} = \frac{\alpha_m}{2(\overline{\Delta y})^2}\,(T_{i+1,j+1} - 2T_{i+1,j} + T_{i+1,j-1})$$

$$+ \frac{\alpha_m}{2(\overline{\Delta y})^2}\,(T_{i,j+1} - 2T_{i,j} + T_{i,j+1}) + G_{i,j}$$

which can be rewritten as

$$-a_j\,T^+_{j-1} + b_j\,T^+_j - c_j\,T^+_{j+1} = d_j \qquad \text{(B.3)}$$

where $T^+_j = T_{i+1,j}$

$$a_j = c_j = \frac{\alpha_m}{2(\overline{\Delta y})^2}$$

$$b_j = \frac{\alpha_m}{(\overline{\Delta y})^2} + \frac{v_{z\,i,j}}{\Delta z}$$

and $$d_j = \frac{v_{z\,i,j}\,T_{i,j}}{\Delta z} + G_{i,j} + \frac{\alpha_m}{2(\overline{\Delta y})^2}\,(T_{i,j+1} - 2T_{i,j} + T_{i,j-1})$$

Given the solution at the step i, the coefficients a_j, b_j, c_j and d_j can all be evaluated. Equation (B.3) is then used to solve for the temperatures at the following step, T^+.

Equation (B.3) gives rise to a tridiagonal matrix equation and a simple elimination method is used to solve exactly the matrix equation. Two formulae are used to solve the tridiagonal system of equations according to the two types of boundary conditions:

(i) Both boundary temperatures specified

$$T^{+}_{j-1} = \Omega_{j-1}\, T_r + \psi_{j-1}$$

for $j = m, m-1, \ldots\ldots, 2$

where $T_r = T\ (y = H)$

$\psi_1 = T\ (y = 0)$

$\Omega_1 = 0$

and
$$\left.\begin{aligned} \Omega_j &= \frac{c_j}{b_j - a_j\, \Omega_{j-1}} \\ \psi_j &= \frac{d_j + a_j\, \psi_{j-1}}{b_j - a_j\, \Omega_{j-1}} \end{aligned}\right\} j = 2, 3, \ldots\ldots, m$$

(ii) Temperature specified at one boundary and temperature gradient at the other

$$T^{+}_{j+1} = \frac{T^{+}_j - \psi_j}{\Omega_j}$$

for $j = 1, 2, \ldots\ldots, m-1$

where $T^{+}_1 = T\ (y = 0)$

$$\psi_m = -\overline{\Delta y} \left(\frac{\partial T}{\partial y}\right)_{y=H}$$

$$\left.\begin{aligned} \text{and} \quad \Omega_{j-1} &= \frac{b_j - c_j/\Omega_{j-1}}{a_j} \\ \psi_{j-1} &= \frac{\psi_j\,(b_j - a_j\,\Omega_{j-1}) - d_j}{a_j} \end{aligned}\right\} j = m,\ m-1,\ \ldots\ldots,\ 2$$

Full derivation of these formulae can be found in [62].

B.2 Temperature Gradients at Boundaries

The temperature gradients at boundaries such as the melt/solid interface and barrel and shaft - e.g. point A in Figure B.1 - were evaluated numerically using the temperatures at the three points adjacent to the boundary.

i.e. $$\left(\frac{\partial T}{\partial y}\right)_A \simeq \frac{-3\,T_A + 4\,T_B - T_C}{2\Delta y}$$

with a truncation error of the order of $(\Delta y)^2$.

B.3 Solution of the Melting Equations

A simple Euler's method was used to solve for the differential equations of melting. Typically $\frac{dH}{dz} = F$ was replaced by:

$$\frac{H_{i+1} - H_i}{\Delta z} \simeq F_i$$

with a truncation error of the order of Δz. Given the solution at i,

$$H_{i+1} = \Delta z\, F_i + H_i$$

B.4 Newton-Raphson Iterative Method

Let $$F_i = F_i(x_1, x_2, \ldots\ldots, x_n) = F_i(x_i)$$

The solutions x_i of the equation

$$F_i(x_i) = 0 \qquad (B.4)$$

are required. If x_i^o are close to the solution x_i, then in general $x_i = x_i^o + h_i$ where h_i are small changes in the values of x_i. Using Taylor's expansion up to the first derivative only,

$$F_i(x_i^o + h_i) = F_i(x_i^o) + h_1\left(\frac{\partial F_i}{\partial x_1}\right)_{x_i^o} + h_2\left(\frac{\partial F_i}{\partial x_2}\right)_{x_i^o} + \ldots\ldots + h_n\left(\frac{\partial F_i}{\partial x_n}\right)_{x_i^o}$$

Since $x_i^o + h_i$ are the solutions of equation (B.4), $F_i(x_i^o + h_i) = 0$ and hence

$$0 = F_i\, x_i^o + h_1\left(\frac{\partial F_i}{\partial x_1}\right)_{x_i^o} + h_2\left(\frac{\partial F_i}{\partial x_2}\right)_{x_i^o} + \ldots\ldots + h_n\left(\frac{\partial F_i}{\partial x_n}\right)_{x_i^o} \qquad (B.5)$$

Expanding equation (B.5), the following matrix equation is obtained

$$\begin{bmatrix} \frac{\partial F_1}{\partial x_1} & \frac{\partial F_1}{\partial x_2} & \cdots & \frac{\partial F_1}{\partial x_n} \\ \frac{\partial F_2}{\partial x_1} & \frac{\partial F_2}{\partial x_2} & \cdots & \frac{\partial F_2}{\partial x_n} \\ \vdots & \vdots & & \vdots \\ \frac{\partial F_n}{\partial x_1} & \frac{\partial F_n}{\partial x_2} & \cdots & \frac{\partial F_n}{\partial x_n} \end{bmatrix}_{x_i^o} \begin{bmatrix} h_1 \\ h_2 \\ \vdots \\ h_n \end{bmatrix} = - \begin{bmatrix} F_1(x_i^o) \\ F_2(x_i^o) \\ \vdots \\ F_n(x_i^o) \end{bmatrix} \qquad (B.6)$$

The iterative method consists of:

(i) Estimating values for x_i^o and evaluating $F_i(x_i^o)$ and all the derivatives.

(ii) Solving for h_i in equation (B.6) using a Gaussian elimination method.

(iii) Improving the solutions by $x_i = x_i^o + h_i$ and using these values of x_i to start a new cycle of iteration.

(iv) The procedure was continued until convergence in the values of x_i occurred when $\max \left| \frac{h_i}{x_i} \right| < 0.00001$.

Note: The evaluation of $F_i(x_i^o)$ was straightforward given the functions $F_i(x_i)$. A numerical method was required for evaluating the derivatives, for example,

$$\left(\frac{\partial F_i}{\partial x_1}\right)_{x_i^o} = \frac{F_i(x_1^o + \delta x,\ x_2^o,\ \ldots.,\ x_n^o) - F_i(x_1^o,\ x_2^o,\ \ldots.,\ x_n^o)}{\delta x}$$

where δx was a small number, e.g. 0.00001.

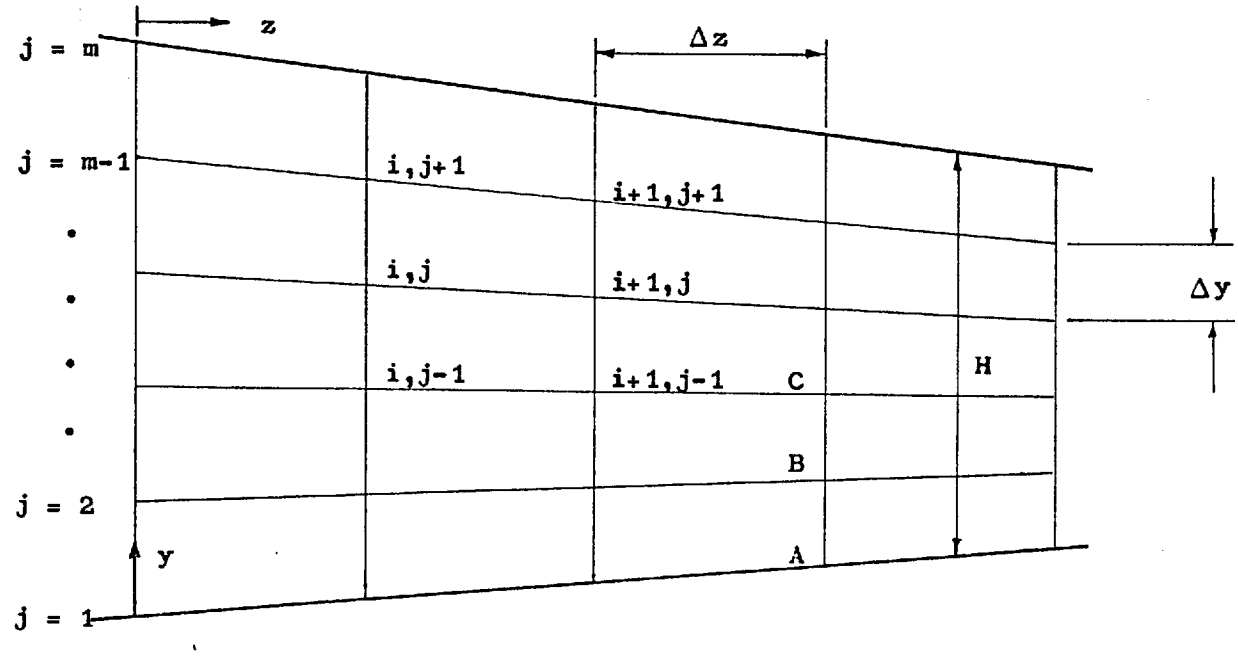

FIG. B.1 - GRID USED FOR NUMERICAL SOLUTION METHODS

APPENDIX C

NON-NEWTONIAN POLYMER MELT FLOW IN AN ANNULAR SLIT

The contents of this appendix are a summary of part of previous work [62] on polymer melt flow in the annular channel of the continuous ram extruder. For a narrow annular slit, a rectangular coordinate system was used and the flow region was assumed to be bounded by two flat plates. The coordinate system was, however, not truly rectangular in that a small degree of convergence or divergence of the plates was tolerated. The geometry and the grid used for the numerical solution of the equations were therefore similar to that shown in Figure B.1, with the x-direction perpendicular to the plane of the diagram.

The relevant equations of motion were

$$\frac{d}{dy}\left(\mu \frac{dv_x}{dy}\right) = 0 \quad \text{and} \quad \frac{d}{dy}\left(\mu \frac{dv_z}{dy}\right) = P_z \qquad (C.1)$$

with boundary conditions $v_x(y=0) = 0$ and $v_z(y=0) = 0$

$v_x(y=H) = V$ $\quad$ $v_z(y=H) = 0$

The equation of energy conservation was

$$\rho_m c_m v_z \frac{\delta T}{\delta z} = km \frac{\delta^2 T}{\delta y^2} + \mu \left[\left(\frac{dv_x}{dy}\right)^2 + \left(\frac{dv_z}{dy}\right)^2\right] \qquad (C.2)$$

with boundary conditions $T(y=0) = T_b(z)$

$T(y=H) = T_{shaft}(z)$ or $\left(\frac{\delta T}{\delta y}\right)_{y=H} = 0$ at all z

and $T(z=0) = T'(y)$

Equations (C.1) and (C.2) were coupled by

$$\mu = \mu_o \left[\left(\frac{dv_z}{dy}\right)^2 + \left(\frac{dv_x}{dy}\right)^2\right]^{\frac{n-1}{2}} \exp\left[-b\,(T - T_o)\right] \qquad (C.3)$$

The solution for the velocity profiles v_x and v_z was carried out in terms of dimensionless parameters. These were defined as

$$\left.\begin{aligned} W = \frac{v_z}{V} \quad , \quad U = \frac{v_x}{V} \quad , \quad Y = \frac{Y}{H} \\ T^* = b\,(T - T_{bo}) \quad \text{and} \quad \pi_p = \frac{P_z\, H}{\bar{\tau}} \end{aligned}\right\} \quad (C.4)$$

where $T_{bo} = T_b \ (z = 0)$

and $$\bar{\tau} = \mu_o \left| \frac{V}{H} \right|^n \exp \left[- b\,(T_b - T_o) \right]$$

Because H could vary with z, some of the dimensionless parameters were also defined with reference to H_o at $z = 0$,

$$\text{e.g.} \quad \pi_{p_o} = \frac{P_z\, H_o}{\bar{\tau}_o} \quad \text{with} \quad \bar{\tau}_o = \mu_o \left| \frac{V}{H_o} \right|^n \exp \left[- b\,(T_{bo} - T_o) \right]$$

Substituting equations (C.3) and (C.4) into equations (C.1) and after some rearrangement

$$\left.\begin{aligned} \pi_p &= \frac{d}{dY} \left[\frac{dW}{dY} \left(\sqrt{4I_2'} \right)^{n-1} \exp \left(- T^* \right) \right] \exp \left(T_b^* \right) \\ 0 &= \frac{d}{dY} \left[\frac{dU}{dY} \left(\sqrt{4I_2'} \right)^{n-1} \exp \left(- T^* \right) \right] \exp \left(T_b^* \right) \end{aligned}\right\} \quad (C.5)$$

where $4I_2' = \left(\frac{dW}{dY} \right)^2 + \left(\frac{dU}{dY} \right)^2$

Integrating equations (C.5) and after some algebraic manipulation,

$$\frac{dW}{dY} = \pi_p \,(Y - Y_o)\, G\,\{Y\}$$

$$\frac{dU}{dY} = \Phi\, G\,\{Y\}$$

$$\text{where} \quad G\{Y\} = \left[(\pi_P Y - \pi_P Y_o)^2 + \Phi^2\right]^{\frac{n-1}{2n}} \exp\left(\frac{T^* - T_b^*}{n}\right) \qquad (C.6)$$

and Y_o and Φ are constants of integration. The velocity profiles were obtained as

$$\left.\begin{aligned} W &= \pi_P \int_o^Y (\alpha_v - Y_o)\, G\{\alpha_v\}\, d\alpha_v + A \\ \text{and} \quad U &= \Phi \int_o^Y G\{\alpha_v\}\, d\alpha_v + B \end{aligned}\right\} \qquad (C.7)$$

where α_v is a dummy variable and A = B = 0 because U(Y=0) = W(Y=0) = 0.

The dimensionless volumetric flow rate π_Q was obtained as

$$\pi_Q = \frac{Q}{C\,H\,V} = \pi_P \left[(1 + Y_o)\, J_1 - J_2 - Y_o\, J_o\right] \qquad (C.8)$$

where Q is the volumetric flow rate, C is the mean circumference of the annular slit and

$$J_m = \int_o^1 \alpha_v^m\, G\{\alpha_v\}\, d\alpha_v$$

In order to evaluate the velocity profiles in equations (C.7) it was necessary to determine π_P, Y_o and Φ beforehand. Given the volumetric flow rate, equation (C.8) expresses a relationship between the three variables π_P, Y_o and Φ. Two further equations were obtained from equations (C.7) using U(Y=1) = 1 and W(Y=1) = 0 as

$$0 = \pi_P (J_1 - Y_o J_o) \qquad (C.9)$$

and $$1 = \Phi J_o \qquad (C.10)$$

Equations (C.8), (C.9) and (C.10) were then used to solve for the three unknown parameters for a given π_Q. These were rewritten as

$$F_1 = 0 = \pi_P + J_o \pi_Q/(J_o J_2 - J_1^2)$$

$$F_2 = 0 = \pi_P Y_o + J_1 \pi_Q/(J_o J_2 - J_1^2)$$

and $$F_3 = 0 = \Phi - 1/J_o$$

i.e. $F_i(x_i) = 0$ where $x_1 = \pi_P$, $x_2 = \Phi$ and $x_3 = \pi_P Y_o$.

Given initial estimates x_i^o, the solution was obtained using the Newton-Raphson iterative method described in Appendix B. The initial estimates were obtained from a Newtonian analysis and these were [62]:

$$\pi_P = -12\ \pi_Q$$

$$\pi_P Y_o = -6\ \pi_Q$$

and $$\Phi = 1$$

Note that in equation (C.6) the temperatures T* were required. At the start, i.e. at z = 0, these were specified as a known boundary condition T'(y). Thus, the equations of motion were effectively uncoupled from the energy conservation equation. The velocities therefore changed with z only because T changed with z due to the thermal convection term $(\rho_m c_m v_z \frac{\partial T}{\partial z})$ in equation (C.2). Further discussion on

this topic can be found in [62].

Before the velocity profiles could be evaluated at the following downstream position, the temperature profile was required at the new position. This was obtained by solving equation (C.2) with the appropriate boundary conditions using the numerical method described in Appendix B. The solution was then propagated until either the changes in the temperature profiles at two successive steps were negligible when thermally fully developed flow was achieved, or when the length z exceeded the physical length of the flow channel.